

A Compositional Assessment of the
Enormous South Pole - Aitken Basin
Grounded in Laboratory Spectroscopy of
Pyroxene-Bearing Materials

By

Daniel Patrick Moriarty III

B.S., The University of Massachusetts, 2009

Sc.M., Brown University, 2012

A dissertation

Submitted in partial fulfillment of the requirements for the degree of
Doctor of Philosophy in the Program of Earth, Environmental, and
Planetary Sciences at Brown University

Providence, Rhode Island

May, 2016

© Copyright 2016 by Daniel Patrick Moriarty III

This dissertation by Daniel P. Moriarty III is accepted in its present form by the Department of Geological Sciences as satisfying the dissertation requirement for the degree of Doctor of Philosophy.

Date

Professor Carle M. Pieters, Brown University, Advisor

Recommended to the Graduate Council

Date

Professor James W. Head, Brown University, Reader

Date

Professor E. Marc Parmentier, Brown University, Reader

Date

Professor Stephen W. Parman, Brown University Reader

Date

Professor Jessica Sunshine, University of Maryland, Reader

Approved by the Graduate Council

Date

Peter M. Weber
Dean of the Graduate School

CURRICULUM VITAE

Daniel Patrick Moriarty III

Brown University

Department of Earth, Environmental, and Planetary Sciences

324 Brook Street | Providence, RI 02912

401.258.7926 | Daniel_Moriarty@Brown.edu

Education

Brown University

Ph.D. in Earth, Environmental, and Planetary Sciences

Advisor: Dr. Carlé Pieters

Thesis Title: A Compositional Assessment of the Enormous
South Pole - Aitken Basin Grounded in Laboratory
Spectroscopy of Pyroxene-Bearing Materials

Providence, RI

Expected May 2016

Brown University

Sc.M. in Geological Sciences

Advisor: Dr. Carlé Pieters

Thesis Title: Compositional Heterogeneity of Central Peaks
within the South Pole - Aitken Basin

Providence, RI

May 2012

University of Massachusetts

B.S. in Physics

B.S. in Astrophysics

Advisor: Dr. Grant Wilson

Thesis Title: IDL to C++ Translation of the AzTEC
Submillimeter Camera Data Pipeline

Amherst, MA

May 2009

Employment

Johns Hopkins University Applied Physics Lab

Advisor: Karl Hibbitts

Position: Laboratory Assistant

Responsibilities: FTIR spectroscopy (transmission and
reflectance) of lunar and cometary materials; Design,
maintenance, and implementation of ultra-high vacuum
environment chamber; Water/ice deposition and desorption
experiments

Laurel, MD

2009-2010

First-Authored Publications

Moriarty III, D. P. and C. M. Pieters (2016), Complexities in pyroxene compositions derived from absorption band centers: Examples from Apollo samples, HED meteorites, synthetic pure pyroxenes, and remote sensing data, *Meteoritics and Planetary Science*, doi: 10.1111/maps.12588.

Moriarty III, D. P. and C. M. Pieters (2015), The nature and origin of Mafic Mound in the South Pole - Aitken Basin, *Geophysical Research Letters*, 42:19:7907-7915, doi: 10.1002/2015GL065718.

Moriarty III, D. P., C. M. Pieters, and P. J. Isaacson (2013), Compositional heterogeneity of central peaks within the South Pole-Aitken Basin, *Journal of Geophysical Research*, 118, 2310-2322, doi: 10.1002/2013JE004376.

In preparation:

Moriarty III, D. P. and C. M. Pieters (in preparation), The character of South Pole - Aitken I: Patterns of surface and sub-surface composition.

Moriarty III, D. P. and C. M. Pieters (in preparation), The character of South Pole - Aitken II: Models of crust/mantle stratigraphy.

Co-Authored Publications

Pieters, C. M., K. Donaldson Hanna, L. Cheek, D. Dhingra, T. Prissel, C. Jackson, **D. Moriarty**, S. Parman, and L. A. Taylor (2014), The distribution of Mg-spinel across the Moon and constraints on crustal origin, *American Mineralogist*, 99:1893-1910, doi: 10.2138/am-2014-4776.

Cheek, L. C., C. M. Pieters, J. W. Boardman, R. N. Clark, J. P. Combe, J. W. Head, P. J. Isaacson, T. B. McCord, **D. Moriarty**, J. W. Nettles, N. E. Petro, J. M. Sunshine, and L. A. Taylor (2011), Goldschmidt crater and the Moon's north polar region: Results from the Moon Mineralogy Mapper (M3), *Journal of Geophysical Research E: Planets*, 116:2, doi: 10.1029/2010JE003702.

In preparation:

Prissel, T. C., **D. P. Moriarty III**, C. M. Pieters, J. W. Head, and S. W. Parman (in preparation), Characterization and identification of low-FeO, high Al₂O₃ extrusive deposits on the Moon by VNIR spectroscopy.

Extended Abstracts (First-Authored Only)

Moriarty III, D. P. and C. M. Pieters (2016), South Pole - Aitken Basin as a probe to the lunar interior, *Lunar Planet. Sci. Conf.*, XLVII, abstract 1763.

Moriarty III, D. P. and C. M. Pieters (2016), Impact melt and magmatic processes in central South Pole - Aitken Basin, *Lunar Planet. Sci. Conf.*, XLVII, abstract 1735.

Moriarty III, D. P. and C. M. Pieters (2015), The composition of Mafic Mound: An unusual feature within the South Pole - Aitken Basin, *Lunar Planet. Sci. Conf.*, XLVI, abstract 2105. (Oral Presentation)

- Moriarty III, D. P.** and C. M. Pieters (2015), Compositional diversity across the Humboldtianum Basin, *Lunar Planet. Sci. Conf.*, XLVI, abstract 2100. (Poster Presentation)
- Moriarty III, D. P.** and C. M. Pieters (2014), LSCC samples as ground truth: Using spectral parameters developed for M³ to assess composition and maturity, *Lunar Planet. Sci. Conf.*, XLV, abstract 2532. (Poster Presentation)
- Moriarty III, D. P.** and C. M. Pieters (2014), Evaluation of stratigraphy at the South Pole – Aitken Basin: From local to regional, *Lunar Planet. Sci. Conf.*, XLV, abstract 2516. (Oral Presentation)
- Moriarty III, D. P.**, P. J. Isaacson, and C. M. Pieters (2013), NW-Central South Pole – Aitken: Compositional diversity, geologic context, and implications for basin evolution, *Lunar Planet. Sci. Conf.*, XLIV, abstract 3039. (Oral Presentation)
- Moriarty III, D. P.**, C. M. Pieters, N. Petro, and P. J. Isaacson (2012), Compositional heterogeneity within lunar central peaks, *Lunar Planet. Sci. Conf.*, XLIII, abstract 2399. (Poster Presentation)
- Moriarty III, D. P.**, C. M. Pieters, J. W. Nettles, P. J. Isaacson, L. Cheek, J. W. Head III, S. Tompkins, and N. E. Petro (2011), Finsen and Alder: A compositional study of lunar central peak craters in the South Pole-Aitken basin, *Lunar Planet. Sci. Conf.*, XLII, abstract 2564. (Poster Presentation)
- Moriarty III, D. P.**, C. A. Hibbitts, C. M. Lisse, M. D. Dyar, G. Harlow, D. Ebel, and R. Peale (2010), Near-far IR spectra of sulfide minerals relevant to comets, *Lunar Planet. Sci. Conf.*, XLI, abstract 2447. (Poster Presentation)

Additional Science Talks

- November 2015: Brown University Department of Earth, Environmental, and Planetary Sciences Lunch Bunch / SSERVI Seminar. “South Pole - Aitken Basin: Investigating the Moon's Largest Mysteries”
- July 2015: SSERVI Exploration Science Forum. "The Nature and Origin of Mafic Mound within the South Pole - Aitken Basin"
- April 2015: Brown University Department of Earth, Environmental, and Planetary Sciences Lunch Bunch / SSERVI Seminar. “The Nature and Origin of Mafic Mound in the South Pole - Aitken Basin”
- July 2014: SSERVI Exploration Science Forum. “The Diverse Local and Regional Stratigraphy of the South Pole – Aitken Basin”
- February 2013: Brown University Department of Geological Sciences Lunch Bunch. “The South Pole – Aitken Basin: Compositional Diversity, Geologic Context, and Implications for Basin Evolution from Moon Mineralogy Mapper Spectral Parameters.
- April 2012: Brown University Department of Geological Sciences Lunch Bunch. “Compositional Heterogeneity of Central Peaks within the South Pole -Aitken Basin”

Teaching, Service, and Honors

Teaching Assistant Course: GEOL0220 Physical Processes in Geology Instructors: Dr. Jan Tullis, Dr. Karen Fischer	Brown University Spring 2016
Member Diversity Working Group, Department of Earth, Environmental, and Planetary Sciences,	Brown University 2015-Present
Safety Officer GeoClub	Brown University 2014-2015
Member Organizing Committee	SSERVI LunGradCon 2014
Teaching Assistant Course: GEOL0220 Physical Processes in Geology Instructors: Dr. Jan Tullis, Dr. Karen Fischer	Brown University Fall 2014
Recipient Barringer Travel Grant	LMPEV 2013
Member RELAB Database Working Group	Brown University 2012-2013
Member Asteroid and Lunar Environment Chamber Working Group	Brown University 2011-2012
Recipient First Year Graduate Fellowship	Brown University 2010-2011

Technical Skills

Laboratory preparation of geologic materials; FTIR spectroscopy; Interactive Data Language programming; ASD Field Spec; C++ programming; Kaleidagraph; General use and maintenance of environment chambers; ESRI ArcGIS; Exelis ENVI; USGS ISIS; Adobe Creative Suite (Illustrator, Photoshop, InDesign); Various sound and video editing programs; and MS Office (Word, PowerPoint, Excel).

ACKNOWLEDGEMENTS

I am deeply thankful to my advisor, Carlé Pieters. My first few semesters at Brown were a struggle, and I probably didn't deserve to continue on in the graduate program after receiving my master's degree. Carlé was very honest with me about the severity of the situation. I was fairly discouraged, but after some soul searching I realized I did not want to squander the very special opportunity I had as a graduate student in one of the best planetary science programs in the world.

Over the next year, Carlé worked intensively with me to improve my focus and working habits. Along with my committee, (Jack Mustard and Marc Parmentier at the time), we developed a plan to get me back on track academically. The plan worked, and a year later I was able to pass my Preliminary Examination. I really appreciate Carlé's (and my committee's) patience and understanding. Thank you for the second chance.

Carlé is a wonderful advisor and a model scientist. Carlé's brilliance, work ethic, leadership, and warmth are truly inspirational. Although I have never met anyone who travels quite as much as Carlé, she is always available, responsive, and enthusiastic about discussing science with her graduate students. I am honored to have learned from one of the greatest scientists to ever study the Moon.

Over the years, my committee has provided excellent guidance and structure. Thank you to Jack and Marc, who have been with me since the beginning and helped me settle in after a rough start. Thanks as well to Steve Parman and Amy Barr, who joined my committee for my Preliminary Examination. Steve has provided great feedback ever since, and has really helped sharpen my understanding of pyroxene behavior. Through classes and research discussions, Amy reshaped the way I thought about impacts and

planetary science in general. Never have I met a better teacher. I am also indebted to Jim Head, who has joined my committee for my thesis defense. Although he officially joined only recently, I have met with Jim many times over the years to discuss research, and he has been an integral part of the team. I am incredibly fortunate to have such an accomplished committee.

Thank you to Jessica Sunshine, my outside reader. I appreciate your willingness and enthusiasm to be a part of the thesis defense, and greatly look forward to your feedback.

I am thankful to many other Brown faculty and staff members for their help along the way. Pete Schultz has helped me understand impact processes, and always has really thoughtful feedback on research. Ralph Milliken has inspired more detailed spectral analyses, and has greatly helped to clarify figures in several of my papers. Jeff Nettles was my first resource when I started at Brown, showing me the ropes of working with M^3 data. Takahiro Hiroi was an immense help while learning sample preparation and data collection in RELAB, and also provides excellent feedback on research. Jay Dickson is an invaluable asset for help with ArcGIS and lunar datasets. Bill Collins, Bill Fripp, Henry Johnson, and Margaret Doll have kept the research machine well oiled and running smoothly, with few exceptions. The administrative staff in both the front office and Lincoln Field has graciously handled last-minute requests and paperwork, helping me to focus on science while dealing with deadlines and other stressors.

At Brown, we have a fairly close-knit community of graduate students and post-docs. My peers were incredibly helpful throughout my graduate studies. "Team Carle" has been an invaluable asset throughout my time at Brown. Leah, Kerri, Deepak, Sandra,

and Peter were always available to answer questions, and each helped me mature as a graduate student, either through advice or acting as a role-model. Thank you for teaching me how to be "professional." Noah, my awesome officemate of several years, taught me how one can be a little "unprofessional," but still accomplish excellent research! Kei, thanks for being a great housemate! Excellent research discussions were had with a number of other graduate students, including Tabb Prissel, David Hollinbaugh Baker, Jennifer Whitten, Colin Jackson, Lauren Jozwiak, and Will Vaughan. I am lucky to consider many other grad students in the department friends, and you all helped at some point in the journey.

I must thank those who helped me get started in planetary science: Grant Wilson, for taking me on as an undergraduate student in astronomy at UMass and giving me my first real research project; Darby Dyar, for showing me the world of planetary science and introducing me to Karl and Carlé; and Karl Hibbitts, for hiring me as a laboratory assistant straight out of undergrad and challenging me to go back to graduate school and become something more than a "lab rat."

Of course, I couldn't have done it without my family and friends. I'm in a pretty unique scenario based on the fact that I grew up fifteen miles from Brown. While this may have been distracting at times, I really felt "at home" my entire time at Brown. Throughout everything, my parents have been my biggest supporters, going as far as to put me up while dealing with housing lapses or broken bones. Speaking of, thanks to the staff at Rhode Island Hospital, South County Hospital, University Orthopedics, South County Orthopedics, and Brown Health Services for, if not keeping me in one piece, at least being able to put the pieces back together. My brother Kyle is my best friend and an

inspiration, holding down a physical education job while studying for his masters degree and somehow becoming one of the best professional disc golfers in the world. My grandmother has also been a wonderful help, doing the occasional load of my laundry, sewing buttons back on shirts, and making the best pancakes ever served. My grandfather passed away last Fall, and the outpouring of support from extended family and friends really helped the grieving process, especially as I was in the heat of thesis preparation. Thanks to Chelsea, who has stood by my side through almost everything. And thanks to Nick, Pete, Harry, Dean, and Dan: playing music with you guys has helped me get through a lot of tough times. Joe and Pat from the Rocket Truck: you guys make awesome food, and you were my only social interaction for the months leading up to my Prelims. Thanks for becoming great friends! To all my friends, family, peers, and mentors who I haven't had space to name: you have all made a positive impact on my life and studies, and I am extremely grateful.

TABLE OF CONTENTS

Table of Contents

A Compositional Assessment of the Enormous South Pole - Aitken Basin Grounded in Laboratory Spectroscopy of Pyroxene-Bearing Materials	i
CURRICULUM VITAE.....	iv
ACKNOWLEDGEMENTS	viii
TABLE OF CONTENTS	xii
INTRODUCTION.....	1
References	7
CHAPTER 1: Complexities in pyroxene compositions derived from absorption band centers: Examples from Apollo samples, HED meteorites, synthetic pure pyroxenes, and remote sensing data.....	12
Abstract	13
1 Introduction.....	14
2 Background.....	15
2.1 The Origin of Pyroxene Absorption Bands in the NIR	16
2.2 Modeling Pyroxene Absorptions	18
2.3 Pyroxene Composition and Spectral Properties	20
2.3.1 Effects of $Mg^{2+}/Ca^{2+}/Fe^{2+}$ and crystal structure on the 1 μm and 2 μm band	20
2.3.2 The 1.2 μm band: Fe^{2+} in the M1 cation site	23
2.4 Description of Sample Collections	24
2.4.1 Synthetic Pyroxenes	24
2.4.2 Lunar Rock and Mineral Characterization Consortium Mineral Separates	26

2.4.3	Howardite, Eucrite, and Diogenite Meteorites	28
2.4.4	Lunar Soil Characterization Consortium Soils	29
2.5	Remote Sensing Example: Moon Mineralogy Mapper	31
3	The PLC Technique	31
3.1	Linear Continuum Fitting and Removal	32
3.2	Parabolic Fits of Absorption Bands	34
4	Results	35
4.1	Synthetic Pyroxene Band Centers.....	35
4.2	LRMCC Band Centers	37
4.3	HED Band Centers.....	38
4.4	LSCC Band Centers.....	38
5	Discussion.....	39
5.1	Composition - Band Center Relationships for Synthetic Pyroxenes as Measured by PLC ...	39
5.2	Composition - Band Center Relationships for Natural Pyroxenes	40
5.3	Composition - Band Center Relationships for Pyroxene Mixtures.....	41
5.4	Effects of the 1.2 μm Band on the 1 μm Band Center	46
6	The Humboldtianum Region as seen by M^3.....	47
6.1	Overview and Approach	47
6.2	PLC Results from Humboldtianum.....	49
6.3	Geologic Implications.....	51
7	Conclusions	52
8	Acknowledgements.....	56
9	References	57
10	Tables.....	69
11	Figure Captions.....	70
12	Figures	76

CHAPTER 2: The nature and origin of Mafic Mound in the South Pole - Aitken

Basin	96
Abstract	97
1 Introduction and Background.....	98
2 Observations	99
2.1 Composition	99
2.1.1 SPA HCP-Bearing Materials.....	100
2.1.2 Modified Craters in Central SPA	101
2.2 Morphology Topography, and Gravity	103
3 The Origin of Mafic Mound	104
3.1 Evaluation of Mafic Mound Formation Resulting from Common Lunar Processes.....	104
3.1.1 Uplifted Mantle	104
3.1.2 Compositionally Distinct Impact Melt	105
3.1.3 Basalt-Filled Impact Crater	106
3.1.4 Volcanic Construct.....	107
3.2 A Hybrid Origin for Mafic Mound	108
4 Conclusions	110
5 Acknowledgements.....	111
6 References	111
7 Figure Captions	119
8 Figures.....	121
CHAPTER 3: The composition and topography of an extensive resurfacing deposit	
in central South Pole - Aitken Basin	125
Abstract	126
1 Introduction.....	126

2	Background:	128
2.1	The Formation and Composition of SPA	128
2.2	M ³ Data and PLC Analysis.....	129
3	Deriving Compositional Information from M³ Spectra	130
4	Properties of Central SPA	132
4.1	Topographic Structure of SPA.....	132
4.2	A Distinctive Compositional Zone in Central SPA.....	133
4.3	Spatial Extent of SPACA	135
4.4	The Composition of SPACA Materials.....	136
5	Possible Origin of the SPACA	138
5.1	Impact Melt.....	138
5.2	Magmatic Resurfacing	139
5.3	Discussion.....	140
6	Conclusions	142
7	Acknowledgements	143
8	References	143
	Figures and Captions.....	152
CHAPTER 4: Pyroxene Abundance and Composition across the South Pole - Aitken Basin		162
	Abstract	163
1	Introduction	163
2	Background	164
2.1	The Composition of SPA.....	164
2.2	The Lunar Stratigraphy	166
3	Data and Methods	167

4	Results: The Compositional Structure of SPA	170
4.1	Pyroxene Abundance from Diagnostic Absorption Band Depths	170
4.2	Pyroxene Composition from Diagnostic Absorption Band Centers.....	171
4.3	Distinct Compositional Zones within SPA	173
5	Origin of Mg-rich Pyroxene-Bearing Materials within SPA	174
6	Summary	177
7	Acknowledgements.....	178
8	References	178
	Table 1: Large Impact Structures in the SPA Region	186
	Figures and Captions.....	188
	CHAPTER 5: Synthesis.....	197
1	Introduction	198
2	Summary of Major Findings from Chapters 1-4.....	198
2.1	Fundamental Spectroscopy of Pyroxene-Bearing Materials	198
2.2	The Nature and Origin of Mafic Mound	200
2.3	The Compositional Structure of South Pole - Aitken Basin	201
2.3.1	The SPA Compositional Anomaly and Central Depression	201
2.3.2	The Mg-Pyroxene Annulus	202
2.3.3	The Heterogeneous Annulus	203
2.3.4	South Pole - Aitken Exterior	203
3	Interpretation and Implications of South Pole - Aitken's Compositional Structure	203
3.1	The Stratigraphy of South Pole - Aitken Basin.....	204
3.2	South Pole - Aitken as a Probe to the Lunar Interior	207
3.3	Origin of the Central Depression	215
3.4	Origin of the South Pole - Aitken Compositional Anomaly	215

4	Summary.....	219
5	Outstanding Issues and Future Directions.....	220
6	References.....	222
	Figures and Captions.....	230
Appendix A: Description of the PLC technique and supplemental figures for		
	Chapter 1	233
	The PLC Method:.....	234
	Table S1: PLC Parameter Values for the Example Spectra.....	238
	Supplemental Figures.....	239
Appendix B: Location and description of all spectral and topographic observations		
	(Chapter 2).....	245
Appendix C: Supplemental Figures for Chapter 2.....		
		258
Appendix D: Supplemental Spectra for Chapters 3,4,5		
		267

INTRODUCTION

The past several years of lunar exploration have rewarded lunar geologists with a suite of rich, powerful, and diverse data. The Lunar Reconnaissance Orbiter Camera (LOLA) [Robinson *et al.*, 2010] has changed the way we see the Moon, offering a glimpse of the lunar surface with sub-meter scale spatial resolution. The Gravity Recovery and Interior Laboratory (GRAIL) [Zuber *et al.*, 2010] has allowed us to peer beyond the lunar surface, revealing unseen masses that lie beneath. The Lunar Orbiter Laser Altimeter (LOLA) [Smith *et al.*, 2010] affords an understanding of the shape of the Moon with unprecedented precision. The Moon Mineralogy Mapper (M³) [Pieters *et al.*, 2009a] captures complex, systematic interactions between sunlight and surface materials, painting a colorful compositional picture. The integrated use of these extensive and versatile datasets allow lunar scientists to investigate long-standing lunar mysteries in a level of detail never before possible.

One such mystery is the nature of the vast, ancient South Pole - Aitken Basin on the lunar farside. First mapped in 1978 [by *Stuart-Alexander*], SPA is more than 2200 km across and 12 km deep [Spudis *et al.*, 1994; Garrick-Bethell and Zuber, 2009]. SPA is the largest confirmed impact basin on the Moon, and possibly the entire solar system. Because of its massive size and age, SPA is central to several fundamental issues in lunar and planetary science.

South Pole - Aitken Basin can serve as a probe to the lunar interior, revealing the compositional structure of the lithosphere. The materials excavated by the SPA-forming impact are thought to be among the deepest available for study on the lunar

surface. Therefore, the study of SPA materials can help us to understand the composition of the lower crust and possibly upper mantle. This information can help to inform models of lunar evolution, including processes such as magma ocean crystallization, mantle overturn, and formation of the Mg-suite.

As the largest impact basin on the Moon, **SPA can serve as an endmember to constrain models of impact basin formation and evolution.** Impacts are one of the most important processes in shaping both planetary surfaces and the solar system at large. SPA provides a key link between small, localized impact craters and the giant impacts that exert influence on a planetary scale. Impact basin formation is a dynamic process that vaporizes, melts, displaces, and excavates target materials, with the potential to form local melt seas [Warren *et al.* 1996; Morrison, 1998; Hurwitz and Kring; 2014; Vaughan and Head, 2014] or affect the thermodynamics of the underlying mantle [Elkins-Tanton and Hagar, 2005]. In addition to these localized effects, large impacts have been theorized to trigger geochemical and geophysical effects over a global scale, such as antipodal and/or global magma production and ascent [Schultz and Crawford, 2011; Kring *et al.*, 2015] or even (d) cumulate overturn of the mantle [Kring *et al.*, 2015]. Through the study of SPA, the formation and evolution of large impact structures can be better understood.

In addition to being the largest impact basin on the moon, SPA is also the oldest [Wilhelms *et al.*; 1987]. **Establishing an absolute age for SPA can anchor the lunar chronology derived from crater counting.** Given the global coverage and high spatial resolution of modern topography and imagery data, an absolute age for SPA would allow ages for other areas of the lunar surface to be accurately measured.

Of course, the best way to arrive at definitive answers to these science questions is through analysis of samples returned from South Pole - Aitken. SPA sample return has been designated a high-priority target by the *National Research Council* [2003; 2011], and a sample return mission (**Moonrise**) has been proposed by *Jolliff et al.* [e.g. 2003]. While such a mission may be years from fruition, integrated remote sensing analyses can continue to address some of the outstanding science issues in the interim. Additionally, remote sensing data can guide landing site selection and mission design, optimizing the science return from future missions.

In this dissertation, we examine several aspects of the South Pole - Aitken Basin with modern remote sensing data. Our primary analyses are grounded in compositional assessments from M³ and are supplemented with additional data from, LOLA, LROC, GRAIL, and sample analyses.

The Moon Mineralogy Mapper was an imaging spectrometer with unprecedented spectral and spatial resolution. M³ returned terabytes of complex hyperspectral data. This rich dataset has many potential applications, from the identification and quantification of water across the lunar surface [*Pieters et al.*, 2009b] to the investigation of the enigmatic lunar swirls [*Pieters et al.*, 2014]. Sensitive to near-infrared light, the instrument was designed to resolve crystal field absorptions of silicate minerals comprising the lunar surface. The shape, strength, and position of these crystal field absorptions are often highly diagnostic of mineralogy [e.g. *Burns*, 1993] and can be used in tandem with other spectral properties to identify and characterize lunar materials.

M³ is well-suited for mineralogical analyses of SPA. Compositional variations across SPA are dominated by differences in the abundance and composition of pyroxenes

[e.g. *Pieters et al.*, 2001]. Pyroxenes exhibit diagnostic 1 μm and 2 μm absorption bands that reflect their composition and abundance. Since M^3 fully resolves these absorption bands, it effectively captures the primary compositional variations across the basin.

In lunar pyroxenes, mineralogical variations are dominated by the abundances of Fe, Mg, and Ca in the octahedral cation site. Using synthetic pure pyroxenes, *Klima et al.* [2007; 2011] quantified the highly systematic relationship between Fe,Mg,Ca content in the octahedral cation site and the 1 μm and 2 μm absorption band centers. While these relationships are useful to guide interpretation of pyroxene band centers in remote sensing data, it is important to consider the complex optical properties of natural pyroxene-bearing materials in order to make well-justified compositional interpretations.

Assessing the complex nature of natural material spectra is the subject of **Chapter 1**. In this chapter, we incorporate spectral and compositional laboratory analyses of four pyroxene-bearing sample collections: synthetic pure pyroxenes [*Klima et al.*, 2007; 2011], Lunar Rock and Mineral Characterization Consortium basaltic rocks [*Isaacson et al.*, 2011], Lunar Soil Characterization Consortium mare and non-mare soils [*Noble et al.*, 2006], and Howardite-Eucrite-Diogenite meteorites. The chapter investigates how the systematic relationships between Fe,Mg,Ca content and absorption band centers are propagated through the complex optical properties inherent in natural materials. Such complexities include physical mixing of multiple rock types, mineral assemblages with multiple distinct pyroxene and non-pyroxene phases, and small compositional variations within individual pyroxene phases due to zoning or other natural crystallization processes. Because of these complexities, band center measurements are shown to be non-unique in that they do not robustly predict the presence of specific pyroxene components. Rather, 1 μm and 2 μm bands for natural materials are composite bands arising from the presence of many individual pyroxene and non-pyroxene components interacting non-linearly. However, relative relationships between band centers and Fe,Mg,Ca content are preserved and can be used

to identify and characterize compositional diversity in remote sensing data. This approach is applied to M³ target-mode data from the Humboldtianum Basin, identifying four distinct lithologies. Additional discussion of this approach is presented in Chapter 3. Chapter 1 also describes and validates the Parabola and Linear Continuum (PLC) method for quantifying absorption band properties and continuum slopes. Chapter 1 has been published in *Meteoritics and Planetary Science* [Moriarty and Pieters, 2016].

Chapter 2 investigates the nature and origin of "Mafic Mound" in central SPA. Mafic Mound is an unusual compositional and topographic feature ~1 km high and ~75 km across. Using PLC analyses of M³ data, Mafic Mound is shown to have a similar average pyroxene composition to mare basalts. However, Mafic Mound materials are brighter than mare basalts, suggesting a different mineral assemblage. Through compositional and topographic analyses, Mafic Mound is shown to be dissimilar to a suite of nearby flooded craters. Instead, the mound is topographically similar to various lunar volcanic domes and complexes, and exhibits a volumetrically homogeneous composition consistent with such structures. Mafic Mound also exhibits a positive Bouguer anomaly, suggesting that it is not simply a surface feature. Based on its elevated topography, unusual homogeneous composition, positive Bouguer anomaly, and location in the center of SPA, Mafic Mound is interpreted to be a magmatic construct related to the formation and evolution of SPA. Chapter 2 has been published in *Geophysical Research Letters* [Moriarty and Pieters, 2015].

Chapter 3 investigates the geology of central SPA. Using LOLA topography, a roughly elliptical central depression is identified that may represent the extent of a thick central melt sheet. Much of this central depression exhibits relatively smooth terrain and a relative paucity of impact craters. This smooth terrain continues across an irregular region of slightly higher topography directly to the north. Several impact craters within these regions appear flooded and/or buried. The surface of this smooth region exhibits a roughly similar average pyroxene composition to mare basalts, but with slightly lower Ca (and possibly Fe). This is unusual for

SPA, as most non-mare materials in the basin exhibit Mg-rich, low-Ca pyroxene-bearing compositions. Based on these observations, a "central **SPA** **C**ompositional **A**nomaly" (SPACA) is identified. Characteristic SPACA materials are exposed in the walls and peaks of several large craters throughout the region, suggesting the presence of a ~5 km thick deposit. Several central peaks in the region expose Mg-rich pyroxene-bearing materials, placing an upper limit of ~10 km on the thickness of the SPACA deposit. Considering these observations, SPA impact melt and volcanic flooding are evaluated as possible origin scenarios for the SPACA region. Based on the paucity of impact craters and series of filled/buried craters, volcanic flooding appears to be the most consistent scenario. This would require a somewhat unusual magma composition, as the SPACA materials do not resemble typical mare basalts observed elsewhere SPA.

Chapter 4 continues the geologic investigation of SPA, identifying, characterizing, and mapping materials excavated and exposed in the SPA-forming impact. Outside of SPACA, the mafic component of non-mare materials is dominated by Mg-rich pyroxenes. Immediately outside of SPACA, SPA materials exhibit uniformly high pyroxene abundance. These materials are exposed in a range of craters, from small (~1 km) to very large (~500 km). This thick, extensive "Mg-Pyroxene Annulus" is interpreted to represent remnant portions of the SPA transient cavity and therefore exposes abundant materials from beneath the feldspathic crust. Outside of the Mg-Pyroxene Annulus, feldspathic materials are heterogeneously interspersed with localized Mg-rich pyroxene-bearing deposits. This "Heterogeneous Annulus" is interpreted to represent proximal SPA ejecta mixed with a feldspathic crustal substrate.

Chapter 5 presents a synthesis of the first four chapters, including the overall conclusions and outstanding questions. Specifically, we combine compositional observations with geologic context and impact models to infer the general stratigraphy of SPA, as well as the origin of the SPACA resurfacing material and Mg-Pyroxene Annulus material excavated during the basin-forming impact. Future research directions are also discussed. Chapters 3, 4, and 5 are

being prepared for publication as two separate papers discussing the compositional structure and evolution of SPA, to be submitted to the Journal of Geophysical Research.

References

Burns R. G. 1993. *Mineralogical applications of crystal field theory*, 2nd ed. Cambridge, UK: Cambridge University Press. 551.

Elkins-Tanton, L. T. and B. H. Hager (2005), Giant meteoroid impacts can cause volcanism, *Earth and Planet. Sci. Let.*, 239, 219-232.

Garrick-Bethell, I. and M. T. Zuber (2009), Elliptical structure of the lunar South Pole-Aitken basin, *Icarus*, 204, 399-408, doi:10.1016/j.icarus.2009.05.032.

Hurwitz, D. M. and D. A. Kring (2014), Differentiation of the South Pole – Aitken basin impact melt sheet: Implications for lunar exploration, *J. Geophys. Res.*, 119:1110-1113.

Isaacson P. J., Basu Sarbadhikari A., Pieters C. M., Klima R. L., Hiroi T., Liu Y., and Taylor L. A. 2011a. The lunar rock and mineral characterization consortium: Deconstruction and integrated mineralogical, petrologic, and spectroscopic analyses of mare basalts. *Meteoritics and Planetary Science* 46:2:228-251.

Jolliff, B. L., Haskin, L. A., Korotev, R. L., Papike, J. J., Shearer, C. K., Pieters, C. M., & Cohen, B. A. (2003), Scientific expectations from a sample of regolith and rock fragments from the interior of the lunar South Pole-Aitken basin, *Lunar Planet. Sci.* XXXIV, #1989.

- Klima R. L., Pieters C. M., and Dyar M. D. 2007. Spectroscopy of synthetic Mg-Fe pyroxenes I: Spin-allowed and spin-forbidden crystal field bands in the visible and near-infrared. *Meteoritics and Planetary Science* 42:2:235-253.
- Klima R. L., Dyar M. D., and Pieters C. M. 2011. Near-infrared spectra of clinopyroxenes: Effects of calcium content and crystal structure. *Meteoritics and Planetary Science* 46:3:379-395.
- Kring, D. A., P. J. McGovern, R. W. K. Potter, G. S. Collins, M. L. Grange, and A. A. Nemchin (2015), Was an epoch of lunar magmatism triggered by the South Pole - Aitken Basin Impact?, *Early Solar System Impact Bombardment III*, abstract 3009.
- Moriarty, D. P., & Pieters, C. M. (2015). The nature and origin of Mafic Mound in the South Pole- Aitken Basin. *Geophysical Research Letters*,42(19), 7907-7915.
- Moriarty, D. P., & Pieters, C. M. (2016). Complexities in pyroxene compositions derived from absorption band centers: Examples from Apollo samples, HED meteorites, synthetic pure pyroxenes, and remote sensing data. *Meteoritics & Planetary Science*.
- Morrison, D. A. (1998), Did a thick South Pole-Aitken Basin melt sheet differentiate to form cumulates?, *Lunar and Planet. Sci. Conf.*, XXIX, #1657.
- National Research Council (2003), New Frontiers in the Solar System: An Integrated Exploration Strategy, *The National Academies Press*, Washington, D.C..
- National Research Council (2011), Vision and Voyages for Planetary Science in the Decade 2013-2022, *The National Academies Press*, Washington, D.C..

- Noble S. K., Pieters C. M., Hiroi T., and Taylor L. A. 2006. Using the modified Gaussian model to extract quantitative data from lunar soils. *Journal of Geophysical Research* 111:E11009.
- Pieters, C. M., J. W. Head, L. Gaddis, B. Jolliff, and M. Duke (2001), Rock types of South Pole - Aitken basin and extent of basaltic volcanism, *J. Geophys. Res.*, 106, 28,001–28,022, doi:10.1029/2000JE001414.
- Pieters, C. M., J. Boardman, B. Buratti, A. Chatterjee, R. Clark, T. Glavich, R. Green, J. W. Head III, P. Isaacson, E. Malaret, T. McCord, J. Mustard, N. Petro, C. Runyon, M. Staid, J. Sunshine, L. Taylor, S. Tompkins, P. Varanasi, and M. White (2009a), The Moon Mineralogy Mapper (M³) on Chandrayaan-1, *Current. Sci.*, 96(4), 500-505.
- Pieters, C. M., et al. (2009b), Character and spatial distribution of OH/H₂O on the surface of the Moon as seen by M³ on Chandrayaan-1, *Science*, 326:5952:568-572.
- Pieters, C. M., D. P. Moriarty III, and I. Garrick-Bethell (2014), Atypical regolith processes hold the key to enigmatic lunar swirls, *LPSC 45*, abstract 1408.
- Robinson M. S., Brylow S. M., Tschimmel M., Humm D., Lawrence S. J., Thomas P. C., Denevi B. W., Bowman-Cisneros E., Zerr J., Ravine M. A., Caplinger M. A., Ghaemi F. T., Schaffner J. A., Malin M. C., Mahanti P., Bartels A., Anderson J. Tran T. N., Eliason E. M., McEwen A. S., Turtle E., Jolliff B. L., and Hiesinger H. 2010. Lunar Reconnaissance Orbiter Camera (LROC) instrument overview. *Space Science Reviews* 150:81-124.

- Schultz, P. H. and D. A. Crawford (2011), Origin of nearside structural and geochemical anomalies on the Moon, *Geo. Soc. Am. Special Papers*, 477, 141-159, doi:10.1130/2011.2477(07).
- Smith, D. E., Zuber, M. T., Neumann, G. A., Lemoine, F. G., Mazarico, E., Torrence, M. H., and Aharonson, O. (2010). Initial observations from the lunar orbiter laser altimeter (LOLA). *Geophysical Research Letters*, 37(18).
- Spudis, P. D., R. A. Reisse, and J. J. Gillis (1994), Ancient multiring basins on the Moon revealed by Clementine laser altimetry, *Science*, 266, 1848–1851, doi:10.1126/science.266.5192.1848.
- Stuart-Alexander, D. E. (1978), Geologic map of the central far side of the Moon, *U.S. Geol. Survey*, Reston, VA.
- Vaughan, W. M. and J. W. Head III (2014), Impact melt differentiation in the South Pole – Aitken basin: Some observations and speculations, *Planet. Space Sci.*, 91, 101-106.
- Warren, P. H., Claeys, P., & Cedillo-Pardo, E. (1996). Mega-impact melt petrology (Chicxulub, Sudbury, and the Moon): Effects of scale and other factors on potential for fractional crystallization and development of cumulates. *The Cretaceous-Tertiary event and other catastrophes in Earth history*, 105-124.
- Wilhelms, D. E., McCauley, J. F., and Trask, N. J. 1987. *The Geologic History of the Moon*, USGS Professional Paper, 1938:302.
- Zuber, M. T., D. E. Smith, M. M. Watkins, S. W. Asmar, A. S. Konopliv, F. G. Lemoine, H. J. Melosh, G. A. Neumann, R. J. Phillips, S. C. Solomon, M. A. Wieczorek, J. G. Williams, S. J. Goossens, G. Kruizinga, E. Mazarico, R. S. Park, and D. N.

Yuan (2013), Gravity Field of the Moon from the Gravity Recovery and Interior Laboratory (GRAIL) Mission, *Science*, 339(6120), 668-671.

CHAPTER 1: Complexities in pyroxene compositions derived
from absorption band centers: Examples from Apollo samples,
HED meteorites, synthetic pure pyroxenes, and remote sensing
data

D. P. Moriarty III and C. M. Pieters

Department of Earth, Environmental, and Planetary Sciences

Brown University | Providence, RI 02912

Submitted to:

Meteoritics and Planetary Science

January, 2015

Revised:

August, 2015

Accepted:

October, 2015

Abstract

We reexamine the relationship between pyroxene composition and near-infrared absorption bands, integrating measurements of diverse natural and synthetic samples. We test an algorithm (PLC) involving a two-part linear continuum removal and parabolic fits to the 1 and 2 μm bands - a computationally simple approach which can easily be automated and applied to remote sensing data. Employing a suite of synthetic pure pyroxenes, the PLC technique is shown to derive similar band centers to the Modified Gaussian Model. PLC analyses are extended to natural pyroxene-bearing materials, including: (1) bulk lunar basalts and pyroxene separates, (2) diverse lunar soils, and (3) HED meteorites. For natural pyroxenes, the relationship between composition and absorption band center differs from that of synthetic pyroxenes. These differences arise from complexities inherent in natural materials such as exsolution, zoning, mixing, and space weathering. For these reasons, band center measurements of natural pyroxene-bearing materials are compositionally non-unique and could represent three distinct scenarios: (1) pyroxene with a narrow compositional range, (2) complexly zoned pyroxene grains, or (3) a mixture of multiple pyroxene (or non-pyroxene) components. Therefore, a universal quantitative relationship between band centers and pyroxene composition cannot be uniquely derived for natural pyroxene-bearing materials without additional geologic context. Nevertheless, useful relative relationships between composition and band center persist in most cases. These relationships are used to interpret M3 data from the Humboldtianum Basin. Four distinct compositional units are identified: (1) Mare Humboldtianum basalts, (2) distinct outer basalts, (3) low-Ca pyroxene-bearing materials, and (4) feldspathic materials.

1 Introduction

Pyroxene minerals provide clues to understanding silicate bodies throughout the solar system. This is true for several reasons: (1) Pyroxenes are common on the surface of many silicate bodies, such as Earth's moon, asteroids, and Mars. (2) Pyroxenes exhibit strong diagnostic absorption bands in the near-infrared wavelength range. These absorption bands can be accurately measured by remote sensing. (3) The wavelength positions of these absorption bands are systematically related to pyroxene composition and crystal structure through fundamental physical principles. (4) Pyroxene mineralogy is closely linked to geologic processes related to the thermal and chemical evolution of a planet. Following this logic, remote sensing observations that identify pyroxene compositions have been used extensively throughout the literature to constrain the formation and evolution of many planetary bodies.

Understanding the relationship between pyroxene composition and optical properties is crucial for interpreting the results of recent hyperspectral datasets from pyroxene-bearing bodies such as the Moon (Moon Mineralogy Mapper) (Pieters et al. 2009) and Vesta (Dawn Visible and Infrared Spectrometer) (De Sanctis et al 2011). In this paper, we build upon well-established compositional trends observed in pyroxene spectra (e.g. Adams 1974; Hazen et al. 1978; Cloutis and Gaffey 1991; Klima et al. 2007; Klima et al. 2011). We seek to develop a new approach to measure and interpret pyroxene band centers that is straightforward to automate and apply to the large volumes of data typically returned by remote sensing instruments. To optimize and validate this

technique, we consider laboratory spectra of several diverse but well-characterized sample collections: (1) synthetic pure pyroxenes with well-controlled compositions, (2) natural pyroxene separates and bulk samples derived from lunar basalts, (3) bulk howardite-eucrite-diogenite (HED) meteorites, and (4) diverse lunar soils. The sample collections span an array of compositions, formation conditions, geologic histories, pyroxene abundances, and optical maturities, simulating a variety of scenarios encountered in remote sensing. Our goal is to understand how the systematic relationship between pyroxene composition and absorption band centers is manifested under these different conditions. Due to the complexity of this relationship, we intentionally do not provide quantitative algorithms to predict pyroxene compositions from spectra. As shown in the following discussion, such an approach is not appropriate for many natural materials. Instead, we discuss and document multiple natural variables and illustrate compositional trends across the pyroxene quadrilateral defined by Mg-, Fe-, and Ca-bearing compositions. We then apply these tools to Moon Mineralogy Mapper data from the Humboldtianum Basin, identifying the spatial diversity of pyroxene compositions across the western extent of the basin.

2 Background

The following subsections provide an overview of the physical origin and behavior of pyroxene absorption bands, including discussion of several previous approaches to interpreting spectra of pyroxene-bearing materials. This background is provided for those unfamiliar with pyroxene spectroscopy.

2.1 The Origin of Pyroxene Absorption Bands in the NIR

Several example pyroxene spectra are given in Fig. 1. Each pyroxene spectrum exhibits primary absorption bands near 1 μm and 2 μm . As seen in these spectra, there is significant variation in the strength, shape, and position of these absorption bands. These band properties are dependent on pyroxene mineralogy in ways that will be described in the next several subsections.

In pyroxenes, near-infrared (NIR) absorption bands arise from the presence of transition metal cations (such as Fe^{2+}) in the crystal structure (e.g., Burns 1993). These cations reside in two possible sites in the pyroxene structure, known as M1 and M2. Cations in the M1 and M2 sites are in coordination with 6 or more oxygen atoms and are therefore referred to as octahedral cations. These closely-packed oxygen atoms surrounding the octahedral cations represent a ligand field, which results in a non-uniform electrostatic field across the M1 and M2 sites.

At ground state, the valence (outer) electrons of transition metal cations occupy *d*-orbitals. The several different *d*-orbitals are normally degenerate, meaning that they represent equivalent energy states. However, when a transition metal cation is subjected to a non-uniform electrostatic field (as when occupying the M1 or M2 cation site), the *d*-orbitals to lose their degeneracy and split into slightly separate energy levels. This is referred to as crystal field splitting (e.g., Burns 1993).

When crystal field splitting has occurred, valence electrons can transition between the different *d*-orbitals when supplied with precisely the right amount of energy (namely, the energy difference between the *d*-orbitals imposed by the ligand field). This energy can be supplied by incident photons of the appropriate wavelength. Such photons are

thus absorbed by the cation. When this process occurs, it results in absorptions at certain energies (wavelengths) in mineral spectra (e.g., Burns 1993). Due to normal small-scale perturbations in the crystal structure, a distribution of photon energies are absorbed, resulting in absorption bands rather than absorption lines (see below for further details).

The nature of these absorption bands (strength, wavelength, shape, etc.) is controlled by the character of the transition metal ion and the properties of the ligand field at the M1 and M2 sites (e.g., Burns 1993). The exact arrangement of oxygen atoms in coordination with each cation site controls the electrostatic field and therefore the degree of *d*-orbital splitting and resulting absorption band properties. Therefore, properties of pyroxene composition and structure that affect the ligand field control absorption band properties. It follows that absorption bands are a sensitive measure of the composition and structure of pyroxenes.

The ligand fields at the M1 and M2 sites are quite different, and therefore transition metal cations in each site contribute absorptions that are distinct in character and strength (e.g., Burns 1993). The contributions from each site are generalized in Fig. 2. The M2 site is larger and more asymmetric. This asymmetry results in relatively strong absorption bands at $\sim 1 \mu\text{m}$ and $\sim 2 \mu\text{m}$. The M1 site is smaller and more symmetric, resulting in somewhat weaker absorptions at $\sim 1 \mu\text{m}$ and $\sim 1.2 \mu\text{m}$.

The size difference between cation sites controls which cations can be accommodated in each site. As summarized in Fig. 2, the $1.2 \mu\text{m}$ band arises from the M1 site alone, the $2 \mu\text{m}$ band arises from the M2 site alone, and the $1 \mu\text{m}$ band is a superposition of absorptions from the M1 and M2 sites. This paper focuses primarily on the compositional trends of the $1 \mu\text{m}$ and $2 \mu\text{m}$ composite bands. However, the $1.2 \mu\text{m}$

band plays a significant role in pyroxene spectra and must be understood in order to properly interpret these spectra.

2.2 Modeling Pyroxene Absorptions

As discussed above, pyroxene absorption band properties are sensitive to the precise crystal structure of the pyroxene. Essentially, the bond length between M1 (and M2) site cations and ligands is controlled by pyroxene composition (Sunshine et al. 1990). However, random processes such as thermal vibrations result in small-scale deviations in bond lengths, even across pyroxenes of a single composition (Sunshine et al. 1990). Therefore, exact bond lengths in any given pyroxene are randomly distributed about a central value. Since absorption bands result from a statistically large number of photons interacting with a large number of transition metal cations in the ligand field, the central limit theorem states that the bond length distribution can be described by a Gaussian function (Sunshine et al. 1990).

The average cation-ligand bond length is a property of the ligand field and can be related to the *d*-orbital energy splitting (and thus absorption band center) through a power law (Sunshine et al. 1990; Burns 1993). Therefore, convolving the bond length Gaussian distribution through this power law results in a model of absorption band shape that is rooted in the physical processes of absorption. In the Modified Gaussian Model (MGM), these physically realistic shapes are used to model and deconvolve superimposed absorption bands (Sunshine et al. 1990; Sunshine and Pieters 1993).

Since physically realistic absorption band shapes are invoked in MGM, it is a useful tool for deconvolving overlapping absorption bands from multiple minerals and cation sites (Sunshine et al. 1990; Sunshine and Pieters 1993), representing a significant

improvement over standard Gaussian fitting (e.g. Farr et al. 1980). An example of MGM deconvolution for an orthopyroxene reflectance spectrum is provided in Fig. 2. The figure illustrates how individual MGM bands are combined with a spectral continuum to produce a model spectrum. The individual modified Gaussian bands near 1 μm , 1.2 μm , and 2 μm correspond to absorptions from transition metal cations in the M1 and M2 sites (as indicated in the figure).

For transmission spectra of individual mineral grains, the Beer-Lambert law can be used in conjunction with MGM to relate total absorption to the absorption coefficient and optical path length (Sunshine et al. 1990). Reflectance spectra, however, involve interactions of radiation with multiple grains in random orientation. Therefore, quantitative mineral abundance measurements using reflectance spectra are more complicated due to effects such as Fresnel reflectance, multiple scattering, particle size, photometry, and nonlinear mixing of materials with different optical constants. However, several studies have validated MGM (and absorption band depths and centers in general) as a useful tool to derive composition and relative mineral abundances from reflectance spectra of minerals (e.g. Sunshine et al. 1990; Sunshine and Pieters 1993).

The current MGM tools often require significant user interaction and are best applied to individual high-quality spectra. In this paper, we seek to complement MGM with tools better suited to working with large volumes of data that may be affected by noise or other artifacts, which is the case for several hyperspectral datasets.

2.3 Pyroxene Composition and Spectral Properties

2.3.1 Effects of $\text{Mg}^{2+}/\text{Ca}^{2+}/\text{Fe}^{2+}$ and crystal structure on the 1 μm and 2 μm band

In pyroxenes, the M1 and M2 sites can host a variety of cations including Ca^{2+} , Na^+ , Mn^{2+} , Mg^{2+} , Fe^{2+} , Fe^{3+} , Cr^{3+} , Cr^{2+} , Ti^{3+} , Ti^{4+} , and Al^{3+} . For lunar pyroxenes, sample analyses have shown these sites to be dominated by just three cations: Ca^{2+} , Mg^{2+} , and Fe^{2+} (e.g. Papike et al. 1991). For most pyroxenes derived from lunar samples (both mare and non-mare), the abundance of cations other than Ca^{2+} , Mg^{2+} , and Fe^{2+} is less than 5% (as summarized Appendix A Fig. S2 and references therein). While mare samples exhibit a slightly higher abundance of other cations, only three pyroxene samples (out of the 99 reported) exhibit more than 10% of these other cations. Given these compositional analyses, it is clear that the principal transition metal cation present in lunar pyroxenes is Fe^{2+} . It follows that Fe^{2+} in the M1 and M2 sites is the primary driver of NIR spectral absorptions for such pyroxenes. However, the presence of Mg^{2+} and Ca^{2+} affects the crystal structure and ligand field, which in turn affect absorption band properties.

As mentioned in Section 2.1, the M2 site is larger than the M1 site. Because cations also differ in size, specific cations exhibit preferences for certain sites (Burns 1993; Klima et al. 2011). For instance, Ca^{2+} is a relatively large cation that can only be accommodated in the larger M2 site. This restricts the total Ca^{2+} cation number in pyroxenes to 50% or less (as it can only inhabit one of the two total possible sites). Mg^{2+} and Fe^{2+} are smaller cations that can be accommodated in either the M1 or M2 site. Since Fe^{2+} is slightly larger than Mg^{2+} , it exhibits a slight preference for the M2 site when possible (Burns 1993; Klima et al. 2011). For simplicity, cation valences will not be explicitly stated for the remainder of the paper.

Since the pyroxene system is largely constrained to three variables (Mg, Fe, and Ca), pyroxene compositions can be represented on a ternary diagram. Since the total Ca content in pyroxenes is limited to 50% or less (as described above), pyroxene compositions are commonly represented on a quadrilateral plot, which is simply the Ca<50% segment of the Mg-Fe-Ca ternary diagram. Example pyroxene quadrilaterals showing compositions for several pyroxene-bearing materials (including the sample collections analyzed here) are given in Fig. 3. These pyroxene composition quadrilaterals are considered in more detail below.

For reflectance spectra of natural pyroxenes, the broad relationship between Ca, Mg, Fe, and absorption band properties in reflectance spectra was first described by Adams (1974), Hazen et al. (1978) and Cloutis and Gaffey (1991). These compositional relationships were studied in detail in a suite of papers by Klima et al. (2007; 2008; 2011). In these analyses, Klima et al. used a carefully prepared collection of synthetic pyroxenes with well-controlled compositions. The octahedral cations were limited to Mg, Fe, and Ca in order to explore the relationship between composition and band center without the complicating effects of minor cations. The compositions of the synthetic pyroxenes analyzed by Klima et al. are indicated in Fig. 3A by the open black symbols. It is important to note that several of the synthetic pyroxene compositions are not heavily represented in the compositional range of natural samples. For instance, lunar and HED pyroxenes seldom exhibit compositions with Ca >47%, while several synthetic clinopyroxenes with this composition were synthesized and measured. These very-high-Ca synthetic pyroxenes are indicated by dotted open circles for the remainder of the paper.

Using the Modified Gaussian Model, Klima et al. (2007; 2011) quantified the systematic relationships between synthetic pure pyroxene composition and the band centers of the 1 μm and 2 μm bands. These relationships are illustrated in Fig. 4. In general, orthopyroxenes (open squares) exhibit shorter-wavelength band centers than clinopyroxenes (open circles). For orthopyroxenes (which nominally contain no Ca), both the 1 μm and 2 μm band centers shift to longer wavelengths with increasing Fe content (and therefore decreasing Mg content). For clinopyroxenes, the precise relationship between band center and composition is more complicated. In general, clinopyroxene band centers tend to shift to longer wavelengths with increasing Ca content (as seen in Figs. 4A,B). However, at Ca content greater than $\sim 30\%$, the 2 μm band remains relatively constant, but with significant scatter (Klima et al., 2011). The observed trends confirmed the findings of earlier studies (e.g. Adams 1974; Hazen et al. 1978; Cloutis and Gaffey 1991) with higher precision due to the well-controlled compositions of the synthetic samples. When minor cations such as Ti and Cr are present, band centers are often shifted to longer wavelengths than predicted based on the Fe-Mg-Ca content (e.g. Hazen et al. 1978; Cloutis and Gaffey 1991; Cloutis 2002).

The MGM-derived band center trends for synthetic pyroxenes are summarized in Fig. 5. Plotting the composite 1 μm band center vs. 2 μm band center effectively illustrates the compositional trends of the synthetic pure pyroxene samples. Mg-rich orthopyroxenes exhibit the shortest wavelength band centers. As Fe content increases, band centers shift to longer wavelengths. Low-Ca clinopyroxenes exhibit band centers that shift to longer wavelengths with increasing Ca (and Fe) content. High-Ca clinopyroxenes exhibit the longest-wavelength absorption bands. For high-Ca pyroxenes,

only the 1 μm band center exhibits a systematic shift to longer wavelengths with increasing Ca content. The 2 μm band center exhibits significant scatter but no overall trend (Klima et al. 2011).

Temperature can also have an effect on absorption band properties. At higher temperatures, absorption bands tend to widen. While the wavelength position of the 1 μm band remains relatively constant from ~80 k to ~450 k, the 2 μm band shifts to shorter wavelengths for clinopyroxene and longer wavelengths for orthopyroxenes with increasing temperature (Singer and Roush, 1985). These effects are not considered in this paper, as all samples were measured at room temperature.

2.3.2 The 1.2 μm band: Fe^{2+} in the M1 cation site

As mentioned above, the primary 1 μm and 2 μm pyroxene absorption bands arise from Fe in the larger, more distorted M2 octahedral cation site. Fe in the M1 site produces additional absorptions (albeit much weaker) at 1 μm and 1.2 μm (e.g. Klima et al. 2008; 2011). Although not the focus of this analysis, these weaker M1 site absorptions must be considered in order to correctly interpret observations of the 1 μm and 2 μm bands.

The M1 1 μm absorption is not usually observed as an independent feature, as the 1 μm composite band is typically dominated by the much stronger M2 absorption (except for the most Ca-rich pyroxenes) (Klima et al. 2011). When present, the 1.2 μm band is manifested as a subtle feature on the long-wavelength shoulder of the 1 μm band. The relative positions of these bands are illustrated in Fig. 2. The 1.2 μm band is observable in many of the spectra presented in this paper.

As mentioned above, Fe generally prefers the M2 site to the M1 site due to its size. However, it can be partitioned into M1 by three mechanisms: (1) very high Ca content which completely fills the M2 sites and forces Fe into M1, (2) high Fe content (<50%) which would partition Fe into M1 after completely filling the M2 sites, or (3) rapid cooling and crystallization which can trap Fe in the M1 site before it has a chance to diffuse into M2 (e.g. Klima et al. 2008). Therefore, the presence and relative strength of the 1.2 μm band is related to both pyroxene composition and cooling history (Klima et al. 2008).

2.4 Description of Sample Collections

To reliably interpret spectra of pyroxene-bearing materials, it is necessary to understand the effects of additional factors affecting these spectra in the natural environment, including natural variations in pyroxene composition, mixing with non-pyroxene minerals, and space weathering. For a general overview of these effects, we have selected four diverse sample collections for spectral analysis. The sample collections are described in the following sections and summarized in Table 1. Our analysis focuses on reanalysis of existing spectra collected at the NASA Reflectance Experiment Laboratory (RELAB, <http://www.planetary.brown.edu/relab/>).

2.4.1 Synthetic Pyroxenes

The suite of synthetic pyroxenes analyzed in this study was used by Klima et al. (2007; 2011) to characterize the fundamental relationship between pyroxene composition and absorption band properties. The effects of Fe cation site occupancy (M1 vs. M2) on the strength of the 1.2 μm band were also studied using these samples (Klima et al. 2008). Example synthetic pyroxene spectra (orthopyroxenes, low-Ca clinopyroxene, and

high-Ca clinopyroxene) are given in Fig. 1. The compositional range of the synthetic pyroxene suite is given in Fig. 3A. These samples are crucial in the efforts to understand the fundamental spectral behavior of pyroxenes and serve as a standard to directly compare our approach to MGM.

The synthetic nature of the samples allowed their spectral properties to be characterized in the absence of complicating effects such as minor cations, impurities, zoning, or exsolution. The pyroxenes were synthesized using techniques described in Turnock et al. (1973). Compositions were strictly controlled so that only Ca, Mg, and Fe are present in the M1 and M2 octahedral cation sites. The oxygen fugacity was buffered at iron-wüstite, favoring Fe^{2+} over Fe^{3+} (appropriate for reducing environments such as the Moon). The resulting pyroxene powders are very fine grained and were sieved to $<45 \mu\text{m}$ for NIR spectral measurements. The fine grain size (the size of pyroxene crystals directly related to crystallization properties) may be distinctly different than the average particle size (a physical property of the sample in its current state). For the synthetic pyroxene samples, the particle size was typically larger than the grain size. The distinction between grain size and particle size is an important consideration for laboratory analyses and remote sensing applications and will be maintained throughout this paper.

For the synthetic pyroxene suite, typical spectra exhibit very strong 1 and 2 μm absorption bands superposed on a variable but relatively flat continuum, as shown in the example spectra in Fig. 1. A strong 1.2 μm band is observed across a wide range of compositions. For Fe-free and very high Ca pyroxenes, significantly different absorption band properties are observed. However, these pyroxenes are rare on the Moon and HEDs

(as shown in Fig. 3A). Because only small quantities of sample were available (often 10-30 mg), the absolute brightness measured in these spectra is not fully reliable.

Reanalysis of the synthetic pyroxene spectra with new techniques described below allows direct comparison (and validation) with the existing Klima et al. (2007; 2008; 2011) MGM analyses as well as further characterization of the fundamental relationship between pyroxene composition and absorption band properties (e.g. Hazen et al. 1978; Cloutis and Gaffey 1991; Cloutis 2002).

2.4.2 Lunar Rock and Mineral Characterization Consortium Mineral Separates

The Lunar Rock and Mineral Characterization Consortium (LRMCC) used lunar basalts to study the relationships between mineralogy, petrology, and spectroscopy of lunar materials (Isaacson et al. 2011a). For the LRMCC analyses, four basalt samples were separated into their component minerals, including plagioclase, two pyroxenes (generally grouped into low-Ca and high-Ca), olivine, and ilmenite. The separates and bulk samples were crushed and sieved into two particle size fractions for spectroscopic measurement: coarse (<125 μm) and fine (<45 μm). Spectra and compositional information including mineral abundance were obtained for each mineral separate, as well as the bulk rock. The corresponding MGM analyses provide a record of how individual mineral components contribute to spectra of lunar rocks, serving as groundtruth for spectral mixing models of lunar materials (Isaacson et al. 2011a).

For our analyses, we focus on the pyroxene separates and their relationship with bulk rock spectra. Example pyroxene and bulk rock spectra derived from a single basalt sample are given in Fig. 6. Generally, the pyroxene separates are spectrally similar to the synthetic pyroxenes in that they exhibit very strong 1 μm and 2 μm absorption bands

superposed on a relatively flat continuum. The 1.2 μm band is less pronounced in the LRMCC pyroxene separate samples, although it is clearly visible in the spectra of several samples. Bulk sample spectra tend to be dominated by pyroxene signatures. In Fig. 6, the bulk sample spectrum is clearly dominated by a mixture of the pyroxene components, even though it also contains non-pyroxene components such as plagioclase (Isaacson et al. 2011a). When present, ilmenite strongly affects the overall continuum as well as pyroxene absorption band properties, especially for the fine particle size samples. Bulk rock spectra exhibiting the effects of ilmenite are given in Appendix A Fig. S3.

As stated above, two pyroxene separates (“low-Ca” and “high-Ca”) were obtained for each LRMCC basalt (Isaacson et al. 2011a). However, compositional analyses revealed a considerable compositional range present in each individual pyroxene separate, resulting from natural crystallization processes such as zoning and exsolution (Klima and Pieters 2008; Isaacson et al. 2011a). This range in composition for each separate is illustrated in Fig. 3B. For each separate, the average pyroxene composition is given by a solid symbol. These average compositions are calculated from ~30-60 measurements. The range of compositions among the individual measurements is given in Fig. 3B by the dashed (“low-Ca” pyroxene) and solid (“high-Ca” pyroxene) lines. From this figure, it is clear that individual pyroxene separates do not represent single pyroxene compositions, regardless of how carefully selected. Rather, each pyroxene separate is a composite of a range of co-crystallized compositions. These natural pyroxene separates exhibit more complex composite spectra than the synthetic pure pyroxenes. However, these composite spectra can be accurately modeled using MGM (Klima and Pieters 2008).

Analysis of the LRMCC samples with our simplified techniques (Sec. 4.2) allows comparison between synthetic pure pyroxenes and natural (more complex) lunar pyroxenes in the same framework. Additionally, analysis of bulk rock spectra demonstrate the propagation of pyroxene spectral signatures through mixtures of multiple well-characterized pyroxene and non-pyroxene components.

2.4.3 Howardite, Eucrite, and Diogenite Meteorites

Howardites, eucrites, and diogenites (HEDs) are meteorites that likely originated on 4 Vesta (or possibly other basaltic asteroids) (e.g. Mittlefehldt et al. 1998; Keil 2002; Pieters 2006). HED meteorites exhibit similar O isotopes but different mineralogies, suggesting that they represent assemblages formed under different conditions on the same parent body (e.g. Clayton 1993). HEDs range in composition from basaltic to orthopyroxenitic (Delaney et al. 1984; Bowman et al. 1997; Mittlefehldt et al. 1998). Diogenites are dominated by orthopyroxenes, typically with minor (<5% volume) contributions from olivine and clinopyroxenes (Bowman et al. 1997). Eucrites exhibit significant plagioclase content as well as diverse pyroxene compositions, generally containing higher proportions of clinopyroxene (Delaney et al. 1984). Howardites are brecciated mixtures of diogenitic and eucritic materials (Delaney et al. 1983). Measured pyroxene compositions for several example HED meteorites are given in Fig. 3A.

For this study, we reanalyze spectra from two groups of HED samples. The first group (HEDs ground and sieved to <25 μm) was obtained by T. Hiroi (in association with Burbine et al, (2001)) and used by Klima et al. (2008) to constrain the effects of Fe in the M1 cation site on the strength of the 1.2 μm band. The second group (mostly howardites ground and sieved to <75 μm) is currently in use by Mittlefehldt et al. (2014)

in efforts to constrain compositional effects on HED reflectance spectra, providing groundtruth measurements useful for interpreting results from the recent Dawn mission at 4 Vesta (Russell et al. 2012; De Sanctis et al. 2011).

Although the exact mineral compositions and abundances differ, HEDs are spectrally dominated by pyroxenes, as evident in Fig. 7. The strong 1 μm and 2 μm pyroxene absorptions are superposed on a relatively flat continuum. The 1.2 μm band is observed in most samples, but is especially pronounced for eucrites (Klima et al. 2008; Mayne et al. 2010). Pyroxene compositions for several example HEDs are given in Fig. 3A. For eucrites, open circles represent bulk pyroxene compositions, while the solid symbols connected by lines show exsolution trends.

For our analyses, HEDs provide excellent examples of natural pyroxene mixtures, as they contain multiple diverse pyroxenes as well as other components. Howardites represent a special case, as they are physical mixtures of diogenitic and eucritic components. The two sample groups (<25 μm and <75 μm particles) allow comparison of pyroxene spectral trends across different particle sizes.

2.4.4 Lunar Soil Characterization Consortium Soils

Through a series of papers, the Lunar Soil Characterization Consortium (LSCC) has worked to link the mineralogy, petrology, maturity, particle size, and other characteristics of both mare and non-mare lunar soils to the soils' optical properties (e.g. Pieters et al. 2000; Taylor et al. 2001; 2010; Noble et al. 2006). For the LSCC analyses, soils were sieved into four particle sizes: <45 μm , <10 μm , 10-20 μm , and 20-45 μm . The soils contain a diverse mixture of mineral and glassy components. The relative abundances of these components depend on particle size. For example, the <10 μm

material is spectrally dominated by highly-weathered particles and does not exhibit strong NIR spectral absorptions. Due to the lack of relevant spectral absorptions, the <10 μm fraction is not included in our analyses.

Spectra of the three relevant particle sizes for example mare and non-mare soils are given in Fig. 8. LSCC soils exhibit spectra markedly different than those of the other sample groups. The soil spectra exhibit weak pyroxene absorption bands superimposed on steep, red-sloped spectral continua. In order to evaluate absorption band properties, it is necessary to perform continuum removal as described below. In general, mare soils are darker and exhibit stronger absorption bands than non-mare soils. A weak 1.2 μm band is observed in both mare and non-mare soils.

Average pyroxene compositions for the soils are given in Fig. 3C. The range in soil pyroxene compositions is similar to that of the LRMCC pyroxene separates and the additional pyroxene samples given in Figs. 3A+B. Fig. 3C also gives relative pyroxene abundances for the LSCC soils, as larger symbols correspond to a higher pyroxene abundance. Mare soils exhibit a greater overall pyroxene abundance, as well as a higher relative abundances of high-Ca pyroxene. The non-mare soils exhibit lower pyroxene abundance, although the Apollo 14 soils are relatively rich in low-Ca pyroxene.

LSCC soil samples were chosen for this paper to allow analysis of complex mixtures of lunar materials. These soils are similar to the materials that remote sensing spectrometers observe on the lunar surface. LSCC soils allow the effects of optical maturity and mineral mixing on spectral properties of pyroxene-bearing materials to be evaluated. These samples also provide a direct comparison between mare and non-mare soils.

2.5 Remote Sensing Example: Moon Mineralogy Mapper

The overarching goal of these laboratory analyses of pyroxene-bearing materials is to aid in the interpretation of remote-sensing data. In Section 6, we demonstrate the effectiveness of these techniques by applying them to Moon Mineralogy Mapper (M³) images of Mare Humboldtianum, investigating the spatial distribution and geologic context of pyroxene diversity across the western extent of the basin.

M³ was an imaging spectrometer sensitive from 0.42-3.0 μm (Pieters et al. 2009). This covers a similar wavelength range as the sample spectra in Figs. 1 and 6-8. The instrument operated in two modes: global and target. The majority of M³ data was acquired in global mode, with 86 spectral channels and a pixel size of 140 m to 240 m (Boardman et al. 2011). For a few high-interest areas of the Moon (including Mare Humboldtianum), target mode data are available. Target mode data have higher spectral and spatial resolution, with 260 spectral channels (10 nm resolution) and a pixel size of 70 m to 140 m. For this paper, we work exclusively with target mode data.

3 The PLC Technique

As discussed above, the Modified Gaussian Model is an effective technique for characterizing crystal field absorptions, as it employs a band shape rooted in physical processes to deconvolve spectra into component absorptions that are often superimposed (Sunshine et al. 1990). MGM is interactive, requiring user input for several parameters including constraints on continuum type, number of absorption bands, and the initial wavelength position and strength of the absorptions. When several of these variables are unknown, MGM is not ideal for working with large volumes of data, such as

hyperspectral image cubes. Additionally, MGM may produce unreliable results when used with spectra exhibiting low spectral contrast, noise, or other artifacts that could limit the model's ability to accurately detect overlapping absorption bands.

As a practical alternative to MGM, we developed a technique to characterize the properties of pyroxene absorption bands using **p**arabolas and a two-part **l**inear **c**ontinuum (PLC) (Moriarty and Pieters, 2013). The PLC technique is similar to techniques employed by Cloutis and Gaffey (1991) and others, who also use two-part linear continuum removal and quadratic fitting. A principal difference is PLC offers a fully-automated algorithm to select continuum tiepoints and the wavelength range over which absorption bands are fit (see Appendix A), while the earlier Cloutis and Gaffey (1991) method relies more on *a priori* user input.

In the following sections, we evaluate the similarities and systematic differences between pyroxene band center measurements obtained with PLC and the more physically realistic MGM technique. Like MGM, PLC can be applied to single spectra with reliable results (as demonstrated below). Where PLC excels is its application to hyperspectral images, as demonstrated in Section 6. Throughout the remainder of this paper, we show PLC to be a practical, benchmarked technique for characterizing the spatial diversity of pyroxenes in hyperspectral images, and provide recommendations and cautions on compositional interpretations. A detailed description of the PLC approach and examples of specific PLC applications are given in Appendix A.

3.1 Linear Continuum Fitting and Removal

In near-infrared (NIR) reflectance spectra, absorption bands are superimposed on an overall spectral continuum. The continuum arises from one (or more) of several

disparate processes, depending on the material properties and observing conditions. For lunar soils, the continuum is dominated by space weathering processes that deposit nanophase iron particles on the surface of soil particles (e.g. Pieters et al. 2000). Lunar-style space weathering results in overall darkening, weakening of absorption bands, and a pronounced red-sloped continuum, all of which can be observed in the lunar soil spectra presented in Fig. 8. Other factors affecting the continuum (in both weathered and unweathered samples) include non-crystal-field absorptions such as charge transfer, multiple scattering, and Fresnel reflectance (e.g. Gaffey 1976; Pieters 1978; Marfunin 1979; McCord et al. 1981; Clark and Roush 1984; Huguenin and Jones 1986; Yon and Pieters 1988; Burns 1993).

The specific form of the continuum is strongly dependent on factors such as composition, texture/particle size, observation conditions, and optical maturity. Since spectral absorptions are superimposed on a complex spectral continuum, it is useful to remove the continuum to characterize absorption band properties. This is especially important when spectra exhibit weak absorption bands or pronounced continua. The sample collections and remote sensing data presented here differ greatly in the origins and expressions of their spectral continua. However, consistent treatment of the continuum between these datasets allows direct comparisons of absorption band properties.

Since spectral continua result from a complex interaction of several factors, they are difficult to precisely model. Instead, PLC employs a two-part linear approximation. This serves as an “average” continuum in the vicinity of the primary pyroxene absorptions near 1 and 2 μm . Example continuum fits are presented in Figs. 9 and S1.

Continuum removal is performed by dividing the reflectance spectrum by the derived continuum. The resulting continuum-removed spectra are shown in Figs. 10 and S1.

The PLC continuum is fit using three tiepoints derived from each spectrum. Each tiepoint is calculated from the mean of three consecutive wavelength channels to reduce the effect of noise. The short-wavelength and long-wavelength tiepoints are fixed for each spectrum, targeting the local reflectance maxima near 700 nm and 2600 nm. The middle tiepoint is allowed to range from 1100 nm to 1700 nm and is selected by a fitting routine that minimizes the number of wavelength channels with values greater than one in the resulting continuum-removed spectrum.

For some spectra, the pyroxene absorption bands extend beyond 2600 nm, which is the long-wavelength boundary of RELAB bidirectional reflectance data. If the longest available wavelengths are arbitrarily used as the third tiepoint, it can result in a negative slope across the 2 μm region. An example negative 2 μm slope is given in Figs. 9 and S1. For particulate silicate materials such as found on the Moon and Vesta, negative continuum slopes across the NIR are assumed to be unrealistic. For this reason, a flat continuum across the 2 μm region is used when the automatically calculated 2 μm slope is negative.

3.2 Parabolic Fits of Absorption Bands

As shown by Sunshine et al. (1990), the shape of crystal field absorptions is accurately modeled by a modified Gaussian function. Alternatively, PLC employs parabolas to fit the 1 μm and 2 μm bands of continuum-removed reflectance spectra. The purpose of this fit, however, is only to identify the wavelength of the band minimum, regardless of band shape. Example parabolic fits are given in Figs. 10 and S1. The exact

fitting parameters vary depending on spectral resolution and band properties, but the general procedure involves fitting parabolas to subsets of the 1 μm and 2 μm bands (see details in Appendix A). By incorporating many wavelength channels in the parabolic fits, the effect of noise and other measurement artifacts is minimized.

In addition to band center, an estimated band depth is calculated at the wavelength of the parabola minimum. This band depth is equal to 1 minus the continuum-removed reflectance value of the parabola minimum. Using this formulation, spectra with no discernable pyroxene bands have band depths of 0. Spectra with deep pyroxene bands have higher band depth values. In mixtures of pyroxenes with more weakly-absorbing materials, stronger bands can imply higher pyroxene abundances, provided all other variables are the same. However, several other properties also affect band depths, including pyroxene composition, mixing with other minerals, and optical maturity.

4 Results

PLC analyses were performed for each spectrum in each sample collection. The band center results are presented and compared in the following subsections using 1 μm band center vs. 2 μm band center plots (similar to Fig. 5). Band center measurements for all sample collections are compared to pure synthetic pyroxenes. This analysis is intended to validate the PLC procedure and aid in the compositional interpretation of remote sensing data.

4.1 Synthetic Pyroxene Band Centers

Synthetic pyroxene spectra provide a crucial test of the PLC technique. Comparing PLC band center results to the existing MGM analyses (Klima et al. 2007;

2011) tests PLC's ability to accurately measure absorption band centers of pure pyroxenes. A comparison between PLC- and MGM-derived band centers for the synthetic pure pyroxene spectra is given in Fig. 11. The PLC band center trend is nearly identical to the MGM results, confirming that there is good agreement between the two techniques.

On average, PLC measurements of the 1 μm band center are 2.85 nm longer than the corresponding MGM measurement. The average magnitude of separation between PLC and MGM measurements (calculated using the root-mean-square difference (RMS)) 5.96 nm. The mean difference is a significant fraction of the RMS difference, which indicates that there is significant systematic error between PLC and MGM measurements of the 1 μm band center. Specifically, the 1 μm band center measurements are typically ~ 3 nm longer for PLC than for MGM for synthetic pyroxene spectra. This is observed in Fig. 11, as many of the PLC datapoints fall slightly above the corresponding MGM points.

For the 2 μm band, the mean difference (1.45) is a much smaller fraction of the RMS difference (17.01), as compared to the 1 μm band. This indicates that the differences between PLC and MGM 2 μm band center measurements result primarily from random errors rather than a systematic offset. The general band center trend is very similar for both PLC and MGM measurements. Throughout the rest of the paper, PLC band center measurements of natural materials will be compared to PLC measurements of the synthetic pyroxenes.

4.2 LRMCC Band Centers

As materials returned from the lunar surface, the LRMCC pyroxene separates and bulk rock samples provide important groundtruth for interpreting remote sensing data from the Moon. As reviewed above, pyroxenes formed under natural conditions often exhibit significant differences from the synthetic pyroxenes, including exsolution, inversion, compositional zoning, and the inclusion of octahedral cations other than Ca, Fe, and Mg. It is important to constrain the impact of such factors on PLC band center measurements of pyroxene separates from natural basalts. Additionally, the bulk samples provide examples of well-constrained mixtures of multiple pyroxenes and additional components.

PLC band center measurements for the LRMCC pyroxene separates and bulk rock samples are given in Fig. 12. The LRMCC pyroxene band centers are slightly offset from the synthetic pure pyroxene results, but follow a very similar trend. The low-Ca pyroxenes exhibit short-wavelength absorption bands, while the high-Ca pyroxenes exhibit longer-wavelength absorptions. The Apollo 15 bulk rock samples plot between the low-Ca and high-Ca pyroxene separate clusters, as expected for mixtures of these pyroxenes. The Apollo 17 bulk rock samples are significantly offset from the lunar and synthetic pyroxene trend. This is due to the high modal abundance of ilmenite in these samples (>17%), which is highly absorbing and strongly affects the reflectance spectra, as seen in Appendix A Fig. S3 (Isaacson et al. 2011a; 2011b). When ilmenite is not a significant component, particle size does not have a significant effect on these band center measurements.

4.3 HED Band Centers

The HED meteorites provide several additional examples of natural pyroxene mixtures. HED pyroxenes formed under different conditions on a different planetary body than the LRMCC pyroxenes and thus exhibit different chemistries and textures. The howardites provide additional complexity, as they represent mechanical mixtures (through impact processes) of diogenites (mainly low-Ca pyroxene) and eucrites (plagioclase and higher-Ca pyroxene).

The PLC-measured band centers for HEDs are given in Fig. 13. Similarly to the LRMCC pyroxene separates, the HED band centers are slightly offset from the synthetic pure pyroxenes but follow a comparable trend. As would be expected from their pyroxene chemistry, diogenites exhibit the shortest-wavelength absorption bands, while eucrites exhibit the longest-wavelength absorptions. The howardite band centers plot between those of eucrites and diogenites, as is expected from physical mixtures of the two. Overall, the HEDs plot at shorter wavelengths than most of the LRMCC pyroxene separates and bulk soils. Particle size does not exhibit a significant effect on band center measurements at these scales, based on the overlapping band centers for the <75 μm and <25 μm samples.

4.4 LSCC Band Centers

The majority of the lunar surface is covered in well-developed soils. These soils contain a diverse mixture of minerals and non-crystalline components fragmented and redistributed by impacts. Lunar surface soils also exhibit significant nanophase iron on the surface of soil particles due to space weathering, specifically exposure to energetic particles and micrometeorite bombardment. As discussed above, lunar space weathering

processes impart a steep, red-sloped continuum and significantly reduce absorption band strengths. Constraining the effects of these processes on band center measurements is integral to interpreting remote sensing data from large areas of the Moon.

The PLC band center results for the LSCC soils are given in Fig. 14. The mare and non-mare soils plot in two clusters offset from the synthetic pyroxene trend. There is significant spread in the band centers normal to the synthetic pyroxene trend. These systematic and random errors in the LSCC soil band center measurements are significant and result largely from the weak absorption bands, which amplify the contribution of non-compositional secondary effects on band center measurements. Even with these errors, several compositional trends are apparent in the band center relationships. Overall, the non-mare soils exhibit shorter-wavelength absorption bands than the mare soils. The mare soils exhibit a wider range in band center (and thus pyroxene composition) along the synthetic pyroxene trend. Particle size does not exhibit an obvious effect except for the Ti-rich Apollo 17 soils. For these soils, the smallest particle size fraction is strongly affected by the presence of a significant amount of ilmenite-bearing pyroclastic glass (Taylor et al. 2001), resulting in anomalous band center measurements.

5 Discussion

5.1 Composition - Band Center Relationships for Synthetic Pyroxenes as Measured by PLC

In the above discussion, the PLC technique was demonstrated to be an effective method for measuring pyroxene absorption band centers for a variety of sample types.

PLC is a suitable approximation of MGM for spectra of pure pyroxenes. Additionally, the relationship between composition and band center for these pyroxenes is similar for both MGM and PLC band center measurements. This relationship is illustrated in Fig. 15. Thus, PLC is an effective technique for measuring pyroxene band centers and successfully reproduces the compositional relationships reported by Klima et al. (2007; 2011).

5.2 Composition - Band Center Relationships for Natural Pyroxenes

PLC also provides useful composite band center measurements for lunar pyroxene separates derived from basalts. These natural pyroxenes exhibit considerably more complexity than the synthetic pure pyroxenes, including compositional zoning and a wider range of octahedral site cations (e.g. Klima and Pieters, 2008; Isaacson et al., 2011). Essentially, individual natural pyroxenes can exhibit significant compositional range over a very fine spatial scale, such as within a single mineral grain. This is demonstrated in Fig. 3B, as each pyroxene separate from the LRMCC basalts is shown to exhibit a significant range in composition. Even with this complexity, PLC-measured band centers for the pyroxene separates closely follow the synthetic pure pyroxene trend, as shown in Fig. 12. Furthermore, the PLC-measured band centers effectively demarcate lower-Ca and higher-Ca pyroxenes, with the former exhibiting shorter-wavelength band centers and the latter exhibiting longer-wavelength band centers.

The explicit relationships between absorption band centers and average pyroxene composition for the LRMCC pyroxene separates are given in Fig. 15. The lunar pyroxenes exhibit systematic relationships between band center and composition. Ca and to a lesser extent Mg are directly correlated with band center, while Fe exhibits a more

complex relationship. However, these relationships differ significantly from those of the synthetic pyroxenes. For all cations, the LRMCC pyroxenes exhibit band centers intermediate to the synthetic pure orthopyroxene and synthetic pure clinopyroxene trends. These natural pyroxene separates behave as a complex mixture of multiple pyroxene components. Therefore, band centers for synthetic pure pyroxenes should not be used to derive quantitative compositional information from composite absorption band centers of complex natural pyroxenes.

5.3 Composition - Band Center Relationships for Pyroxene Mixtures

While the LRMCC pyroxene separates exhibit mixture-like behavior, they are not mixtures in the typical sense. Rather, they represent individual pyroxene grains with a compositional range resulting from natural crystallization processes. This is a different scenario than typical mixtures, which usually include two or more distinct minerals or other components.

Several distinct types of natural mixtures were analyzed above. Figs. 12, 13, and 14 illustrate band center relationships for mixtures including one or more pyroxene component. The eucrites, diogenites, and LRMCC bulk rocks are each single rocks containing multiple co-crystallizing minerals. Howardites are a brecciated mixture of multiple rocks (eucrites and diogenites), each composed of their own individual mixture of minerals. LSCC lunar soils are particulate mixtures of rock, mineral, and glassy fragments redistributed by impacts.

Although multiple pyroxene compositions may be present in a mixture, PLC returns only one band center measurement for the 1 μm and 2 μm bands of each spectrum. These band centers do not necessarily correspond to a specific pyroxene

composition physically present in the material. Instead, the band centers describe a composite pyroxene composition related to the composition and abundance of pyroxene components in the mixture. Although the nature of the relationship is complex due to non-linear interactions of several components, PLC band center measurements are systematically related to sample composition for the mixture types analyzed here.

The LRMCC Apollo 15 bulk rock samples contain significant quantities of low-Ca pyroxene, high-Ca pyroxene, olivine, and plagioclase, as well as minor amounts of accessory minerals, metals, and glasses (Klima and Pieters 2008; Isaacson et al. 2011a). The bulk rock spectra are nevertheless dominated by the pyroxene component, as demonstrated in Fig. 6. In Fig. 12, the band centers for the Apollo 15 bulk rocks plot along the general pyroxene trend, and bulk rocks plot between their low-Ca and high-Ca pyroxene separate endmembers. Given the presence of two distinct pyroxene components, PLC successfully reports intermediate band center values for the bulk rock, relatively unaffected by the presence of non-pyroxene components. The bulk rock band centers do not necessarily correspond to an individual pyroxene composition physically present in the sample. However, the measured band centers can be used to infer the relative abundance of low-Ca and high-Ca pyroxenes in such samples.

In contrast, the LRMCC Apollo 17 bulk rock samples contain abundant ilmenite (>17%, Isaacson et al. 2011a; 2011b). This has a dramatic effect on the bulk rock spectra when the ilmenite is intimately mixed with the other minerals (see Appendix A Fig. S3). The coarse fraction retains a significant pyroxene signature due to the more linear optical interaction between pyroxene and ilmenite. The pyroxene signature is nearly lost in the fine fraction, where the components interact in a distinctly non-linear manner. The

continuum is severely distorted, causing large errors in band center measurements. This is reflected in the PLC band center results seen in Fig. 12. While band centers for both the coarse and fine fractions are significantly offset from the general pyroxene trend, the fine fraction is much more so. Although PLC band center values offset in this manner may not provide reliable information on pyroxene composition, they may be diagnostic of high ilmenite content.

HEDs represent mixtures with a wide range in average pyroxene composition, as shown in Figs. 3A and 13. Although the HEDs represent complex mixtures that formed under different conditions than the synthetic pure pyroxenes and lunar samples, their PLC-measured band centers fall neatly parallel to the synthetic pyroxene trend.

Diogenites are dominated by Mg-rich orthopyroxenes and exhibit short-wavelength absorption bands. Eucrites include significant plagioclase and clinopyroxene, exhibiting longer-wavelength band centers. Howardites are mechanical mixtures of eucrites and diogenites. The howardite band centers span the gap between eucrite and diogenites, overlapping each group. The band center values for each howardite reflect the different proportions and compositions of eucrite and diogenite components in the sample. PLC band centers can therefore constrain the rock type and relative pyroxene composition for the HEDs.

The LSCC lunar soils are also mixtures, dominated by plagioclase, low-Ca pyroxene, high-Ca pyroxene, and agglutinates (e.g. Taylor et al. 2001; Noble et al. 2006; Taylor et al. 2010). The PLC band center results for the LSCC soils are presented in Fig. 14. Even with the aforementioned complexities, the soil sample band centers follow the general synthetic pure pyroxene trend (although with the largest overall divergence of the

sample groups). As mentioned above, there is significant spread in the PLC band center values normal to the synthetic pyroxene trend, resulting from both systematic and random error. The spread in band center values could be expected for several reasons: (1) the pyroxene abundance (and therefore absorption band strength) of non-mare soils is low, (2) space weathering has reduced the overall band strength, spectral contrast, and albedo of the soils samples, (3) each soil particle size separate contains a diverse collection of components, including highly-absorbing opaque minerals and glasses, and (4) the soils contain a complex mixture of pyroxene compositions which are affected by zoning, exsolution, inversion, and unconstrained octahedral cations. Although non-compositional effects that weaken absorption band strengths are not expected to affect the actual band centers, they can amplify the effects of band shape and continuum approximations, as well as such secondary factors as noise, measurement artifacts, and non-pyroxene components. These effects result in measured band center values that deviate from the true band centers.

Even though the soils are inherently complex, compositional information is nevertheless present in the PLC band center measurements. In general, the non-mare soils (which contain a higher proportion of low-Ca pyroxene) exhibit shorter-wavelength absorption bands, while the mare soils (containing a high proportion of high-Ca pyroxene) exhibit longer-wavelength absorption bands. The mare soils exhibit significant band center variations parallel to the synthetic pyroxene trend, suggesting a wider range in pyroxene composition than the non-mare soils. This is consistent with mineralogical analyses of the soils (Taylor et al. 2001; 2010), which show a greater range in low-Ca to high-Ca pyroxene ratio for mare pyroxenes than for non-mare pyroxenes

(meaning that the mare soils exhibit greater diversity in pyroxene composition) (Noble et al. 2006). The ilmenite-rich Apollo 17 soils exhibit band centers significantly offset from the synthetic pyroxene trend and remainder of the sample group. The nature of this offset is similar to that of the ilmenite-rich Apollo 17 bulk rock sample.

Non-mare soils exhibit more tightly-clustered band centers than mare soils. Both mare and non-mare soils exhibit significant variations normal to the synthetic pyroxene trend. This variation could arise from several mechanisms, including (1) lower pyroxene abundance resulting in weaker absorption bands (and therefore a magnification of the effects of measurement artifacts, as mentioned above), and (2) variation in the strength of the 1.2 μm band (see below).

As has been well-established through decades of study, natural pyroxenes can exhibit significant compositional diversity over a wide range of spatial scales – from intra-grain zoning to mixtures of multiple distinct pyroxene compositions within a rock. Natural materials are inherently complex, resulting in complex relationships between composition and spectral properties. Therefore, band center measurements of natural pyroxene-bearing materials usually cannot be used to uniquely identify quantitative pyroxene chemistry. However, these analyses have shown PLC band center measurements to reliably capture general compositional information about the composite pyroxene composition in a sample, following relationships well-established in the existing literature (e.g. Adams 1974; Hazen et al. 1978; Cloutis and Gaffey 1991; Klima et al. 2007; Klima et al. 2011). Band centers can be used to identify and characterize compositional diversity. A direct comparison between the band center measurements for the four sample collections in this analysis is given in Fig. 16. The sample collections

exhibit distinct band center trends that are directly related to their compositional properties.

5.4 Effects of the 1.2 μm Band on the 1 μm Band Center

While the differences between PLC and MGM for the synthetic pyroxenes appear mostly random for the 2 μm band, the 1 μm band is systematically offset by around 3 nm. This offset is visually apparent in Figs. 11 and 15, as the majority of the PLC-measured 1 μm band center values plot slightly above the MGM-measured values. The 2 μm band centers do not exhibit an obvious systematic offset.

In pure pyroxenes, this systematic offset in the 1 μm band arises in part from the presence of the 1.2 μm band. As discussed in Section 2.3.2, the 1.2 μm band results from Fe in the M1 site. Although Fe prefers the M2 site, it can be trapped in the M1 site through either rapid crystallization or high Fe (or Ca) content. A 1.2 μm band is observed in the majority of the synthetic pure pyroxene samples. MGM normally accounts for the 1.2 μm band with a separate absorption, as shown in Fig. 2. PLC does not separately account for the 1.2 μm band. Therefore, PLC measurements of the 1 μm band will be offset relative to MGM measurements when a 1.2 μm band is present.

For the LSCC soils, differential 1.2 μm band strengths could potentially explain the greater offset for mare soil band centers than for non-mare soil band centers seen in Fig. 14. Mare basalts are extrusive and thus cool and crystallize relatively quickly, potentially trapping Fe in the M1 site. The pyroxenes in non-mare soils are likely crustal or intrusive, probably cooling slower and allowing Fe to diffuse into the preferred M2 site. This would result in a higher proportion of Fe in the M1 site for mare pyroxenes,

contributing to a stronger 1.2 μm band and therefore a greater offset from the MGM-measured synthetic pyroxene trend.

However, it is important to note that this interpretation is non-unique for natural samples and mixtures. An additional feature near 1 μm to 1.2 μm could arise from the presence of crystalline plagioclase, olivine, ilmenite, or glass (Nash and Conel 1974; Singer 1981; Crown and Pieters 1987; Cheek and Pieters 2014; Horgan et al. 2014). Such non-linear mineral mixture analyses are complex and well beyond the scope of this study on pyroxene composition.

Systematic offsets from the synthetic pyroxene trend are pervasive for PLC measurements of natural pyroxenes and mixtures. However, the magnitude of this offset is generally small and does not obscure the relationship between band center and composition. Instead, the magnitude of a measured offset may be used to provide additional information on the relative cooling history of pyroxenes with similar compositions or constrain the presence of additional mineral components.

6 The Humboldtianum Region as seen by M^3

6.1 Overview and Approach

In the above discussion, the PLC technique has been described and validated as an effective method to derive compositional information from spectra of pyroxene-bearing materials. PLC is optimized to handle complex remote sensing data, as it is engineered to handle large volumes of data while limiting the effects of noise and other measurement artifacts. PLC analyses can be quickly applied to hyperspectral images without requiring significant user input. This allows the creation of a variety of compositionally sensitive

parameter maps, including band centers, band depths, and spectral continuum slopes for the 1 μm and 2 μm regions. These parameter maps can be used to assess the overall spectral diversity of a region in geologic context and identify areas for more detailed spectroscopic analyses.

As an example of this approach, the PLC technique has been applied to Moon Mineralogy Mapper target data from the Humboldtianum Basin, one of a few regions where M^3 high-resolution target data is available. Regional context images for Humboldtianum are presented in Fig. 17.

Humboldtianum is a Nectarian-age multiring basin (Wilhelms 1987). Humboldtianum features a large expanse of dark mare basalt within its inner ring known as Mare Humboldtianum. Additionally, several smooth basalt exposures are present in the area between the inner and outer basin rings. Previous studies have suggested that both the central Mare Humboldtianum basalts and the inter-ring basalts exhibit a range in composition and age (Belton et al. 1994; Hiesinger et al. 1996; Hiesinger et al. 2000).

The M^3 target image cube used in this analysis is M3T20090630T103803, covering the western subregion of Humboldtianum demarcated in Fig. 18. Several maps of this subregion derived from the M^3 image cube are given in Fig. 18: (a) the 2980 nm radiance (M^3 supplemental band 3) highlights local topography, (b) the 750 nm reflectance gives local albedo, and (c) the PLC-derived 1 μm band depth map highlights the relative pyroxene abundance (and/or optical immaturity) across the region.

Using PLC analyses of M^3 data, four distinct compositional units are identified in the region: (1) central Mare Humboldtianum basalts (within the inner ring, hereby referred to as the inner mare), (2) basalts between the inner and outer ring (outer mare),

(3) lower-Ca pyroxene-bearing units on the southwestern inner ring massifs, and (4) feldspathic materials on the inner ring and other non-mare basin deposits.

6.2 PLC Results from Humboldtianum

From the albedo, topography, and 1 μm band depth maps, an overview of the local geology can be inferred. The large, low albedo region corresponds to the western extent of Mare Humboldtianum (inner mare). Several additional mare units are also visible as dark patches in the southwest portion of the image (outer mare). These inter-ring mare patches exhibit a somewhat higher albedo than the inner mare. In general, mare soils exhibit relatively strong 1 μm absorption (as seen in Fig. 18c). The inner ring massif material is heterogeneous. Much of the northern portion of the ring exhibits very weak-to-nonexistent 1 μm absorptions, while several small areas of the southern portion exhibit strong 1 μm absorptions. The remainder of the non-mare basin materials also exhibit weak-to-non-existent 1 μm absorptions. The inner ring massifs exhibit a much higher albedo than the mare basalts.

For a more detailed analysis of pyroxene compositions throughout the region, spectra were extracted from several areas exhibiting high 1 μm band strengths (>0.15). These areas are indicated by the colored arrows in Fig. 18. Such pyroxene-rich exposures were observed in Mare Humboldtianum (inner mare) basalts (red arrows), the outer mare deposits (blue arrows), and the inner ring massifs (green arrows). These high band strength areas typically represent ~ 10 -100 contiguous pixels from small, fresh craters or steep slopes that expose optically immature pyroxene-bearing materials. For comparison, 3x3 pixel average spectra from a selection of small, fresh craters with weak or

nonexistent 1 μm band strengths (and therefore low pyroxene abundance) were also analyzed. These areas are indicated with white arrows.

Spectra for several example exposures (indicated by the large arrows in Fig. 18) are given in Fig. 19. Additional example spectra (from locations indicated by the small arrows in Fig. 18) are given in Appendix A Fig. S5). Several differences between the surface units are immediately apparent in reflectance spectra. Materials with low pyroxene abundance are relatively bright. The inner mare materials are relatively dark. The outer mare and inner ring massif exposures exhibit intermediate albedos, with the ring massif materials being somewhat brighter. In continuum-removed reflectance spectra, the pyroxene-bearing inner ring massif exposures clearly exhibit shorter-wavelength absorption bands than the mare materials.

The differences in absorption band center are quantified through PLC analyses, presented in Fig. 20. PLC analyses were performed for spectra corresponding to mafic-rich exposures given by both the large and small colored arrows in Fig. 18. The PLC-derived band centers neatly separate the inner ring massif exposures (shorter-wavelength band centers) from the mare exposures (longer-wavelength band centers). As discussed in the laboratory sample analyses, the band center values for these exposures do not necessarily correspond to specific pyroxene compositions physically present. However, the band center values are related to the overall pyroxene composition in each exposure. From these band center results, it is clear that the inner ring massif pyroxenes exhibit a much lower average Ca content than the mare pyroxenes. This is consistent with the geologic context, as the inner ring massif materials likely originated in the noritic lower crust, while mare basalts typically contain significant high-Ca pyroxene.

The inner and outer mare basalts exhibit a similar range in band centers, suggesting that they are similar in average pyroxene composition. However, these materials differ in several ways. The inner mare basalts exhibit a lower albedo than the outer mare basalts. This could indicate a lower plagioclase content or higher opaque content in the Mare Humboldtianum basalts. The inner basalts also exhibit a wider range in 1 μm band center than the outer basalts. If this is due primarily to variations in the 1.2 μm band strength, this suggests a wider range in cooling histories for the inner basalts. Alternatively, the inner basalts could contain a variable proportion of glass or olivine, causing an absorption feature near 1.2 μm .

Pyroxene abundance varies significantly throughout the region, as indicated by the 1 μm band depth map in Fig. 18b. The two distinct mare units and small areas within the southwestern portion of the inner ring massifs exhibit strong 1 μm absorption bands, indicating significant pyroxene abundance. The remaining basin materials deposits do not exhibit significant 1 μm absorption bands. Since pyroxene absorptions are typically observed in mixtures with even small abundances of pyroxene (Crown and Pieters 1987; Cheek and Pieters 2014), this lack of a 1 μm band indicates a highly feldspathic composition for these materials. This is not simply a result of space weathering, as even immature materials exposed by small, fresh craters exhibit very weak absorption bands (as seen in Fig. 19).

6.3 Geologic Implications

Several geologic conclusions can be drawn from the PLC analysis of M³ target data for the Humboldtianum Basin. (1) Pyroxene abundance varies greatly across the region. Mare basalts exhibit the most pyroxene-rich soils. The inner ring massifs exhibit

significant heterogeneity in pyroxene abundance. The non-mare basin surface exhibits a feldspathic composition. (2) The inner Mare Humboldtianum basalts exhibit the lowest albedo in the region. Feldspathic materials in the region exhibit higher albedo. The outer mare basalts and pyroxene-bearing inner ring massifs exhibit intermediate albedo. (3) The inner Mare Humboldtianum basalt and outer mare basalt exposures are similar in pyroxene composition, based on their similar 1 μm and 2 μm band centers. (4) The inner Mare Humboldtianum basalt pyroxenes exhibit more variation in the 1 μm band than the inter-ring mare deposits. This is most likely due to variable 1.2 μm band strengths probably related to different cooling histories or non-pyroxene mineral components. (5) Pyroxenes in the inner ring massifs are lower in Ca than pyroxenes in the mare basalts and are likely derived from crustal sources. (6) Using PLC analyses, four distinct materials were identified across this subregion of Humboldtianum: inner Mare Humboldtianum basalts, outer mare basalts, feldspathic materials on the inner ring massifs and non-mare basin deposits, and low-Ca pyroxene-bearing materials on the inner ring massifs.

7 Conclusions

In the discussion above, we have re-examined systematic relationships between pyroxene composition and 1 and 2 μm absorption band centers. PLC analyses were performed on spectra from a diverse group of pure pyroxenes and natural pyroxene-bearing lithologies.

Natural pyroxenes exhibit significantly more complex compositional and spectral characteristics than pure pyroxenes. The diversity inherent in natural pyroxenes affects

the overall relationship between composition and measured absorption band center. However, relative relationships between composition and band centers for natural materials are readily detected and are extremely useful for analyzing and interpreting remote sensing data of pyroxene-bearing materials. The specific conclusions from these integrated analyses fall into three distinct categories: **(1)** the development and evaluation of PLC approach itself, **(2)** the character of band center measurements for natural pyroxene-bearing materials, and **(3)** the compositional properties of our example target area, the Humboldtianum Basin.

(1) The **Parabola** and two-part **Linear Continuum (PLC)** approach provides measurement of band centers and depths for the diagnostic 1 μm and 2 μm pyroxene absorption bands.

- For synthetic pure pyroxenes, PLC band center measurements accurately reflect MGM band center measurements to within ~ 6 nm for the 1 μm band and ~ 17 nm for the 2 μm band. The PLC-derived relationship between band center and pyroxene composition (Fe,Ca,Mg) directly reflects the relationships derived from the MGM analyses of Klima et al. (2007; 2011).
- PLC measures a single band center value for the diagnostic 1 μm and 2 μm bands of each pyroxene-bearing spectrum. For natural materials and mixtures, spectra exhibit composite bands resulting from multiple pyroxene and non-pyroxene components. The single band center values reported by PLC do not attempt to deconvolve individual contributions from multiple components, but serve to identify the overall properties of the mixture. The interpretation of these band centers is non-unique (see below).

- Nevertheless, previously established relative relationships between average pyroxene composition and absorption band center were confirmed using three natural sample collections: (1) lunar bulk basalt and pyroxene separates from the Lunar Rock and Mineral Characterization Consortium, (2) lunar soils from the Lunar Soil Characterization Consortium, and (3) howardite, eucrite, and diogenite meteorites.
- PLC analyses of the 1 μm pyroxene absorption band can provide indirect evidence for the presence of Fe^{2+} in the M1 pyroxene site due to the effects of a resulting 1.2 μm band. The presence of a strong 1.2 μm band can be observed as a shift in the PLC-measured 1 μm band center to longer wavelengths without affecting the 2 μm band center measurement.

(2) We emphasize that natural pyroxene-bearing materials are inherently complex, and several issues should be considered when interpreting band center measurements:

- Natural crystallization processes such as zoning or exsolution often lead to a wide compositional range within individual pyroxene grains, as observed in the LRMCC pyroxene separates. This compositional range results in composite absorption band centers that are inherently different from those that would be measured for a synthetic pure pyroxene with the same average composition.
- Rocks and soils often include multiple coexisting pyroxene components. For example, the LRMCC basalts and LSCC soils each contain many distinct pyroxene grains of different average compositions (e.g. low-Ca and high-Ca).

PLC band center measurements represent composite band centers for each sample, corresponding to a nonlinear mixture of several components.

- Measurements of the 1 μm and 2 μm bands of natural rock and soil samples should therefore be interpreted as mixtures of multiple pyroxene components. This diversity in pyroxene composition is pervasive in natural materials, as it occurs on very fine scales such as within individual pyroxene grains.
- Because mixing within samples can be nonlinear, absorption band centers measured for natural pyroxene-bearing materials do not necessarily correspond to simple linear mixtures of pure pyroxene components.
- Although band center measurements of natural materials do not uniquely correspond to specific pyroxene compositions, relative compositional relationships can be reliably determined from comparison of band center values when the data are from the same geologic reference frame.

(3) The PLC approach is well-suited to working with large, complex volumes of remote sensing data. Applying the PLC technique to high spectral resolution M^3 target data from the Humboldtianum Basin, four distinct materials were identified based on their pyroxene content and composition:

- Mare Humboldtianum basalts (within the inner ring) exhibit long-wavelength band centers and low albedo, indicating a basaltic composition rich in high-Ca pyroxene. Significant deviations in the 1 μm band center are observed, suggesting variations in the 1.2 μm band strength corresponding to either

heterogeneous cooling histories of the pyroxenes or variations in the abundance of other non-pyroxene components (e.g. plagioclase, olivine).

- Other mare materials (located between the inner and outer rings of the basin) also exhibit long wavelength band centers, indicating a basaltic composition.

However, these materials have a higher albedo than the basalts within Mare Humboldtianum. This could be due to a higher plagioclase content, lower opaque content, or more significant mixing with crustal materials in the regolith. These basalts exhibit less variation in their 1 μm band centers, indicating a more uniform composition and thermal evolution.

- Pyroxene-rich materials are also found as small exposures in a few non-mare areas, especially the southwest extent of the inner ring and surrounding massifs. These materials exhibit distinctly shorter-wavelength band centers than the mare materials, indicating the presence of a lower Ca (more Mg-rich) pyroxene. These small exposures also exhibit a higher albedo than the basaltic materials, most likely related to a higher plagioclase content.
- The bulk of the non-mare areas (inner basin ring, other non-mare basin deposits) exhibit very weak to non-existent absorption bands, indicating a very low pyroxene abundance and overall highly feldspathic character.

8 Acknowledgements

This paper is supported through the NASA LASER (NNX12AI96G) and SSERVI (NNA13AB01A) programs. Thanks to Dr. Ralph Milliken, Dr. Rachel Klima, Dr. Sarah

Noble, and Dr. Peter Isaacson for helpful discussions while preparing the manuscript.
Two anonymous reviewers provided excellent feedback that improved the manuscript.

9 References

- Adams J. B. 1974. Visible and near-infrared diffuse reflectance spectra of pyroxenes as applied to remote sensing of solid objects in the solar system. *Journal of Geophysical Research* 79:32:4829-4836.
- Agrell S. O., Scoon J. H., Muir I. D., Long J. V. P., McConnell J. D. C., and Peckett A. 1970. Observations on the chemistry, mineralogy, and petrology of some Apollo 11 lunar samples. *Proceedings of the Apollo 11 Lunar Science Conference* pp. 93-128.
- Albee A. L., Chodos A. A., Gancarz A. J., Haines E. L., Papanastassiou D. A., Ray L., Tera F., Wasserburg G. J., and Wen T. 1972. Mineralogy, petrology, and chemistry of a Luna 16 basaltic fragment, sample B-1. *Earth and Planetary Science Letters* 13:353–367.
- Belton M. J., Greeley R., Greenberg R., Geissler P., McEwen A., Klassen K. P., Hefferman C., Breneman H., Johnson T. V., Head III J. W., Pieters C. M., Neukum G., Chapman C. R., Anger C., Carr M. H., Davies M. E., Fanale F. P., Gierasch P. J., Thompson W. R., Veverka J., Sagan C., Ingersoll A. P., and Pilcher C. B. 1994. Galileo multispectral imaging of the north polar and eastern limb regions of the moon. *Science* 20:264(5162):1112-5.

- Bence A. E. and Papike J. J. 1972. Pyroxenes as recorders of lunar basalt petrogenesis: Chemical trends due to crystal-liquid interaction. *Proceedings of the Lunar Science Conference III* pp. 431–469.
- Bence A. E., Papike J. J., and Prewitt C. T. 1970. Apollo 12 clinopyroxenes: Chemical trends. *Earth and Planetary Science Letters* 8:393-399.
- Boardman J. W., Pieters C. M., Green R. O., Lundeen S. R., Varanasi P., Nettles J., Petro N., Isaacson P., Besse S., and Taylor L. A. 2011. Measuring moonlight: An overview of the spatial properties, lunar coverage, selenolocation, and related Level 1B products of the Moon Mineralogy Mapper. *Journal of Geophysical Research* 116:E00G14.
- Bowman L. E., Spilde M. N., and Papike J. J. 1997. Automated energy dispersive spectrometer modal analysis applied to the diogenites. *Meteoritics & Planetary Science* 32:6:869-875.
- Boyd F. R. and Smith D. 1971. Compositional zoning in pyroxenes from lunar rock 12021, Oceanus Procellarum. *Journal of Petrology*, 12:439–464.
- Brown G. M., Emeleus C. H., Holland J. G., and Phillips R. 1970. Mineralogical, chemical, and petrological features of Apollo 11 rocks and their relationship to igneous processes. *Proceedings of the Apollo 11 Lunar Science Conference* pp. 195-219.
- Burbine T. H., Buchanan P. C., Binzel R. P., Bus S. J., Hiroi T., Hinrichs J. L., Meibom A., and McCoy T. J. 2001. Vesta, Vestoids, and the howardite, eucrite, diogenite group: Relationships and the origin of spectral differences. *Meteoritics & Planetary Science* 36:6:761-781.

- Burns R. G. 1993. *Mineralogical applications of crystal field theory*, 2nd ed. Cambridge, UK: Cambridge University Press. 551.
- Cheek L. C. and Pieters C. M. 2014. Reflectance spectroscopy of plagioclase-dominated mineral mixtures: Implications for characterizing lunar anorthosites remotely. *American Mineralogist* 99:10:1871-1892.
- Clark R. N. and Roush T. L. 1984. Reflectance spectroscopy: Quantitative analysis techniques for remote sensing applications. *Journal of Geophysical Research* 89:6329-6240.
- Clayton R. N. 1993. Oxygen isotopes in meteorites. *Annual Review of Earth and Planetary Sciences* 21:A94-10876 01-91:115-149.
- Cloutis E. A. 2002. Pyroxene reflectance spectra: Minor absorption bands and effects of elemental substitutions. *Journal of Geophysical Research* 107:E6:5039.
- Cloutis E. A. and Gaffey M. J. 1991. Pyroxene spectroscopy revisited: Spectral-compositional correlations and relationship to geothermometry. *Journal of Geophysical Research: Planets* 96:E5:22809-22826.
- Crown D. A. and Pieters C. M. 1987. Spectral properties of plagioclase and pyroxene mixtures and the interpretation of lunar soil spectra. *Icarus* 72:492-506.
- Delaney J. S., Takeda H., Prinz M., Nehru C. E., and Harlow G. E. 1983. The nomenclature of polymict basaltic achondrites. *Meteoritics* 18:2:103-111.
- Delaney J. S., Prinz M., and Takeda H. (1984) The polymict eucrites. *Journal of Geophysical Research: Solid Earth* 89:S01:C251-C288.

- Dence M. R., Douglas J. A. V., Plant A. G., and Traill R. J. 1971. Mineralogy and petrology of some Apollo 12 samples. *Proceedings of the Lunar Science Conference II*, pp. 285–299.
- De Sanctis, M.C., A. Coradini, E. Ammannito, G. Filacchione, M.T. Capria, S. Fonte, E. Magni, A. Barbis, A. Bini, M. Dami, I. Fikai-Veltroni, G. Preti, the VIR team (2011). The VIR spectrometer. *Space Sci. Rev.*, 163 (2011), pp. 329–369
- Dixon J. R. and Papike J. J. 1975. Petrology of anorthosites from the Descartes region of the Moon: Apollo 16. *Proceedings of the Lunar Science Conference VI* pp. 263–291.
- Dymek R. F., Albee A. L., and Chodos A. A. 1975. Comparative mineralogy and petrology of Apollo 17 mare basalts: Samples 70215, 71055, 74255, and 75055. *Proceedings of the Lunar Science Conference VI*, pp. 49–77.
- Farr T. G., Bates B. A., Ralph R. L., and Adams J. B. 1980. *Proceedings of the Lunar and Planetary Science Conference XI*, pp. 719-729.
- Gaffey M. J. 1976. Spectral reflectance characteristics of the meteorite classes. *Journal of Geophysical Research*, 81:905-920.
- Gancarz A. J., Albee A. L., and Chodos A. A. 1971. Petrologic and mineralogic investigations of some crystalline rocks returned by the Apollo 14 mission. *Earth and Planetary Science Letters* 12:1–18.
- Hazen R. M., Bell P. M., and Mao H. K. 1978. Effects of compositional variation on absorption spectra of lunar pyroxenes. *Proceedings of the Lunar and Planetary Science Conference IX*, pp. 2929-2934.

- Hargraves R. B. and Hollister L. S. 1972. Mineralogic and petrologic study of lunar anorthosite slide 15415,18. *Science* 175:430–432.
- Hiesinger H., Oberst J., Jaumann R., Neukum G., and Head III J. W. Observations of Mare Humboldtianum: Topography, ages, and multispectral characteristics. *Lunar and Planetary Science Conference XXVII* #547.
- Hiesinger H., Jaumann R., Neukum G., and Head III J. W. 2000. Ages of mare basalts on the lunar nearside. *Journal of Geophysical Research: Planets* 105:E12:29238-29275.
- Hodges F. N. and Kushiro I. 1974. Apollo 17 petrology and experimental determination of differentiation sequences in model Moon compositions. *Proceedings of the Lunar Science Conference V* pp. 505–520.
- Hollister L. S. and Hargraves R. B. 1970. Compositional zoning and its significance in pyroxenes from two coarse grained Apollo 11 samples. *Proceedings of the Apollo 11 Lunar Science Conference* pp. 541–550.
- Hollister L. S., Trzcinski W. E. Jr., Hargraves R. B., and Kulick C. G. 1971. Petrogenetic significance of pyroxenes in two Apollo 12 samples. *Proceedings of the Lunar Science Conference II*, pp. 529–557.
- Horgan B. H. N., Cloutis E. A., Mann P., and Bell J. F. 2014. Near-infrared spectra of ferrous mineral mixtures and methods for their identification in planetary surface spectra. *Icarus* 234:132-154.
- Huguenin R. L. and Jones J. L. 1986. Intelligent information extraction from reflectance spectra: Absorption band positions. *Journal of Geophysical Research* 91:9585-9598.

- Isaacson P. J., Basu Sarbadhikari A., Pieters C. M., Klima R. L., Hiroi T., Liu Y., and Taylor L. A. 2011a. The lunar rock and mineral characterization consortium: Deconstruction and integrated mineralogical, petrologic, and spectroscopic analyses of mare basalts. *Meteoritics and Planetary Science* 46:2:228-251.
- Isaacson P. J., Pieters C. M., Hiroi T., Liu Y., Dhingra D., Klima R. L., and Taylor L. A. 2011b. Reflectance spectroscopy of ilmenite: New constraints from Apollo sample measurements, *Lunar and Planetary Science Conference XLII* #2130.
- Keil K. 2002. Geological history of asteroid 4 Vesta: The “smallest terrestrial planet.” In *Asteroids III*, edited by Bottke Jr. W. F., Cellino A. Paolicci P., and Binzel R. P. Tuscon, University of Arizona Press, pp. 573-584.
- Klima R. L. and Pieters C. M. 2008. MGM analysis of pyroxene mineral separates from Apollo 15 and 17. *Lunar and Planetary Science Conference XXXIX*. #1756.
- Klima R. L., Pieters C. M., and Dyar M. D. 2007. Spectroscopy of synthetic Mg-Fe pyroxenes I: Spin-allowed and spin-forbidden crystal field bands in the visible and near-infrared. *Meteoritics and Planetary Science* 42:2:235-253.
- Klima R. L., Pieters C. M., and Dyar M. D. 2008. Characterization of the 1.2 μm M1 pyroxene band: Extracting the cooling history from near-IR spectra of pyroxenes and pyroxene-dominated rocks. *Meteoritics and Planetary Science* 43:10:1591-1604.
- Klima R. L., Dyar M. D., and Pieters C. M. 2011. Near-infrared spectra of clinopyroxenes: Effects of calcium content and crystal structure. *Meteoritics and Planetary Science* 46:3:379-395.

- Kushiro I. and Nakamura Y. 1970. Petrology of some lunar crystalline rocks.
Proceedings of the Apollo 11 Lunar Science Conference pp. 607–626.
- Laul J. C., Vaniman D. T., Papike J. J., and Simon S. 1978. Chemistry and petrology of size fractions of Apollo 17 deep drill core 70009–70006. *Proceedings of the Lunar and Planetary Science Conference IX* pp. 2065–2097.
- Lucey P., Gillis J. J., Korotev R. L., Taylor L. A., Lawrence D., Elphic R., Feldman B., Hood L. L., Hunten D., Mendillo M., Noble S., Papike J. J., and Reedy R. C. 2006. Understanding the lunar surface and space-moon interactions. In *New views of the Moon* 1st ed., edited by Jolliff B. L., Wieczorek M. A., Shearer C. K., and Neal C. R. Chantilly, Mineralogical Society of America. pp. 83-221.
- Mason B., Jarosewiche E. and Nelen J. A. 1979. The pyroxene-plagioclase achondrites. *Smithsonian Contributions to Earth Science* 22:27-45.
- Marfunin, A. S. 1979. *Physics of Minerals and Inorganic Materials*, New York, Springer-Verlag, 340 pp.
- Mayne R. G., Sunshine J. M., McSween H. Y., McCoy T. J., Corrigan C. M., and Gale A. 2010. Petrologic insights from the spectra of the unbrecciated eucrites: Implications for Vesta and basaltic asteroids. *Meteoritics & Planetary Science* 45:7:1074-1092.
- McCallum I. S. and Mathez E. A. 1975. Petrology of noritic cumulates and a partial melting model for the genesis of Fra Mauro basalts. *Proceedings of the Lunar Science Conference VI* pp. 395–414.

- McCord, T. B., Clark R. N., Hawke B. R., McFadden L. A., Owensby P. D., Pieters C. M., and Adams J. B. 1981. Moon: Near-infrared spectral reflectance: A first good look. *Journal of Geophysical Research* 86:10833-10892.
- Mittlefehldt D. W., McCoy T. J., Goodrich C. A., and Krachner A. 1998. Non-chondritic meteorites from asteroidal bodies. In *Planetary Materials*, edited by Papike, J. J.. Chantilly, Mineralogical Society of America, pp. 4-001 – 4-196.
- Mittlefehldt D. W., Ammannito E., Hiroi T., De Angelis D. P., Moriarty D. P., Di Iorio T., Pieters C. M., and Pieters C. M. 2014. Compositional diversity of the vestan regolith derived from howardite compositions and Dawn VIR spectra (abstract #3906). *Goldschmidt 2014*.
- Moriarty III D. M. and Pieters C. M. 2014. LSCC samples as ground truth: Using spectral parameters developed for M³ data to assess composition and maturity. *Lunar and Planetary Science Conference XLX #2532*.
- Nash D. B. and Conel J. E. 1974. Spectral reflectance systematics for mixtures of powdered hypersthene, labradorite, and ilmenite. *Journal of Geophysical Research* 79:11:1615-1621.
- Newton R. C., Anderson A. T., and Smith J. V. 1971. Accumulation of olivine in rock 12040 and other basaltic fragments in the light of analysis and synthesis. *Proceedings of the Lunar Science Conference II* pp. 575–582.
- Noble S. K., Pieters C. M., Hiroi T., and Taylor L. A. 2006. Using the modified Gaussian model to extract quantitative data from lunar soils. *Journal of Geophysical Research* 111:E11009.

- Papike J. J., Bence A. E., and Lindsley D. H. 1974. Mare basalts from the Taurus-Littrow region of the Moon. *Proceedings of the Lunar Science Conference V* pp. 471–504.
- Papike J., Taylor L., and Simon S. 1991. Lunar minerals. In *Lunar sourcebook: A user's guide to the Moon*, 1st ed., edited by Heiken G. H., Vaniman D. T. and French B. M. Cambridge, Cambridge University Press, pp. 121-182.
- Pieters, C. M. 1978. Mare basalt types on the front side of the Moon: A summary of spectral reflectance data. *Proceedings of the Lunar and Planetary Science Conference, IX*. 2825-2849.
- Pieters C. M., Taylor L. A., McKay D. S., Wentworth S., Morris R. V., and Keller L. P. 2000. Spectral characterization of lunar mare soils (Abstract #1865). *Lunar Planet. Sci. XXXI*.
- Pieters C. M., Binzel R., Bogard D., Hiroi T., Mittlefehldt D. W., Nyquist L., Rivkin A., and Takeda H. 2006. Asteroid-meteorite links: The Vesta conundrum(s). *Asteroids, Comets, Meteors: Proceedings of the IAU Symposium No. 229*.
- Pieters C. M., Boardman J., Buratti B., Chatterjee A., Clark R., Glavich T., Green R., Head III J., Isaacson P., Malaret E., McCord T., Mustard J., Petro N., Runyon C., Staid M., Sunshine J., Taylor T., Tompkins S., Varanasi P., White M. 2009. The Moon Mineralogy Mapper (M³) on Chandrayaan-1. *Current Science* 96:4:500-505.
- Robinson M. S., Brylow S. M., Tschimmel M., Humm D., Lawrence S. J., Thomas P. C., Denevi B. W., Bowman-Cisneros E., Zerr J., Ravine M. A., Caplinger M. A., Ghaemi F. T., Schaffner J. A., Malin M. C., Mahanti P., Bartels A., Anderson J.

- Tran T. N., Eliason E. M., McEwen A. S., Turtle E., Joliff B. L., and Hiesinger H. 2010. Lunar Reconnaissance Orbiter Camera (LROC) instrument overview. *Space Science Reviews* 150:81-124.
- Russell C. T., Raymond C. A., Coradini A., McSween H. Y., Zuber M. T., Nathues A., De Sanctis M. C., Jaumann R., Konopliv A. S., Preusker F., Asmar S. W., Park R. S., Gaskell R., Keller H. U., Mottola S., Roatsch T., Scully J. E. C., Smith D. E., Tricarico P., Toplis M. J., Christensen U. R., Feldman W. C., Lawrence D. J., McCoy T. J., Prettyman T. H., Reedy R. C., Sykes M. E., and Titus T. N. 2012. *Science* 11:6082:684-686.
- Sclar C. B. and Bauer J. F. 1975. Shock-induced subsolidus reduction-decomposition of orthopyroxene and shock-induced melting in norite 78235. *Proceedings of the Lunar Science Conference VI* pp. 799–820.
- Shervais J. W., Taylor L. A., and Lindstrom M. M. 1985. Apollo 14 mare basalts: Petrology and geochemistry of clasts from consortium breccia 14321. *Proceedings of the Lunar and Planetary Science Conference XV*, in *Journal of Geophysical Research* 89:C375–C395.
- Singer R. B. 1981. Near-infrared spectral reflectance of mineral mixtures: Systematic combinations of pyroxenes, olivine, and iron oxides. *Journal of Geophysical Research: Solid Earth* 86:B9:7967-7982.
- Singer R. B. and Roush T L. 1985, Effects of temperature on remotely sensed mineral absorption features. *J. Geophys. Res.* 90:B14:12,434-12444.
- Smith J. V., Anderson A. T., Newton R. C., Olsen E. J., Wyllie P. J., Crewe A. V., Isaacson M. S., and Johnson D. 1970. Petrologic history of the Moon inferred

- from petrography, mineralogy, and petrogenesis of Apollo 11 rocks. *Proceedings of the Apollo 11 Lunar Science Conference* pp. 897–925.
- Smyth J. R. 1975. Intracrystalline cation order in a lunar crustal troctolite. *Proceedings of the Lunar Science Conference XI* pp. 821–832.
- Sunshine J. M. and Pieters C. M. 1993. Estimating modal abundances from the spectra of natural and laboratory pyroxene mixtures using the Modified Gaussian Model. *Journal of Geophysical Research* 98:E5:9075-9087.
- Sunshine J. M., Pieters C. M., and Pratt S. F. 1990. Deconvolution of mineral absorption bands – An improved approach. *Journal of Geophysical Research – Planets* 98:9075-9087.
- Takeda H. 1997. Mineralogical records of early planetary processes on the howardite, eucrite, diogenite parent body with reference to Vesta. *Meteoritics and Planetary Science* 32:841-853
- Taylor L. A., Pieters C. M., Morris R. V., Keller L. P., and McKay D. S. 2001. Lunar mare soils: Space weathering and the major effects of surface-correlated nanophase Fe. *Journal of Geophysical Research* 106:E11:27,985-28,000.
- Taylor L. A., Pieters C. M., Patchen A., Taylor D. H. S., Morris R. V., Keller L. P., and McKay D. S. 2010. Mineralogical and chemical characterization of lunar highland soils: Insights into the space weathering of soils on airless bodies. *Journal of Geophysical Research* 115:E02002:14.
- Turnock A. C., Lindsley D. H., and Grover J. E. 1973. Synthesis and unit cell parameters of Ca-Mg-Fe pyroxenes. *American Mineralogist* 58:50-59.

- Vaniman D. T. and Papike J. J. 1977. The Apollo 17 drill core: Characterization of the mineral and lithic component (sections 70007, 70008, 70009). *Proceedings of the Lunar Science Conference VIII* pp. 3123–3159.
- Vaniman D. T. and Papike J. J. 1980. Lunar highland melt rocks: Chemistry petrology and silicate mineralogy. In *Proceedings of the Conference on the Lunar Highlands Crust* edited by J. J. Papike and R. B. Merrill. New York, Pergamon, pp. 271–337.
- Weigand P. W. and Hollister L. S. 1973. Basaltic vitrophyre 15597: An undifferentiated melt sample. *Earth and Planetary Science Letters* 19:61–74.
- Wilhelms, D. E., McCauley, J. F., and Trask, N. J. 1987. *The Geologic History of the Moon*, USGS Professional Paper, 1938:302.
- Yon S. A. and Pieters C. M. 1988. Interactions of light with rough dielectric surfaces: Spectral reflectance and polarimetric properties. *Proceedings of the Lunar and Planetary Science Conference XVIII* 581-592.

10 Tables

Table 1: Description of sample collections (and references documenting detailed compositional and spectroscopic data).

Sample Collection	Description	References
Synthetic Pyroxenes	Laboratory-synthesized orthopyroxenes and clinopyroxenes with compositions strictly limited to Fe ²⁺ , Ca ²⁺ , and Mg ²⁺ in the octahedral cation sites.	Turnock et al., 1973; Klima et al., 2007, 2008, 2011
Lunar Rock and Mineral Characterization Consortium	Unweathered mineral separates (pyroxene, plagioclase, olivine, ilmenite) and bulk rock samples from Apollo 15 and 17 basalts.	Klima and Pieters, 2008; Isaacson et al., 2011
Lunar Soil Characterization Consortium	Highland and mare soil samples obtained from several Apollo landing sites. Soils have been sieved to obtain several particle size separates, which affects the type and proportion of soil components in each separate.	Pieters et al., 2000; Taylor et al., 2001; Noble et al., 2006; Taylor et al., 2010
HEDs	Howardite, eucrite, and diogenite meteorite samples.	Klima et al., 2008; Mittlefehldt et al., 2014

11 Figure Captions

Fig. 1: Example spectra for several synthetic pure pyroxenes, including orthopyroxene (black), low-Ca clinopyroxene (grey, solid), and high-Ca pyroxene (grey, dashed). This group of samples were previously analyzed using the Modified Gaussian Model by Klima et al. (2007; 2008; 2011).

Fig. 2: An example Modified Gaussian Model (MGM) (Sunshine et al., 1990) spectral deconvolution for orthopyroxene (Mg70Fs30). The measured reflectance spectrum is modeled by several modified Gaussian-shaped absorptions superposed on a continuum. The absorption bands corresponding to transition metal cations in the M1 and M2 sites are labeled. The RMS error on the MGM fit is also given.

Fig. 3: Pyroxene compositions for several groups of synthetic and natural pyroxenes. (A) Compositions for the synthetic pyroxenes used in the Klima et al. (2007; 2008; 2011) analyses are shown in black. Synthetic clinopyroxenes with very high Ca contents not typically observed in natural samples are indicated with dotted circles. Compositions for a collection of lunar pyroxenes from a variety of mare (red stars) and non-mare (blue stars) are given, demonstrating the general compositional range of lunar pyroxenes. These lunar data were compiled by Papike et al. (1991) from the sources given in Appendix A Figure S2. HED pyroxene compositions are shown in pink (adapted from Mason et al. (1979) and Takeda (1997)). Solid symbols and their connecting lines show observed exsolution trends. Bulk compositions are given by the

open circles. (B) Composition of LRMCC pyroxene separates from four Apollo basalts. The range in composition is outlined in blue (adapted from Isaacson et al. (2011)). Solid lines give the “high-Ca” pyroxene separate compositional range. Dashed lines give the “low-Ca” pyroxene separate compositional range. Average compositions for each pyroxene separate are given by the solid symbols. (C) Average compositions of pyroxenes measured for the mare (red) and non-mare (orange) LSCC soils (adapted from Noble et al. (2006)). Symbol size corresponds to the relative abundance of that pyroxene composition in the respective soil.

Fig. 4: Relationships between Ca (a-b), Mg (c-d), Fe (e-f) and 1 μm (a,c,e) and 2 μm (b,d,f) band center for synthetic pure pyroxenes as measured by Klima et al. (2007; 2011) using the Modified Gaussian Model. Clinopyroxenes with very high Ca content not typically observed in lunar samples are indicated with dotted circles.

Fig. 5: 1 μm band center vs. 2 μm band center for synthetic pyroxenes as measured by Klima et al. (2007; 2011) using MGM. Clinopyroxenes with very high Ca content not typically observed in natural samples are indicated with dotted circles. This plot effectively separates pyroxenes into the general compositional groups labeled.

Fig. 6: Example reflectance spectra for three components of lunar mare basalt sample 15058: the low-Ca pyroxene separate, the high-Ca pyroxene separate, and the bulk rock. Spectra of the coarse particle size fraction are shown here.

Fig. 7: Example reflectance spectra from four HED meteorites: howardite (Bununu, <25 μm particle size; LEW85313.39, <75 μm), eucrite (GRO 95533.19, <25 μm), and diogenite (A-881526.90, <25 μm).

Fig. 8: Example reflectance spectra of LSCC lunar non-mare (61141, orange) and mare (15071, red) soils for three particle size separates.

Fig. 9: Example PLC continuum fits (dark grey dashed lines) for synthetic clinopyroxene ($\text{Ca}_{10}\text{Mg}_0\text{Fe}_{90}$) and lunar mare soil 15071. For the synthetic clinopyroxene spectrum, the 2 μm band extends beyond the measured wavelength range. If the last datapoint is used as a continuum tiepoint, the resulting continuum would be negative (indicated by the light grey line) and the measured band center would be artificially shifted to shorter wavelengths. In spectra where a negative 2 μm continuum is present, a flat continuum is used over the 2 μm region instead (dark grey line). Additional examples are given in Appendix A.

Fig. 10: Example continuum-removed spectra and parabolic fits to the 1 μm and 2 μm absorption bands for synthetic clinopyroxene ($\text{Ca}_{10}\text{Mg}_0\text{Fe}_{90}$) and lunar mare soil 15071 (same spectra as Fig. 9). The parabolic fits are optimized to target the band minimum of the continuum-removed spectrum, rather than the band width or shape. Additional examples are given in the Appendix A.

Fig. 11: A comparison between the 1 μm band center vs. 2 μm band center trend for synthetic pyroxenes measured using PLC (solid symbols) and MGM (open symbol, values from Klima et al. 2007; 2011).

Fig. 12: PLC-measured band centers for the LRMCC pyroxene separates and bulk rock samples superimposed on the synthetic pyroxene trend. Only the ilmenite-rich Apollo 17 bulk rock samples fall significantly off the synthetic pyroxene trend.

Fig. 13: PLC-measured band centers for HED meteorite samples superimposed on the synthetic pyroxene trend. The full scale is shown in (A). An expanded scale is shown in (B).

Fig. 14: PLC-measured band centers for the LSCC soils superimposed on the synthetic pyroxene trend.

Fig. 15: Relationships between Ca (a-b), Mg (c-d), Fe (e-f) and 1 μm (a,c,e) and 2 μm (b,d,f) band center of synthetic pure pyroxenes (black) as measured by PLC (filled) and MGM (open), Klima et al. 2007; 2011. The superimposed LRMCC lunar pyroxene data (blue) represent the average composition for each pyroxene separate. However, the separates contain a range of pyroxene compositions due to zoning, exsolution, etc. (as seen in Fig. 3B). The LRMCC pyroxenes fall between the synthetic pure orthopyroxene and clinopyroxene trends.

Fig. 16: A comparison of PLC band center measurements for all four sample collections considered in this analysis.

Fig. 17: LROC images (Robinson et al., 2010) orthographically projected and centered on the Humboldtianum Basin (57° N, 81° E). (A) Color-shaded relief. (B) WAC 100 m/pixel global mosaic. The dashed white circles indicate the locations of the inner and outer rings. The red box gives the location of the M³ target image used in these analyses.

Fig. 18: (A) 2980 nm radiance (topography preserved), (B) 750 nm reflectance (topography approximately removed), and (C) PLC-measured 1 μm band depth for the region of the Humboldtianum Basin outlined in Fig. 17. The white arrows correspond to example immature areas with low mafic content. The red, green, and blue arrows correspond to example areas exhibiting strong pyroxene absorptions. Mare materials within the inner ring (Mare Humboldtianum) are marked in red. Mare materials outside the inner ring (outer mare) are marked in blue. Non-mare pyroxene-rich exposures are marked in green. Large arrows correspond to example spectra in Fig. 19. Additional example spectra from the small arrows are given in Appendix A Fig. S5. Band centers for all pyroxene-rich exposures are given in Fig. 20.

Fig. 19: Example reflectance and continuum-removed reflectance spectra from select exposures in the Humboldtianum region (indicated by the large arrows). Colors correspond to the unit types given in Fig. 17. Additional spectra from the region are given in Appendix A Fig. S5.

Fig. 20: PLC band center measurements for the pyroxene-dominated exposures in Mare Humboldtianum superimposed on the PLC-measured synthetic pyroxene trend. The non-mare and mare pyroxenes are effectively separated into different clusters. Differences in the 1 μm band properties between the inner and outer mare exposures are also revealed. Each point corresponds to locations indicated by arrows (large and small) in Fig. 17. In cases where several small exposures are clustered in a small area, arrows correspond to multiple exposures.

12 Figures

Fig. 1

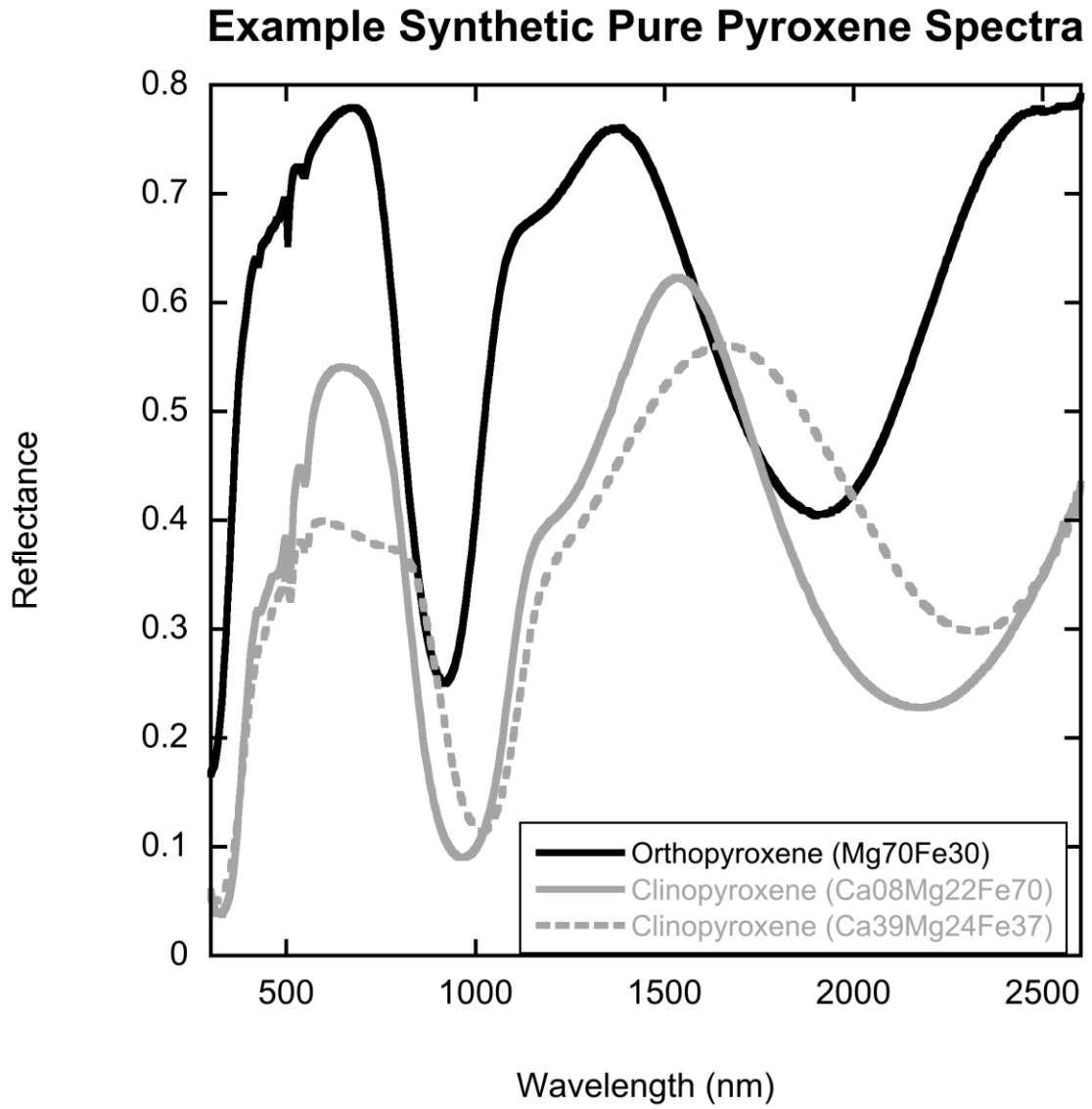


Fig. 2

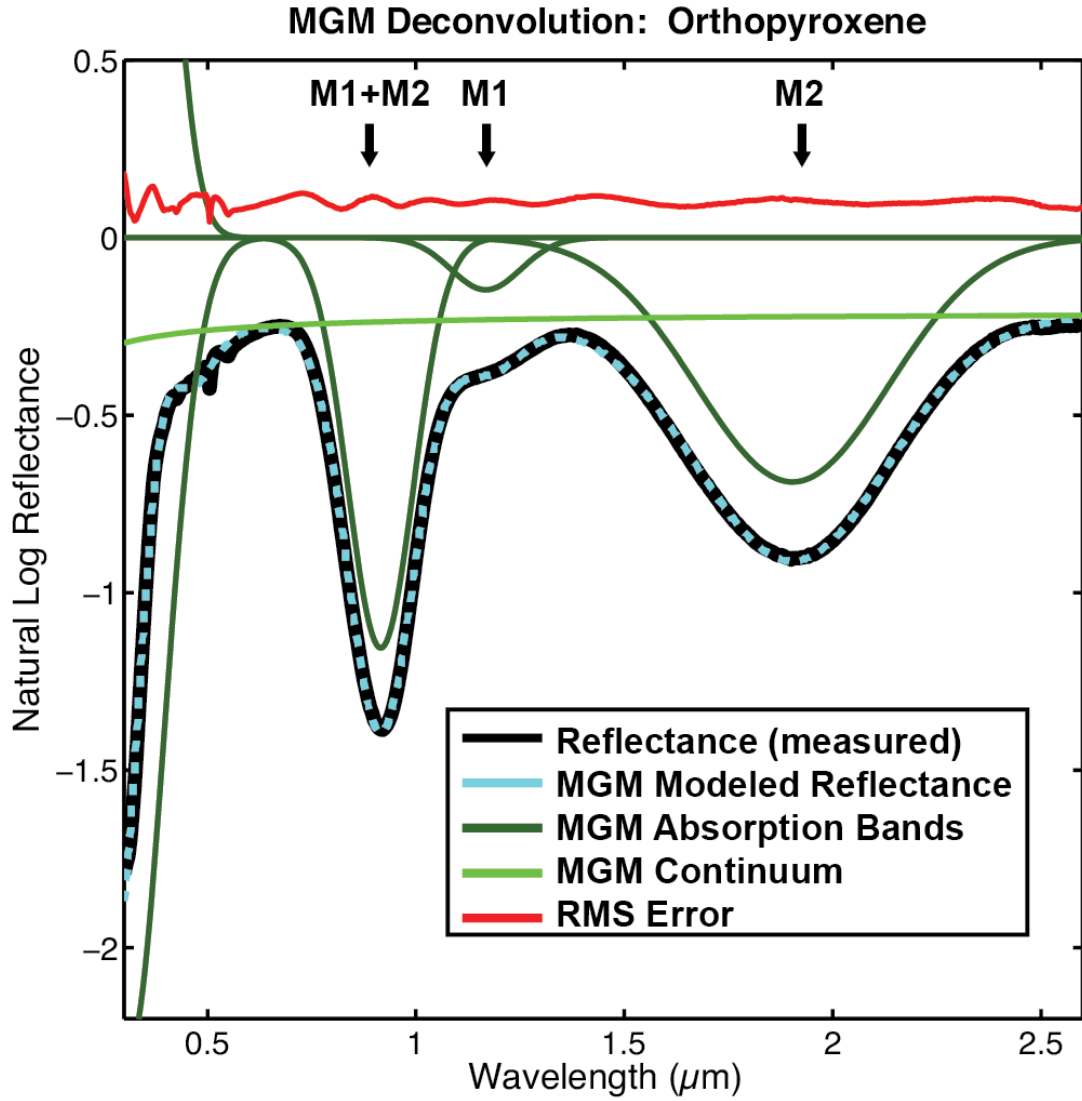


Fig. 3

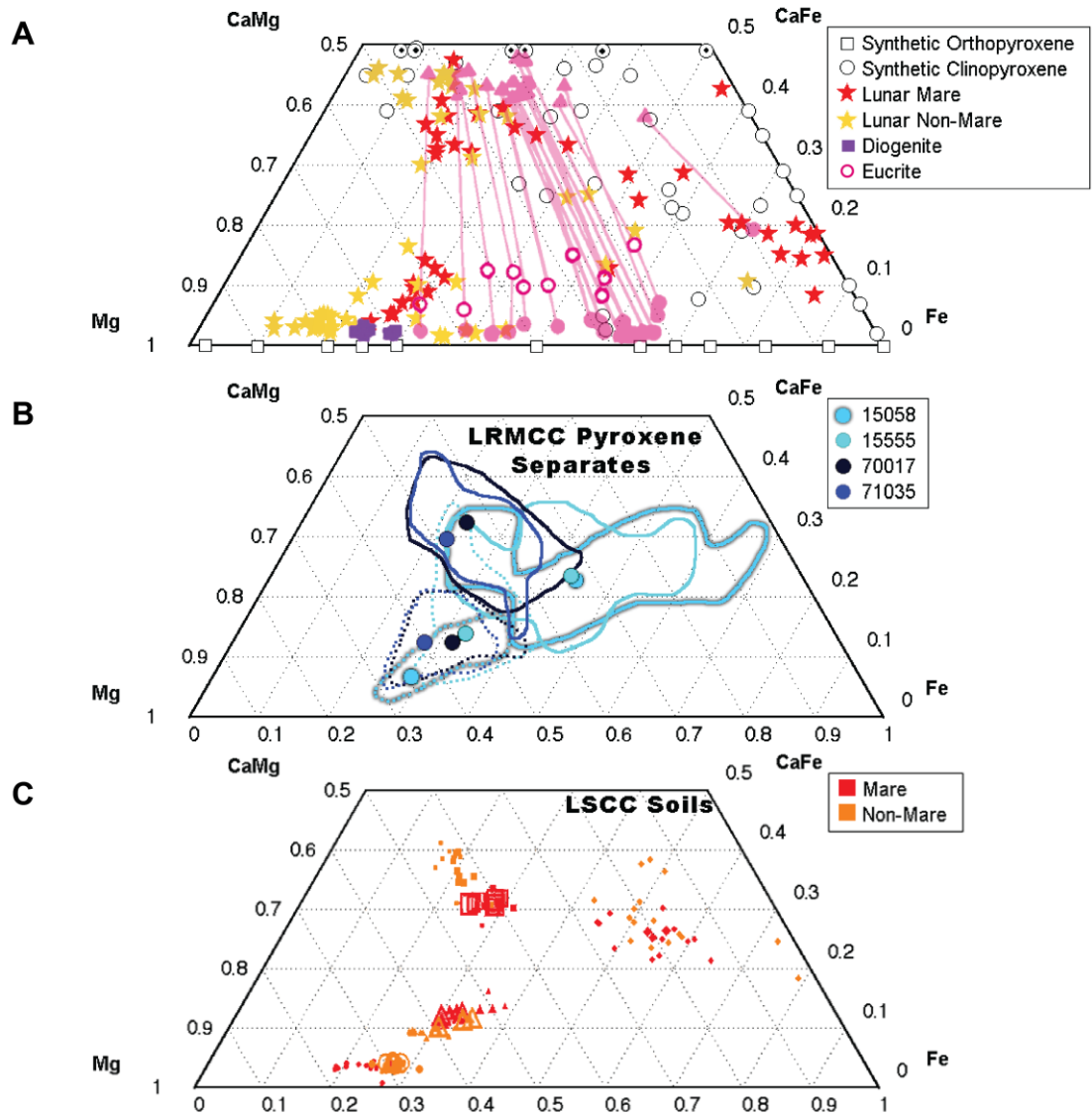


Fig. 4

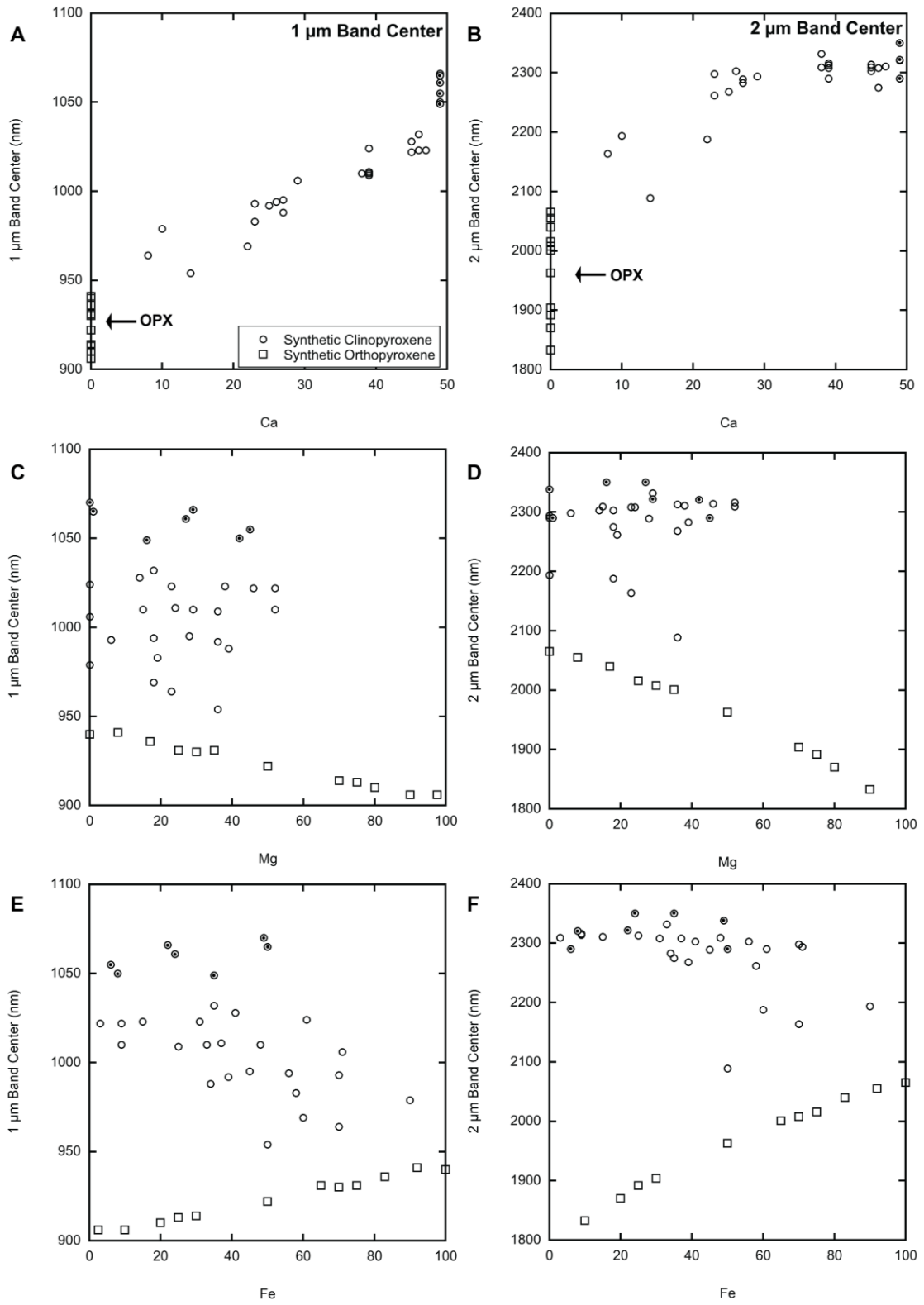


Fig. 5

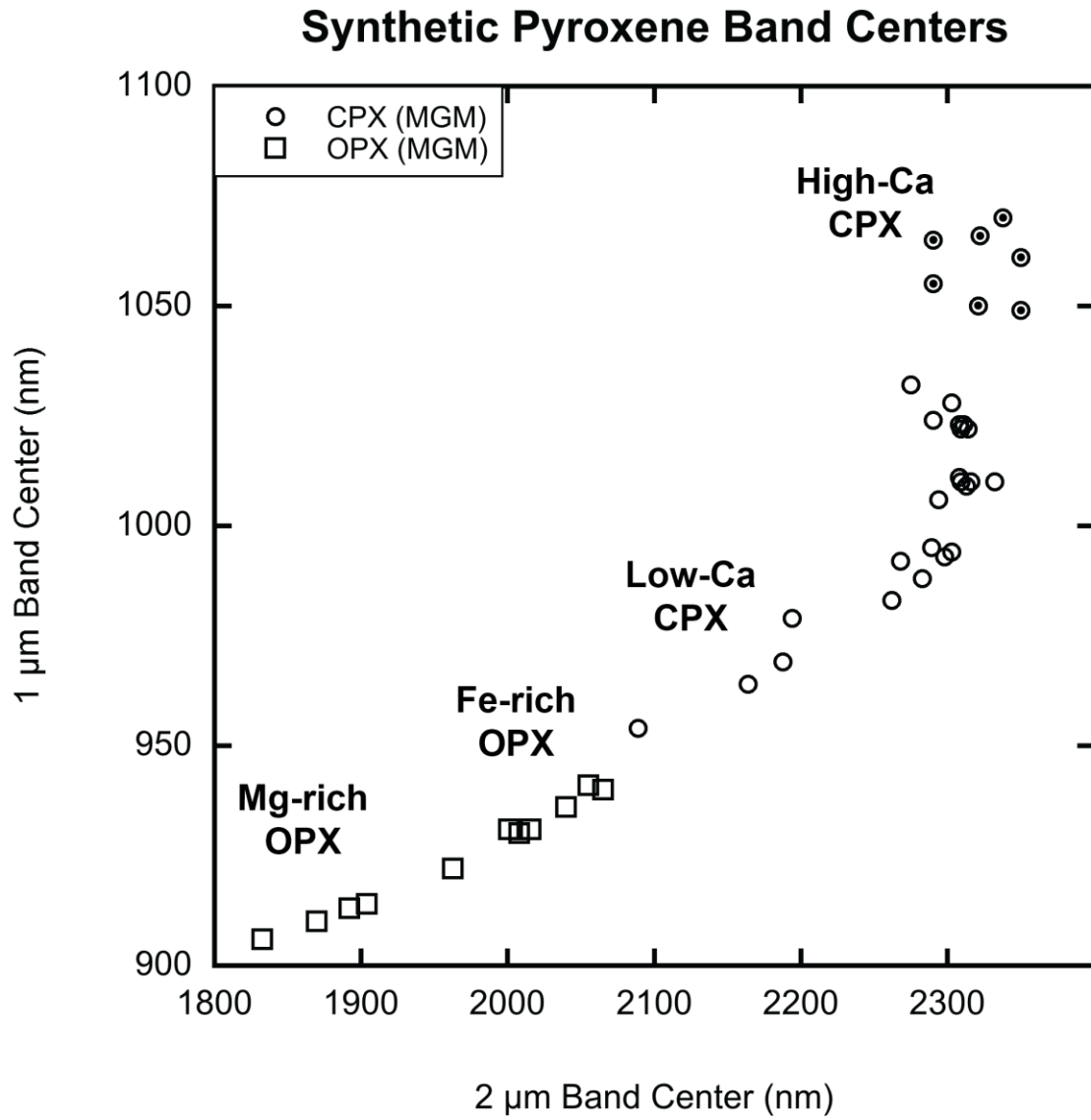


Fig. 6

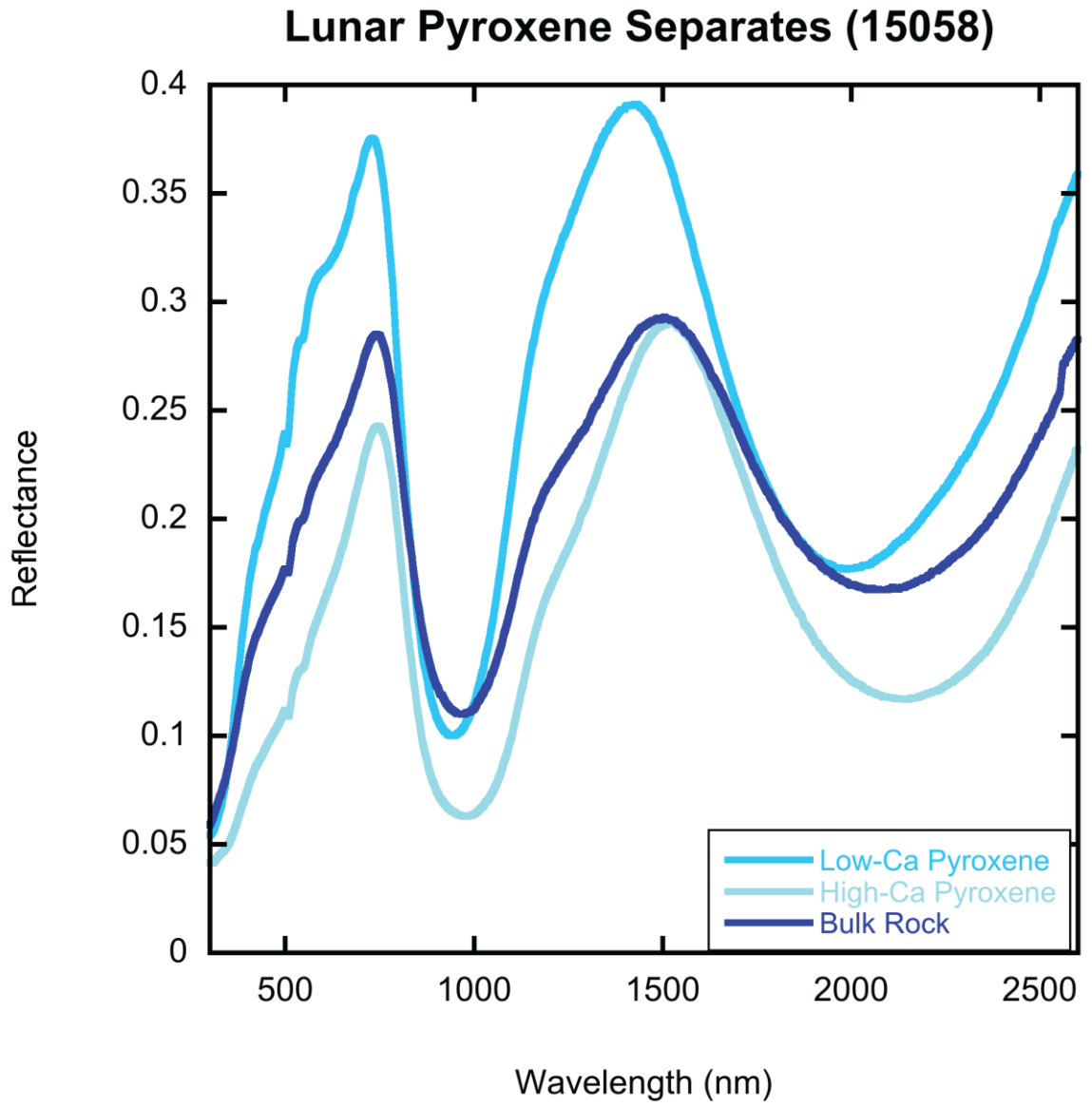


Fig. 7

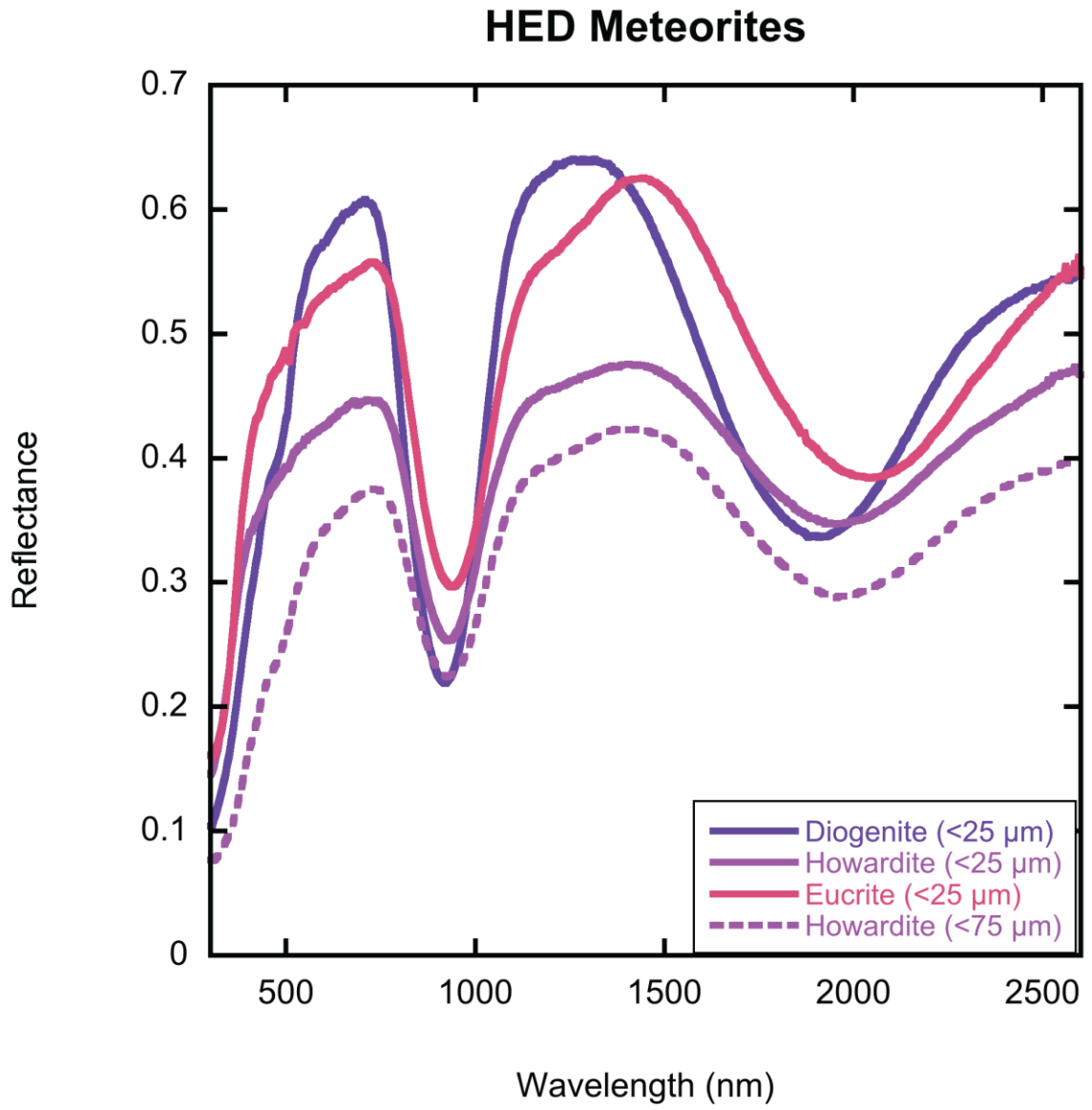


Fig. 8

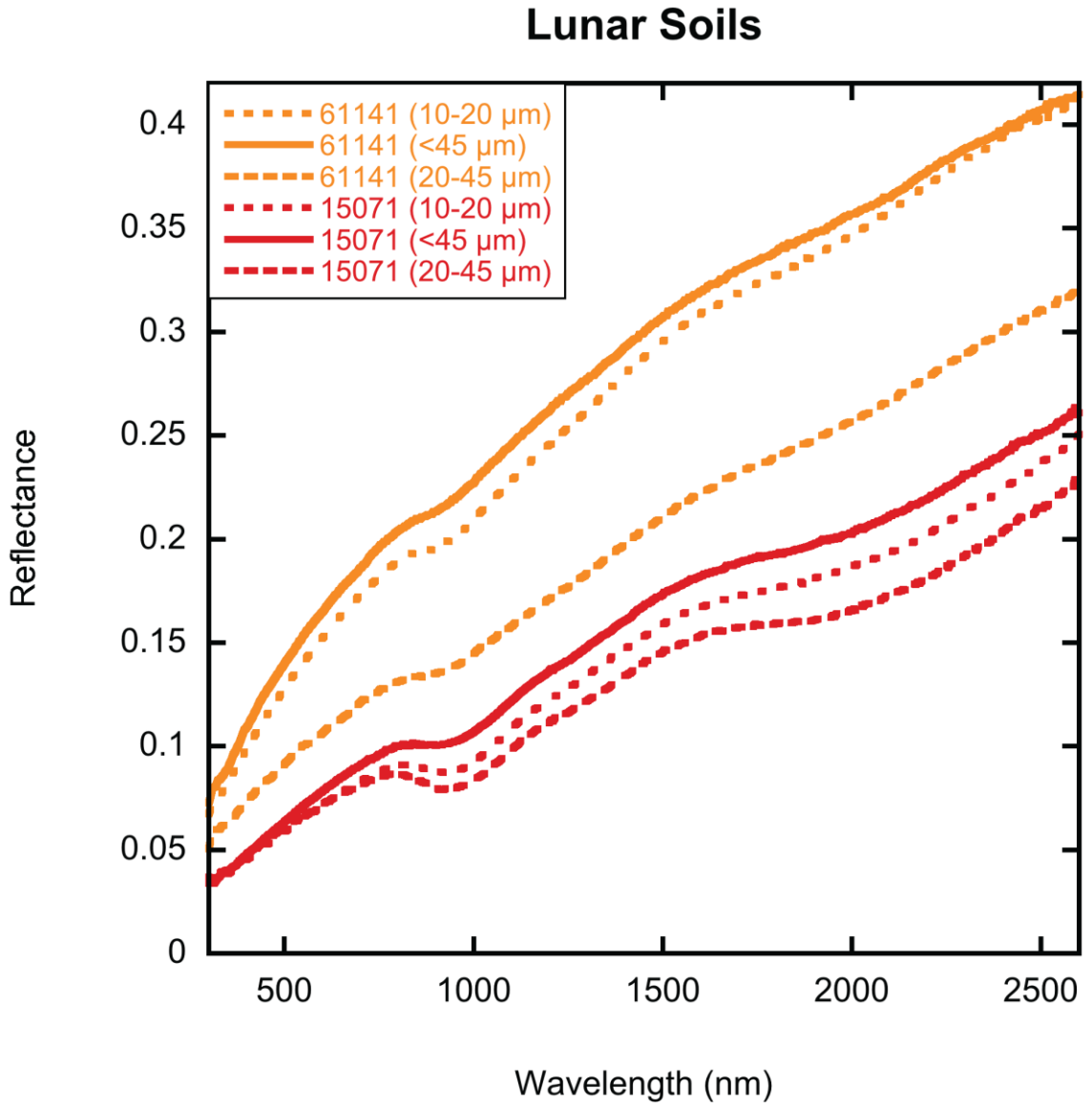


Fig. 9

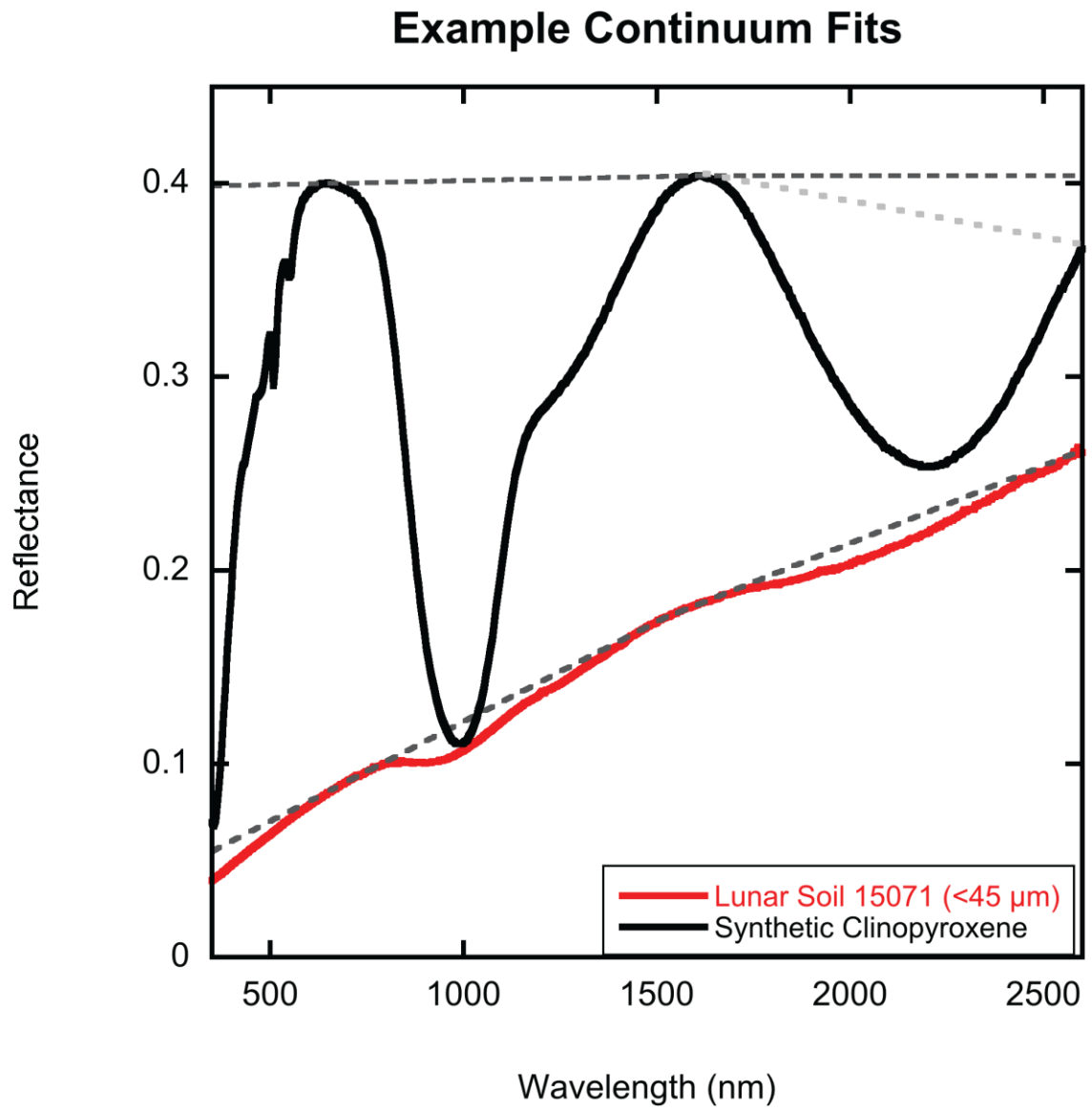


Fig. 10

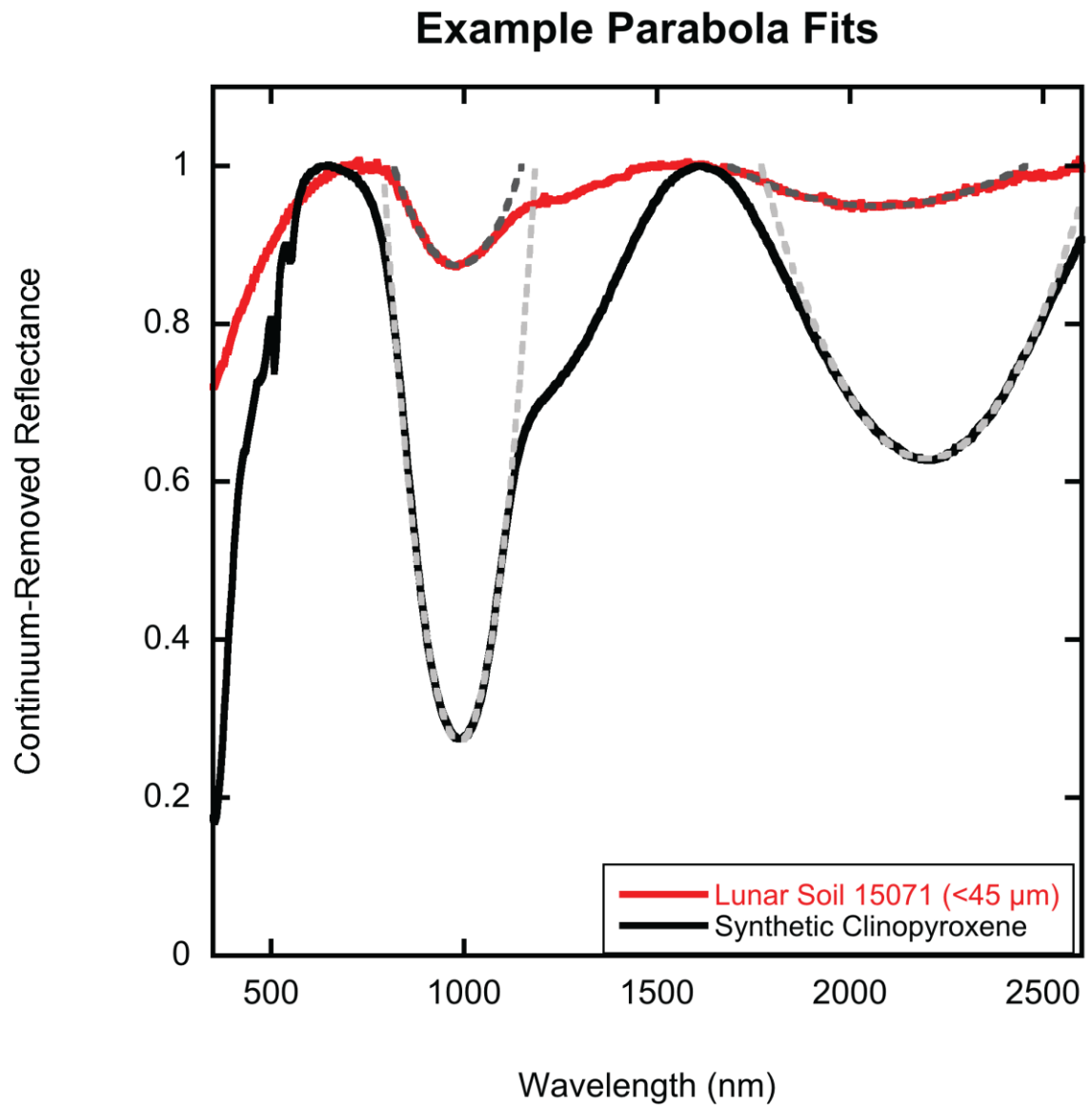


Fig. 11

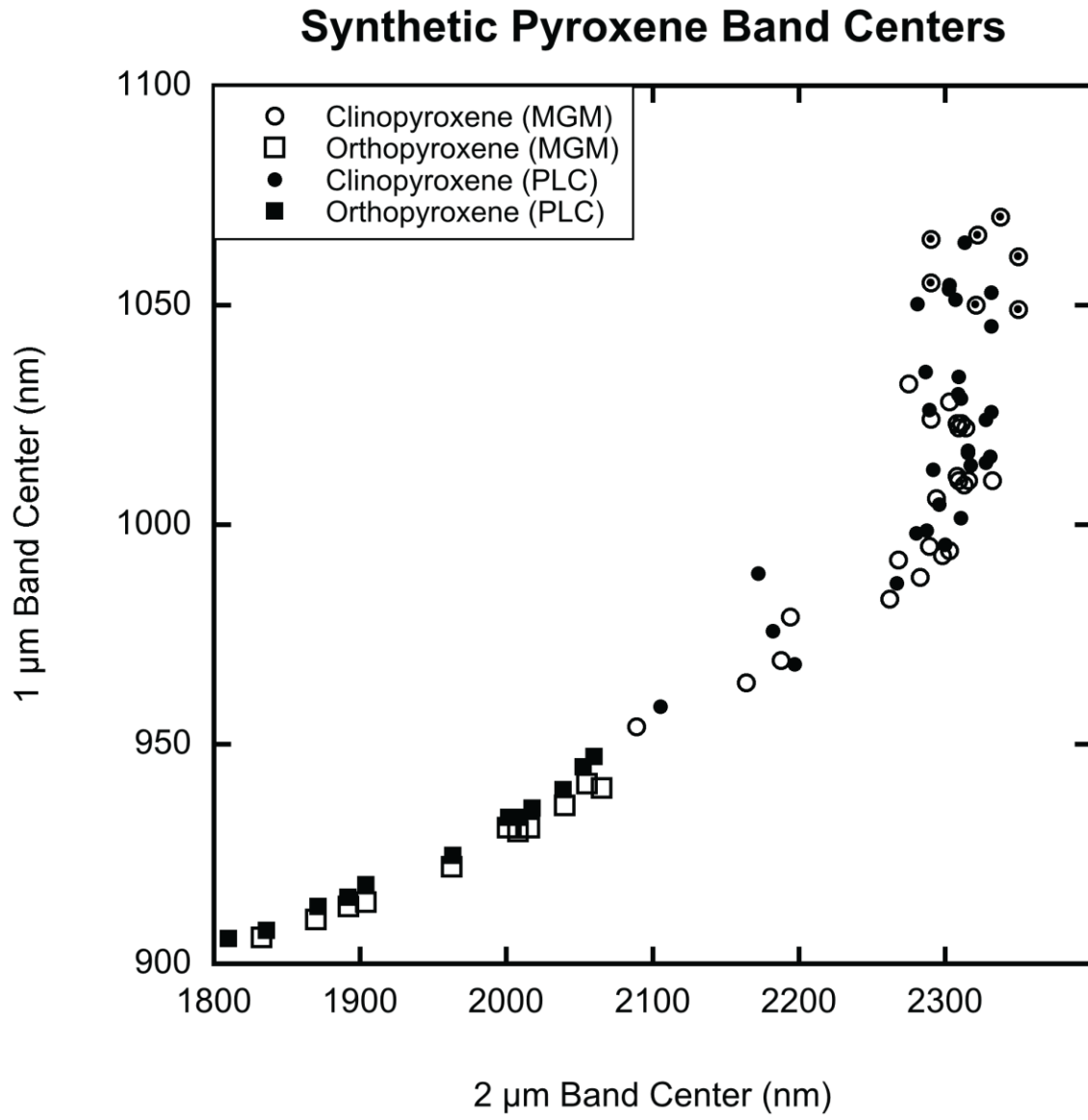


Fig. 12

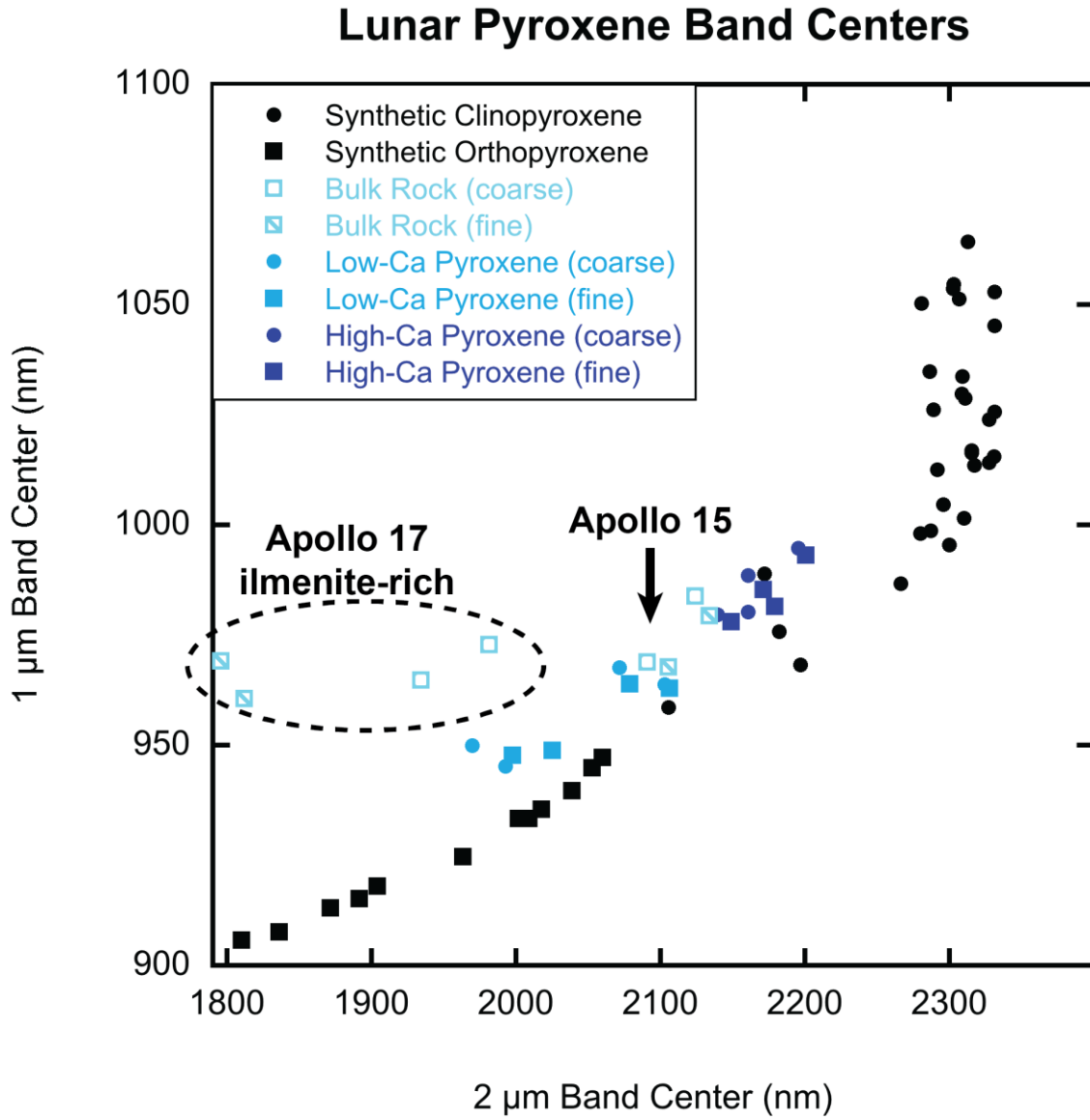


Fig 13

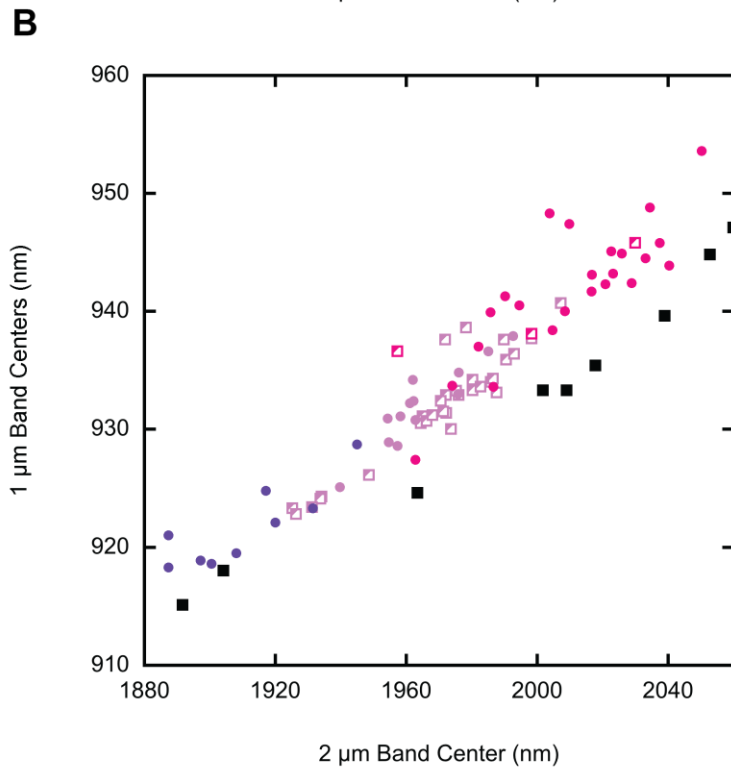
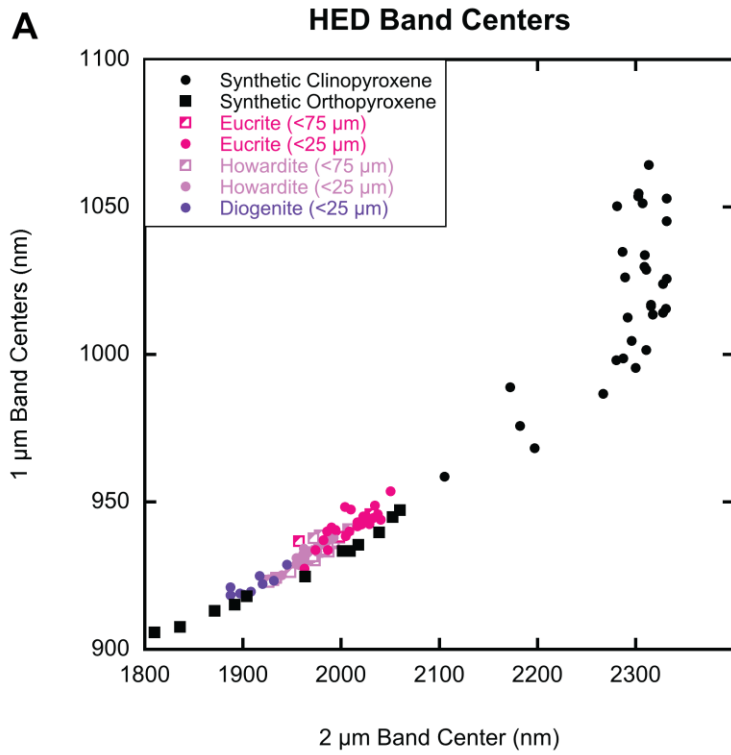


Fig. 15

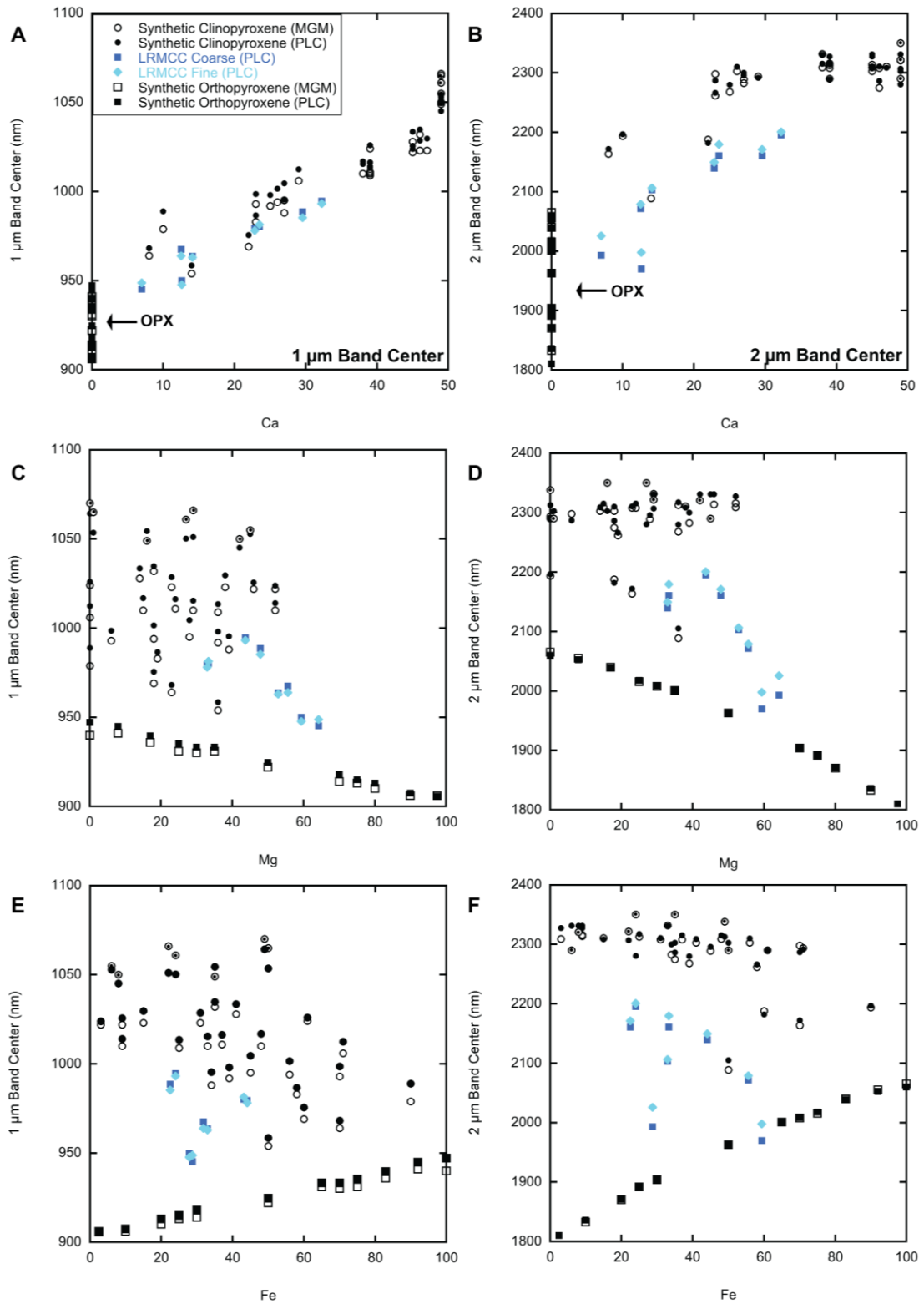


Fig. 16

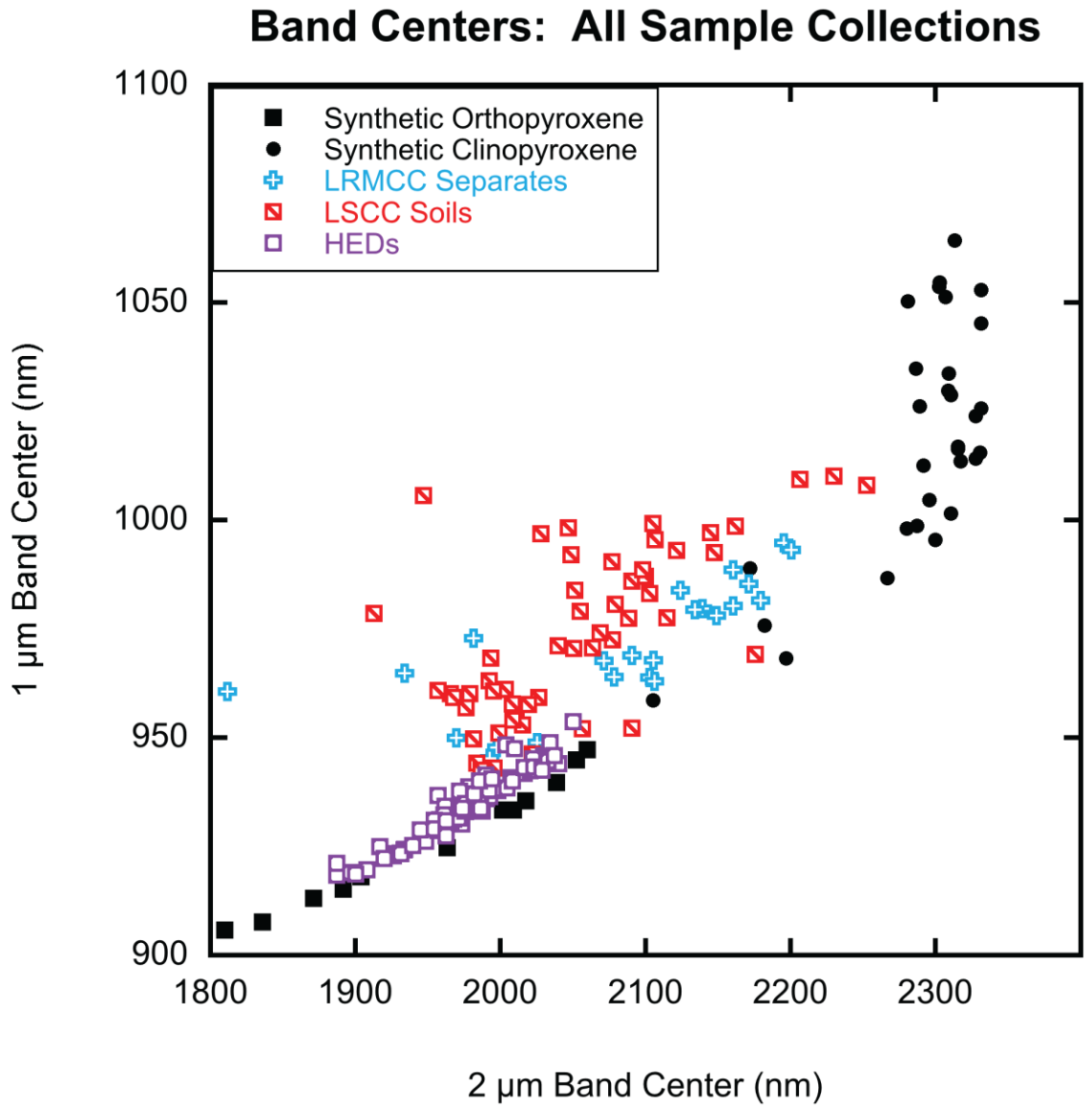


Fig. 17

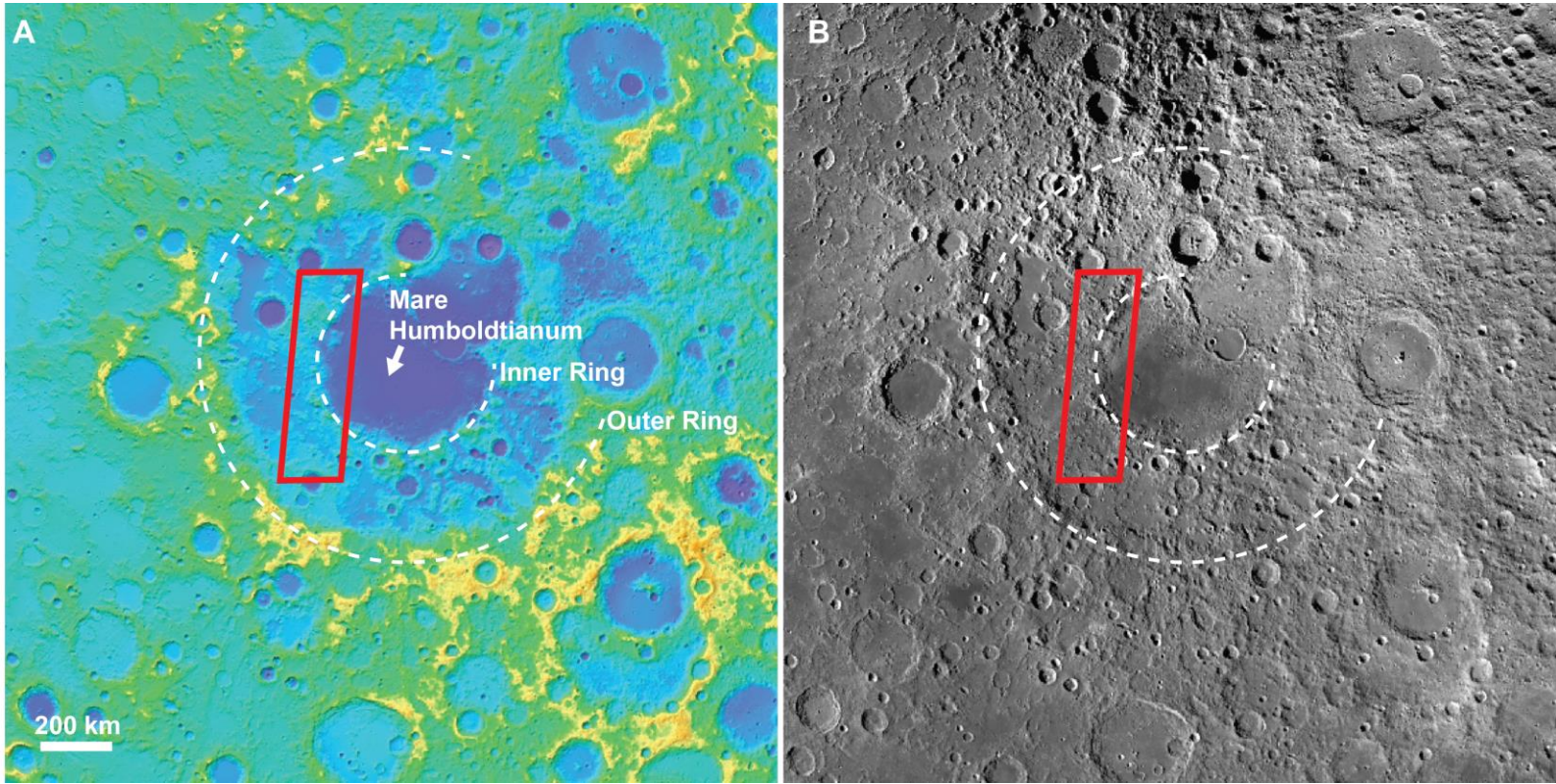


Fig. 18

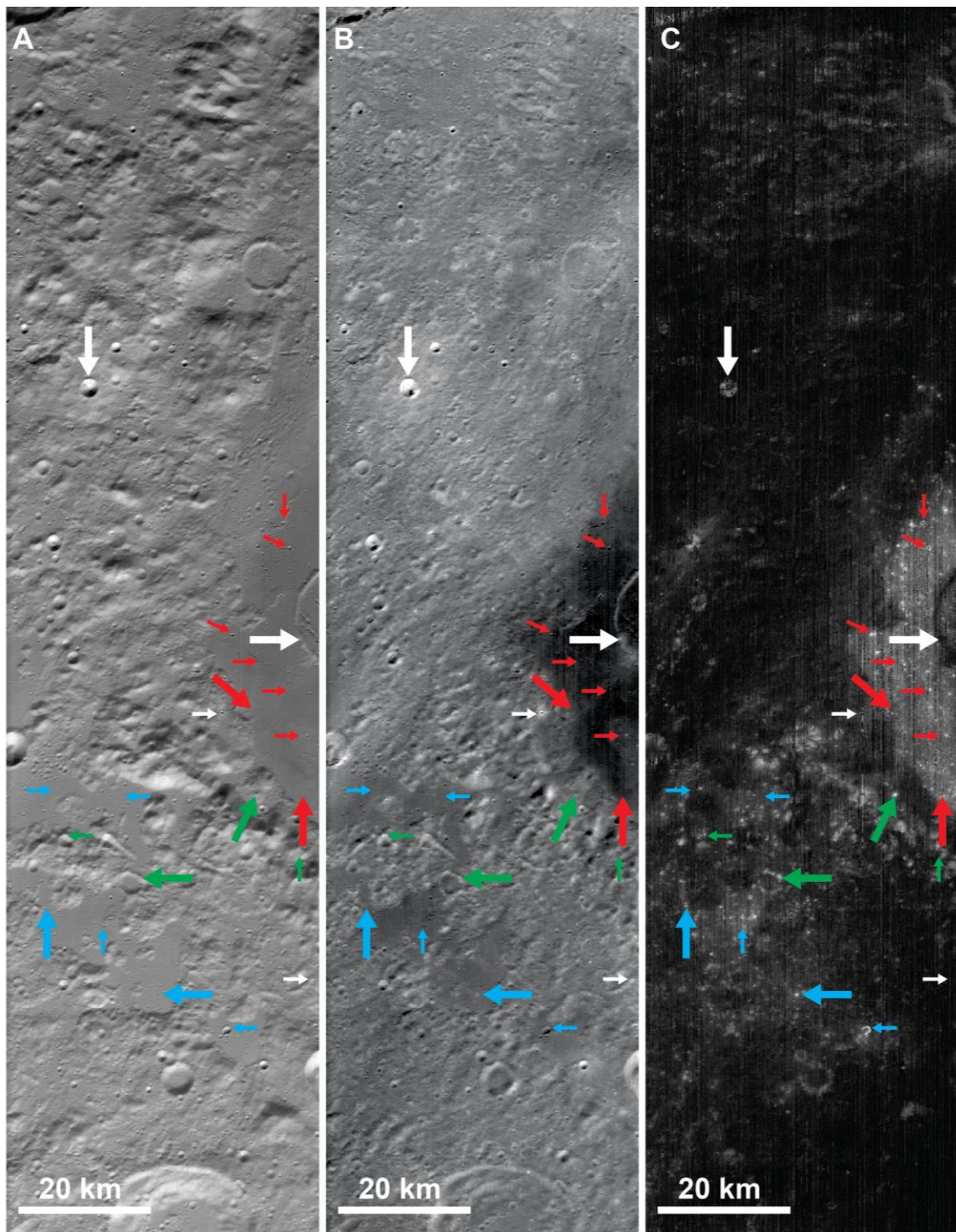


Fig. 19

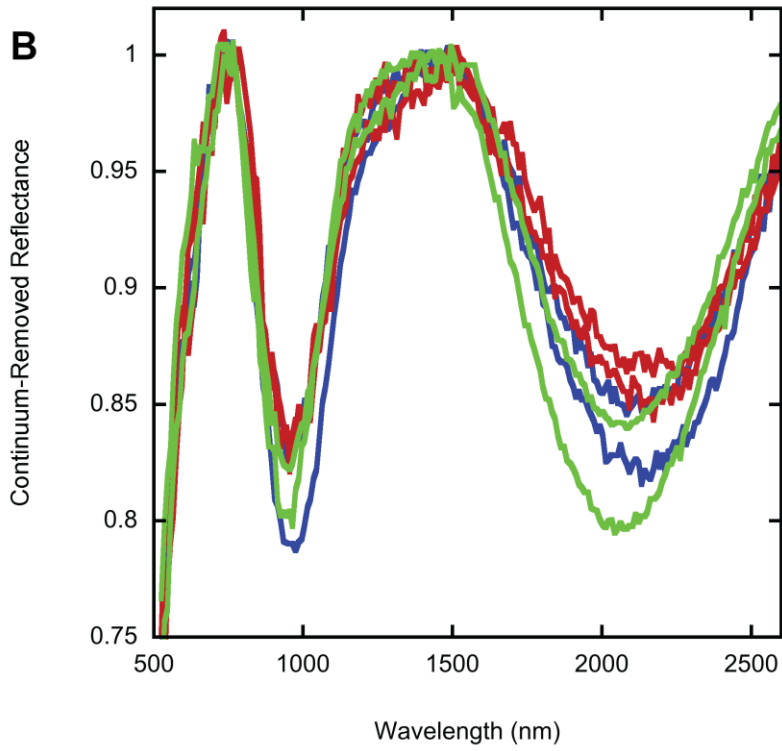
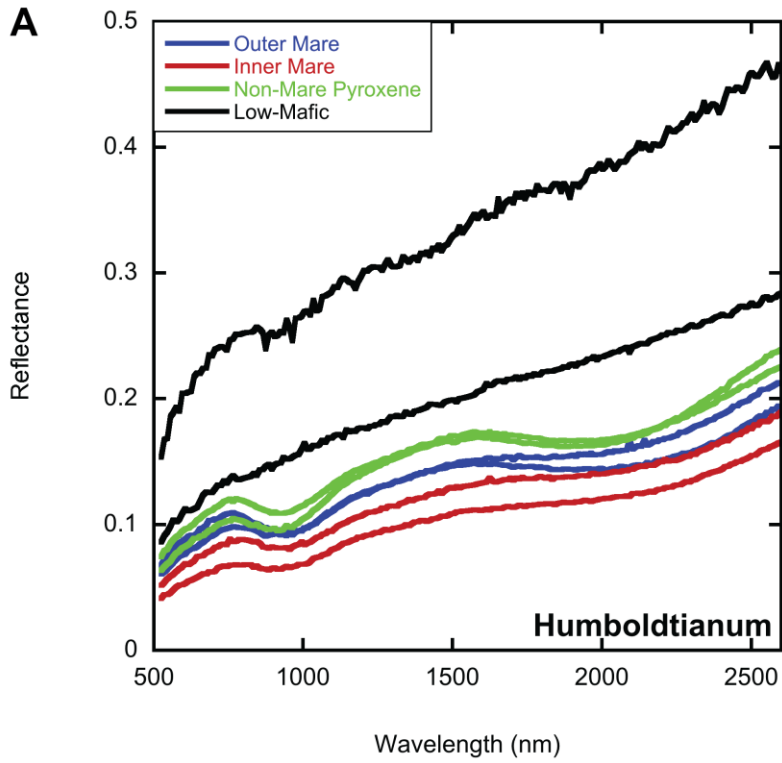
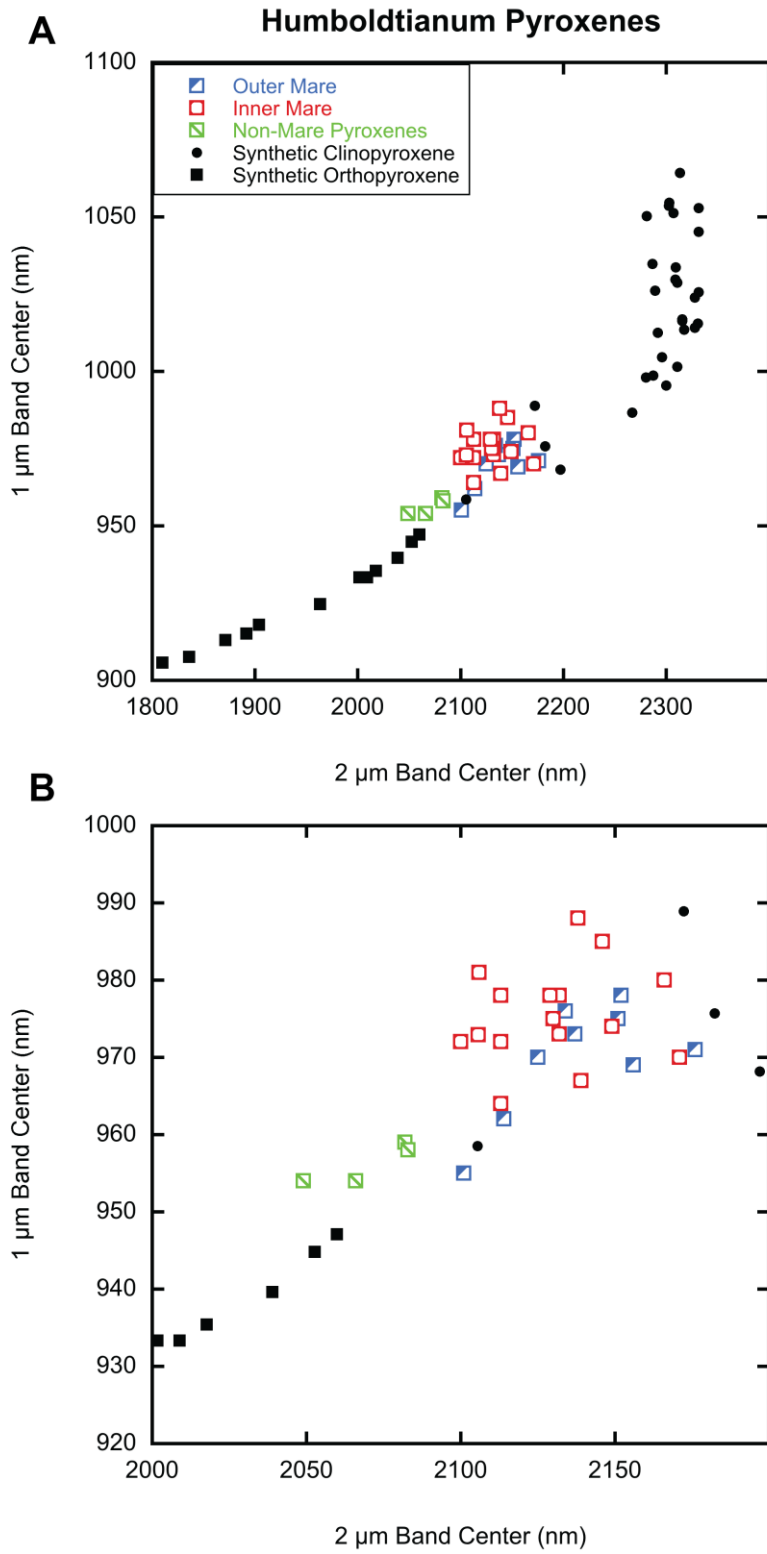


Fig. 20



CHAPTER 2: The nature and origin of Mafic Mound in the South

Pole - Aitken Basin

D. P. Moriarty III and C. M. Pieters

Department of Earth, Environmental, and Planetary Sciences

Brown University | Providence, RI 02912

Submitted to:

Geophysical Research Letters

August 2015

Revised:

September 2015

Accepted:

September 2015

Abstract

“Mafic Mound” is a distinctive and enigmatic feature 75 km across and 1 km high near the center of the vast South Pole – Aitken Basin (SPA). Using several modern datasets, we characterize the composition, morphology, and gravity signature of the structure in order to assess its origin. Mafic Mound is found to exhibit a perched circular depression and a homogeneous high-Ca pyroxene-bearing composition. Several formation hypotheses based on known lunar processes are evaluated, including the possibilities that Mafic Mound represents (1) uplifted mantle, (2) SPA-derived impact melt, (3) a basalt-filled impact crater, or (4) a volcanic construct. Individually, these common processes cannot fully reproduce the properties of Mafic Mound. Instead, we propose a hybrid origin in which Mafic Mound is an edifice formed by magmatic processes induced by the formation and evolution of SPA. This form of non-mare volcanism has not previously been documented on the Moon.

1 Introduction and Background

Near the center of the Moon's largest impact basin, an unusual ~75 km feature rises ~1 km above the surrounding terrain. The feature exhibits distinctive long wavelength 1 μm spectral absorption bands, first recognized by Pieters et al. [2001]. On the basis of its positive topography and strong absorption bands indicating the presence of pyroxene, the feature is informally referred to as "Mafic Mound."

Mafic Mound is located in the central portion of the ~2200 km South Pole - Aitken Basin (SPA) [Garrick-Bethell and Zuber, 2009] as shown in Fig. 1a. Although fairly inconspicuous in imagery such as the Lunar Reconnaissance Orbiter Wide Angle Camera (WAC) image presented in Fig. 1b, Lunar Orbiter Laser Altimeter (LOLA) topography reveals an asymmetric and distinctive structure (Fig. 1c). Our analyses focus on the properties of this structure. Mafic Mound exhibits a perched circular depression approximately 32 km in diameter (Figs. 1c, 4a, S1). Several asymmetric slopes emanate radially from the central depression: gradual, elongated slopes to the north and west, sharper slopes to the south and east. Mafic Mound lies between craters Bhabha (70 km diameter), Bellinsgauzen (63 km), and Stoney (47.5 km) in a topographically deep and relatively flat region in central SPA (Fig. 1).

Spectra from the SPA interior are dominated by pyroxene [Pieters et al., 2001]. Central peaks of large complex craters within SPA typically exhibit significant low-Ca pyroxene (LCP) (Appendix C Fig. S2d), although some variation in pyroxene abundance and composition is observed [Tompkins and Pieters, 1999; Pieters et al., 2001; Cahill et al. 2009; Nakamura et al., 2009; Klima et al., 2011b; Moriarty et al., 2013]. These central peaks uplift materials from significant depths (~10 km or greater [Cintala and

Grieve, 1998]), and the observed LCP-bearing materials are thought to represent thick impact melt or breccia associated with the SPA-forming impact [e.g. Morrison, 1998; Vaughan and Head, 2014; Hurwitz and Kring, 2014]. In several areas throughout SPA, the post-impact surface was subsequently modified by localized mare volcanism [e.g. Stuart-Alexander, 1978; Wilhelms et al., 1979]. This resulted in regions of smooth terrain exhibiting high-Ca pyroxene (HCP) spectral signatures [Yingst and Head, 1999; Pieters et al. 2001; Petro et al., 2010; Whitten and Head, 2015]. Although billions of years of subsequent impacts have mixed and redistributed SPA basin materials [e.g. Haskin et al., 2003; Petro and Pieters, 2008], distinct compositional heterogeneities persist laterally and vertically [e.g. Pieters et al., 2001], allowing the formation and evolution of SPA to be constrained.

In this paper, we incorporate several modern datasets (all publicly available through the NASA Planetary Data System, <https://pds.nasa.gov/>) to characterize the composition, morphology, topography and gravity signature of Mafic Mound. In the context of these observations, we explore several formation hypotheses linked to common lunar processes, as well as a possible causal relationship between Mafic Mound and the vast South Pole – Aitken Basin (SPA).

2 Observations

2.1 Composition

Compositional analyses were performed using Moon Mineralogy Mapper (M^3) Level 2 data that include photometric and thermal corrections [Pieters et al., 2009; Green et al. 2011]. A groundtruth correction has also been applied [Isaacson et al., 2013].

These data include 85 spectral channels across the near-infrared (~500-3000 nm) at a spatial resolution of ~140x240 m per pixel. In this wavelength region, common lunar minerals such as pyroxene, olivine, spinel, and plagioclase exhibit crystal field absorption bands whose strengths, shapes, and positions reflect detailed mineralogical information [e.g. Burns, 1993].

For this analysis, spectra were acquired from fresh craters and steep slopes to minimize the contribution from mixed and space weathered soils. Spectral processing (continuum removal, band depth, and band center measurements) was performed following the Parabolas and Linear Continuum (PLC) technique as documented by Moriarty and Pieters [2014; 2015]. The PLC technique allows for direct assessment of pyroxene compositional heterogeneity, providing band center measurements that are similar to those obtained using the Modified Gaussian Model [Sunshine et al., 1990; Moriarty and Pieters, 2015].

2.1.1 SPA HCP-Bearing Materials

A representative M³ spectrum for Mafic Mound is shown in Fig. 2. Additional Mafic Mound spectra are given in Appendix C Fig. S2a. These spectra confirm the presence of long-wavelength 1 μm absorption bands originally observed in Clementine data [Pieters et al. 2001]. Additionally, M³ spectra show that Mafic Mound materials exhibit a strong, long-wavelength 2 μm absorption band. The strong, relatively long-wavelength 1 μm and 2 μm bands (occurring >960 nm and >2100 nm, respectively) indicate the presence of HCP [e.g. Klima et al., 2007; 2011a; Moriarty and Pieters, 2015]. These HCP-bearing materials are spatially homogeneous across the entire Mafic Mound

structure. This includes the rim of the central depression, as well as several superposed craters ~10 km in diameter.

The most common occurrences of lunar HCP are associated with mare and cryptomare basalts. Fig. 2 presents spectral comparisons between representative Mafic Mound materials and mare/cryptomare basalts from the SPA region. Cryptomare materials were selected from those identified by Whitten and Head [2015]. Additional SPA basalt spectra are given in Appendix C Fig. S2b-c. In general, Mafic Mound exhibits 1 μm and 2 μm band centers similar to those of the mare and cryptomare materials. This indicates that these materials are similar in pyroxene composition. However, Mafic Mound materials are typically brighter than mare and cryptomare materials. This suggests a higher abundance of higher-albedo components in the mineral assemblage (most likely plagioclase) or a lower abundance of opaques.

Band centers of spectra for several diverse rock types from within SPA are measured using PLC and compared in Fig. 3a. The 1 μm and 2 μm band centers for Mafic Mound overlap those from the basalts indicating similar pyroxene compositions. These HCP-bearing materials differ substantially from most SPA central peaks such as Bhabha, which tend to exhibit shorter-wavelength band centers (e.g. 1 μm band < 950 nm, 2 μm band < 2050 nm) indicative of more Mg-rich LCP. The walls of complex craters across SPA typically exhibit LCP-bearing or heterogeneous materials, the wall of Bhabha exhibits long-wavelength absorption bands similar to those of Mafic Mound.

2.1.2 Modified Craters in Central SPA

The central circular structure at the center of Mafic Mound is reminiscent of an impact crater. To evaluate a possible impact-related origin, we compare the circular

structure at Mafic Mound to a suite of modified impact craters from within SPA. We classify these craters into three general categories: (1) flat-floor craters (exhibiting smooth mare fill and relatively well-preserved rims), (2) buried craters (exhibiting highly degraded rims, often discontinuous, with smooth mare materials in both the crater floor and exterior regions), and (3) hummocky-floor craters. Example WAC mosaics of each modified crater class are shown in Fig. 3e-g. One or more spectra were collected from small craters or steep slopes on the rims and floors of each modified crater (Appendix C Fig. S2d-f). A full accounting of data for each feature is provided in Table S1.

The 1 μm and 2 μm absorption band centers for each modified crater group are compared to Mafic Mound materials in Fig. 3(b-d). Both flat-floor and buried craters exhibit systematic differences between their rims and floors, as crater rims typically exhibit shorter-wavelength absorption bands than floor materials. This indicates compositional differences between the pre-existing crater structure and subsequent basaltic fill. The short-wavelength bands of “buried” crater rims suggest that the original rim materials are exposed, and therefore that these rims are not deeply buried. Hummocky-floor craters do not exhibit a clear pattern of compositional differences between floor and rim materials, and do not appear to have formed via primarily extrusive mare fill.

Compared to the basalt-filled craters, Mafic Mound exhibits a different compositional trend. As seen in Fig. 3, band centers of all Mafic Mound materials including the central circular feature and superposed craters all cluster at long wavelengths. These materials represent small craters on the surface as well as several ~10 km craters which excavate ~1 km into the body of the structure, including the rim.

This indicates relatively uniform pyroxene compositions throughout the entire area and volume of Mafic Mound.

2.2 Morphology Topography, and Gravity

In addition to the LOLA topographic maps in Figs. 1 and S1, several topographic profiles of Mafic Mound and modified craters throughout SPA were obtained and compared using the WAC GLD100 digital elevation model [Scholten et al. 2012]. Examples are given in Fig. 4, with additional profiles in Appendix C Fig. S3. The floor of Mafic Mound's central depression is elevated well (~0.5 km) above the surrounding terrain. This differs greatly from the morphology of SPA modified craters. In SPA, all flat-floor, buried, and hummocky-floor craters observed exhibit crater floors that are topographically lower than the surrounding terrain. In contrast, the topography of Mafic Mound appears more similar to lunar volcanic edifices such as domes and larger complexes (Fig. 4c) [e.g. Head and Gifford, 1980; Spudis et al., 2013].

As revealed in GRAIL data [Zuber et al. 2013], Mafic Mound is also associated with a localized, positive Bouguer anomaly (Appendix C Fig. S4). This implies that Mafic Mound is associated with significant excess mass relative to its surroundings, suggesting the presence of a relatively dense mineral assemblage. Although gravity models can be non-unique, the ~50 km diameter of the localized anomaly is most consistent with a mass excess at shallow depths (less than 10-20 km).

3 The Origin of Mafic Mound

On the basis of these observations, we discuss several specific hypotheses for the formation of Mafic Mound. We first evaluate four common, known lunar processes. We then consider a hybrid model involving several of these processes.

3.1 Evaluation of Mafic Mound Formation Resulting from Common Lunar Processes

3.1.1 Uplifted Mantle

Due to SPA's enormous ~2200 km size, impact models suggest that the impact penetrated through the crust, excavating and melting large volumes of mantle materials [e.g. Potter et al., 2012]. Uplift of mantle-related materials is expected to occur at several stages throughout the impact process, including impact rebound and eventual isostatic adjustment [e.g. Potter et al., 2012]. On the Moon, uplift-related processes are responsible for local topographic highs such as crater central peaks (typically much smaller than Mafic Mound) and peak rings [e.g. Cintala and Grieve, 1998; Baker and Head, 2015]. However, for large basin-scale impacts, these central uplifts rapidly collapse into a central pool of impact melt [Head, 1974; Cintala and Grieve, 1998; Potter et al., 2012; Vaughan et al., 2013; Vaughan and Head, 2014]. It is therefore unlikely that Mafic Mound represents a remnant uplifted structure.

The composition of Mafic Mound (mostly HCP+plagioclase) may also be inconsistent with an exposed mantle origin. While such minerals may form late in the process of lunar magma ocean solidification, modeled upper mantle compositions are not typically dominated by this mineral assemblage (e.g. Elkins Tanton et al. [2011]).

Instead, the upper mantle is expected to contain significant proportions of LCP (and/or olivine, if cumulate overturn has occurred).

3.1.2 Compositionally Distinct Impact Melt

As noted above, impact models predict that large volumes of impact melt were created and retained in SPA, forming a melt sheet possibly tens of km thick [e.g. Potter et al. 2012]. Central peak craters throughout central SPA commonly uplift LCP-bearing materials that have been suggested to represent the melt sheet or impact breccia [Tompkins and Pieters, 1999; Pieters et al., 2001; Cahill et al. 2009; Nakamura et al., 2009; Moriarty et al. 2013]. Mafic Mound's HCP-bearing composition is distinct from these materials.

Hurwitz and Kring [2014] suggest that Mafic Mound may represent quenched and rafted SPA impact melt, mirroring an assumed bulk melt composition with an approximately equal ratio of HCP, LCP, and plagioclase. However, as the modeled melt evolves, Hurwitz and Kring [2014] demonstrate that the liquid component becomes enriched in HCP, plagioclase, and Si. From these models, it appears that evolved SPA impact melt is a better fit than quenched bulk melt for the optical properties of Mafic Mound. Differentiated and crystallized SPA impact melt compositions modeled by Vaughan and Head [2014] are dominated by olivine and LCP and are inconsistent with the composition of Mafic Mound.

Alternatively, lunar impact melts are not always well-mixed [e.g. Dhingra et al., 2013]. If large-scale mixing and convection did not occur in the SPA melt sheet, it is possible that Mafic Mound represents impact melt from a different source region than most other SPA melts (possibly involving more deep-seated mantle materials).

Mafic Mound's composition may therefore be consistent with an impact melt origin. However, its topography is inconsistent with conventional impact melt morphologies. While impact melts can drape pre-existing terrain and exhibit topographic complexity due to differential cooling and subsidence (Head, 1974; Hawke and Head, 1977; Vaughan et al., 2013), many impact melt deposits are relatively smooth. Although Mafic Mound materials may be derived from SPA impact melt, some other process would be required to produce the large, localized topographic high in the center of SPA.

3.1.3 Basalt-Filled Impact Crater

Mafic Mound's perched circular depression, basalt-like pyroxene composition, and positive topography initially suggest a possible origin as an impact crater that was later filled (perhaps to the point of overflowing) with mare basalts. However, as discussed in 2.1.2 above, direct topographic and compositional comparisons between Mafic Mound and SPA basalt-filled impact craters reveal clear differences between these features. SPA basalt-filled impact craters typically exhibit compositional differences between the mare fill and the pre-existing crater structure. Mafic Mound exhibits no such heterogeneity as it is dominated by relatively homogeneous HCP-bearing materials throughout. If a compositionally distinct crater substrate was present, it would have been exposed by the several superposed ~10 km impact craters across the face of Mafic Mound. Furthermore, no modified impact craters in SPA exhibit similar topography to Mafic Mound, specifically the elevation of the central depression well above the surrounding terrain.

3.1.4 Volcanic Construct

Topographically, Mafic Mound is more similar to lunar volcanic constructs than SPA basalt-filled craters (Fig. 4). Most lunar volcanic eruptions involve high effusion rates and magmas with low viscosities [e.g. Head, 1976; Head and Wilson, 1992]. These conditions produce smooth, flat, laterally extensive mare flows – the most spatially and volumetrically abundant volcanic features on the Moon. Nevertheless, lunar volcanic constructs such as cones, domes, and complexes have been identified in many locations [e.g. Head and Gifford 1980; Campbell et al., 2009; Jolliff et al., 2011; Spudis et al., 2013]. Formation of such constructs requires lower effusion rates or magmas with higher viscosities. These conditions can be met by several scenarios, including lower magma temperatures, shallow magma chambers, partially-crystallized magmas, or magmas with a more silicic composition [Head, 1976; Head and Gifford, 1980; Weitz and Head, 1999; Wilson and Head, 2003; Wohler et al, 2006].

Typical lunar domes range from ~3-17 km in diameter and are approximately several hundred meters high [Head and Gifford, 1980]. Mafic Mound is several times larger than this in both diameter and height. In contrast, Mafic Mound is much smaller than large lunar volcanic complexes such as the ~35,000 km² Marius Hills [e.g. Head and Gifford, 1980; Besse et al., 2011, Spudis et al., 2013]. Mafic Mound is comparable in size to smaller volcanic complexes such as Compton-Belkovich (~30 km), Mons Rümker (~66 km), and Gardner (~70 km) [e.g. Campbell et al. 2009, Jolliff et al., 2011; Spudis et al., 2013]. Several of these features exhibit central depressions, although less prominent than Mafic Mound's central circular feature (Fig. 4C).

Lunar volcanic complexes typically exhibit multiple volcanic domes and cones across their structures, suggesting a prolonged sequence of volcanic events [e.g. Jolliff et al., 2011; Spudis et al., 2013]. Mafic Mound does not exhibit superposed volcanic features. If Mafic Mound is indeed volcanic, a difference in the style of volcanism from other volcanic complexes is implied. This may indicate an eruption style more similar to mare domes, even though Mafic Mound is closer in size to the volcanic complexes.

Mafic Mound's homogeneous HCP-bearing composition, positive topography, size, and positive Bouguer anomaly are consistent with a volcanic origin. However, there is no directly comparable feature currently found on the Moon.

3.2 A Hybrid Origin for Mafic Mound

None of the common lunar processes discussed above can fully reproduce the observed properties of Mafic Mound. We therefore propose a hybrid origin. Considering Mafic Mound's composition, topography, gravity, and location at the center of SPA, we propose that Mafic Mound is a volcanic construct formed from magmas produced during one of several possible SPA-related melting events described below.

As discussed in Section 3.1.2, partially-evolved SPA impact melt is consistent with the composition of Mafic Mound. Typical lunar impact melts are not known to result in extrusive eruptions. However, large impact melt sheets are expected to undergo significant volume changes due to cooling and crystallization [e.g. Grieve et al., 1991; Warren et al., 1996; Vaughan and Head, 2013]. Such processes (or possibly a later impact event) could lead to favorable eruption conditions at the center of an enormous SPA melt sheet. In this case, a rigid surface layer above the still-molten melt sheet is required to support the weight of the forming volcanic edifice. Perhaps a layer of

quenched melt and/or re-impacted rock fragments [Vaughan and Head, 2013; Hurwitz and Kring, 2014; Vaughan and Head, 2014] could form such a layer.

Basin-related melts might also form through two other processes: (1) decompression melting due to massive excavation or (2) subsequent adiabatic melting due to isostatically-induced convection [Elkins-Tanton and Hager, 2005]. These basin-induced melts are similar to mare basalts in that they are partial melts of mantle materials. However, these melts may exhibit compositional differences from typical mare basalts due to different pressures/depths, temperatures, and degrees of melting. Head et al. [2008] suggest that a similar phenomenon may be responsible for Pantheon Fossae, a system of radial graben at the center of the ~1550 km Caloris Basin on Mercury. In their model, they suggest that the formation of Caloris has localized mantle upwelling near the basin center. They suggest that the radial graben were formed by a magmatic intrusion supplied by adiabatic melting during mantle upwelling. It is possible that Mafic Mound represents an analogous, extrusive scenario.

These proposed melt sources occur in direct association with the evolution of SPA early in lunar history. If Mafic Mound formed from the eruption of such melts, it must be an ancient structure. Although detailed crater counting has not been performed, several observations point to a fairly old age for Mafic Mound. Petro et al. [2011] suggest that Mafic Mound is blanketed by ejecta from Bhabha. If this is the case, Mafic Mound must predate Bhabha, which is neectarian in age [Wilhelms et al., 1979]. Additionally, the several superposed ~10 km craters (of varying degradation states) superposed on Mafic Mound's small surface area suggest a long history of impact events. Even if these ~10

km craters are secondaries from a nearby basin-forming impact (most likely Orientale [Wilhelms et al., 1979]), Mafic Mound must predate this event.

Structures similar to Mafic Mound have not been observed in the center of other lunar basins. Although centralized magmatic activity may have occurred in these basins, extensive mare deposits within nearside basins prevent the identification of such structures. In contrast, SPA is a vast ~2200 km basin that has excavated deep into the crust/mantle and exhibits a relatively well-preserved interior relative to nearside basins. Mafic Mound may therefore represent a uniquely well-preserved example of processes associated with large impact basins.

4 Conclusions

Located at the center of the South Pole - Aitken Basin, Mafic Mound is a highly unusual structure defined by its HCP-bearing composition and positive topography. Several common lunar processes (impact rebound, impact melting, basaltic fill of a pre-existing impact crater, volcanic construction) were investigated as a means to form this distinctive feature. None were found to fully account for the properties of Mafic Mound.

A hybrid origin in which Mafic Mound is a volcanic structure resulting from melting related to the SPA impact is most consistent with the new observations. The magma producing the construct represents either extruded SPA impact melt or melt of the underlying mantle induced via basin excavation and isostatic adjustment. If either is shown to be correct with more detailed modeling and advanced remote sensing, Mafic Mound represents the first documented example of an impact-induced non-mare volcanic construct on the Moon. Its location in the center of SPA offers an exceptional

opportunity for extended investigation through future sample return [e.g. Jolliff et al., 2003].

5 Acknowledgements

Support of this research through NASA LASER (NNX12AI96G) and SSERVI (NNA13AB01A) is gratefully acknowledged. Reviews by Debra (Hurwitz) Needham and Noah Petro greatly improved the manuscript. Discussions with Jim Head, Greg Neumann, Lauren Jozwiak, Jay Dickson, Ross Potter, and David Baker were integral in developing these analyses and discussions. All data used in this manuscript is publicly available through the NASA Planetary Data System, available at: <https://pds.nasa.gov/>.

6 References

Baker, D. M. H., J. W. Head III, G. A. Neumann, D. E. Smith, and M. T. Zuber (2012),

The transition from complex craters to multi-ring basins on the Moon:

Quantitative geometric properties from Lunar Reconnaissance Orbiter Lunar Orbiter Laser Altimeter (LOLA) data, *J. Geophys. Res.*, 117:E12.

Burns R. G. 1993. *Mineralogical applications of crystal field theory*, 2nd ed. Cambridge, UK: Cambridge University Press. 551.

Cahill, J. T. S., P. G. Lucey, and M. A. Wieczorek (2009), Compositional variations of the lunar crust: Results from radiative transfer modeling of central peak spectra, *J. Geophys. Res.*, 114, E09001.

- Campbell, B. A., B. R. Hawke, and D. B. Campbell (2009), Surface morphology of domes in the Marius Hills and Mons Rümker regions of the Moon from Earth-based radar data, *J. Geophys. Res.*, 114:E1.
- Cintala, M. J. and R. A. F. Grieve (1998), Scaling impact melting and crater dimensions: Implications for the lunar cratering record, *Met. Planet. Soc.*, 33(4), 889-912.
- Dhingra, D., C. M. Pieters, J. W. Head III, and P. J. Isaacson (2013), Large mineralogically distinct impact melt feature at Copernicus crater – Evidence for retention of compositional heterogeneity, *Geophys. Res. Lett.*, 10:1-6.
- Elkins-Tanton, L. T. and B. H. Hager (2005), Giant meteoroid impacts can cause volcanism, *Earth and Planet. Sci. Lett.*, 239, 219-232.
- Elkins-Tanton, L. T., S. Burgess, and Q. Yin (2011), The lunar magma ocean: Reconciling the solidification process with lunar petrology and geochronology. *Earth and Planet. Sci. Lett.*, 304, 326-336.
- Garrick-Bethell, I. and M. T. Zuber (2009), Elliptical structure of the lunar South Pole – Aitken basin, *Icarus*, 204, 399-408.
- Green, R. O., Pieters, C., Mouroulis, P., Eastwood, M., Boardman, J., Glavich, T., ... & Tseng, H. (2011). The Moon Mineralogy Mapper (M3) imaging spectrometer for lunar science: Instrument description, calibration, on- orbit measurements, science data calibration and on- orbit validation. *J. Geophys. Res.* 116:E10.
- Grieve, R., Stöffler, D., and Deutsch, A. (1991), The Sudbury Structure- Controversial or misunderstood? *J. Geophys. Res.*, 96:22: 753-22.

- Haskin, L. A., J. J. Gillis, B. L. Jolliff, and R. L. Korotev (2003), Regolith in the South Pole - Aitken Basin is mainly indigenous material, *Lunar and Planet. Sci.*, XXXIV, #1434.
- Hawke, B. R. and J. W. Head (1977), Impact melt on lunar crater rims, *Impact and Explosion Cratering*, Eds: Roddy, D. J., R. O. Pepin, and R. B. Merrill. Pergamon Press, New York, 815-841.
- Head, J. W. (1974), Orientale multi-ringed basin interior and implications for the petrogenesis of lunar highland samples, *The Moon*, 11, 327-356, 1974.
- Head III, J. W. (1976), Lunar volcanism in space and time, *Rev. Geophys.*, 14:2.
- Head III, J. W., and A. Gifford (1980), Lunar mare domes – Classification and modes of origin, *Laboratorio di Astrofisica Spaziale di Frascati, Moon and the Planets*, 22, 235-258.
- Head III, J. W. and L. Wilson (1991), Absence of large shield volcanoes and calderas on the Moon: Consequence of magma transport phenomena? *Geophys. Res. Lett.*, 18:11:2121-2124.
- Head III, J. W. and L. Wilson (1992), Lunar mare volcanism: Stratigraphy, eruption conditions, and the evolution of secondary crusts, *Geochimica et Cosmochimica Acta*, 56:6:2155-2175.
- Head, J. W., S. L. Murchie, L. M. Prockter, M. S. Robinson, S. C. Solomon, R. G. Strom, C. R. Chapman, T. R. Watters, W. E. McClintock, D. T. Blewett, and J. J. Gillis-Davies (2008), Volcanism on Mercury: Evidence from the first MESSENGER flyby, *Science*, 321:5885:69-72.

- Hurwitz, D. M. and D. A. Kring (2014), Differentiation of the South Pole – Aitken basin impact melt sheet: Implications for lunar exploration, *J. Geophys. Res.*, 119:1110-1113.
- Isaacson, P. J., Petro, N. E., Pieters, C. M., Besse, S., Boardman, J. W., Clark, R. N., ... & Taylor, L. A. (2013), Development, importance, and effect of a ground truth correction for the Moon Mineralogy Mapper reflectance data set, *J. Geophys. Res.* 118:3:369-381.
- Jolliff, B. L., Haskin, L. A., Korotev, R. L., Papike, J. J., Shearer, C. K., Pieters, C. M., & Cohen, B. A. (2003), Scientific expectations from a sample of regolith and rock fragments from the interior of the lunar South Pole-Aitken basin, *Lunar Planet. Sci.* XXXIV, #1989.
- Jolliff, B. L., S. A. Wiseman, S. J. Lawrence, T. N. Tran, M. S. Robinson, H. Sato, B. R. Hawke, F. Scholten, J. Oberst, H. H. Hiesinger, C. H. van der Bogert, B. T. Greenhagen, T. D. Glotch, and D. A. Paige (2011), Non-mare silicic volcanism on the lunar farside at Compton-Belkovich, *Nat. Geosci.*, 4:566-571.
- Klima, R. L., C. M. Pieters, and M. D. Dyar (2007), Spectroscopy of synthetic Mg-Fe pyroxenes I: Spin-allowed and spin-forbidden crystal field bands in the visible and near-infrared, *Met. and Planet. Sci.*, 42:2:235-253.
- Klima, R. L., M. D. Dyar, and C. M. Pieters (2011a), Near-infrared spectra of clinopyroxenes: Effects of calcium content and crystal structure, *Met. and Planet. Sci.*, 46:3:379-395.
- Klima, R. L., C. M. Pieters, J. W. Boardman, R. O. Green, J. W. Head III, P. J. Isaacson, J. F. Mustard, J. W. Nettles, N. E. Petro, M. I. Staid, J. M. Sunshine, L. A. Taylor,

- and S. Tompkins (2011), Insights into lunar petrology: Distribution and composition of prominent low-Ca pyroxene exposures as observed by Moon Mineralogy Mapper (M³), *J. Geophys. Res.*, 116:E6.
- Moriarty III, D. P. and C. M. Pieters (2014), LSCC samples as ground truth: Using spectral parameters developed for M³ data to assess composition and maturity, *Lunar Planet. Sci.* XLV, #2532.
- Moriarty III, D. P. and C. M. Pieters (2015), Complexities in pyroxene compositions derived from absorption band centers: Examples from Apollo samples, HED meteorites, Synthetic Pure Pyroxenes, and Remote Sensing Data, *Met. and Planet. Sci.*, in revision.
- Moriarty III, D. P., C. M. Pieters, and P. J. Isaacson (2013), Compositional heterogeneity of central peaks within the South Pole – Aitken basin, *J. Geophys. Res.*, 118, 2310-2322.
- Morrison, D. A. (1998), Did a thick South Pole – Aitken basin melt sheet differentiate to form cumulates?, *Lunar. Planet. Sci.* XXIX, #1657.
- Nakamura, R., T. Matsunaga, Y. Ogawa, S. Yamamoto, T. Hiroi, K. Saiki, N. Hirata, T. Arai, K. Kitazato, H. Takeda, T. Sugihara, S. Kodama, M. Ohtake, J. Haruyama, and Y. Yokota (2009), Ultramafic impact melt sheet beneath the South Pole – Aitken basin on the Moon, *Geophys. Res. Let.*, 36, L22202.
- Petro, N. E. and C. M. Pieters (2008), The lunar-wide effects of basin ejecta distribution on the early megaregolith, *Met. and Planet. Sci.*, 43:8:1517-1529.

- Petro, N. E., S. C. Mest, and Y. Teich (2011), Geomorphic terrains and evidence for ancient volcanism within northeastern South Pole - Aitken Basin, *Geol. Soc. Am., Special Paper 477*, pp. 129-140.
- Pieters, C. M., J. W. Head III, L. Gaddis, B. Jolliff, and M. Duke (2001), Rock types of South Pole – Aitken basin and extent of basaltic volcanism, *J. Geophys. Res.*, 106(E11), 28,001-28,022.
- Pieters, C. M., J. Boardman, B. Buratti, A. Chatterjee, R. Clark, T. Glavich, R. Green, J. W. Head III, P. Isaacson, E. Malaret, T. McCord, J. Mustard, N. Petro, C. Runyon, M. Staid, J. Sunshine, L. Taylor, S. Tompkins, P. Varanasi, and M. White (2009), The Moon Mineralogy Mapper (M³) on Chandrayaan-1, *Current. Sci.*, 96(4), 500-505.
- Potter, R. W. K., G. S. Collins, W. S. Kiefer, P. J. McGovern, and D. A. Kring (2012), Constraining the size of the South Pole – Aitken basin impact, *Icarus*, 220, 730-743.
- Scholten, F, J. Oberst, K. D. Matz, T. Roatsch, M. Wahlisch, E. J. Speyerer, and M. S. Robinson (2012), GLD100: The near-global lunar 100 m raster DTM from LROC WAC stereo image data, *J. Geophys. Res.*, 117(E12).
- Spudis, P. D., P. J. McGovern, and W. S. Kiefer (2013), Large shield volcanoes on the Moon, *J. Geophys. Res.*, 118:5.
- Stuart-Alexander, D. E. (1978), *Geologic map of the central far side of the Moon*, U.S. Geol. Survey, Reston, VA.
- Tompkins, S. and C. M. Pieters (1999), Mineralogy of the lunar crust: Results from Clementine, *Meteorit. Planet. Sci.*, 34, 25-41.

- Vaughan, W. M. and J. W. Head III (2014), Impact melt differentiation in the South Pole – Aitken basin: Some observations and speculations, *Planet. Space Sci.*, 91, 101-106.
- Vaughan, W. M., J. W. Head, L. Wilson, and P. C. Hess (2013), Geology and petrology of enormous volumes of impact melt on the Moon: A case study of the Orientale basin impact melt sea, *Icarus*, 223:749-765.
- Warren, P. H., Claeys, P., & Cedillo-Pardo, E. (1996), Mega-impact melt petrology (Chicxulub, Sudbury, and the Moon): Effects of scale and other factors on potential for fractional crystallization and development of cumulates, *The Cretaceous-Tertiary event and other catastrophes in Earth history*, GSA Special Pubs. 307:105-124.
- Weitz, C. M. and J. W. Head III (1999), Spectral properties of the Marius Hills volcanic complex and implications for the formation of lunar domes and cones, *J. Geophys. Res.*, 104:E8:18,993-18,956.
- Whitten, J. L. and J. W. Head III (2014), Lunar cryptomaria: Physical characteristics, distribution, and implications for ancient volcanism, *Icarus*, 247, 150-171.
- Wilhelms, D. E., K. A. Howard, and H. G. Wilshire (1979), *Geologic map of the south side of the Moon*, U.S. Geol. Survey, Reston, VA.
- Wilson, L. and J. W. Head (2003), Lunar Gruithuisen and Mairan domes: Rheology and mode of emplacement, *J. Geophys. Res.*, 108:E2:5012.
- Wöhler, C., Lena, R., Lazzarotti, P., Phillips, J., Wirths, M., Pujic, Z., and Geologic Lunar Research (GLR) Group (2006), A combined spectrophotometric and

morphometric study of the lunar mare domes near Cauchy, Arago, Hortensius, and Milichius, *Icarus*, 183:237-264.

Yingst, R. A. and J. W. Head III (1999), Geology of the mare deposits in South Pole – Aitken Basin as seen by Clementine UVVIS data, *J. Geophys. Res.*, 104(E8), 18957-18979.

Zuber, M. T., D. E. Smith, M. M. Watkins, S. W. Asmar, A. S. Konopliv, F. G. Lemoine, H. J. Melosh, G. A. Neumann, R. J. Phillips, S. C. Solomon, M. A. Wieczorek, J. G. Williams, S. J. Goossens, G. Kruijinga, E. Mazarico, R. S. Park, and D. N. Yuan (2013), Gravity Field of the Moon from the Gravity Recovery and Interior Laboratory (GRAIL) Mission, *Science*, 339(6120), 668-671.

7 Figure Captions

Fig 1: (A) LOLA topography [Smith et al., 2010] overlaid on a LROC WAC [Robinson et al., 2010] mosaic centered on Mafic Mound (red arrow). Topography data is assigned a nonlinear but monotonic color stretch that highlights the topography of central SPA. Black and grey arrows indicate the location of example mare and cryptomare spectra in Fig. 2. The south pole is indicated by the white circle. (B) LROC WAC mosaic (100 m per pixel) of the Mafic Mound region. Central peak craters Bhabha (70 km diameter) and Bose (93 km) are to the northwest, while Stoney (48 km) lies to the northeast. The approximate extent of the Mafic Mound topographic feature is given by the dashed line. (C) LOLA topography (16 pixels per degree) for the same region as (B). The color stretch assigned highlights variations in local topography. The white dashed line A-A' gives the location of the topographic profile in Fig. 4. A larger version of this topographic map is given in Appendix C Fig. S1.

Fig. 2: (A) Example reflectance spectra from Bhabha's central peak, Mafic Mound, cryptomare, and mare materials. Spectra were obtained from fresh craters and steep slopes to limit the effects of soil development. (B) Same spectra as (A) after continuum removal, facilitating assessment of absorption band properties. These spectra were obtained from the areas indicated by arrows in Fig. 1A. Additional spectra are provided in Appendix C Fig. S2.

Fig. 3: Comparisons between the 1 μm and 2 μm band centers for Mafic Mound and several other materials in SPA, including (A) mare, cryptomare, and central peaks, (B)

flat-floor crater rims and floors, (C) buried crater rims and floors, and (D) hummocky-floor crater rims and floors. The SPA material band centers are compared to pure synthetic pyroxenes measured by Klima et al. [2007; 2011a]. For (B-D), open circles correspond to spectra from crater rims, while closed circles correspond to crater floors. WAC images are provided for an example (E) flat floor crater (42.4° S, 163.6° W), (F) buried crater (46.3° S, 164.4° W), and (G) hummocky-floor crater (50.6° S, 157.8° W) in SPA. White dashed lines in (E-G) indicate the location of topographic profiles given in Fig. 4. Band center measurements are derived from spectra given in Appendix C Fig. S2. The location and other properties of each observation are given in Table S1.

Fig 4: (A) Topographic profile for Mafic Mound derived from the WAC GLD100 DTM [Scholten et al., 2012]. The location of the profile is indicated by the white dashed line in Fig. 1C. (B) Representative topographic profiles of flat-floor, buried, and hummocky-floor craters within SPA. These profiles have been normalized to the same vertical scale to highlight the lower topography of the crater floors compared to the surrounding terrain. The locations of the modified crater profiles are given by the white dashed lines in Fig. 3 (E-G). Additional examples (not normalized) are provided in Appendix C Fig. S3. (C) GLD100 topography for Mafic Mound compared to three lunar volcanic complexes of similar size: Gardner (16°N, 34°E), Möns Rümker (41°N, 59°W), and Compton-Belkovich (61°N, 99.5°E).

8 Figures

Fig. 1

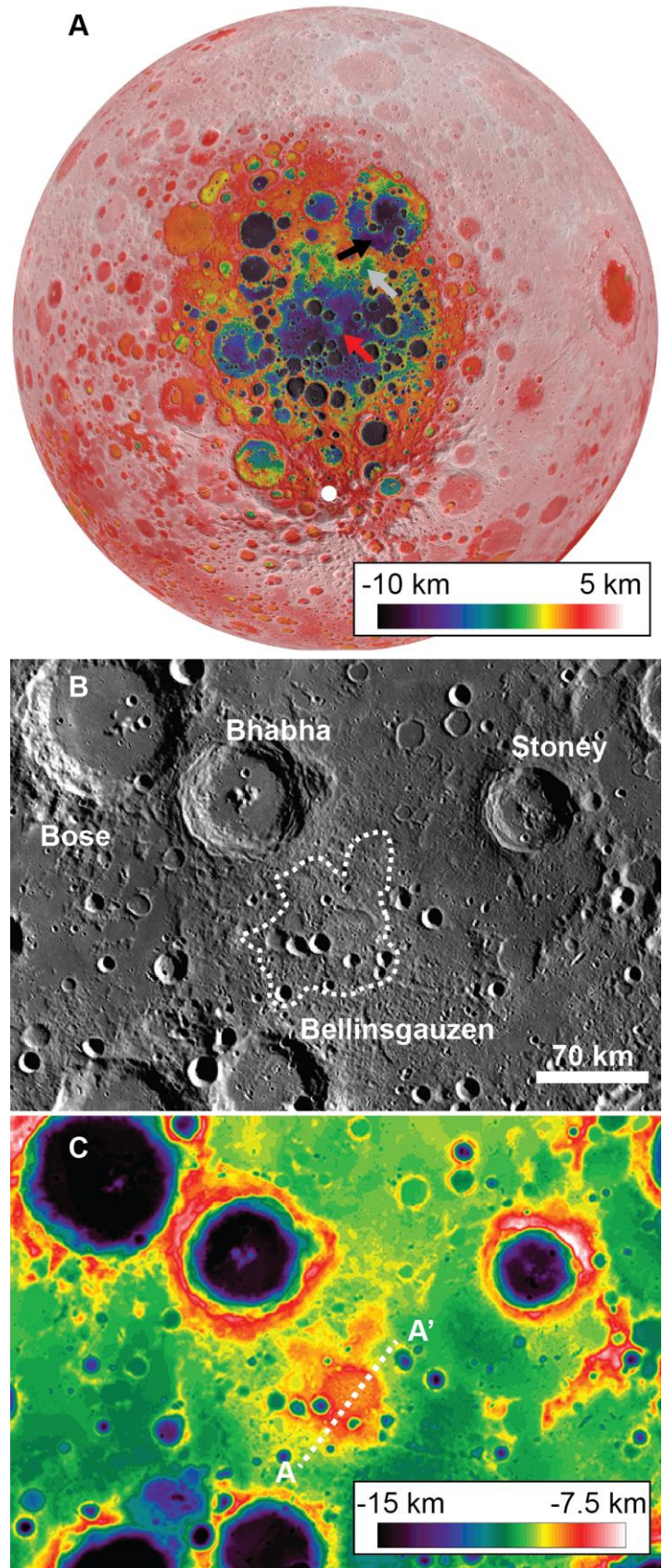
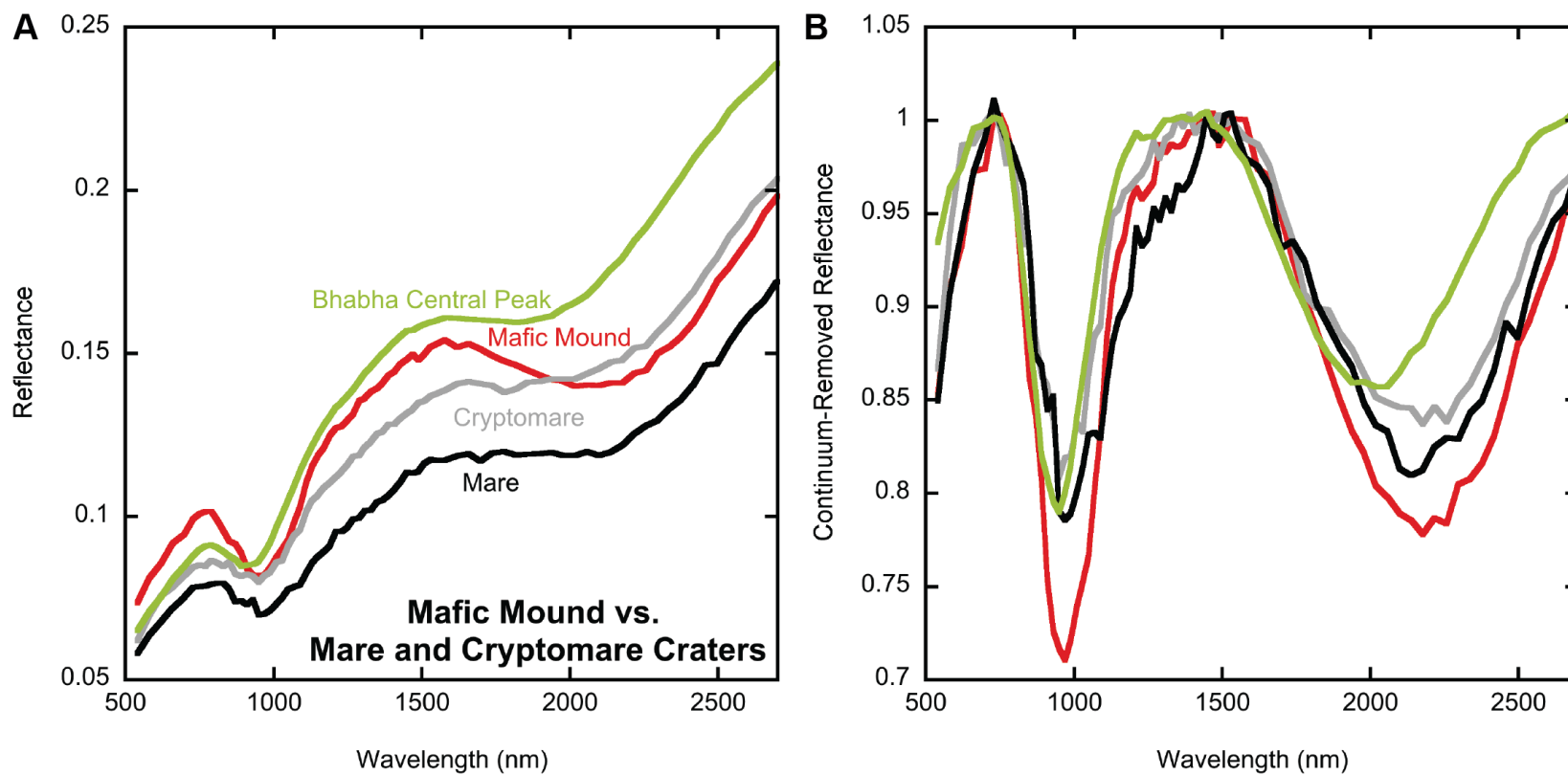


Fig. 2



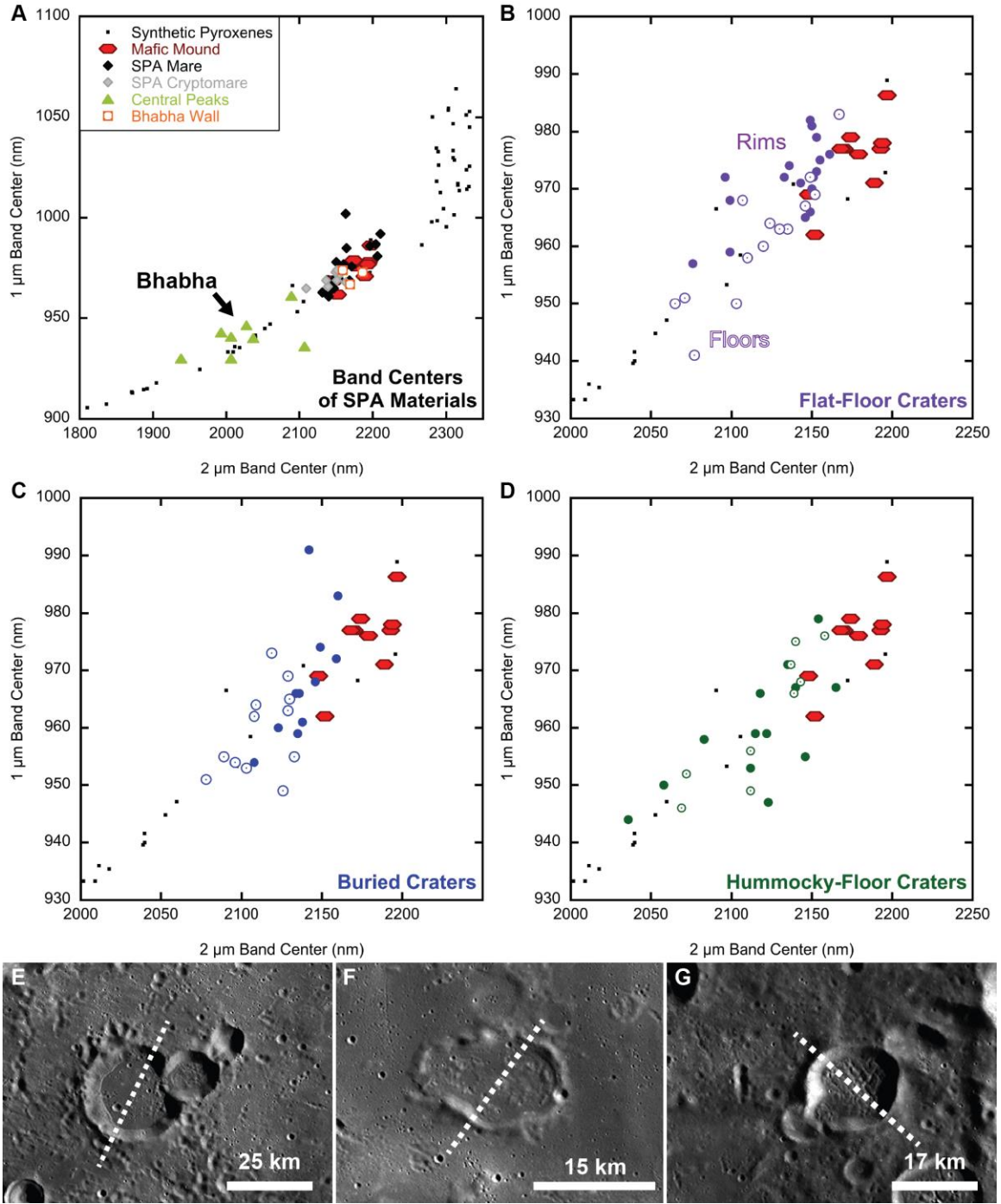
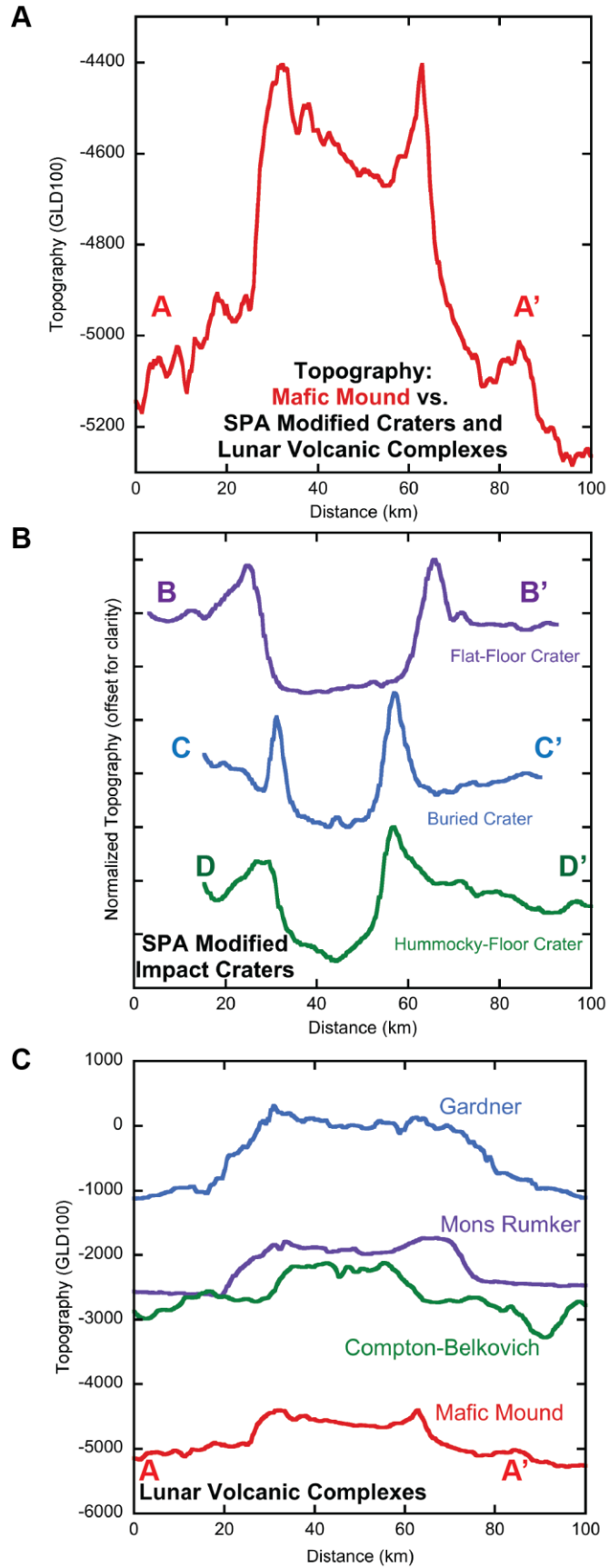


Fig. 3

Fig. 4



CHAPTER 3: The composition and topography of an extensive
resurfacing deposit in central South Pole - Aitken Basin

D. P. Moriarty III

Department of Earth, Environmental, and Planetary Sciences

Brown University | Providence, RI 02912

Abstract

Through an integrated analysis of spectral data, topography, and imagery, we investigate the composition and geology of central South Pole - Aitken Basin. Central SPA exhibits a roughly elliptical depression ~560 km across. This central depression may correspond to a central melt pool that subsided due to cooling and crystallization. Much of the central depression exhibits smooth topography and a relative paucity of impact craters compared to other regions of SPA. This smooth, crater-poor terrain continues within an irregular region of slightly higher topography to the north. Several craters within these regions appear flooded or buried. The surface composition of the smooth terrain exhibits higher-Ca pyroxenes than most non-mare SPA materials, but not quite as high as typical mare basalts. Based on the extent of the smooth terrain and compositional anomaly, we define a "central **SPA C**ompositional **A**nomaly" (SPACA). The Ca,Fe-pyroxene-bearing SPACA surface material is observed in the walls and peaks of several craters in the region, suggesting that the SPACA deposit is several km thick. However, more Mg-rich, low-Ca pyroxenes are observed in multiple central peaks of complex craters throughout the SPACA region, setting an upper limit on the thickness of this surface material. Based on the smooth texture, paucity of impact craters, presence of flooded craters, and unusual composition of the SPACA region, we find that massive magmatic resurfacing is the most consistent mode of origin.

1 Introduction

Impact basin formation is a dynamic process that vaporizes, melts, displaces, and excavates target materials. In addition to these immediate, localized effects, large

impacts may trigger geochemical and geophysical effects over a global scale or extended period of time. For instance, large lunar impacts have been implicated in (a) the production of melt seas that may cool slowly, convect, and differentiate [Warren *et al.* 1996; Morrison, 1998; Hurwitz and Kring; 2014; Vaughan and Head, 2014], (b) localized mantle convection [Elkins-Tanton and Hagar, 2005], (c) antipodal and/or global magma ascent [Schultz and Crawford, 2011; Kring *et al.*, 2015], or even (d) cumulate overturn of the mantle [Kring *et al.*, 2015]. In any scenario, basin-forming impacts are extremely energetic events that have the potential to influence the course of a planet's history.

The South Pole - Aitken Basin (SPA) presents a unique opportunity to study such phenomena. At ~2200 km in diameter [Stuart-Alexander, 1978; Spudis *et al.*, 1994; Garrick-Bethell and Zuber; 2009], SPA is the largest confirmed lunar impact structure on the Moon and therefore serves as an endmember for investigating lunar impacts. Additionally, the topographic and compositional structure is fairly well preserved, as SPA has not been filled with mare basalts to the extent that many nearside basins have.

In this paper, we investigate a topographically and compositionally distinct region in central SPA. This region may have implications for global- and regional-scale effects of the SPA-forming impact. Our primary analyses are performed using modern spectroscopic data from the Moon Mineralogy Mapper (M³) [Pieters *et al.*, 2009]. These spectral data are interpreted based on the fundamental spectra-compositional relationships for pyroxenes explored in Chapter 1. We supplement this compositional data with topography from the Lunar Orbiter Laser Altimeter (LOLA) [Smith *et al.*, 2010] and imagery from the Lunar Reconnaissance Orbiter Camera [Robinson *et al.*,

2010]. A companion analysis [Chapter 4] uses similar data to identify, characterize, and map basin-scale properties of materials excavated in the basin-forming impact. In Chapter 5, we examine these findings in the context of models of basin formation and lunar evolution.

2 Background:

2.1 The Formation and Composition of SPA

Impact crater scaling laws and models of SPA formation suggest that large volumes of lower crust and upper mantle materials were excavated and melted during the impact event [*Melosh, 1989; Hammond et al., 2009; Potter et al., 2012*]. The impact melt produced probably pooled into a thick, centralized melt sheet that may have subsequently differentiated [*Morrison et al., 1998; Hurwitz and Kring, 2014; Vaughan et al., 2013; Vaughan and Head, 2014*]. However, most of these impact models assume vertical impact angles as well as other factors such as impactor velocity, size, and speed. SPA's elliptical shape suggests that the SPA-forming impact may have been highly oblique [e.g. *Garrick-Bethell and Zuber, 2009; Schultz and Crawford, 2011*]. Oblique impact angles or other factors such as low impact velocity or large impactor size can significantly affect the melt volume, melt retention, excavation depth, and ejecta pattern of an impact event [e.g. *Melosh, 1989; Pierazzo et al., 1997; Pierazzo and Melosh, 2000; Schultz and Crawford, 2011; Potter et al., 2012*].

Previous studies have shown the SPA interior to be elevated in Th, Fe, and pyroxene content compared to the feldspathic highlands [e.g. *Jolliff et al., 2000; Pieters et al.; 2001; Ohtake et al. 2014*]. Most non-mare mafic exposures within SPA exhibit

spectra dominated by Mg-rich pyroxenes [*Tompkins and Pieters, 1999; Pieters et al., 2001; Cahill et al. 2009; Nakamura et al., 2009; Klima et al., 2011b; Moriarty et al., 2013; Moriarty and Pieters, in preparation*]. These materials have been interpreted to represent a thick, homogeneous impact melt sheet [e.g. *Nakamura et al., 2009; Vaughan and Head, 2014*] or exposure of excavated upper mantle / lower crust Mg-suite materials [*Klima et al., 2011; Ohtake et al., 2014; Chapter 4*]. However, the center-most portion of SPA exhibits a surface composition dominated by higher-Ca pyroxenes [*Ohtake et al., 2014*]. Establishing the nature and origin of this "central **SPA** **C**ompositional **A**nomaly" (SPACA) is the main subject of this paper.

2.2 M³ Data and PLC Analysis

For this study, compositional information is derived from Moon Mineralogy Mapper (M³) [*Pieters et al., 2009*] data. M³ was a near-infrared imaging spectrometer that combined high spectral resolution (5-40 nm per channel, from 430 nm to 3000 nm) with high spatial resolution (70-240 m per pixel), achieving near-global coverage split into several optical periods (OPs) [*Boardman et al., 2011; Green et al., 2011*]. A summary of the coverage and data properties for the SPA region is provided in Chapter 4. The M³ wavelength range is sensitive to crystal field absorptions from common lunar minerals such as olivine, pyroxene, plagioclase, and spinel [e.g. *Burns, 1993*] and is therefore well-suited to characterize the compositional diversity of lunar materials in spatial context.

Spectra from the SPA interior are dominated by pyroxene signatures. To characterize the composition of these pyroxene-bearing materials, their spectra are analyzed using the **P**arabola and **L**inear **C**ontinuum (PLC) fitting routine [*Moriarty and Pieters, 2016*]. The PLC technique is a straightforward, benchmarked, and well-

documented approach for estimating the centers (EBC) and depths (EBD) of the 1 μm and 2 μm pyroxene absorption bands. These measurements are extremely useful, as pyroxene band centers are systematically related to pyroxene composition [e.g. *Adams, 1974; Hazen et al., 1978; Cloutis and Gaffey, 1991; Klima et al., 2007; 2011a; Moriarty and Pieters, 2016*], while band depths are strongly correlated with pyroxene abundance (as well as other contributing factors such as optical maturity, particle size, and composition). Using PLC fitting [*Moriarty and Pieters, 2016*], absorption band parameter maps (EBC1, EBC2, EBD1, and EBD2) were calculated for each OP covering SPA.

The primary compositional analyses in this Chapter focus on pyroxene compositional information derived from band center measurements. Band depth maps for the SPA region are considered more completely in Chapter 4.

3 Deriving Compositional Information from M^3 Spectra

Synthetic pure pyroxenes exhibit systematic variations in absorption band center related to their Fe, Mg, and Ca content [*Klima et al., 2007; Klima et al. 2011*]. Mg-rich orthopyroxenes exhibit the shortest-wavelength absorption bands, while Ca-rich clinopyroxenes exhibit the longest-wavelength absorption bands. Fe-rich orthopyroxenes and Ca-poor clinopyroxenes exhibit intermediate-wavelength absorption bands. For the synthetic pure pyroxenes, absorption band centers are highly diagnostic of specific pyroxene compositions [*Klima et al., 2007; Klima et al. 2011*].

Meanwhile, natural pyroxene-bearing materials exhibit significant compositional complexity related to crystallization processes and physical mixing [*Moriarty and Pieters, 2016*]. For instance, in any given M^3 pixel, mixing of different compositions can

occur at multiple scales: (a) spatially heterogeneous pixels containing multiple lithologies, (b) physical mixing of multiple rock types in soils or breccias, (c) mineral assemblages incorporating pyroxene and non-pyroxene components such as plagioclase, ilmenite, glass, etc., (d) formation of multiple pyroxene components within a rock (via exsolution or crystallization of distinct phases), and (e) a range in composition within individual pyroxene phases due to zoning or other effects. Point (d) is illustrated in Fig. 1A. In this figure, pyroxene compositions for several lunar basaltic rocks and soils are given based on measurements reported in *Taylor et al.* [1996; 2001; 2002; 2003] and *Isaacson et al* [2011]. Each individual rock or soil sample exhibits multiple pyroxene phases, roughly classified as pigeonite, augite, Fe-pyroxene, and orthopyroxene. Even within individual rocks, each pyroxene phase exhibits a range in composition [e.g. *Isaacson et al*, 2011].

Calculated from the abundance and average composition of each pyroxene phase present, the overall average pyroxene composition for individual rock/soil samples are given in Fig. 1A+B. Remote NIR spectroscopy measures the composite optical properties of the bulk target, meaning that spectra (such as those in Fig. 1C) represent the sum of contributions from many components interacting non-linearly. These components can include multiple pyroxene and non-pyroxene phases. Therefore, absorption band centers for natural pyroxene-bearing materials are inherently non-unique in terms of the composition of specific pyroxene components [*Moriarty and Pieters*, 2016]. Instead, these absorption bands are most closely related to the average pyroxene composition of the material. While the precise relationships between absorption band center and Fe,Mg,Ca content differ between natural and pure synthetic samples, similar relative

trends persist and can be used to identify and characterize compositional diversity in remote sensing data [*Moriarty and Pieters, 2016*].

Understanding the difference between natural materials and synthetic pure pyroxenes is important for interpreting M^3 band centers. Rather than ascribing band center measurements to a single specific pyroxene composition based on comparison to synthetic pure pyroxenes, we are careful to interpret M^3 -derived band center values as arising from average pyroxene compositions with many possible components. The calculated average pyroxene compositions of diverse lunar rocks and soils [*Taylor et al., 1996; 2001; 2002; 2003; Isaacson et al., 2011*] serve as a frame of reference for compositional interpretations of M^3 absorption band centers throughout this paper.

4 Properties of Central SPA

4.1 Topographic Structure of SPA

In order to properly interpret the origin of diverse SPA materials, it is important to understand the physical structure of the basin. While several topographic analyses have focused on the outer rim of SPA [e.g. *Garrick-Bethell and Zuber, 2009; Schultz and Crawford; 2011*], the topography of the interior has not been extensively documented. Fig. 2 provides LOLA topography for the SPA region at several scales. These maps highlight the topographic structure of the basin.

On a global scale, SPA exhibits the lowest topography on the Moon (Fig. 2A). The high-topography rim of SPA is elliptical in shape [*Garrick-Bethell and Zuber, 2009*] and approximately corresponds to the transition from green to red in Fig. 2A . This rim is fairly continuous around the basin except for the southwestern region (near Australe), where it is more ambiguous.

The center-most region of SPA is associated with a roughly elliptical area of low topography ~560 km across. This central depression is especially apparent in Fig. 2B as a dark blue/purple region. Mafic Mound, an unusual volcanic structure ~1 km high and ~75 km across [Moriarty and Pieters, 2015], lies near the center of this region.

Throughout the central depression, the basin floor is relatively smooth and appears to exhibit a paucity of impact craters. A lower crater density compared to other portions of the SPA interior is confirmed using a LOLA-derived catalog of craters ≥ 20 km in diameter [Head *et al.*, 2010; Kadish *et al.*, 2011], as shown in Fig. 3.

This crater-deficient smooth terrain is not confined to the central depression; it extends to the north across an irregular region with slightly higher topography. This irregular area stretches ~525 km across, extending ~315 km north of the central depression. The smooth terrain is readily apparent in Fig. 2B as a contiguous green region just north of the central depression. In addition to a paucity of impact craters ≥ 20 km in diameter [Head *et al.*, 2010; Kadish *et al.*, 2011], several craters throughout this region appear buried, filled, or otherwise modified [Moriarty and Pieters, 2015].

Exterior to the central depression and irregular smooth terrain, the remaining SPA interior is more heavily cratered and exhibits increasingly higher topography approaching the SPA rim. Due to the presence of several superposed basins and large craters (Apollo, Oppenheimer, Leibnitz, Von Kàrman, Poincarè, etc.), this region is fairly discontinuous and exhibits highly variable topography.

4.2 A Distinctive Compositional Zone in Central SPA

Fig. 4 presents a mineralogical overview of central SPA via PLC-measured 1 μm and 2 μm absorption band centers. In the figure, color-stretched band center values are overlaid on an LROC WAC basemap. As discussed above, the PLC technique employs

parabola fits to derive approximate band centers from M^3 spectra that may exhibit noise or other measurement artifacts. Therefore, band center measurements for stronger absorption bands are more reliable than those for weaker absorptions. The very strongest $1\ \mu\text{m}$ absorption bands in SPA exhibit band depths $>15\%$ and are typically associated with optically immature materials such as fresh craters and steeply-sloped areas such as crater walls, rings, and central peaks. In Fig. 4B, pixels with $1\ \mu\text{m}$ band depths $\geq 15\%$ are displayed with full opacity. For a broader sense of the compositional trends, pixels with $1\ \mu\text{m}$ band depths $\geq 10\%$ are also displayed, but with some transparency. These pixels are associated with mafic but more optically mature materials such as soils and older craters. This approach emphasizes the compositional diversity of the most pristine mafic exposures within a broader regional context. Fig. 4A displays all pixels with $1\ \mu\text{m}$ band depths $\geq 10\%$ with the same opacity, to emphasize regional trends. Maps and a more detailed discussion of band depths across SPA are provided in Chapter 4.

The band center maps in Fig. 4 highlight the compositional diversity of SPA. In these maps, materials with long-wavelength absorption bands (such as mare basalts) appear yellow/red, while materials with short-wavelength absorption bands (Mg-rich pyroxenes) appear purple/blue. In central SPA, an irregular region approximately 700 km in diameter exhibits materials with wavelengths intermediate to mare basalts and Mg-Pyroxenes, indicating pyroxenes intermediate in Ca and Fe. These Ca,Fe-pyroxene-bearing materials appear green in Fig. 4. Throughout this paper, we refer to this region of intermediate pyroxene composition as the central **SPA Compositional Anomaly** (SPACA). Outside of SPACA, non-mare mafic materials are spectrally dominated by Mg-pyroxenes. These Mg-pyroxene-bearing zones are further discussed in Chapters 4+5.

4.3 Spatial Extent of SPACA

The precise boundaries of SPACA are fairly amorphous, as they represent complex compositional gradients obscured by superimposed impact craters and mare basalts. However, the approximate boundaries of SPACA can be established using the following criteria (in order of importance): (1) fairly long-wavelength absorption bands (green or longer in Fig. 4), (2) intermediate albedo (brighter than typical mare basalts, but darker than highlands materials, as seen in Fig. 5 and discussed in the next section), (3) smooth, crater-deficient terrain, (4) low topography, and (5) location within the SPA interior. Based on these criteria, the approximate boundaries of SPACA are given in Figs. 2 and 3. Although highly irregular in shape, SPACA spans ~750 km north-to-south and ~650 km east-to-west. SPACA is centrally located within SPA, blanketing the majority of the central depression. The northern boundaries of SPACA are closely correlated with the irregular smooth terrain to the north of the central depression.

Within the SPACA terrain, Ca,Fe-pyroxene-bearing materials are observed in the walls of craters from small (<1 km diameter) to large (e.g. Bhabha (64 km), Finsen (72 km), Stoney (45 km), and White (39 km)). Based on crater scaling relationships [Melosh, 1989], craters excavate materials from depths equal to ~10% of their transient cavity diameter. Therefore, the fairly uniform exposure of Ca,Fe-pyroxene-bearing materials in these crater walls suggests that they are excavated from a compositionally uniform zone several km thick. On the other hand, several central peaks in this region (e.g. Finsen, Bhabha, Stoney) expose materials spectrally dominated by Mg-rich pyroxene. Since central peaks represent the deepest material sampled by any given crater (~10 km depths for these craters) [Cintala and Grieve, 1998], this sets an upper limit of ~10 km on the thickness of the SPACA surface deposit. Interestingly, Ca-Fe-pyroxene-bearing

materials are also observed in Mafic Mound, an unusual volcanic feature ~75 km across and ~1 km high located at the center of SPA [Moriarty and Pieters, 2015].

4.4 The Composition of SPACA Materials

Example spectra for mare basalts, SPACA materials, and Mg-rich pyroxene-bearing materials from SPA are given in Fig. 5. Spectra were collected from locations listed in the caption. To minimize the spectral contribution from mature soils, spectra were collected from fresh craters and steeply-sloped surfaces. Several spectral differences between these three material types are immediately apparent. Of these materials, mare basalts exhibit the lowest albedos, while the Mg-pyroxene-bearing materials exhibit the highest albedos. The SPACA surface deposit exhibits intermediate albedo, but is more similar to Mg-pyroxene-bearing materials than mare basalts. Mare basalts and SPACA surface materials exhibit band centers at somewhat similar wavelengths, while Mg-pyroxene-bearing materials exhibit band centers with much shorter wavelengths.

For a more quantitative assessment of 1 μm and 2 μm band centers, the PLC-measured values for a variety of SPA mare basalts, Mg-pyroxene-bearing materials, and SPACA surface materials are given in Fig. 6. As expected based on spectra and maps, Mg-pyroxene-bearing materials exhibit the shortest-wavelength band centers, while mare basalts exhibit the longest-wavelength band centers. SPACA surface materials exhibit band centers at slightly shorter wavelengths than mare basalts, but with an overlapping distribution.

Employing the lunar soil and rock samples discussed above, Fig. 6 provides a guide for compositional interpretations of these band center measurements. As seen in Fig. 6B, the band center range of SPA materials extends over only a portion of the full

range observed in pure synthetic pyroxenes, excluding high-Ca clinopyroxenes and high-Mg orthopyroxenes. This does not preclude the presence of these minerals on the lunar surface, but rather suggests the average pyroxene compositions observed fall between these endmember compositions.

As emphasized in *Moriarty and Pieters* [2016], band center values from remote sensing data represent average pyroxene compositions of highly complex materials. Relative trends between composition and band center are observed and can be used with *a priori* geologic context and laboratory analyses of samples to make compositional inferences from band center measurements.

On the lunar surface, the longest-wavelength pyroxene absorption bands observed are associated with mare basalts. Because basaltic rock and soil samples have been returned from the moon, their compositions are well-understood through laboratory analyses. Laboratory-measured band center values [*Moriarty and Pieters*, 2016] and compositions [*Taylor et al.*, 1996; 2001; 2002; 2003; *Noble et al.*, 2006; *Isaacson et al* 2011] for example Apollo 11, 15 and 17 basaltic materials are presented in Fig. 6. These band centers are directly compared to M^3 -derived band centers of the Apollo 15 and Apollo 17 mare regions in Fig. 6A-B. As the source regions for the returned samples, these areas of the lunar surface are assumed to be very similar in composition to the samples. Indeed, the soil samples, rock samples, and remote sensing data all exhibit similar band centers, confirming that the PLC technique [*Moriarty and Pieters*, 2016] provides consistent band center measurements across several measurement scenarios.

As seen in Fig. 6A, mare basalts in SPA exhibit similar band centers to the nearside mare, indicating similar average pyroxene compositions. The average pyroxene

compositions of Apollo 11, 15, and 17 soils and rocks are given in Fig. 6C. Because of their similar band centers, it is reasonable to assume that SPA mare basalts exhibit similar average pyroxene compositions as the Apollo 11, 15, and 17 basalts.

To link measured absorption band centers to average pyroxene composition, we define three general compositional groups based on lunar samples, synthetic pure pyroxenes, and remote sensing data:

- A. **Basaltic Clinopyroxene (BCPX):** In band center maps (Fig. 4), these materials appear red/yellow, approximately corresponding to 1 μm band centers > 980 nm and 2 μm band centers > 2100 nm. These materials also exhibit relatively low albedos. Because these materials are closely linked to well-characterized mare basalts, the range in average pyroxene compositions is well-established and is demarcated with the red line in Fig. 6C (and at longer wavelengths than the green line in Fig. 6A). These pyroxenes exhibit a fairly high average Ca,Fe content.
- B. **Non-Mare Clinopyroxene (NMCPX):** In Fig. 4, these materials appear green/yellow, corresponding to 1 μm band centers >960 nm and 2 μm band centers >2050 nm. NMCPX pyroxenes are the dominant mafic component of SPACA surface materials. As shown in Fig. 6A, SPACA materials exhibit slightly shorter-wavelength band centers than mare basalts, but with significant overlap in the distributions. From these distributions, it is reasonable to conclude that the range in NMCPX compositions overlaps the BCPX range, but overall exhibits lower Ca,Fe content. The range in average pyroxene compositions for NMCPX materials is bounded by the green line in Fig. 6A,C.
- C. **Mg-Rich Pyroxene (Mg-pyroxene):** These materials appear blue/purple in Fig. 4, indicating 1 μm band centers <960 nm and 2 μm band centers <2050 nm. Due to their short-wavelength band centers, these materials are probably dominated by Mg-rich pigeonites and orthopyroxenes, similar to the Apollo 14 and 16 soils. The most likely range of average pyroxene compositions is demarcated by the blue line in Fig. 6A,C. Mg-pyroxene-bearing materials across SPA are discussed in more detail in Chapters 4-5.

Representative spectra for each compositional group are given in Fig. 5.

5 Possible Origin of the SPACA

5.1 Impact Melt

Impact models suggest that the SPA-forming impact produced large volumes of impact melt, which may have formed a thick melt sheet at the center of SPA [*Hammond*

et al., 2009; *Potter et al.*, 2012]. Due to the vast size of SPA, the impact melt formed is modeled to be dominated by mantle materials [*Hammond et al.*, 2009; *Potter et al.*, 2012]. Since the upper mantle is probably composed primarily of olivine and/or orthopyroxene [e.g. *Khan et al.*, 2007; *Elkins-Tanton et al.*, 2011], the bulk composition of SPA impact melt is probably dominated by these materials. However, petrologic models demonstrate that differentiation of such melt could produce a near-surface layer of clinopyroxene-bearing materials overlying Mg-rich pyroxene-bearing materials, under certain conditions [*Hurwitz and Kring*, 2014].

Vaughan and Head [2014] estimate that a ~50 km thick melt sheet formed in central SPA. Based on equations given by *Vaughan et al.*, [2013], a ~50 km thick SPA melt sheet would crystallize in ~5 myr. Due to volume changes during cooling and crystallization, thick impact melt sheets are expected to vertically shrink by ~10% when fully crystallized [*Vaughan et al.*, 2013]. In basins such as Orientale, this is thought to produce a roughly elliptical central depression [*Vaughan et al.*, 2013]. The ~560 km central depression in SPA may be an analogous structure. If so, this outlines the extent of the thickest, most coherent part of the SPA melt sheet. Because a minimum melt sheet thickness is required in order to undergo differentiation [*Warren*, 1993], the central depression may represent the portion of the SPA melt sheet most likely to have differentiated.

5.2 Magmatic Resurfacing

Localized mare and cryptomare deposits have been identified across SPA [*Pieters et al.*, 2001; *Yingst and Head*, 1999; *Petro et al.*, 2011; *Whitten et al.*, 2014]. However, SPACA surface materials blanket a much larger, more continuous region than these localized deposits. The physical properties of SPACA may be more consistent with

much larger-scale volcanic flooding, similar to models proposed by *Whitten and Head* [2013]. These models suggest that the paucity of craters in central SPA is consistent with mare basaltic flooding resulting in a ~2 km layer thick throughout the center of the basin.

5.3 Discussion

Under certain conditions, differentiated impact melt could conceivably produce the distinct stratigraphy observed across SPACA: namely, non-mare clinopyroxene-bearing lithologies overlying Mg-rich pyroxene-bearing lithologies. However, impact melt alone cannot account for the paucity of large craters across SPACA. Even if all impacts occurring during the crystallization of the melt sheet failed to form craters, this ~5 myr window is too short to significantly affect the cratering history of the region, even if it occurred during a possible early epoch of enhanced impactor flux [*Morbidelli et al.*, 2012]. In fact, the crystallization time of the melt sheet may have been significantly shorter than 5 myr if the melt sheet was thinner than 50 km or entrained a large proportion of solid clasts. Therefore, the paucity of impact craters in central SPA could not have been caused by a SPA impact melt pool

The impact melt scenario is also inconsistent with several other properties of SPACA. The population of flooded, buried, and otherwise modified craters throughout central SPA [*Moriarty and Pieters*, 2015] provide clear evidence of a complex sequence of resurfacing events postdating the SPA impact, rather than a single event such as melt sheet crystallization. Additionally, the SPACA region extends hundreds of km north of the central depression. If the central depression corresponds to a thick central melt sheet that differentiated to form the observed stratigraphy, it is unlikely that thinner melt deposits outside the central melt pool would have undergone similar differentiation processes.

Instead, the properties of SPACA suggest volcanic resurfacing postdating melt sheet solidification. A volcanic flooding scenario is consistent with the composition, extent, smooth topography, and paucity of impact craters observed throughout the SPACA region.

This volcanic resurfacing scenario is consistent with elements of a volcanic flooding model proposed by *Whitten and Head* [2013]. However, several distinctions are apparent. *Whitten and Head* [2013] suggest that volcanic flooding progressively fills an area beginning with the lowest-available topography. This is inconsistent with the extent of SPACA terrain. SPACA does not completely fill the central depression, but does extend to somewhat higher-topography terrain to the north. Flooding of higher-elevation areas requires magma ascent and extrusion within these higher-elevation areas. Mafic Mound may also represent an additional source vent for SPACA materials, as it is exhibits a similar composition and is interpreted to be volcanic in nature [*Moriarty and Pieters*, 2015].

Continuing the comparison to published flooding models, *Whitten and Head* [2013] suggest that the volcanic fill in SPA is typical mare basaltic magma. As seen in Fig. 6, SPACA surface materials (NMCPX-bearing) exhibit different pyroxene compositions than typical mare basalts (BCPX-bearing). *Whitten and Head* [2013] offer a solution to this issue: To produce the observed composition, they suggest that erupted mare basalts were mixed with subsequent basin ejecta to produce a cryptomare-like deposit. While this scenario is certainly feasible, it would require significant impact gardening across the flooding deposit to produce the relatively uniform SPACA surface material observed across the region. We estimate the SPACA surface deposit to be ~5

km thick, based on uniform exposures in the walls of craters such as Bhabha, Finsen, Stony, and White, while *Whitten and Head* [2013] estimate a fill thickness of ~2 km. Homogeneously mixing a layer several km thick would require a significant number of fairly large impacts. The fact that SPACA exhibits a relatively low crater density suggests that it has been subject to a small number of impacts, limiting the degree of mixing that surface materials could have undergone. Therefore, it is unlikely that SPACA surface materials were produced from typical mare basalts via mixing. This suggests that the SPACA surface materials may represent an inherently unusual magma composition. Given its location in central SPA, the production and ascent of this unusual magma may be related to global- or regional-scale geophysical effects of the SPA-forming impact. The petrologic and geophysical origin of SPACA surface materials is discussed further in Chapter 5.

6 Conclusions

The central SPA Compositional Anomaly (SPACA) exhibits low topography, a non-mare clinopyroxene-bearing surface composition, and a relatively smooth, crater-deficient surface. The region exhibits strong evidence for post-SPA resurfacing, including a relative paucity of impact craters, the presence of several filled/buried craters, and the presence of Mafic Mound, which itself may be an unusual volcanic structure [*Moriarty and Pieters, 2015*]. Although a differentiated impact melt deposit can account for some observed properties of SPACA, magmatic resurfacing is more consistent with the full range of compositional, structural, and topographic observations. SPACA is interpreted to represent flooding by an unusual magma composition that is spectrally distinct from typical mare basalts, exhibiting an average pyroxene composition slightly

lower in Ca (and possible Fe) and a higher albedo. The SPACA region is not a primary feature of the SPA impact, but appears to be the result of later resurfacing.

7 Acknowledgements

Support of this research through NASA LASER (NNX12AI96G) and SSERVI (NNA14AB01A) is gratefully acknowledged. Discussions with Steve Parman and Jim Head were helpful in guiding our interpretations.

8 References

- Adams J. B. 1974. Visible and near-infrared diffuse reflectance spectra of pyroxenes as applied to remote sensing of solid objects in the solar system. *Journal of Geophysical Research* 79:32:4829-4836.
- Boardman, J.W., Pieters, C.M., Green, R.O., Lundeen, S.R., Varanasi, P., Nettles, J., Petro, N., Isaacson, P., Besse, S. and Taylor, L.A., 2011. Measuring moonlight: An overview of the spatial properties, lunar coverage, selenolocation, and related Level 1B products of the Moon Mineralogy Mapper. *Journal of Geophysical Research: Planets (1991–2012)*, 116(E6).
- Burns R. G. 1993. Mineralogical applications of crystal field theory, 2nd ed. Cambridge, UK: Cambridge University Press. 551.
- Cahill, J. T. S., P. G. Lucey, and M. A. Wieczorek (2009), Compositional variations of the lunar crust: Results from radiative transfer modeling of central peak spectra, *J. Geophys. Res.*, 114, E09001, doi:10.1029/2008JE003282.

- Cintala, M. J., and R. A. F. Grieve (1998), Scaling impact melting and crater dimensions: Implications for the lunar cratering record, *Meteorit. Planet. Sci.*, 33, 889–912, doi:10.1111/j.1945-5100.1998.tb01695.x.
- Cloutis E. A. and Gaffey M. J. 1991. Pyroxene spectroscopy revisited: Spectral-compositional correlations and relationship to geothermometry. *Journal of Geophysical Research: Planets* 96:E5:22809-22826.
- Elkins-Tanton, L. T. and B. H. Hager (2005), Giant meteoroid impacts can cause volcanism, *Earth and Planet. Sci. Let.*, 239, 219-232.
- Elkins-Tanton, L. T., S. Burgess, and Q. Yin (2011), The lunar magma ocean: Reconciling the solidification process with lunar petrology and geochronology. *Earth and Planet. Sci. Let.*, 304, 326-336.
- Garrick-Bethell, I. and M. T. Zuber (2009), Elliptical structure of the lunar South Pole-Aitken basin, *Icarus*, 204, 399-408, doi:10.1016/j.icarus.2009.05.032.
- Green, R. O., Pieters, C., Mouroulis, P., Eastwood, M., Boardman, J., Glavich, T., and Tseng, H. (2011). The Moon Mineralogy Mapper (M3) imaging spectrometer for lunar science: Instrument description, calibration, on-orbit measurements, science data calibration and on-orbit validation. *J. Geophys. Res.* 116:E10.
- Hammond, N. P., F. Nimmo, and D. Korykansky (2009), Hydrocode modeling of the South Pole Aitken Basin-forming impact, *Lunar and Planet. Sci. Conf, XL*, #1455
- Hazen R. M., Bell P. M., and Mao H. K. 1978. Effects of compositional variation on absorption spectra of lunar pyroxenes. *Proceedings of the Lunar and Planetary Science Conference IX*, pp. 2929-2934.

Head, J.W., C.I. Fassett, S.J. Kadish, D.E. Smith, M.T. Zuber, G.A. Neumann, and E.

Mazarico (2010), Global distribution of large lunar craters: Implications for resurfacing and impactor populations, *Science*, 329, 1504-1507,

doi:10.1126/science.1195050.

Hurwitz, D. M. and D. A. Kring (2014), Differentiation of the South Pole – Aitken basin

impact melt sheet: Implications for lunar exploration, *J. Geophys. Res.*,

119:1110-1113.

Isaacson P. J., Basu Sarbadhikari A., Pieters C. M., Klima R. L., Hiroi T., Liu Y., and

Taylor L. A. 2011a. The lunar rock and mineral characterization consortium:

Deconstruction and integrated mineralogical, petrologic, and spectroscopic

analyses of mare basalts. *Meteoritics and Planetary Science* 46:2:228-251.

Jolliff, B. L., Gillis, J. J., Haskin, L. A., Korotev, R. L., & Wieczorek, M. A. (2000).

Major lunar crustal terranes: Surface expressions and crust- mantle

origins. *Journal of Geophysical Research: Planets (1991–2012)*, 105(E2), 4197-

4216.

Kadish, S.J, C.I. Fassett, J.W. Head, D.E. Smith, M.T. Zuber, G.A. Neumann, and E.

Mazarico (2011), A global catalog of large lunar crater (≥ 20 KM) from the Lunar

Orbiter Laser Altimeter, *Lunar Plan. Sci. Conf., XLII*, abstract 1006.

Khan, A., Connolly, J.A.D., MacLennan, J., Mosegaard, K., 2007. Joint inversion of seismic and

gravity data for lunar composition and thermal state. *Geophys. J. Int.* 168, 243–

258, <http://dx.doi.org/10.1111/j.1365-246X.2006.03200.x>.

- Klima R. L., Pieters C. M., and Dyar M. D. 2007. Spectroscopy of synthetic Mg-Fe pyroxenes I: Spin-allowed and spin-forbidden crystal field bands in the visible and near-infrared. *Meteoritics and Planetary Science* 42:2:235-253.
- Klima R. L., Dyar M. D., and Pieters C. M. 2011. Near-infrared spectra of clinopyroxenes: Effects of calcium content and crystal structure. *Meteoritics and Planetary Science* 46:3:379-395.
- Klima, R.L., Pieters, C.M., Boardman, J.W., Green, R.O., Head, J.W., Isaacson, P.J., Mustard, J.F., Nettles, J.W., Petro, N.E., Staid, M.I. and Sunshine, J.M., (2011b). New insights into lunar petrology: Distribution and composition of prominent low- Ca pyroxene exposures as observed by the Moon Mineralogy Mapper (M3). *Journal of Geophysical Research: Planets*, 116(E6).
- Kring, D. A., P. J. McGovern, R. W. K. Potter, G. S. Collins, M. L. Grange, and A. A. Nemchin (2015), Was an epoch of lunar magmatism triggered by the South Pole - Aitken Basin Impact?, *Early Solar System Impact Bombardment III*, abstract 3009.
- Melosh, H. J. (1989), *Impact Cratering: A Geologic Process*, Oxford Univ. Press, New York, NY.
- Morbidelli, A., Marchi, S., Bottke, W.F. and Kring, D.A., 2012. A sawtooth-like timeline for the first billion years of lunar bombardment. *Earth and Planetary Science Letters*, 355, pp.144-151.
- Moriarty III, D. P., C. M. Pieters, and P. J. Isaacson (2013), Compositional heterogeneity of central peaks within the South Pole – Aitken basin, *J. Geophys. Res*, 118, 2310-2322.

- Moriarty, D. P., & Pieters, C. M. (2016). Complexities in pyroxene compositions derived from absorption band centers: Examples from Apollo samples, HED meteorites, synthetic pure pyroxenes, and remote sensing data. *Meteoritics & Planetary Science*.
- Moriarty III, D. P. and C. M. Pieters (in preparation), South Pole - Aitken as a probe to the lunar interior.
- Morrison, D. A. (1998), Did a thick South Pole-Aitken Basin melt sheet differentiate to form cumulates?, *Lunar and Planet. Sci. Conf., XXIX*, #1657.
- Nakamura, R., et al. (2009), Ultramafic impact melt sheet beneath the South Pole–Aitken Basin on the Moon, *Geophys. Res. Lett.*, 36, L22202, doi:10.1029/2009GL040765.
- Noble S. K., Pieters C. M., Hiroi T., and Taylor L. A. 2006. Using the modified Gaussian model to extract quantitative data from lunar soils. *Journal of Geophysical Research* 111:E11009.
- Ohtake, M., Uemoto, K., Yokota, Y., Morota, T., Yamamoto, S., Nakamura, R., Haruyama, J., Iwata, T., Matsunaga, T. and Ishihara, Y., 2014. Geologic structure generated by large- impact basin formation observed at the South Pole- Aitken basin on the Moon. *Geophysical Research Letters*, 41(8), pp.2738-2745.
- Petro, N. E., S. C. Mest, and Y. Teich (2011), Geomorphic terrains and evidence for ancient volcanism within northeastern South Pole - Aitken Basin, *Geol. Soc. Am.*, Special Paper 477, pp. 129-140.
- Pierazzo, E, A. M. Vickery, and H. J. Melosh (1997), A reevaluation of impact melt production, *Icarus*, 127, 408-423.

- Pierazzo, E. and H. J. Melosh (2000), Melt production in oblique impacts, *Icarus*, 145, 252-261.
- Pieters, C. M., J. W. Head, L. Gaddis, B. Jolliff, and M. Duke (2001), Rock types of South Pole - Aitken basin and extent of basaltic volcanism, *J. Geophys. Res.*, 106, 28,001–28,022, doi:10.1029/2000JE001414.
- Pieters, C. M., J. Boardman, B. Buratti, A. Chatterjee, R. Clark, T. Glavich, R. Green, J. W. Head III, P. Isaacson, E. Malaret, T. McCord, J. Mustard, N. Petro, C. Runyon, M. Staid, J. Sunshine, L. Taylor, S. Tompkins, P. Varanasi, and M. White (2009), The Moon Mineralogy Mapper (M³) on Chandrayaan-1, *Current. Sci*, 96(4), 500-505.
- Potter, R. W. K., G. S. Collins, W. S. Kiefer, P. J. McGovern, and D. A. Kring (2012), Constraining the size of the South Pole-Aitken basin impact, *Icarus*, 220, 730-743, doi:10.1016/j.icarus.2012.05.032
- Prissel, T. C., J. L. Whitten, S. W. Parman, J. W. Head (in revision), On the Potential for Lunar Highlands Mg-suite Extrusive Volcanism & Implications Concerning Crustal Evolution, *Icarus*.
- Prissel, T. C., D. P. Moriarty III, C. M. Pieters, J.W. Head, and S.W. Parman (in preparation), Characterization and Identification of Low-FeO, High-Al₂O₃ Extrusive Deposits on the Moon by VNIR Reflectance Spectroscopy.
- Robinson M. S., Brylow S. M., Tschimmel M., Humm D., Lawrence S. J., Thomas P. C., Denevi B. W., Bowman-Cisneros E., Zerr J., Ravine M. A., Caplinger M. A., Ghaemi F. T., Schaffner J. A., Malin M. C., Mahanti P., Bartels A., Anderson J. Tran T. N., Eliason E. M., McEwen A. S., Turtle E., Jolliff B. L., and Hiesinger H.

2010. Lunar Reconnaissance Orbiter Camera (LROC) instrument overview. *Space Science Reviews* 150:81-124.
- Schultz, P. H. and D. A. Crawford (2011), Origin of nearside structural and geochemical anomalies on the Moon, *Geo. Soc. Am. Special Papers*, 477, 141-159, doi:10.1130/2011.2477(07).
- Smith, D. E., Zuber, M. T., Neumann, G. A., Lemoine, F. G., Mazarico, E., Torrence, M. H., and Aharonson, O. (2010). Initial observations from the lunar orbiter laser altimeter (LOLA). *Geophysical Research Letters*, 37(18).
- Spudis, P. D., R. A. Reisse, and J. J. Gillis (1994), Ancient multiring basins on the Moon revealed by Clementine laser altimetry, *Science*, 266, 1848–1851, doi:10.1126/science.266.5192.1848.
- Stuart-Alexander, D. E. (1978), Geologic map of the central far side of the Moon, *U.S. Geol. Survey*, Reston, VA.
- Taylor, L.A., A. Patchen, D.H. Taylor, J.G. Chambers, and D.S. McKay, 1996, X-ray digital imaging and petrography of lunar mare soils: Data input for remote sensing calibrations, *Icarus*, 124, 500-512.
- Taylor, L.A., Cahill, J.T., Patchen, A., Pieters, C., Morris, R.V., Keller, L.P., & McKay, D.S., 2001, Mineralogical and chemical characterization of lunar high-land regolith: lessons learned from mare soils. Lunar & Planetary Sci. Conf., LPI CD-ROM # 2196.
- Taylor, L.A., A. Patchen, J. Cahill, C.M. Pieters, R.V. Morris, L.P. Keller, and D.S. McKay, 2002, Mineral and glass characterization of Apollo 14 soils. Lunar &

- Planetary Sci. Conf. XXXIII, LPI CD-ROM #1302. Taylor, L.A., Pieters, C.M., Patchen, A.,
- Taylor, D.H., Morris, R.V., Keller, L.P., and McKay, D.S., 2003, Mineralogical Characterization of Lunar Highland Soils, Lunar & Planet. Sci. XXXIV, LPI CD-ROM #1774
- Tompkins, S., and C. M. Pieters (1999), Mineralogy of the lunar crust: Results from Clementine, *Meteorit. Planet. Sci.*, 34, 25–41, doi:10.1111/j.1945-5100.1999.tb01729.x.
- Vaughan, W. M., J. W. Head, L. Wilson, and P. C. Hess (2013), Geology and petrology of enormous volumes of impact melt on the Moon: A case study of the Orientale basin impact melt sea, *Icarus*, 223:749-765.
- Vaughan, W. M. and J. W. Head III (2014), Impact melt differentiation in the South Pole – Aitken basin: Some observations and speculations, *Planet. Space Sci.*, 91, 101-106.
- Warren, P.H., (1993), March. Limits on differentiation of melt sheets from basin-scale lunar impacts. In *Lunar and Planetary Science Conference* (Vol. 24, pp. 1481-1482).
- Warren, P.H., (1996). Constraining petrologic diversity among mare basalts. *Meteoritics & Planetary Science*, 31(1), pp.3-4.
- Warren, P. H., Claeys, P., & Cedillo-Pardo, E. (1996). Mega-impact melt petrology (Chicxulub, Sudbury, and the Moon): Effects of scale and other factors on potential for fractional crystallization and development of cumulates. *The Cretaceous-Tertiary event and other catastrophes in Earth history*, 105-124.

- Whitten, J. L., and J. W. Head III (2013), Detecting volcanic resurfacing of heavily cratered terrain: Flooding simulations on the Moon using Lunar Orbiter Laser Altimeter (LOLA) data, *Planet. Space Sci.*, 85, 24-37, doi: 10.1016/j.pss.2013.05.013.
- Whitten, J. L. and J. W. Head III (2014), Lunar cryptomaria: Physical characteristics, distribution, and implications for ancient volcanism, *Icarus*, 247, 150-171.
- Yingst, R. A. and J. W. Head III (1999), Geology of the mare deposits in South Pole – Aitken Basin as seen by Clementine UVVIS data, *J. Geophys. Res.*, 104(E8), 18957-18979.

Figures and Captions

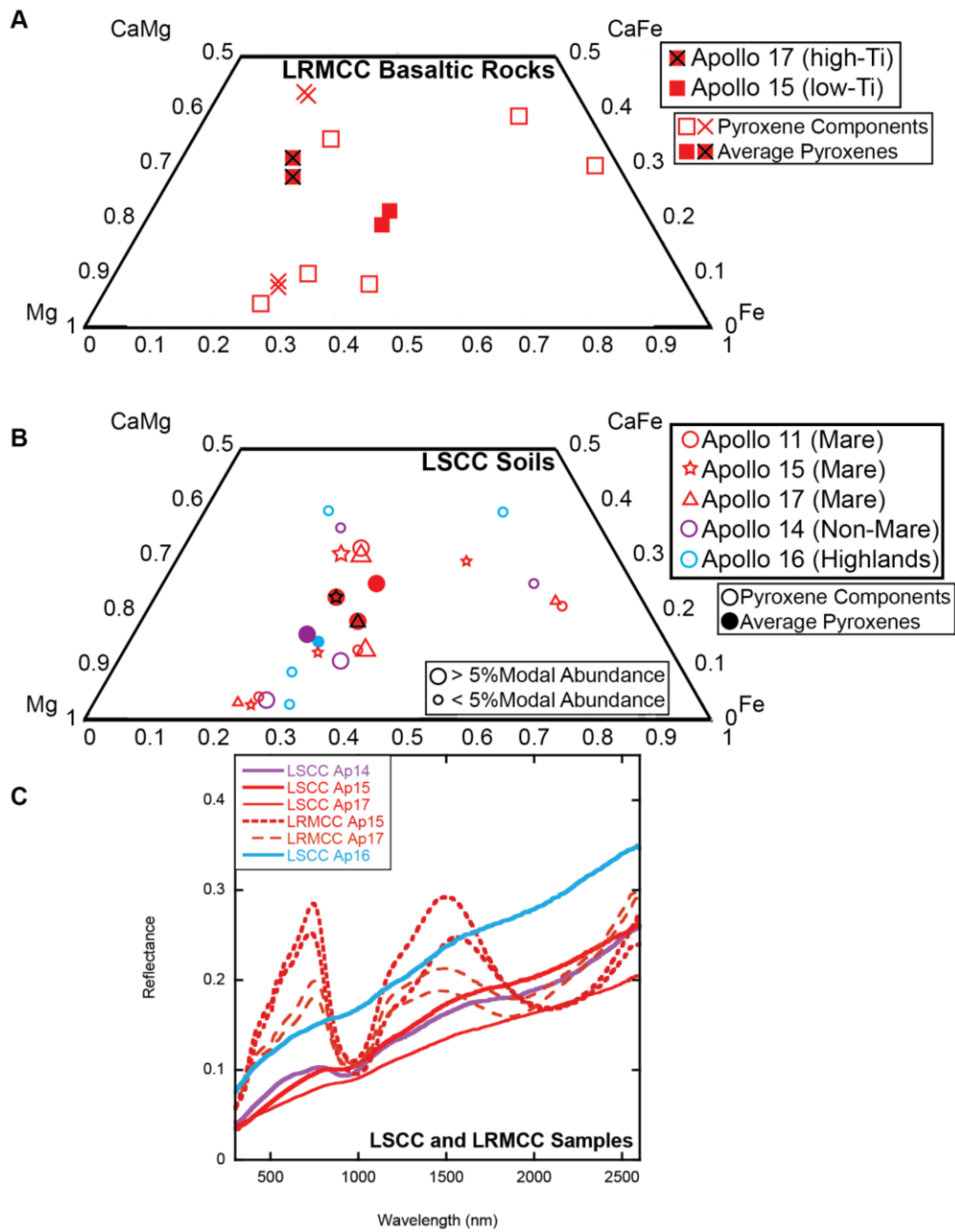


Fig. 1: Average pyroxene compositions and component pyroxene compositions for select (A) Lunar Rock and Mineral Characterization Consortium (LRMCC) [Isaacson *et al.*, 2011] basaltic rocks and (B) Lunar Soil Characterization Consortium (LSCC) [Taylor *et al.*, 1996; 2001; 2002; 2003; Noble *et al.*, 2006] highland and mare soils. For both

sample collections, average pyroxene compositions were calculated from the abundance and composition of individual pyroxene phases reported in the above references and hosted at <http://web.utk.edu/~pgi/data.html> (LSCC) and <http://www.planetary.brown.edu/LRMCC/> (LRMCC). LRMCC samples include two Apollo 17 high-Ti basaltic rocks (70017,541 and 70035,193) and two Apollo 15 low-Ti basaltic rocks (15058,248 and 15555,971). LSCC samples include Apollo 14 non-mare soil (14163), Apollo 16 highlands soil (67481), Apollo 11 high-Ti mare soil (10084), Apollo 15 low-Ti mare soil (15071), and Apollo 17 high-Ti mare soil (70181). For the LSCC soils, the 20-45 μm particle size separate is used here, since this fraction exhibits the highest pyroxene abundance. In (A) and (B), calculated average pyroxene compositions are distinguished from measurements of individual pyroxenes. The relative modal abundance of each pyroxene is indicated by symbol size in (B). In (C), LRMCC spectra are for the "coarse" grain size, and LSCC spectra are for the 20-45 μm particle size.

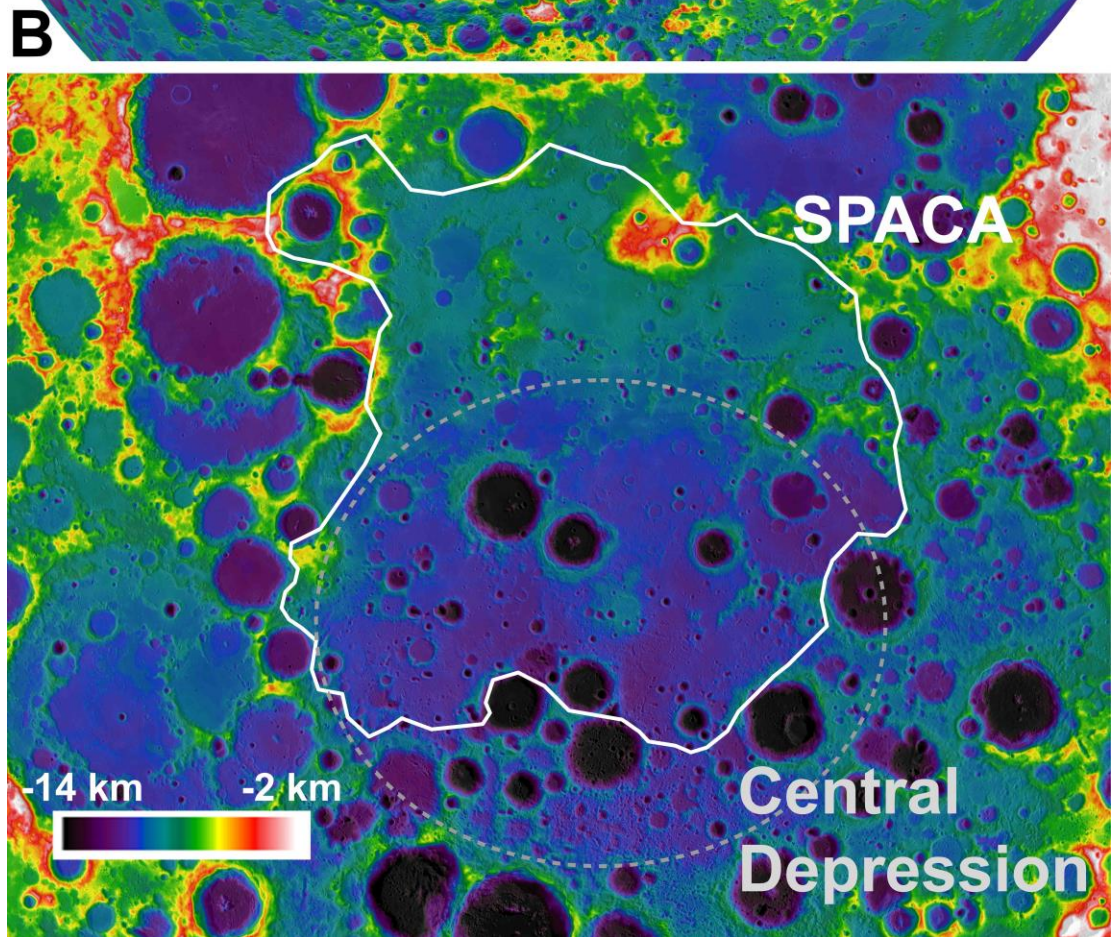
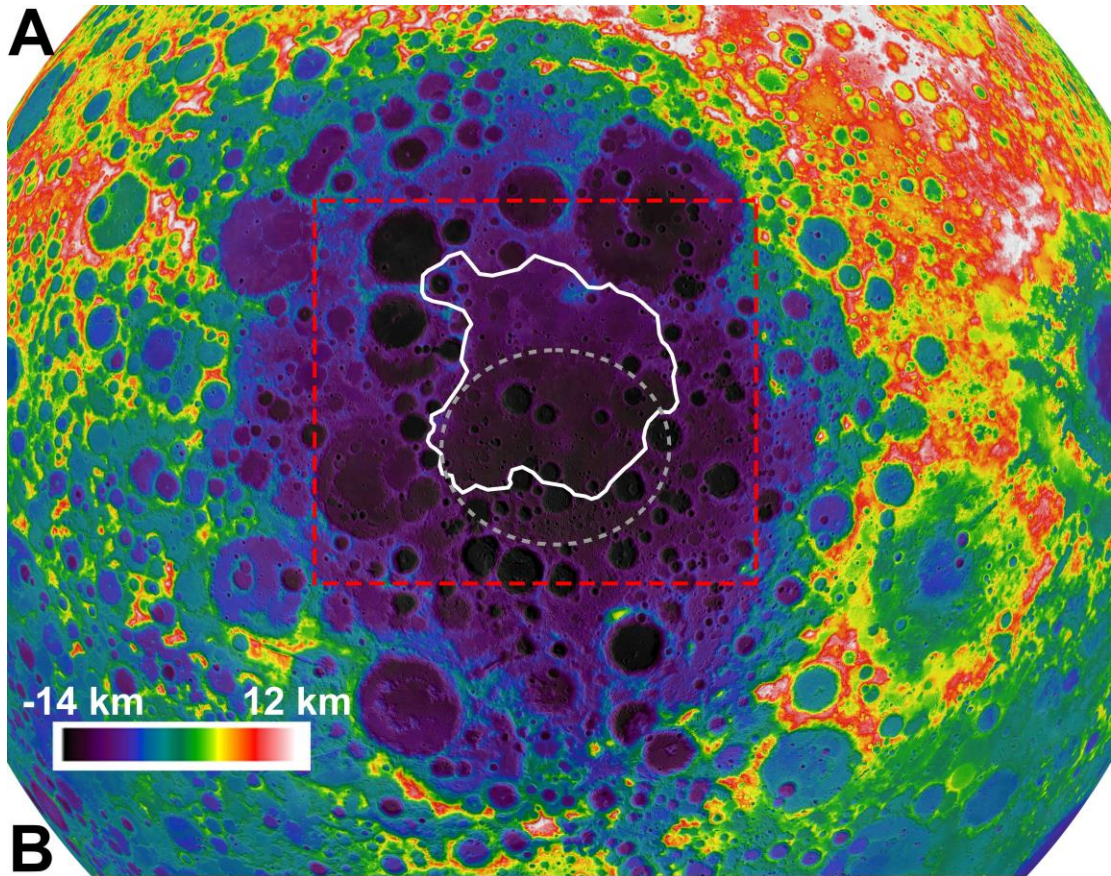


Fig. 2: (A) Lunar Orbiter Laser Altimeter (LOLA) [*Smith et al.*, 2010] topography draped over a Lunar Reconnaissance Orbiter Wide Angle Camera (WAC) [*Robinson et al.*, 2010] mosaic centered on SPA. The central depression (dashed grey) and SPACA (solid white) are outlined. The area indicated by the red dashed rectangle in (A) is shown in (B) with a different color scale to highlight local topography.

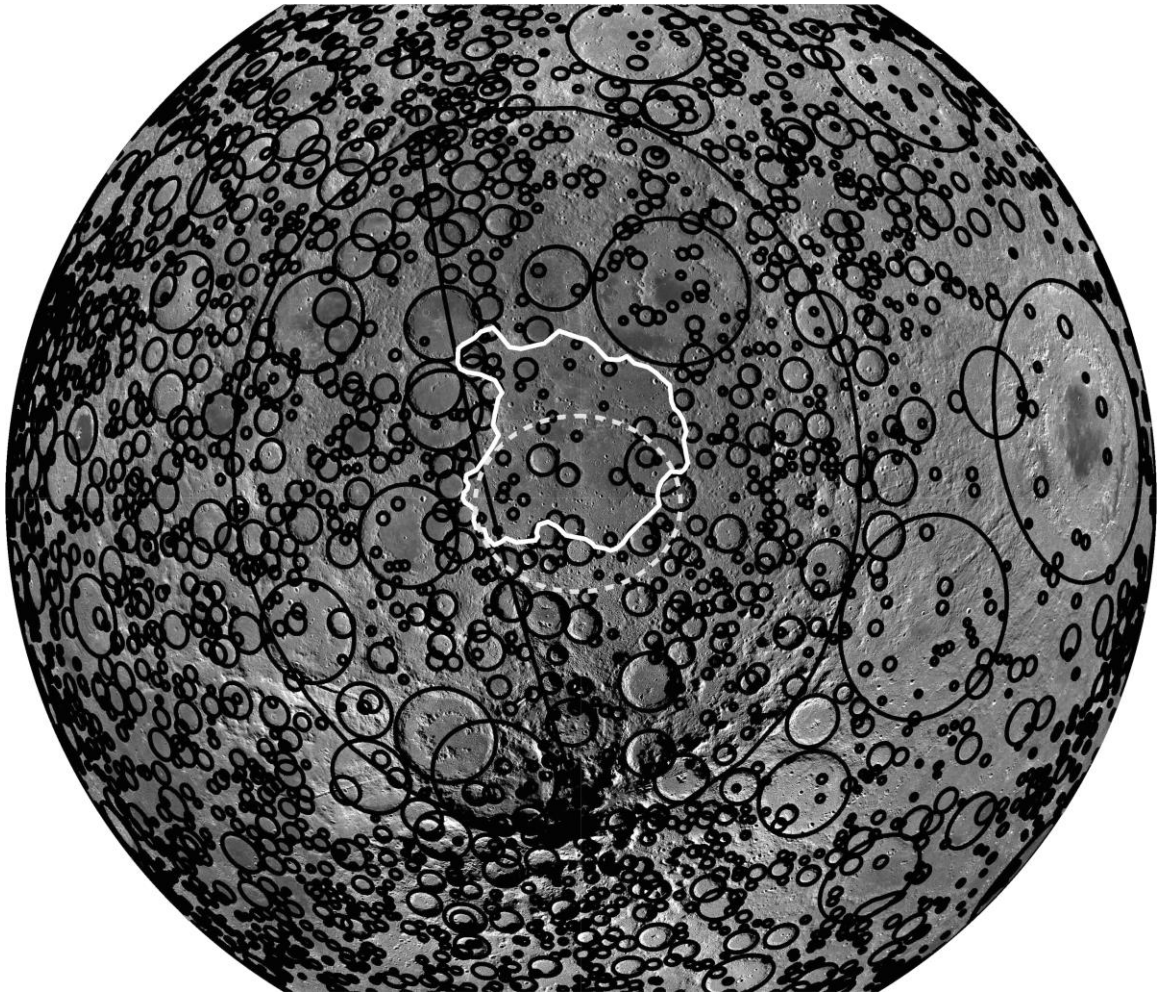


Fig. 3: The distribution of lunar craters greater than 20 km in diameter, as revealed by LOLA topography [Head *et al.*, 2010; Kadish *et al.*, 2011]. The basemap is a LROC WAC [Robinson *et al.*, 2010] mosaic. Central SPA clearly exhibits a lower crater density than the outer portions of the basins. The central depression (dashed grey) and SPACA (solid white) are outlined.

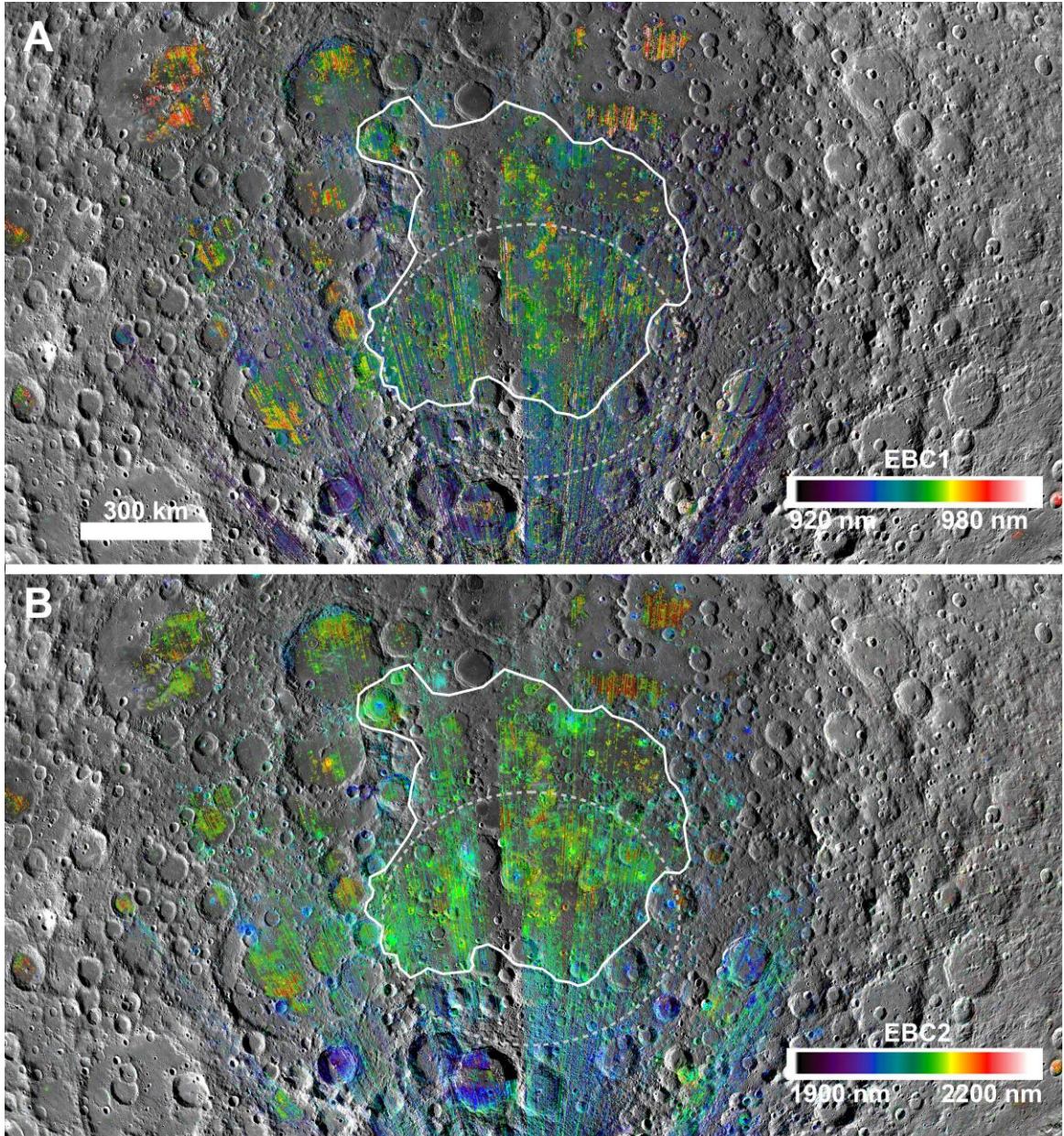


Fig. 4: (A) PLC-measured 1 μm band center for pixels with 1 μm band depths ≥ 0.1 , superimposed on an LROC WAC mosaic. (B) PLC-measured 2 μm band center for the same pixels superimposed on the WAC mosaic. Pixels with 1 μm band depths ≥ 0.15 are superposed to emphasize the freshest, most pristine exposures of mafic-bearing materials. The central depression (dashed grey) and SPACA (solid white) are outlined. In general,

short wavelengths indicate Mg-rich pyroxenes, while long wavelengths indicate Ca-bearing pyroxenes.

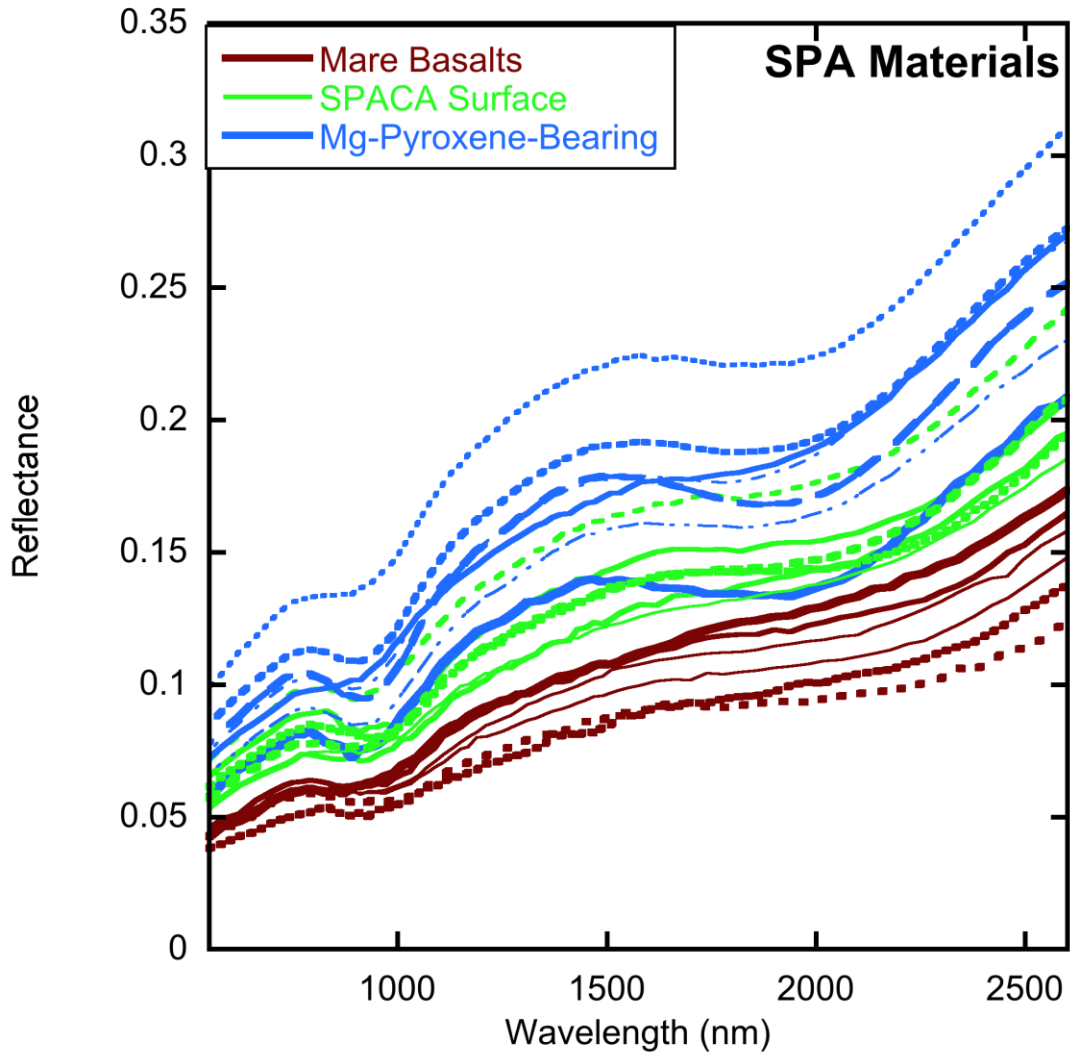


Fig. 5: Example spectra for SPA mare basalts, Mg-rich pyroxene-bearing materials, and SPACA materials. Mare basalt spectra are obtained from Crocco, Mare Ingenii, Apollo Basin, mare between Bose and Bose A, and a mare-filled crater chain between Bose D and Hendrix M. SPACA spectra are obtained from the walls and central peak of White, the walls of Bhabha, Mafic Mound, and a small crater in the irregular smooth terrain south of Apollo Basin. Mg-pyroxene-bearing spectra were obtained from the southeast

rim of Apollo Basin and the central peaks of Bhabha, Finsen, Birkeland, and Dryden Craters. All spectra are derived from Optical Period 2C1 data. Further information about the location of each spectrum is available in the Appendix.

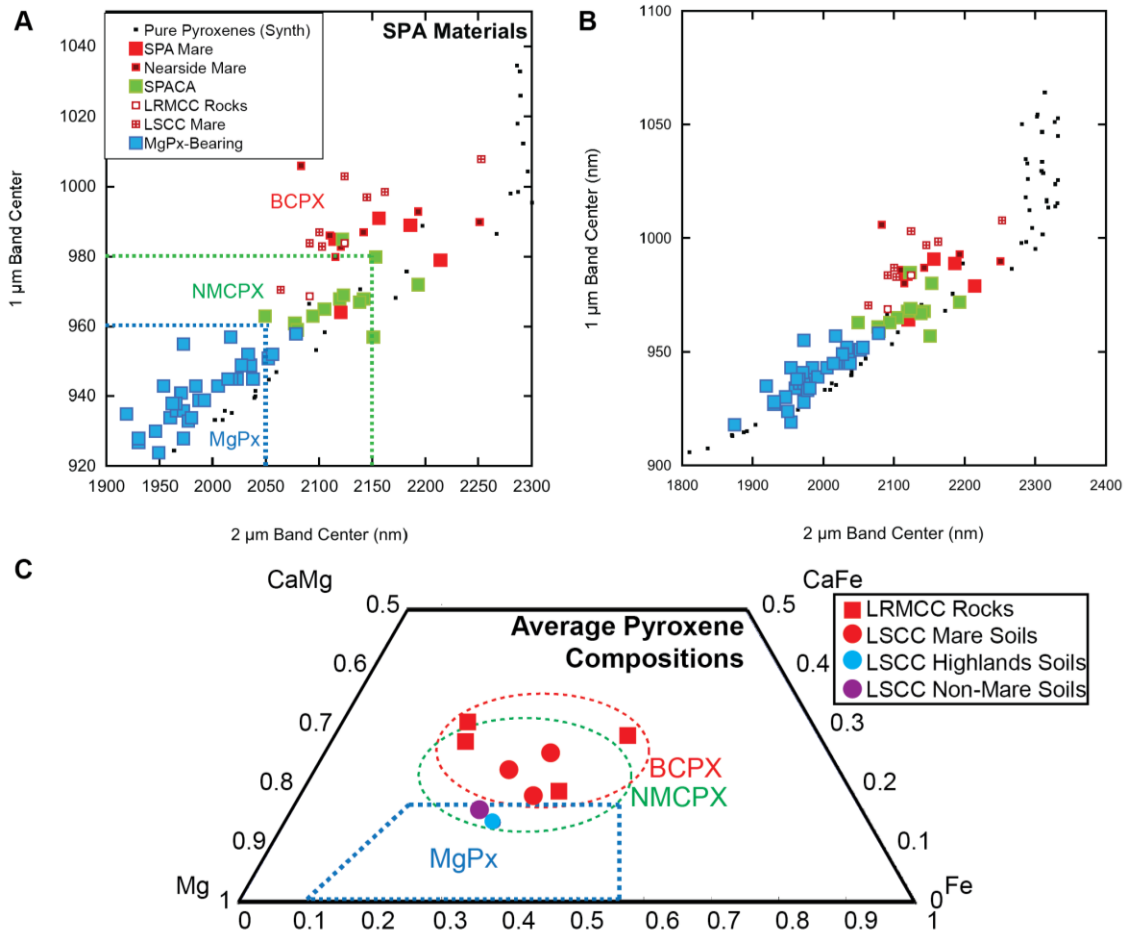


Fig. 6: (A) Plot of PLC-derived 1 μm band center vs. 2 μm band center values for SPA mare basalts, Mg-pyroxene-bearing materials, and SPACA materials. For comparison, laboratory-derived band center values for several LRMCC basaltic rocks (Apollo 15 low-Ti) and LSCC mare soils (Apollo 11 high-Ti, Apollo 15 low-Ti, and Apollo 17 high-Ti) are also provided [Noble *et al.*, 2006; Isaacson *et al.*, 2011; Chapter 1], except for the LRMCC Apollo 17 (which exhibits anomalous values due to ilmenite). To extend the comparison to nearside mare, M^3 -measured band center values for small craters near the Apollo 15 and Apollo 17 landing sites are also given. (B) Same as (A) with an expanded scale to show the full range of band center values for synthetic pure pyroxenes [Klima *et al.*, 2007; 2011]. (C) Laboratory-measured average pyroxene compositions for several

LRMCC and LSCC lunar rock and soil samples. Based on these average pyroxene compositions and relative spectral relationships, the range of average pyroxene compositions for Basaltic Clinopyroxene (BCPX), Non-Mare Clinopyroxene (NMCPX), and Mg-Pyroxene found across SPA are inferred.

CHAPTER 4: Pyroxene Abundance and Composition across the
South Pole - Aitken Basin

D. P. Moriarty III

Department of Earth, Environmental, and Planetary Sciences

Brown University | Providence, RI 02912

Abstract

Using Moon Mineralogy Mapper data, we identify and characterize materials exposed across the South Pole - Aitken Basin. Using these compositional distinctions, several distinct zones are identified. Outside of the central resurfaced region (the central **SPA Compositional Anomaly, or SPACA zone), non-mare mafic materials are dominated by Mg-rich, low-Ca pyroxenes (Mg-pyroxene). Immediately surrounding SPACA lies a fairly uniform annulus exhibiting a significant mafic component. Throughout this ~500 km wide annulus, Mg-pyroxene-bearing materials are exposed across a wide range of crater sizes, from small ~1 km craters to large ~500 km basins. The extent of this "Mg-Pyroxene Annulus" suggests the presence of a laterally extensive Mg-pyroxene-bearing zone tens of km thick, corresponding to remnants of the SPA transient cavity. Outside of the Mg-Pyroxene Annulus, localized Mg-pyroxene-bearing exposures are heterogeneously mixed with relatively feldspathic materials. This "Heterogeneous Annulus" represents proximal SPA ejecta mixed with a feldspathic crustal substrate. Given the massive, uniform character of Mg-pyroxene-bearing material in the Mg-Pyroxene Annulus and the presence of similar material interspersed in proximal ejecta, these Mg-pyroxene-bearing materials appear to represent relatively pristine materials that were excavated and exposed from beneath the feldspathic crust during the SPA-forming impact.**

1 Introduction

As the oldest and largest definitive impact structure on the Moon [*Stuart-Alexander, 1978; Spudis et al., 1994*], the South Pole – Aitken Basin (SPA) undoubtedly

shaped the course of lunar history. Through analysis of existing remote sensing data and future SPA sample return, a number of fundamental and diverse lunar science questions can be addressed. Relevant issues include the composition of the lower crust and/or upper mantle, the absolute ages of lunar impact basins and other features, and the nature of the large-scale impacts that forged our solar system.

For stratified targets such as the primary lunar crust, basin formation models can be used to evaluate specific predictions about the post-impact distribution of materials arising from processes such as excavation and impact melting [Melosh, 1989; Cintala and Grieve, 1994; Morrison *et al.*, 1998; Hammond *et al.*, 2009; Stewart, 2011; Potter *et al.*, 2012; Vaughan and Head, 2013; Hurwitz and Kring; 2014; Vaughan and Head; 2014]. Therefore, the observed spatial distribution of materials may place constraints on the basin formation process, as well as the pre-impact stratigraphy of the crust and upper mantle.

Materials excavated by the SPA impact are thought to be some of the deepest lunar materials available for study. In this paper, we investigate the character, distribution, and origin of materials excavated in the impact. In Chapter 5, we further consider the role of SPA as a probe to the lunar interior, interpreting these findings in the context of lunar and basin evolution models. Additionally, Chapters 3 and 5 discuss the role of impact melt and volcanic flooding in the evolution of the SPA interior.

2 Background

2.1 The Composition of SPA

In general, SPA materials are enriched in mafic content relative to the highlands feldspathic crust [e.g. Pieters *et al.*, 2001]. Across the basin, the most common mafic

component appears to be Mg-rich, low-Ca pyroxenes (Mg-pyroxene) [Tompkins and Pieters, 1999; Pieters et al., 2001; Cahill et al. 2009; Nakamura et al., 2009; Klima et al., 2011b; Moriarty et al., 2013]. The pervasive nature of these Mg-pyroxene-bearing materials across the basin suggests that they are a product of SPA formation, either as impact melt [e.g. Nakamura et al., 2009; Vaughan and Head, 2014] or excavated materials from the lower crust and/or upper mantle [Lucey et al., 1998; Blewett et al., 1999; Pieters et al., 2001; Klima et al., 2011; Ohtake et al., 2014]. In a ~700 km region near central SPA, surface materials exhibit a more Ca-rich pyroxene composition [Ohtake et al., 2014; Moriarty et al., in preparation]. Observations including a paucity of impact craters and the presence of multiple filled/buried/breached craters suggest that this central **SPA Compositional Anomaly** (SPACA) arose from volcanic flooding of central SPA, and therefore does not represent pristine materials excavated in the SPA-forming impact [Chapter 3]. The composition and origin of SPACA are considered in more detail in Chapter 3.

Additional mafic materials such as mare/cryptomare basalts [Yingst and Head, 1999; Pieters et al. 2001; Petro et al., 2011; Whitten and Head, 2014] and basin ejecta [e.g. Haskin et al., 2003; Petro and Pieters, 2008] are also present within SPA. Trace amounts of olivine have been observed near the SPA rim [e.g. Yamamoto et al., 2012]. However, these small exposures are closely associated with feldspathic materials and probably represent crustal products rather than excavated mantle cumulates.

Based on Clementine-derived maps of Fe abundance [Lucey et al., 1998], Jolliff et al. [2000] define two regions within SPA: an inner zone with higher Fe content (interpreted to represent excavated materials) and an outer zone with lower Fe content

(interpreted to represent proximal ejecta). In this analysis, we use Moon Mineralogy Mapper [Pieters *et al.*, 2009] (M³) spectral data to build on these general properties.

2.2 The Lunar Stratigraphy

Due to its vast ~2200 km diameter [Stuart-Alexander, 1978; Spudis *et al.*, 1994; Garrick-Bethell and Zuber, 2009], SPA is thought to have excavated and melted very deep-seated materials [e.g. Hammond *et al.*, 2009; Potter *et al.*, 2012]. Since the SPA-forming impact involved deep-seated materials, it is important to consider the stratigraphy of the lunar crust and mantle. The Moon's stratified nature (feldspathic crust and ultramafic mantle) is a result of an early, deep, and global magma ocean [Wood, 1970]. In the magma ocean scenario, early crystallizing species (first olivine, then pyroxene) are denser than the co-existing liquid and sink to form the mantle [e.g. Wood, 1970; Snyder *et al.*, 1992; Hess and Parmentier, 1995; Elkins-Tanton *et al.*, 2011]. After ~80% crystallization of the magma ocean, plagioclase grains begin to form [e.g. Snyder *et al.*, 1992; Elkins-Tanton *et al.*, 2011]. These grains are less dense than the coexisting liquid and therefore float to the top, forming an anorthositic flotation crust. At this point, the formerly molten portion of the mantle exhibits a stratigraphy following its crystallization sequence, i.e. an olivine-dominated base overlaid by pyroxenes and heavy, incompatible-rich materials [e.g. Snyder *et al.*, 1992; Hess and Parmentier, 1995; Elkins-Tanton *et al.*, 2011]. This is gravitationally unstable, as the underlying layer is less dense than the overlying layer [Hess and Parmentier, 1995]. For this reason, mantle overturn is expected to occur, transporting the less-dense olivine-bearing layer into the upper mantle [e.g. Hess and Parmentier, 1995; Elkins-Tanton *et al.*, 2011].

Several lines of evidence indicate that the lunar crust is inherently stratified (independent of the impact-driven layering of basin ejecta, soils, and megaregolith).

Deep-seated crustal materials excavated and uplifted by large highland craters and basins often excavate mafic materials, suggest a compositional gradient in the crust ranging from an anorthositic upper crust to a somewhat more mafic lower crust [*Reid et al.*, 1977; *Ryder and Wood*, 1977; *Bussey and Spudis*, 2000; *Tompkins and Pieters*, 1999; *Cahill et al.*, 2009; *Ohtake et al.*, 2009]. Two possible sources for the mafic material in the lower crust have been proposed: (1) coexisting liquid trapped between floating anorthosite grains during magma ocean crystallization [e.g. *Warren*, 1990; *Wieczorek and Zuber*, 2001], or (2) subsequent magmatic activity such as dykes and plutons [*Reid et al.*, 1977; *Ryder and Wood*, 1977; *Pieters and Wilhelms*, 1985; *Pieters and Tompkins*, 1999; *Shearer and Papike*; 2005]. Some of these lower-crustal mafic materials may correspond to a class of lunar samples known as the "Mg-suite," which are thought to have originated as unusual mantle melts that were emplaced near the base of the feldspathic crust soon after primary crustal formation [e.g. *Hess*, 1994; *Shearer and Papike*, 1999; *Elardo et al.*, 2011; *Shearer et al.*, 2015]. It is unclear if these Mg-suite materials represent a global phenomenon, or if they are localized within the Procellarum KREEP terrain.

The stratigraphic layers of the crust and mantle can serve as mineralogical markers for materials melted and excavated by SPA, offering clues into the dynamic nature of the impact event. In turn, SPA provides insight into the composition of the lower crust and upper mantle by excavating material from these deep-seated layers.

3 Data and Methods

Spectral variations across SPA are dominated by the abundance and composition of pyroxenes. Therefore, compositional properties of SPA materials can be effectively captured using measurements of the 1 μm and 2 μm band centers and depths. These

absorption bands are well-resolved in Moon Mineralogy Mapper (M^3) data [Pieters *et al.*, 2009]. For lunar pyroxenes, absorption band centers are closely linked to the Fe, Mg, and Ca content of the octahedral cation sites [Burns, 1993]. Mg-rich orthopyroxenes exhibit the shortest-wavelength band centers, while Ca-rich clinopyroxenes exhibit the longest-wavelength band centers [e.g. Klima *et al.*, 2007; 2011]. In mixtures, absorption band depths are correlated with pyroxene abundance, although other factors such as optical maturity also play a role.

For quantitative estimates of absorption band depths (EBD) and centers (EBC), we employ a fitting routine using **P**arabolas and a two-part **L**inear **C**ontinuum removal (PLC) [Moriarty and Pieters, 2016]. The PLC technique is a well-documented method for identifying and characterizing compositional diversity in natural pyroxene-bearing materials [Moriarty and Pieters, 2016]. Further explanation of compositional interpretations from PLC-derived band center values is provided by Moriarty and Pieters [2016; in preparation].

M^3 achieved almost full coverage of SPA, as shown in Fig. 1a. However, observing conditions (such as phase angle, detector temperature, spacecraft altitude, etc.) changed throughout the mission, affecting the behavior of the instrument [Boardman *et al.*, 2011]. To account for these changing conditions, M^3 data is divided into several Optical Periods (OPs). Several calibration steps were taken to produce a near-uniform dataset, but small differences in data quality persist between the OPs.

While very little of SPA remained un-imaged by M^3 , the coverage of the basin is divided between several OPs, as shown in Fig. 1. OP2C1 and OP2C2 offer the best

coverage of SPA, while additional coverage is also available in OP1A, OP1B, OP2A, and OP2C3.

To characterize regional trends in pyroxene composition and abundance, we perform PLC analysis on M³ global mosaics constructed by *Boardman et al.* [2011]. While the global mosaics have a lower spatial resolution than individual M³ images, they provide an excellent overview of compositional heterogeneity across SPA. Each mosaic contains only data from a single OP. PLC analyses were performed for all OPs.

Preceding PLC analyses, a ground truth correction [*Isaacson et al.*, 2013] was applied. For M³ data, two multiplicative ground truth correction factors were derived: one for when the detector was "hot;" another for when it was "cold" [*Isaacson et al.*, 2013]. All OPs but OP2C2 correspond to a single temperature state of the detector, and the appropriate correction was applied. OP2C2 straddles both "hot" and "cold" detector states, so no groundtruth correction was applied to the OP2C2 mosaic.

Using PLC fitting [*Moriarty and Pieters*, 2016], absorption band parameter maps (EBC1, EBC2, EBD1, and EBD2) were calculated for each OP covering SPA. EBD2 maps for each OP are presented in Fig. 2.

As mentioned above, the M³ instrument behaved somewhat differently in each optical period [*Boardman et al.*, 2011]. This results in slightly different band center and depth measurements for the same areas in different OPs. The differences in instrument behavior between OPs preclude precise, quantitative compositional analysis using multiple optical periods without additional corrections. However, relative relationships within single OPs are preserved and are useful in evaluating local and regional compositional trends.

For several reasons, OP2C1 data appear to be the best-suited optical period for analysis of SPA. OP2C1 offers the most complete coverage of central SPA. The other OPs with significant SPA coverage (OP2A, OP2C2) clearly exhibit effects from instrument artifacts in their EBC2 maps, including along-track striping and across-track calibration artifacts. The OP2C1 data does not suffer from these artifacts to the same degree. Additionally, OP2C2 data are not groundtruth-corrected. For the remainder of the paper, the analysis will be grounded in OP2C1 data and supplemented with data from other OPs where necessary.

4 Results: The Compositional Structure of SPA

4.1 Pyroxene Abundance from Diagnostic Absorption Band Depths

Fig. 3 provides a map of 2 μm band depths across the SPA region, using additional OPs to supplement OP2C1 data. This map offers a general overview of relative pyroxene abundance across SPA. From the EBD2 map, SPA materials can be divided into four major EBD classes. While assigning EBD classes is useful to guide the discussion, these classes are not intended to represent discrete compositions. SPA materials follow a continuous distribution of EBD values, and therefore the boundaries between EBD classes are not absolute. Additionally, several non-compositional factors such as optical maturity and grain size can affect EBD measurements. A summary of the general properties and distribution of each EBD class is as follows:

- I. Optically immature pyroxene-dominated materials. These materials appear red/yellow in the band depth maps, indicating band depths greater than ~ 0.1 . These exposures are mostly confined to central SPA and are associated with fresh craters and highly-sloped surfaces such as crater walls and central peaks. EBD Class I materials represent the freshest exposures of pyroxene-dominated materials in SPA.
- II. Optically mature pyroxene-dominated materials. These materials appear green in the band depth map, indicating band depths greater than ~ 0.05 . EBD Class II

materials are pervasive throughout the SPA interior and represent pyroxene-rich soils and older craters.

- III. Mixed mafic/feldspathic materials. These materials appear blue in the band depth maps, indicating weak absorption bands with depths less than ~ 0.5 . EBD Class III materials represent feldspathic materials with a small but nonzero mafic component.
- IV. Highly feldspathic materials. These materials appear purple/black in the band depth maps, indicating the absence of mafic absorption bands. EBD Class V materials are highly feldspathic in nature.

Example spectra for each EBD class are given in Fig. 4. By definition, the EBD classes are chosen based only on absorption band strength, which can be used as a proxy for pyroxene abundance (and optical maturity). Therefore, it is possible for materials with different mineralogies to fall into the same EBD class, as long as they are similar in pyroxene abundance and optical maturity. To further characterize the compositional diversity of materials across SPA, it is also necessary to consider absorption band center measurements.

4.2 Pyroxene Composition from Diagnostic Absorption Band Centers

As emphasized by *Moriarty and Pieters* [2016; Chapter 3], typical lunar surface materials are complex mixtures of multiple pyroxene and non-pyroxene components. Optically, these components interact in a complex, nonlinear manner to produce the composite 1 μm and 2 μm absorption bands observed in remote sensing data [*Moriarty and Pieters*, 2016; Chapter 3]. Therefore, the composite band center values are inherently non-unique in terms of specific pyroxene compositions. However, relative trends between composition and band center are observed and can be used with *a priori* geologic context to make compositional inferences about average pyroxene compositions. Here, we will follow the convention for average pyroxene compositions established in Chapter 3: (1) **Basaltic Clinopyroxene** (BCPX) for the most Ca,Fe-rich pyroxenes (typically observed in mare basalts), (2) **Non-mare Clinopyroxene** (NMCPX) for pyroxenes slightly lower in Ca,Fe, and (3) **Mg-Rich Pyroxene** (Mg-pyroxene).

An overview of band center variations across SPA is given in Fig. 5, derived from band center measurements discussed more fully in Chapter 3. In this figure, colorized EBC2 values for mafic-rich areas are superimposed over gray-scale topography. To reduce the effects of measurement artifacts, EBC values are only shown for pixels with 1 μm band depths greater than 0.1. In the map, BCPX materials with average pyroxene compositions rich in high-Ca pyroxene (resulting in long-wavelength EBC values) appear red/yellow, while Mg-pyroxene-dominated materials (associated with short-wavelength EBC values) appear blue/purple. NMCPX, which represent intermediate and mixed materials, appear green. Outside of the volcanically-resurfaced SPACA region [Chapter 3], EBC2 values for mare basalts are masked out in order to emphasize the compositional diversity of more non-mare SPA materials.

A schematic representation of the compositional diversity and stratigraphy in complex craters and basins across SPA is superposed in Fig. 5. To construct this schematic, a survey of large complex craters and basins in the SPA region was performed. An accounting of impact structures analyzed is given in Table 1. For each structure, representative absorption band centers and depths were derived. These values are represented schematically by overlaid symbols. Wall/rim materials are represented by colored circles, while central peak/ring materials are represented by colored triangles. The symbols are color-coded according to the band center color stretch given. Feldspathic materials are represented with white symbols. Where observed, compositional heterogeneity is accounted for by using multiple colors within a symbol. This schematic representation provides a regional overview of compositional trends.

Additionally, local stratigraphic relationships can be inferred by comparing central peak and wall materials, where possible.

Within the central SPA compositional anomaly (SPACA), crater walls typically exhibit relatively long wavelength absorption bands. Just outside of SPACA, crater walls and peaks are dominated by fairly short-wavelength absorption bands, suggesting a composition dominated by Mg-rich pyroxenes. Further from the basin center, feldspathic materials begin to dominate crater structures, although significant diversity in pyroxene abundance and composition is observed.

4.3 Distinct Compositional Zones within SPA

Although SPA exhibits complex compositional heterogeneity, the integrated analyses of topography, morphology, pyroxene abundance, and pyroxene composition provide a relatively clear picture of the compositional structure of the basin. Based on these observations, it is straightforward to define four general compositional zones related to the formation and evolution of SPA. The approximate boundaries of these zones are given in Figs. 3+5.

- **SPACA:** The "central SPA Compositional Anomaly" (SPACA) [Chapter 3] region is dominated by materials with relatively strong (EBD Class I-II), long-wavelength absorption bands, indicating an average pyroxene composition with significant Ca content (NMCPX). As noted in Chapter 3+5, these materials do not represent pristine products of the SPA-forming impact. Instead, they represent either impact melt or early magmatic resurfacing [Chapter 3; Chapter 5].
- **Mg-Pyroxene Annulus:** Immediately outside of the SPACA lies an annulus of material that exhibits significantly shorter average band center values, while band depth values remain uniformly elevated (EBD Class I-II). This suggests the presence of abundant Mg-pyroxene-bearing materials. The "Mg-rich Pyroxene Annulus" is up to ~500 km wide and exhibits relatively homogeneous pyroxene composition among craters of a variety of sizes, from small surficial craters (<1 km in diameter) to the walls, peaks, rings, floors, and ejecta of larger impact structures such as Lyman (84 km), Antoniadi (143 km), and the southern portion of Apollo Basin (538 km). A small region of more feldspathic materials is present in the northwest quadrant of the Mg-Pyroxene Annulus, excavated in the

walls and peaks of neighboring craters Alder (77 km), Leibnitz (245 km), and Von Kármán (180 km)

- **Heterogeneous Annulus:** Exterior to the Mg-Pyroxene Annulus, localized areas exhibiting mafic signatures (EBD Class I-II) are heterogeneously mixed with more feldspathic areas (EBD Class III-IV). Although some heterogeneity in mafic composition is observed, the dominant non-mare mafic component in this "Heterogeneous Annulus" exhibits short wavelength absorption bands similar to materials in the Mg-Pyroxene Annulus, as seen in Fig. 5. Gradients in both the frequency of EBD Class I-II exposures (frequent to less-frequent) and the mafic content of general soils (EBD Class III to EBD Class IV) are observed with distance from the Mg-Pyroxene Annulus (Figs. 3+5).
- **SPA Exterior:** The proportion of mafic material drops significantly outside of the Heterogeneous Annulus, whose outer boundary roughly corresponds to the topographic rim of SPA. Materials in the "SPA Exterior" exhibit nearly featureless spectra indicating a negligible mafic component. Of course, local areas such as Australe to the southwest exhibit significant mare basalt emplacements.

5 Origin of Mg-rich Pyroxene-Bearing Materials within SPA

The observed compositional structure of SPA is a direct result of specific

processes related to the formation and evolution of the basin. Considering the four zones identified in the previous section can provide insight into these processes.

Outside of the central SPA Compositional Anomaly (which exhibits clinopyroxene-bearing materials not representative of pristine SPA materials [Chapter 3]), the Mg-Pyroxene Annulus represents an expanse of relatively homogeneous material dominated by Mg-pyroxene. The uniform presence of these materials in the walls and peaks of several large craters and basins indicates that this component dominates to depths of at least several tens of km, and there is no evidence that this layer terminates anywhere in the near-surface. Due to the large lateral extent and vertical thickness of the Mg-Pyroxene Annulus, we conclude that this region represents pristine material exposed from a very thick, relatively homogeneous layer of the pre-impact target.

Impact models suggest that the transient cavity associated with the SPA impact was likely between ~500 and ~1150 km in diameter [Potter *et al.*, 2012]. Assuming a maximum excavation depth of ~10% of the transient cavity diameter [Melosh, 1989], the SPA-forming impact excavated material from up to ~50-100 km beneath the pre-impact surface, although the exact depth could be somewhat shallower for highly oblique impacts [e.g. Schultz, 1997; Schultz and Crawford, 2011]. Since the lunar feldspathic crust is estimated to be ~40 km thick on average (based on recent crustal thickness models using GRAIL gravity data [Wieczorek *et al.*, 2012]), the SPA-forming impact may have excavated completely through the feldspathic crust. Therefore, sub-crustal materials may be prominent in the walls and floor of the transient cavity. Although the transient cavity is by definition "transient," remnant portions of the structure likely comprise portions of the SPA interior. Outside of the central melt pool (which appears to be mostly confined to the SPACA zone [Chapter 3]), SPA basement materials comprising the remnant transient cavity are exposed, although the top km or so may be heavily mixed with subsequent basin ejecta [e.g. Haskin *et al.*, 2003; Petro and Pieters, 2008]. These regions are also expected to include significant volumes of impact melt and breccia, but outside of the central melt sheet these materials are unlikely to differentiate and therefore still represent the bulk composition of the excavated and melted material. Due to the thick, homogeneous nature of the Mg-Pyroxene Annulus, we interpret these Mg-pyroxene-bearing materials to represent relatively pristine materials excavated and exposed from beneath the feldspathic crust by the SPA-forming impact.

The Heterogeneous Annulus provides further evidence for the exposure of sub-crustal components. Impact models suggest that the deepest-seated ejecta in an impact

are typically emplaced close to the transient cavity rim [e.g. *Potter et al.*, 2012]. For SPA, most of the proximal ejecta is deposited within a region that then slumps and collapses inward during the collapse of the transient cavity (the "modification stage") [*Potter et al.*, 2012]. Therefore, the deepest excavated material largely remains within the observed topographic rim of SPA [*Potter et al.*, 2012]. This proximal ejecta initially lands exterior to the transient cavity on the feldspathic highlands. These substrate crustal materials would have undergone large-scale mixing with mafic SPA ejecta during two distinct phases of SPA formation: (1) massive, ballistic deposition of proximal ejecta, and (2) entrainment during faulting, slumping, and inward translation during collapse of the transient cavity.

Although it is apparent that mafic materials in the Mg-Pyroxene Annulus and Heterogeneous Annulus represent sub-crustal exposures, the petrological origin of these materials is uncertain. The two most straightforward possibilities are (1) exposure of the upper mantle [e.g. *Lucey et al.*, 1998; *Blewett et al.*, 1999; *Ohtake et al.*, 2014] and (2) exposure of lower-crustal materials enriched in a Mg-suite component [e.g. *Pieters et al.*, 2001; *Klima et al.*, 2011b]. These possibilities are explored further in Chapter 5.

As seen in Figs. 6-7, there is some compositional diversity in average pyroxene composition among Mg-pyroxene-bearing materials observed in SPA. The shortest-wavelength (most Mg-rich) materials are associated with several craters in the southwest region of SPA and the Apollo basin. The longer-wavelength (more Ca,Fe-rich) Mg-pyroxene-bearing materials are found in exposures such as Bhabha's central peak, which may sample the SPA melt sheet [*Nakamura et al.*, 2009; *Moriarty et al.*, 2013; *Moriarty*

and Pieters, in preparation]. Again, this compositional diversity is considered further in Chapter 5.

6 Summary

Through spatial compositional assessment using Moon Mineralogy Mapper data, there is evidence for extensive exposure of deep-seated materials in two distinct regions of SPA. The laterally extensive, vertically thick Mg-rich Pyroxene Annulus exhibits a relatively uniform composition dominated by Mg-rich pyroxenes. This annulus is interpreted to correspond to melt and breccia from a portion of the remnant SPA transient cavity. Since the transient cavity is expected to have excavated through the ~40 km feldspathic crust, this region is composed of predominantly sub-crustal materials. Exterior to the Mg-Pyroxene Annulus, the Heterogeneous Annulus, which exhibits localized areas of similar pyroxene-rich material, is interpreted to represent ejected deep-seated materials mixed with feldspathic crust during ejecta emplacement and basin modification. Since the Mg-rich pyroxene-bearing materials originate from beneath the feldspathic crust, it is reasonable to suggest that they represent upper mantle compositions or lower crustal Mg-suite lithologies. The central SPA Compositional Anomaly has been affected by impact melt and/or volcanic flooding, and is therefore not likely to be representative of pristine excavated materials from the crust or mantle. The four zones identified across SPA are useful to guide future science and exploration. The petrologic origin and stratigraphy of these zones is further discussed in Chapter 5.

7 Acknowledgements

Support of this research through NASA LASER (NNX12AI96G) and SSERVI (NNA14AB01A) is gratefully acknowledged. Discussions with Jim Head were helpful in guiding our interpretations.

8 References

- Blewett, D.T., Taylor, G.J., Lucey, P.G., Hawke, B.R. and Gillis, J., (1999), High-resolution, quantitative remote sensing of South Pole-Aitken Basin. In *Lunar and Planetary Science Conference* (Vol. 30, p. 1438).
- Boardman, J.W., Pieters, C.M., Green, R.O., Lundeen, S.R., Varanasi, P., Nettles, J., Petro, N., Isaacson, P., Besse, S. and Taylor, L.A., 2011. Measuring moonlight: An overview of the spatial properties, lunar coverage, selenolocation, and related Level 1B products of the Moon Mineralogy Mapper. *Journal of Geophysical Research: Planets* (1991–2012), 116(E6).
- Bussey, D. B. J. and P. D. Spudis (2000), Compositional studies of the Orientale, Humorum, Nectaris, and Crisium lunar basins, *J. Geophys. Res.*, 105, 4235-4243.
- Burns R. G. 1993. Mineralogical applications of crystal field theory, 2nd ed. Cambridge, UK: Cambridge University Press. 551.
- Cahill, J. T. S., P. G. Lucey, and M. A. Wieczorek (2009), Compositional variations of the lunar crust: Results from radiative transfer modeling of central peak spectra, *J. Geophys. Res.*, 114, E09001, doi:10.1029/2008JE003282.
- Cintala, M. J. and R. A. F. Grieve (1994), The effects of differential scaling of impact melt and crater dimensions on lunar and terrestrial craters: Some brief examples,

Large Meteorit. Impacts and Planet. Evolution, Geol. Soc. Amer. Spec. Pap. 293,
Boulder, CO.

Elardo, S.M., Draper, D.S. and Shearer, C.K., (2011), Lunar Magma Ocean
crystallization revisited: Bulk composition, early cumulate mineralogy, and the
source regions of the highlands Mg-suite. *Geochimica et Cosmochimica
Acta*, 75(11), pp.3024-3045.

Elkins-Tanton, L. T., S. Burgess, and Q. Yin (2011), The lunar magma ocean:
Reconciling the solidification process with lunar petrology and geochronology.
Earth and Planet. Sci. Lett., 304, 326-336.

Hammond, N. P., F. Nimmo, and D. Korykansky (2009), Hydrocode modeling of the
South Pole Aitken Basin-forming impact, *Lunar and Planet. Sci. Conf, XL*,
#1455 Melosh, H. J. (1989), *Impact Cratering: A Geologic Process*, Oxford Univ.
Press, New York, NY.

Haskin, L. A., J. J. Gillis, B. L. Jolliff, and R. L. Korotev (2003), Regolith in the South
Pole - Aitken Basin is mainly indigenous material, *Lunar and Planet. Sci.*,
XXXIV, #1434.

Hess, P.C., 1994. Petrogenesis of lunar troctolites. *Journal of Geophysical Research:
Planets*, 99(E9), pp.19083-19093.

Hess, P. C. and E. M. Parmentier (1995), A model for the thermal and chemical evolution
of the Moon's interior: Implications for the onset of mare volcanism, *Earth
Planet. Sci. Lett.*, 134, 501-514, doi:10.1016/0012-821X(95)00138-3.

- Hurwitz, D. M. and D. A. Kring (2014), Differentiation of the South Pole – Aitken basin impact melt sheet: Implications for lunar exploration, *J. Geophys. Res.*, 119:1110-1113.
- Isaacson, P. J., Petro, N. E., Pieters, C. M., Besse, S., Boardman, J. W., Clark, R. N., and Taylor, L. A. (2013), Development, importance, and effect of a ground truth correction for the Moon Mineralogy Mapper reflectance data set, *J. Geophys. Res.* 118:3:369-381.
- Jolliff, B. L., Gillis, J. J., Haskin, L. A., Korotev, R. L., & Wieczorek, M. A. (2000). Major lunar crustal terranes: Surface expressions and crust- mantle origins. *Journal of Geophysical Research: Planets (1991–2012)*, 105(E2), 4197-4216.
- Klima R. L., Pieters C. M., and Dyar M. D. 2007. Spectroscopy of synthetic Mg-Fe pyroxenes I: Spin-allowed and spin-forbidden crystal field bands in the visible and near-infrared. *Meteoritics and Planetary Science* 42:2:235-253.
- Klima R. L., Dyar M. D., and Pieters C. M. 2011a. Near-infrared spectra of clinopyroxenes: Effects of calcium content and crystal structure. *Meteoritics and Planetary Science* 46:3:379-395.
- Klima, R.L., Pieters, C.M., Boardman, J.W., Green, R.O., Head, J.W., Isaacson, P.J., Mustard, J.F., Nettles, J.W., Petro, N.E., Staid, M.I. and Sunshine, J.M., (2011b). New insights into lunar petrology: Distribution and composition of prominent low- Ca pyroxene exposures as observed by the Moon Mineralogy Mapper (M3). *Journal of Geophysical Research: Planets*, 116(E6).

- Lucey, P. G., G. J. Taylor, B. R. Hawke, and P. D. Spudis (1998), FeO and TiO₂ concentrations in the South Pole – Aitken Basin: Implications for mantle composition and basin formation, *J. Geophys. Res.*, *103*, 3701-3708, doi:10.1029/97JE03146.
- Moriarty III, D. M. and C. M. Pieters (in preparation), Impact melt and magmatic processes in central South Pole - Aitken Basin
- Moriarty III, D. P., C. M. Pieters, and P. J. Isaacson (2013), Compositional heterogeneity of central peaks within the South Pole – Aitken basin, *J. Geophys. Res.*, *118*, 2310-2322.
- Moriarty, D. P., & Pieters, C. M. (2016). Complexities in pyroxene compositions derived from absorption band centers: Examples from Apollo samples, HED meteorites, synthetic pure pyroxenes, and remote sensing data. *Meteoritics & Planetary Science*.
- Morrison, D. A. (1998), Did a thick South Pole-Aitken Basin melt sheet differentiate to form cumulates?, *Lunar and Planet. Sci. Conf.*, *XXIX*, #1657.
- Nakamura, R., et al. (2009), Ultramafic impact melt sheet beneath the South Pole–Aitken Basin on the Moon, *Geophys. Res. Lett.*, *36*, L22202, Pieters, C. M., J. W. Head, L. Gaddis, B. Jolliff, and M. Duke (2001), Rock types of South Pole - Aitken basin and extent of basaltic volcanism, *J. Geophys. Res.*, *106*, 28,001–28,022, doi:10.1029/2000JE001414.
- Ohtake, M., Uemoto, K., Yokota, Y., Morota, T., Yamamoto, S., Nakamura, R., Haruyama, J., Iwata, T., Matsunaga, T. and Ishihara, Y., 2014. Geologic structure

- generated by large- impact basin formation observed at the South Pole- Aitken basin on the Moon. *Geophysical Research Letters*, 41(8), pp.2738-2745.
- Petro, N. E. and C. M. Pieters (2008), The lunar-wide effects of basin ejecta distribution on the early megaregolith, *Met. and Planet. Sci.*, 43:8:1517-1529. Petro, N. E., S. C. Mest, and Y. Teich (2011), Geomorphic terrains and evidence for ancient volcanism within northeastern South Pole - Aitken Basin, *Geol. Soc. Am.*, Special Paper 477, pp. 129-140.
- Pieters, C. M. and D. E. Wilhelms (1985), Origin of olivine at Copernicus, *Proceedings of the Fifteenth Lunar Planet. Sci. Conf.*, 2, *J. Geophys. Res.*, C415-C420.
- Pieters, C. M., J. Boardman, B. Buratti, A. Chatterjee, R. Clark, T. Glavich, R. Green, J. W. Head III, P. Isaacson, E. Malaret, T. McCord, J. Mustard, N. Petro, C. Runyon, M. Staid, J. Sunshine, L. Taylor, S. Tompkins, P. Varanasi, and M. White (2009), The Moon Mineralogy Mapper (M³) on Chandrayaan-1, *Current. Sci*, 96(4), 500-505.
- Ohtake, M. et al. (2009), The global distribution of pure anorthosite on the Moon, *Nature*, 461, 236-240.
- Potter, R. W. K., G. S. Collins, W. S. Kiefer, P. J. McGovern, and D. A. Kring (2012), Constraining the size of the South Pole-Aitken basin impact, *Icarus*, 220, 730-743, doi:10.1016/j.icarus.2012.05.032
- Reid, A. M., A. R. Duncan, and S. H. Richardson (1977), In search of LKFM, *Proc. Lunar Sci. Conf.*, 8th, 2321-2338.

- Ryder, G. and J. A. Wood (1977), Serenitatis and Imbrium impact melts: Implications for large-scale layering in the lunar crust, *Proc. Lunar Planet. Sci. Conf.*, 8th, 655-668.
- Schultz, P.H., 1997, March. Forming the south-pole Aitken basin-The extreme games. In *Lunar and Planetary Science Conference* (Vol. 28, p. 1259).
- Schultz, P. H. and D. A. Crawford (2011), Origin of nearside structural and geochemical anomalies on the Moon, *Geo. Soc. Am. Special Papers*, 477, 141-159, doi:10.1130/2011.2477(07).
- Shearer, C.K. and Papike, J.J., (1999). Magmatic evolution of the Moon. *American Mineralogist*, 84, pp.1469-1494.
- Shearer, C. K. and J. J. Papike (2005), Early crustal building processes on the Moon: Models for the petrogenesis of the magnesian suite, *Geochimica et Cosmochimica Acta*, 69, 3445-3461.
- Snyder, G. A., L. A. Taylor, and C. Neal (1992), A chemical model for generating the sources of mare basalts: Combined equilibrium and fractional crystallization of the lunar magmasphere, *Geochim. Cosmochim. Acta*, 56, 3809-3823, doi:10.1016/0016-7037(92)90172-F.
- Shearer, C.K., Elardo, S.M., Petro, N.E., Borg, L.E. and McCubbin, F.M., (2015), Origin of the lunar highlands Mg-suite: An integrated petrology, geochemistry, chronology, and remote sensing perspective. *American Mineralogist*, 100(1), pp.294-325.

- Spudis, P. D., R. A. Reisse, and J. J. Gillis (1994), Ancient multiring basins on the Moon revealed by Clementine laser altimetry, *Science*, 266, 1848–1851, doi:10.1126/science.266.5192.1848.
- Stewart, S. T. (2011), Impact basin formation: The mantle excavation paradox resolved, *Lunar and Planet. Sci. Conf., XLII*, #1633
- Stuart-Alexander, D. E. (1978), Geologic map of the central far side of the Moon, *U.S. Geol. Survey*, Reston, VA.
- Tompkins, S., and C. M. Pieters (1999), Mineralogy of the lunar crust: Results from Clementine, *Meteorit. Planet. Sci.*, 34, 25–41, doi:10.1111/j.1945-5100.1999.tb01729.x.
- Vaughan, W. M., J. W. Head, L. Wilson, and P. C. Hess (2013), Geology and petrology of enormous volumes of impact melt on the Moon: A case study of the Orientale basin impact melt sea, *Icarus*, 223:749-765.
- Vaughan, W. M. and J. W. Head III (2014), Impact melt differentiation in the South Pole – Aitken basin: Some observations and speculations, *Planet. Space Sci.*, 91, 101-106.
- Warren, P. H. (1990), Lunar anorthosites and the magma-ocean plagioclase-flotation hypothesis: Importance of FeO enrichment in the parent magma, *Am. Mineral.*, 75, 46-58.
- Whitten, J. L. and J. W. Head III (2014), Lunar cryptomaria: Physical characteristics, distribution, and implications for ancient volcanism, *Icarus*, 247, 150-171.

- Wieczorek, M. A., and M. T. Zuber (2001), The composition and origin of the lunar crust: Constraints from central peaks and crustal thickness modeling, *Geophys. Res. Lett.*, 28, 4023 – 4026, doi:10.1029/2001GL012918.
- Wieczorek, M.A., Neumann, G.A., Nimmo, F., Kiefer, W.S., Taylor, G.J., Melosh, H.J., Phillips, R.J., Solomon, S.C., Andrews-Hanna, J.C., Asmar, S.W. and Konopliv, A.S., (2013), The crust of the Moon as seen by GRAIL. *Science*, 339(6120), pp.671-675.
- Wood, J. A., J. S. Dickey, U. B. Marvin, and B. N. Powell (1970), Lunar anorthosites and a geophysical model of the moon, *Proc. Apollo 11 Lun. Sci. Conf.*, 1, 965-988.
- Yamamoto, S., Nakamura, R., Matsunaga, T., Ogawa, Y., Ishihara, Y., Morota, T., Hirata, N., Ohtake, M., Hiroi, T., Yokota, Y. and Haruyama, J., (2012), Olivine-rich exposures in the South Pole-Aitken basin. *Icarus*, 218(1), pp.331-344.
- Yingst, R. A. and J. W. Head III (1999), Geology of the mare deposits in South Pole – Aitken Basin as seen by Clementine UVVIS data, *J. Geophys. Res.*, 104(E8), 18957-18979.

Table 1: Large Impact Structures in the SPA Region

<i>Crater</i>	<i>Latitude</i>	<i>Longitude</i>	<i>Diameter (km)</i>	<i>Stratigraphic Age¹</i>	<i>Morphology</i>	<i>M³ Coverage²</i>
Aitken	16.6° S	173.3° E	137.94	Upper Imbrian	Central Peak	OP2C1*, OP2C2
Alder	48.6° S	177.4° W	82	Lower Imbrian	Central Peak	OP1A*, OP2C1, OP2C2
Antoniadi	69.2° S	173.1° W	137.9	Upper Imbrian	Basin	OP2C1*, OP2C2
Apollo	36° S	152.1° W	524	Pre-Nectarian	Basin	OP2A*, OP2C1*, OP2C2 OP1B, OP2A, OP2C1, OP2C2, OP2C3
Ashbrook	81° S	109° W	157.7	Pre-Nectarian	Crater	OP2A, OP2C1, OP2C2
Baldet	53.3° S	151.96 W	55.76		Crater	OP2A, OP2C1, OP2C2
Barringer	28.2° S	150.5° E	66.89	Nectarian	Central Peak	OP2C1
Bellingsgauzen	60.7° S	161.8° W	63	Nectarian	Crater	OP2C1
Berlage	63.2° S	163.5° W	93.7	Pre-Nectarian	Crater	OP2C1, OP2C2
Bhabha	55.4° S	165.4° W	66.22	Nectarian	Central Peak	OP2C1
Birkeland	30.1° S	173.9° E	84.3	Eratosthenian	Central Peak	OP1A, OP2C2
Bok	20.3° S	171.6° W	43	Eratosthenian	Central Peak	OP2C1
Borman	39.1° S	148.3° E	46.3	Lower Imbrian	Central Peak	OP2A, OP2C2
Borman V	37.6° S	151.3° W	28		Central Peak	OP2A, OP2C1, OP2C2
Bose	53.9° S	169.4° W	95.3	Nectarian	Central Peak	OP2C1*
Boyle	53.3° S	177.9° E	54.6	Nectarian	Central Peak	OP2C1, OP2C2
Buffon	40.6° S	133.6° W	105.8	Nectarian	Central Peak	OP2A, OP2C3
Cabannes	61.1° S	170.3° W	81.3	Pre-Nectarian	Crater	OP2C1
Cabannes M	64.3° S	170.3° W	47.9		Central Peak	OP2C1
Cabannes Q	63.5° S	174.9° W	49.6	Nectarian	Central Peak	OP2C1, OP2C2
Chaffee	39.1° S	154.6° W	51.75	Nectarian	Central Peak	OP2A, OP2C1, OP2C2
Chaffee F	38.9° S	153° W	36	Nectarian	Central Peak	OP2A, OP2C1, OP2C2
Chebyshev	33.9° S	133.2° W	179	Nectarian	Central Peak	OP2A, OP2C3
Cori	50.5° S	152.9° W	67.2	Nectarian	Crater	OP2A, OP2C1, OP2C2
Crommelin	67.4° S	148.1° W	93.5	Pre-Nectarian	Central Peak	OP2A, OP2C1*, OP2C2
Crommelin C	65.5° S	144.2° W	39.1	Nectarian	Central Peak	OP2A, OP2C2
Crookes	10.4° S	165.1° W	49.7	Copernican	Central Peak	OP1A*, OP2C1
Davisson	38.0° S	175.0° W	92.5	Nectarian	Central Peak	OP2C1, OP2C2*
Dawson	67.1° S	135.1° W	44.3	Lower Imbrian	Central Peak	OP2A, OP2C3
De Forest	77° S	163° W	56.3	Upper Imbrian	Central Peak	OP2C1
De Vries	19.7° S	176.7° W	57.5	Upper Imbrian	Central Peak	OP2C1, OP2C2 OP1B, OP2A, OP2C1, OP2C2
Doerfel	69° S	108.4° W	68.6	Upper Imbrian	Central Peak	OP2A*, OP2C1, OP2C2
Dryden	33.2° S	156.2° W	53.4	Upper Imbrian	Central Peak	OP1B, OP2A, OP2C1, OP2C2, OP2C3
Drygalski	79.7° S	88.4° W	162.5	Pre-Nectarian	Central Peak	OP2A, OP2C2*
Eijkman	63.2° S	142.7° W	56.4	Nectarian	Central Peak	OP1A*, OP2C1, OP2C2
Finsen	42.4° S	178.0° W	73	Eratosthenian	Central Peak	OP2A, OP2C3
Fizeau	58.3° S	134.3° W	104	Upper Imbrian	Central Peak	OP2A, OP2C2
Grissom M	49.0° S	148.4° W	35	Lower Imbrian	Central Peak	OP2C1*
Hale	74.1° S	91.7° E	84.4	Upper Imbrian	Central Peak	OP1B, OP2A*, OP2C1*, OP2C2
Hausen	65° S	88° W	163	Eratosthenian	Central Peak	OP1A*, OP2C1*, OP2C2*
Hopmann	50.96° S	159.5° E	88.8	Nectarian	Central Peak	OP1A*, OP2C1, OP2C2
Ingenii	33.7° S	163.5° E	315	Pre-Nectarian	Basin	OP2A*, OP2C1, OP2C3*
Langmuir	36.0° S	129.0° W	91.5	Nectarian	Central Peak	
Leavitt	46° S	219.5° E	80	Nectarian	Central Peak	
Leavitt Z	42.7° S	139.5° W	63.6	Nectarian	Central Peak	
Leeuwenhoek	29.3° S	182.3° E	125	Nectarian	Central Peak	OP1A*, OP2C1, OP2C2
Leibnitz	38.6° S	179.1° E	236	Pre-Nectarian	Basin	OP1A*, OP2C1*, OP2C2
Lemaître	61.3° S	149.9° W	93.7	Nectarian	Crater	OP2A, OP2C21, OP2C2
Lemaître S	61.8° S	156.9° W	34.5	Nectarian	Central Peak	OP2A, OP2C1, OP2C2 OP1A, OP1B, OP2A, OP2C1, OP2C2, OP2C3
Lippmann	55.6° S	114.4° W	160	Pre-Nectarian	Crater	OP1A, OP1B, OP2A, OP2C1, OP2C2, OP2C3
Lippmann L	57.5° S	112.4° W	57.1		Central Peak	OP1A, OP1B, OP2A, OP2C1, OP2C2, OP2C3
Lippmann R	57.1° S	121.4° W	36.3		Central Peak	OP2C1, OP2C2, OP2C3
Lundmark	38.7° S	152.9° E	103.4	Pre-Nectarian	Central Peak	OP1A*, OP2C2*
Lundmark F	39.1° S	157.4° E	25.6		Central Peak	OP2C2
Lyman	64.9° S	162.5° E	83.3	Upper Imbrian	Central Peak	OP2C1*, OP2C2*

Maksutov	40.4° S	168.6° W	89	Upper Imbrian	Central Peak	
McNair	35.9° S	147.9° W	32		Central Peak	OP2A, OP2C2
Mendel	49° S	110° W	139.7	Pre-Nectarian	Central Peak	OP1A*, OP1B, OP2A, OP2C1, OP2C2
Mendel J	51.5° S	107.1° W	57.6	Lower Imbrian	Central Peak	OP2A, OP2C1, OP2C2
Minnaert	67.3° S	178.6° E	137.3	Pre-Nectarian	Central Peak	OP2C1, OP2C2
Numerov	70.6° S	162.4° W	108.9	Nectarian	Central Peak	OP2C1, OP2C2*
O'Day	30.6° S	157.5° E	72.7	Copernican	Central Peak	OP2C2
<i>Crater</i>	<i>Latitude</i>	<i>Longitude</i>	<i>Diameter (km)</i>	<i>Stratigraphic Age¹</i>	<i>Morphology</i>	<i>M³ Coverage²</i>
Oppenheimer	35.3° S	67° W	201	Nectarian	Crater	OP2C1*, OP2C2*
Oppenheimer V	32.1° S	173.1° W	29.3	Eratosthenian	Central Peak	OP1A*, OP2C1, OP2C2*
Oresme V	40.9° S	165.7° E	56.1	Upper Imbrian	Central Peak	OP2C1, OP2C2
Orlov	25.8° S	174.8° w	63.8	Nectarian	Central Peak	OP2C1*, OP2C2
Paracelsus	23.1° S	163.4° E	85.9	Pre-Nectarian	Central Peak	OP1A, OP2C1, OP2C2
Pauli	44.8° S	137.2° E	95.3	Lower Imbrian	Central Peak	OP2C1 OP1B, OP2A, OP2C1, OP2C2
Petzval	62.7° S	110.6° W	93	Nectarian	Central Peak	OP2C2
Planck	57.3° S	136.4° E	319.5	Pre-Nectarian	Basin	OP2A*, OP2C1*, OP2C2
Plummer	24.7° S	154.9° W	67.5	Nectarian	Central Peak	OP2A, OP2C1, OP2C2
Plummer M	26.3° S	154.7° W	38.7	Upper Imbrian	Central Peak	OP2A, OP2C1, OP2C2
Poincare	57.1° S	162.7° E	346	Pre-Nectarian	Basin	OP1A*, OP2C1, OP2C2
Prandtl	59.8° S	141.4° E	87.5	Nectarian	Central Peak	OP2C1
Ramsay	40.1° S	145.1° E	61.3	Nectarian	Central Peak	OP2C1
Rumford	28.8° S	169.7° W	60.8	Lower Imbrian	Central Peak	OP1A*
Rumford A	25.2° S	169° W	30		Central Peak	
Rumford T	28.5° S	172.2° W	111.7	Pre-Nectarian	Central Peak	OP1A*, OP2C1, OP2C2*
Schrodinger	74.5° S	133.4° E	316.4	Lower Imbrian	Basin	OP2C1, OP2C2*
Sierpinski	27° S	154.6° E	66.9	Nectarian	Central Peak	OP1B*, OP2C2
Sniadecki	22.4° S	168.8° W	41	Nectarian	Central Peak	
Stoney	55.5° S	156.6° W	47.8	Nectarian	Central Peak	OP2A, OP2C1, OP2C2
Unnamed "A"	81.1° S	165.8° W	135.8		Central Peak	OP2A*, OP2C1, OP2C2
Unnamed "B"	24.7° S	171.9° W	60.7		Central Peak	OP1A*, OP2C1 OP1A*, OP2C1*, OP2C2*
Unnamed "C"	60.3° S	172° E	95.1		Central Peak	OP1A*, OP2C1*, OP2C2*
Unnamed "D"	56.5° S	171.1° E	56		Central Peak	OP2C2*
Van de Graaf	27.6° S	171.9° E	245.5	Nectarian	Central Peak	OP2C1, OP2C2
Von Kármán	44.8° S	176.3° E	187	Pre-Nectarian	Central Peak	OP1A*, OP2C1*, OP2C2
Walker W	24.5° S	164° W	44		Central Peak	OP2C1
White	44.8° S	159.2° W	40	Upper Imbrian	Central Peak	OP2C1, OP2C2 OP2A, OP2C1*, OP2C2*, OP2C3
Zeeman	74.8° S	135.8° W	192.4	Nectarian	Central Peak	

¹Ages from *Wilhelms et al.*, 1987.

²Stars indicate optical periods with limited or partial coverage.

Figures and Captions

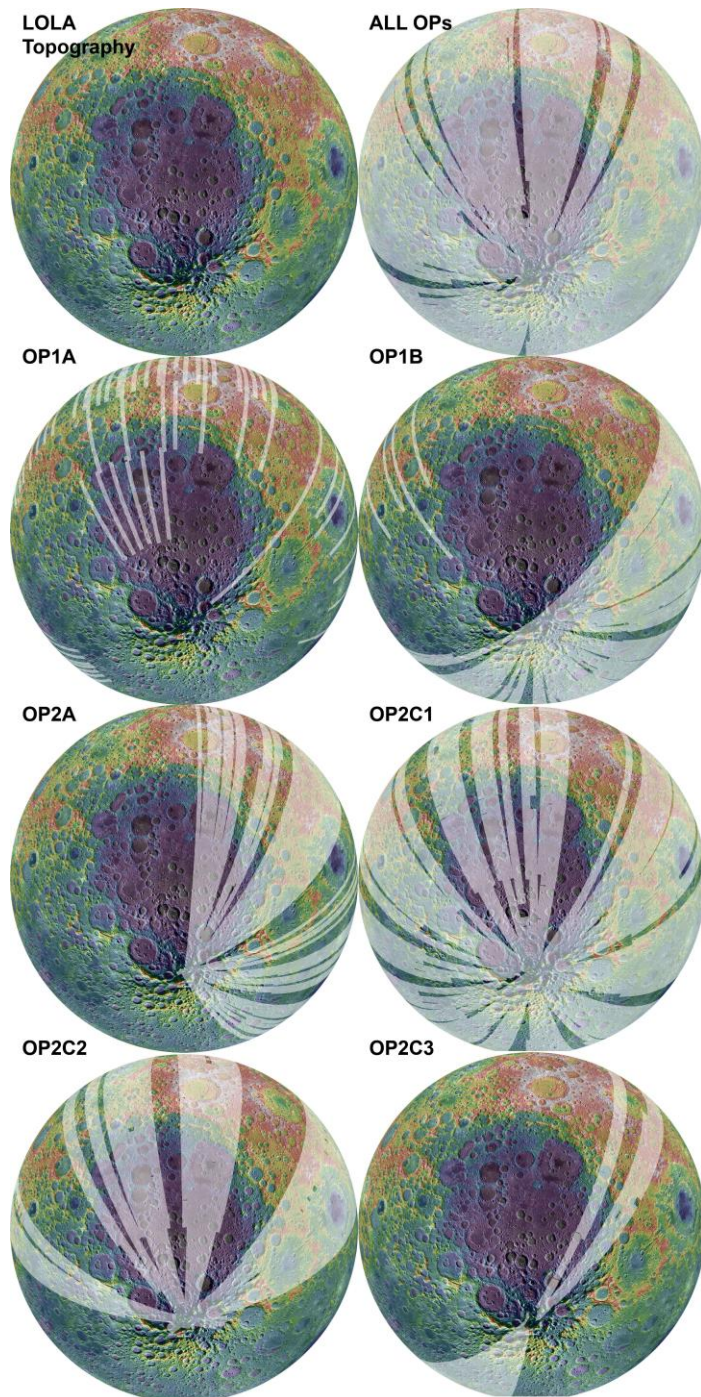


Fig. 1: A summary of the M³ coverage of SPA, superimposed on Lunar Orbiter Laser Altimeter (LOLA) [Smith *et al.*, 2010] topography. The SPA coverage in each optical period [Boardman *et al.*, 2011] is indicated by the overlaid white stripes.

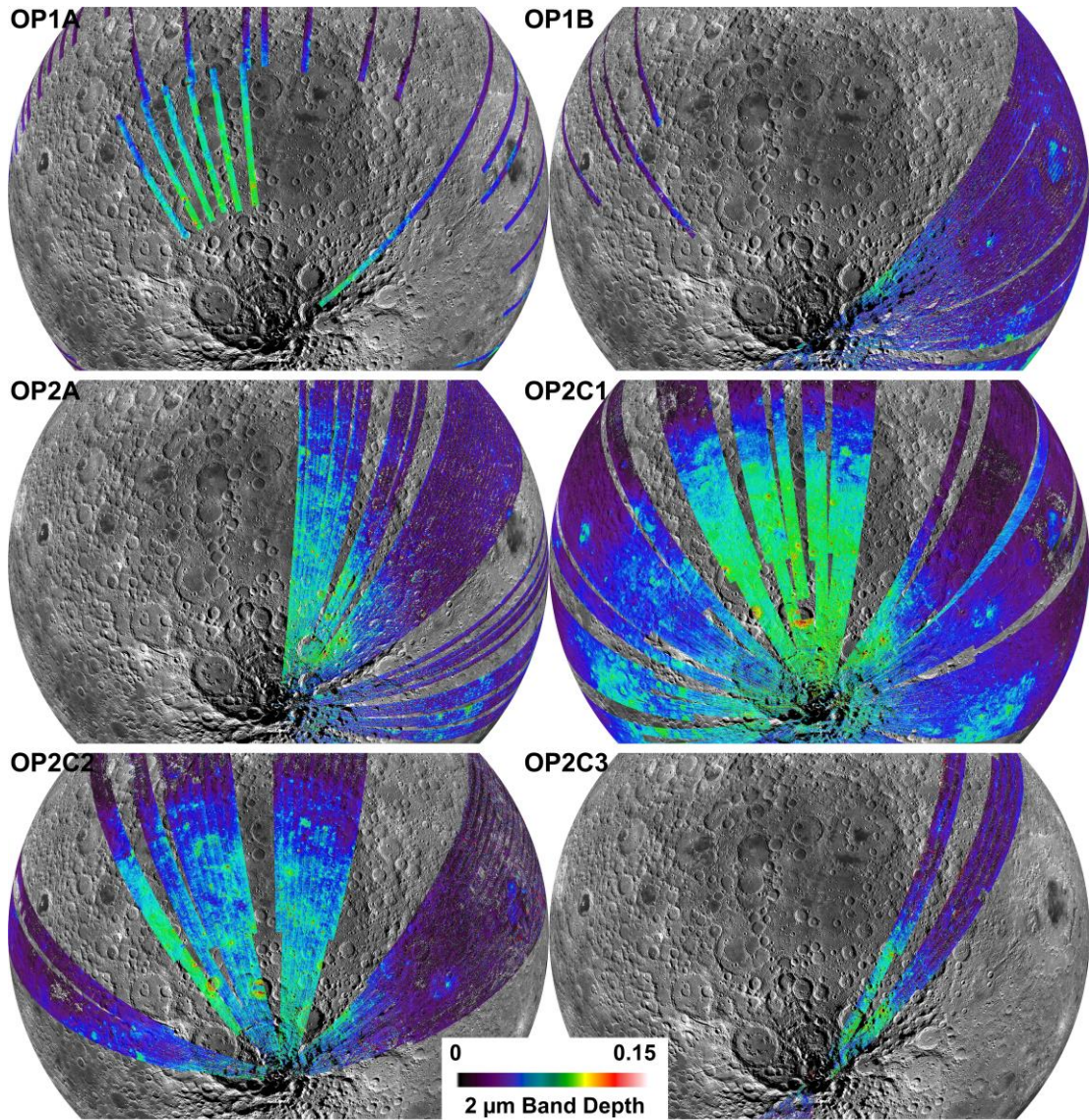


Fig. 2: PLC-derived 2 μm band depth maps of SPA as measured during each M³ optical period. Band depth maps are overlain on a Lunar Reconnaissance Orbiter Camera (LROC) Wide Angle Camera (WAC) [Robinson *et al.*, 2010] mosaic. Band depths are sensitive to pyroxene abundance.

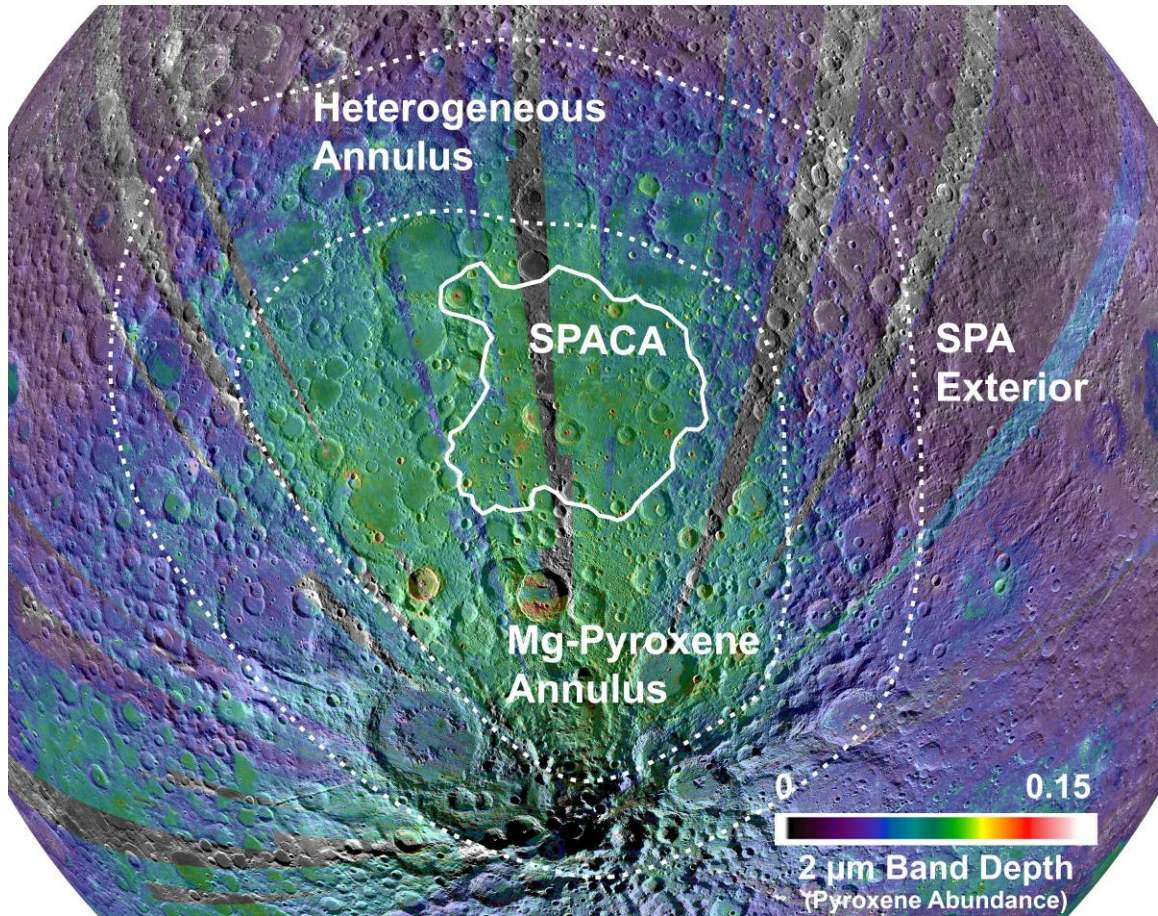


Fig. 3: A composite 2 μm band depth map for the SPA region incorporating data from all optical periods. Absorption band depths are correlated with pyroxene abundance. The approximate boundaries of the central SPA compositional anomaly (SPACA), Mg-Pyroxene Annulus, Heterogeneous Annulus, and SPA Exterior are given.

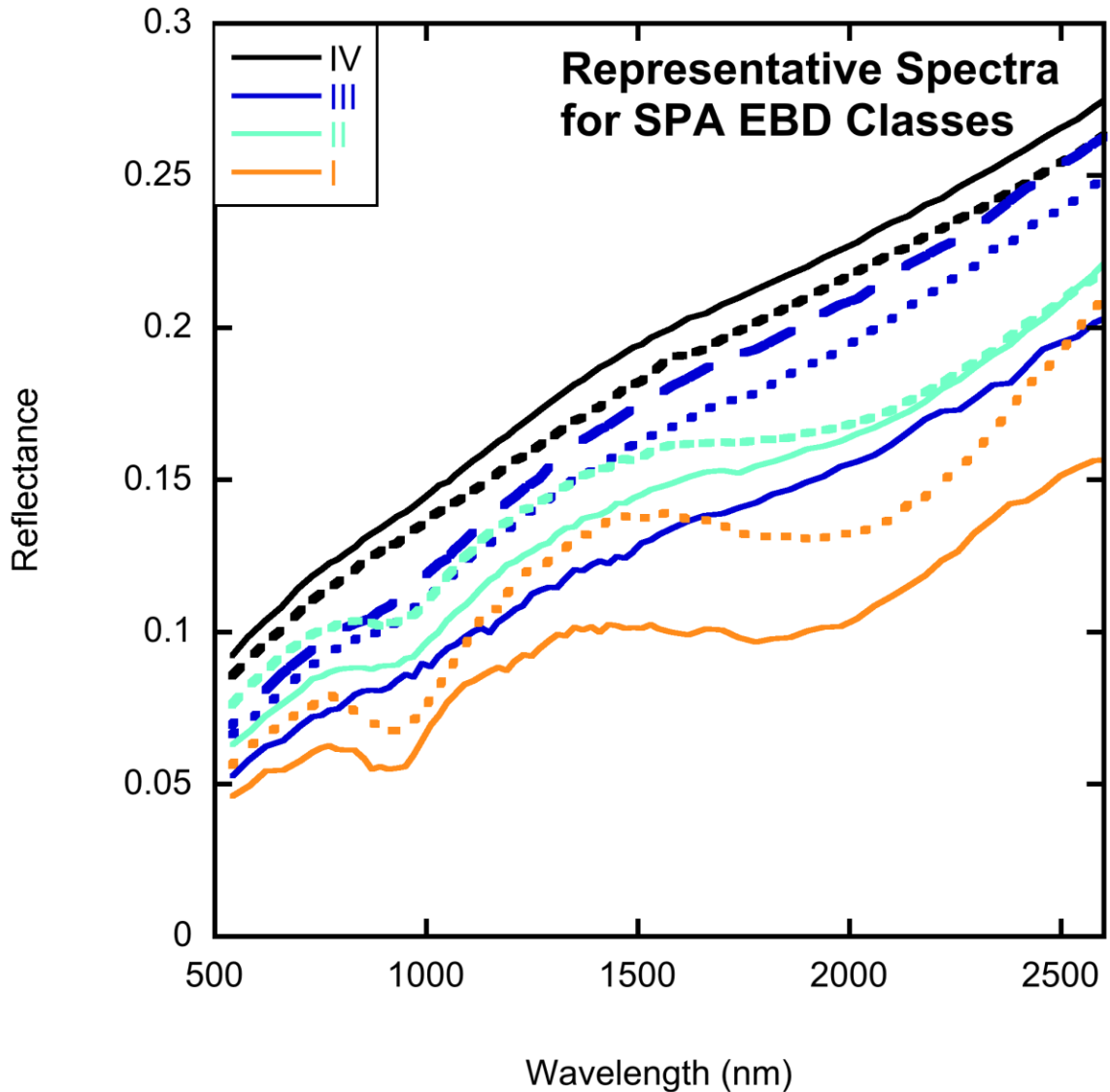


Fig. 4: Representative M^3 spectra for each Estimated Band Depth (EBD) class in SPA. EBD Class IV spectra were obtained from highlands craters in northwestern SPA Exterior. Class III spectra were obtained from the peak ring of Apollo Basin, the rim of Thomson Crater, and the rim of Alder Crater. Class II spectra were obtained from SPACA soils southwest of Apollo and Mg-rich Pyroxene Annulus soils southeast of Ingenii. Class I spectra were obtained from the central peaks of Lyman Crater and Bhabha Crater.

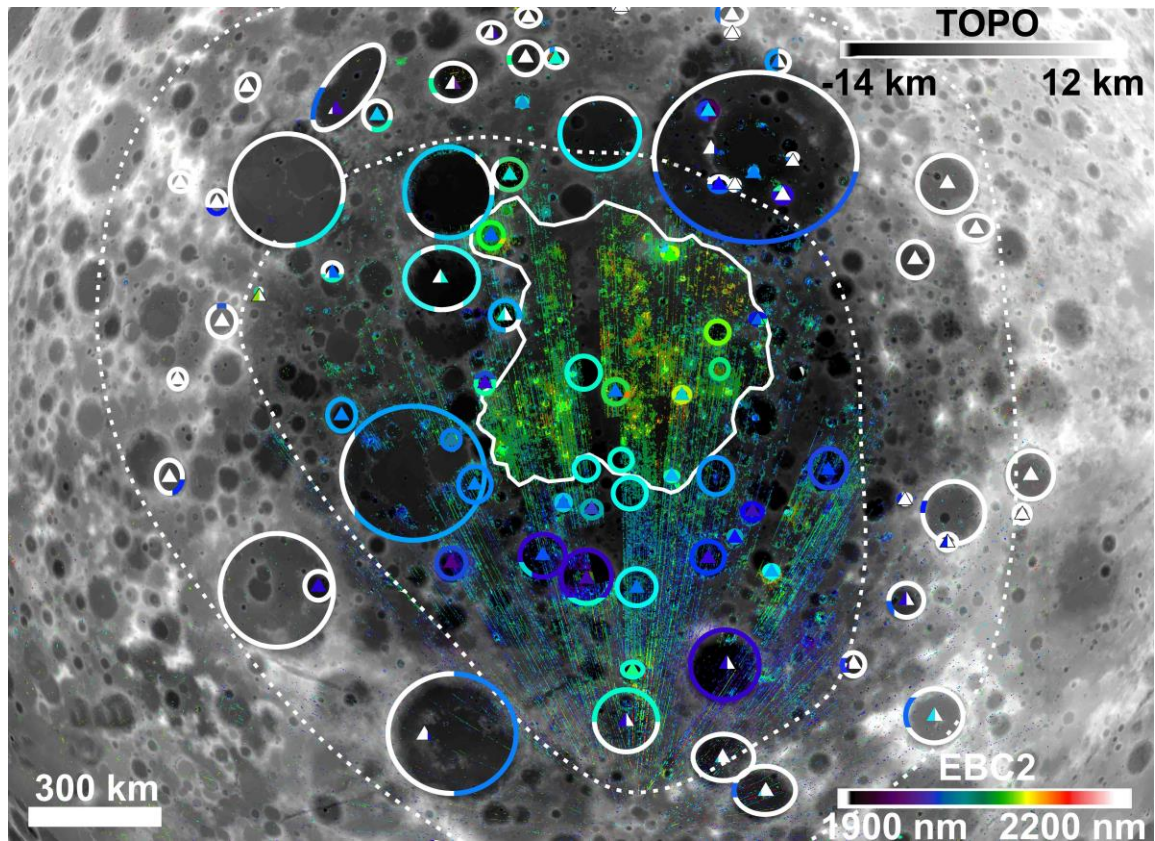


Fig. 5: PLC-derived 2 μm absorption band center (EBC2) and compositional inference overlaid on LOLA topography. To emphasize the most reliable band center measurements, band centers are only displayed for pixels with 1 μm band depths greater than 0.1. Superposed symbols (ellipses, triangles) highlight the compositional diversity inferred from the suite of large impact structures given in Table 1. In these symbols, non-white colors correspond to the dominant pyroxene compositions observed (blues/purples indicating Mg-pyroxenes, greens/reds indicating Ca,Fe-pyroxenes). White indicates the presence of feldspathic materials. Multiple colors are used where significant heterogeneity is observed. Ellipses correspond to crater rims and walls, while triangles correspond to central peaks of complex craters. The approximate extents of SPACA (solid), Mg-rich Pyroxene Annulus, Heterogeneous Annulus, and SPA Exterior (dashed) are given.

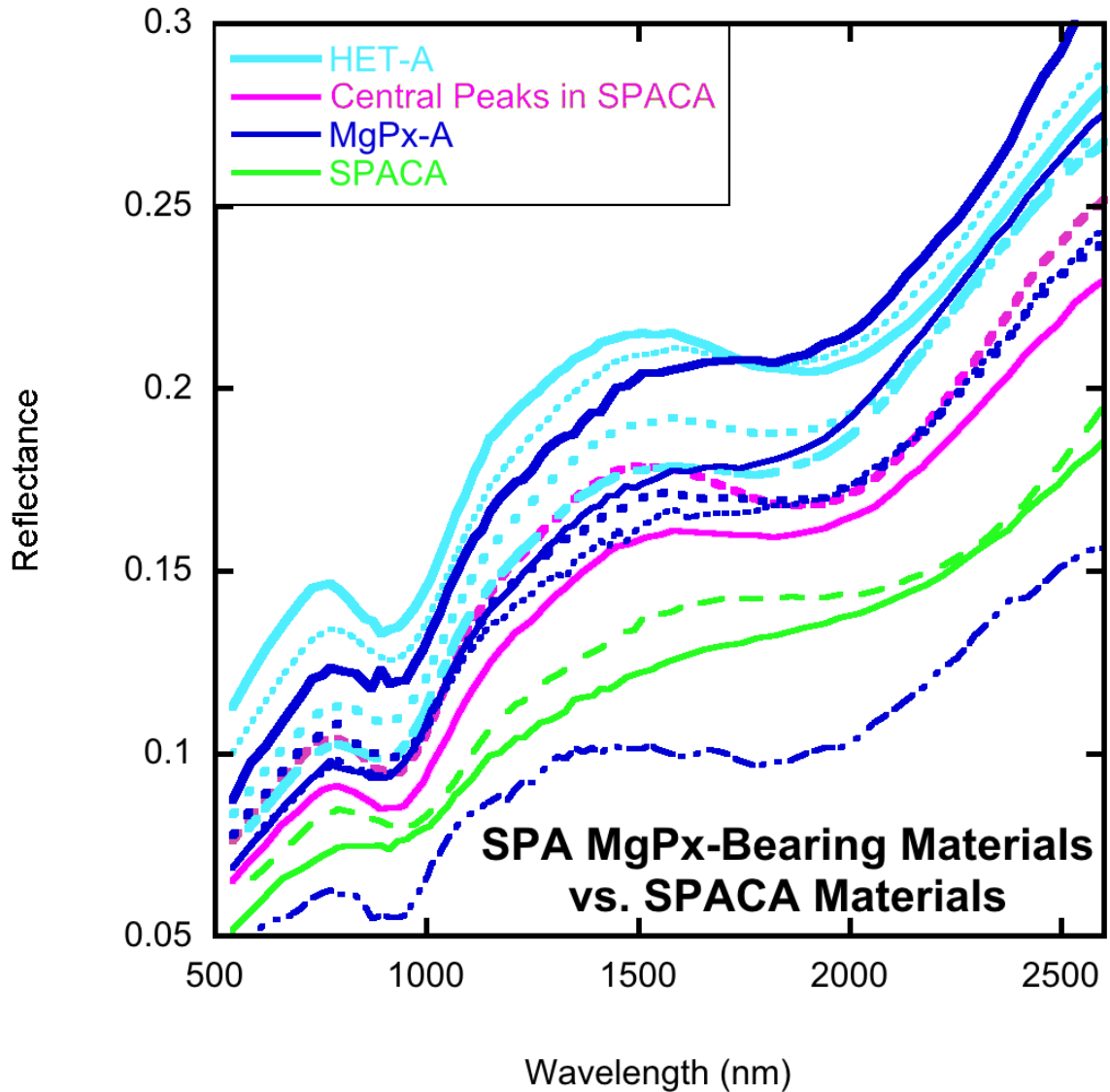


Fig. 6: Spectra for representative Mg-rich pyroxene-bearing materials from the Mg-pyroxene Annulus, Heterogeneous Annulus, and central peaks within SPACA. Spectra are 3x3 pixel average derived from full-resolution OP2C1 M³ global data. Spectra from central peaks within SPACA (which expose material from beneath the Ca,Fe-pyroxene-bearing SPACA surface deposit) were obtained from Bhabha Crater and Finsen Crater. Heterogeneous Annulus spectra were obtained the central peaks of Plummer Crater, Dryden Crater, Van de Graaf Crater, and the rim of Ingenii Basin. Mg-Pyroxene

Annulus spectra were obtained from the central peaks of Numerov Crater and Lyman Crater and the rims of Leibnitz Crater, Oppenheimer Crater and the Apollo Basin. For comparison, spectra of characteristic SPACA material were obtained from Mafic Mound and the walls of Bhabha Crater.

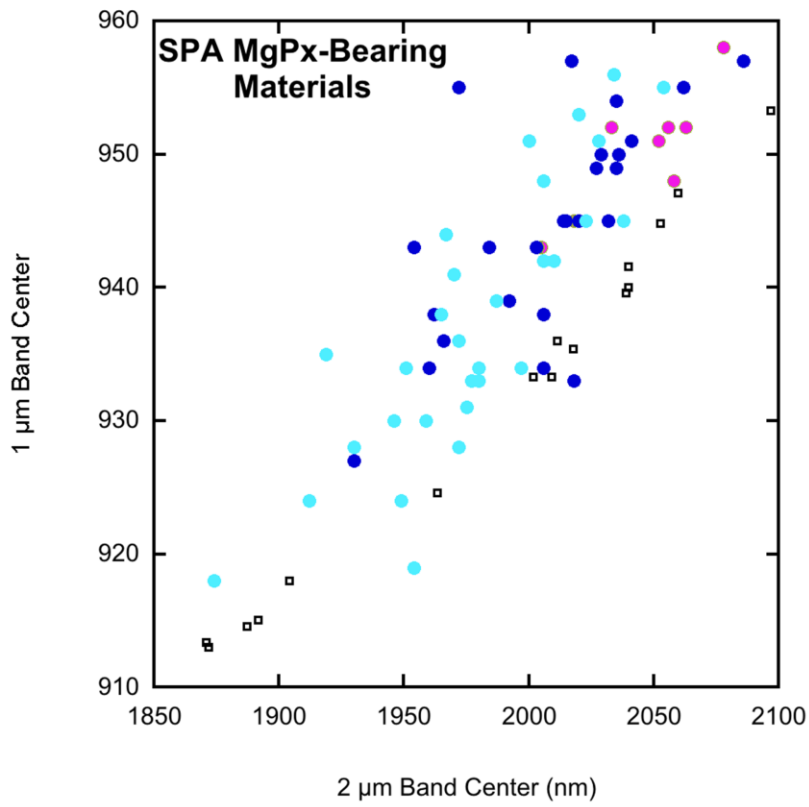
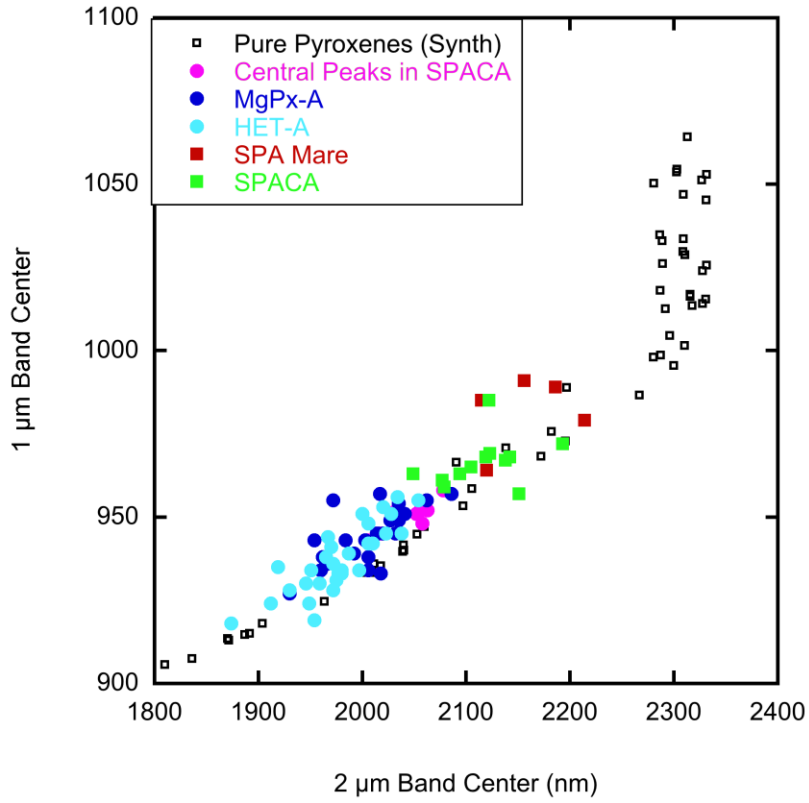


Fig. 7: PLC-derived band center measurements for Mg-pyroxene-bearing materials in the Mg-Pyroxene Annulus, Heterogeneous Annulus, and central peaks within SPACA. In (A), a full scale is provided for comparison to select SPA mare deposits, SPACA deposits, and synthetic pure pyroxenes [*Klima et al., 2007; 2011*]. In (B), only Mg-pyroxene-dominated materials are shown. Band center measurements were obtained from the walls and peaks of the impact structures listed in Table 1. For each crater/basin, representative band center values for all relevant structures (walls, peak rings, central peaks, etc.) are reported. Representative band center values were selected by comparing mean and median band center values for well-illuminated areas of crater structures.

CHAPTER 5: Synthesis

D. P. Moriarty III

Department of Earth, Environmental, and Planetary Sciences

Brown University | Providence, RI 02912

1 Introduction

In this dissertation, we have investigated the structure of South Pole - Aitken Basin with remote sensing data, especially focusing on near-infrared spectra returned by the Moon Mineralogy Mapper. In Chapter 1, we explored the complex relationship between pyroxene composition and absorption band centers for natural materials, developing and testing an approach using Parabolas and Linear Continua to evaluate the diagnostic properties of pyroxene absorption bands. This fundamental analysis facilitated the interpretation of M^3 data in the remaining chapters. In Chapter 2, we applied this approach (along with topography, gravity) and found the enigmatic Mafic Mound to have formed via volcanic construction. In Chapters 3 and 4, we mapped the abundance and composition of pyroxenes across SPA. Using these properties, five general zones were identified across SPA.

In this Chapter, we synthesize and interpret the previous findings. Here, we seek to establish an overall stratigraphy for SPA. In this basic stratigraphy, each stratigraphic unit identified across the basin is interpreted in the context of several models, including basin formation, the lunar magma ocean, gravitational overturn, and Mg-suite production. This synthesis provides a greater understanding of the South Pole - Aitken Basin, as well as its role in lunar evolution.

2 Summary of Major Findings from Chapters 1-4

2.1 Fundamental Spectroscopy of Pyroxene-Bearing Materials

An important step in any analysis is to understand the strengths and limitations of the tools being used. Throughout this dissertation, our analyses were grounded in compositional assessment of pyroxene minerals using their 1 μm and 2 μm absorption

band centers as measured by the Moon Mineralogy Mapper (M³) [Pieters *et al.*, 2009]. While it is fairly well-understood that these band centers are dependent on Fe, Mg, and Ca content [Adams, 1974; Hazen *et al.*, 1978; Cloutis and Gaffey, 1991; Klima *et al.*, 2007, 2011], it was important to consider how these relationships are propagated in tandem with other factors affecting remote sensing data of the Moon in order to justifiably interpret these measurements.

Since lunar spectra exhibit a significant continuum slope, it was necessary to remove this continuum in order to accurately measure the properties of absorption bands. In the interest of efficiently analyzing large volumes of complex remote sensing data, we implemented a practical band fitting routine involving Parabolas and a two-part Linear Continuum (PLC). For spectra of synthetic pure pyroxenes, PLC was shown to derive similar band center measurements as more physically realistic techniques such as the Modified Gaussian Model (MGM) [Sunshine *et al.*, 1990]. The advantage of a simple technique such as PLC is the ability to easily automate the routine and apply to entire hyperspectral image cubes, quickly analyzing large areas of the lunar surface. Although similar fitting routines are fairly common throughout the literature, the PLC technique is optimized for remote sensing analyses in several ways, which were documented in Chapter 1.

In Chapter 1, the PLC technique was validated on a variety of synthetic and natural samples including Lunar Rock and Mineral Characterization Consortium (LRMCC) [Isaacson *et al.*, 2011] basaltic rocks, Lunar Soil Characterization Consortium (LSCC) [Taylor *et al.* 2001; Noble *et al.* 2006; Taylor *et al.* 2010] mare and non-mare soils, and Howardite-Eucrite-Diogenite meteorites, confirming the relative trends

between absorption band centers and Fe,Mg,Ca content. The precise relationship between Fe,Mg,Ca content and absorption band center was shown to be somewhat different for synthetic pure pyroxenes natural pyroxene-bearing materials. This is logical, as natural materials exhibit composite spectra resulting from complex mixtures of multiple pyroxene and non-pyroxene components interacting non-linearly. These differences are due to inherent complexities in natural materials at several scales. For instance, (1) rocks are typically multi-mineral assemblages that including multiple distinct mineral phases, (2) many materials (breccias, soils, etc.) are physical mixtures of different lithologies, and (3) individual pyroxene phases often exhibit compositional variations due to processes such as zoning and exsolution. In conclusion, proper interpretation of remote sensing data requires natural materials to be treated as complex mixtures, rather than ascribing band center measurements to a single pyroxene composition.

2.2 The Nature and Origin of Mafic Mound

In Chapter 2, the PLC technique was used to evaluate the composition of Mafic Mound, an unusual structure at the center of South Pole - Aitken. Mafic Mound was found to exhibit long-wavelength 1 μm and 2 μm absorptions, indicating relatively Ca-rich pyroxenes similar to mare basalts. However, Mafic Mound materials appeared spectrally brighter than typical mare basalts in the region, suggesting a different mineral assemblage. Based on multiple exposures of this material in several ~ 10 km craters across the face of Mafic Mound, the structure was interpreted to be volumetrically homogeneous. This was found to be distinct from the compositional structure of volcanically filled craters throughout central SPA. These craters exhibited clear

compositional differences between volcanic fill and pre-existing crater structures. Additionally, Mafic Mound was found to be morphologically distinct from these filled craters, as the entire Mound structure is topographically higher than the surrounding terrain. Of the ~30 modified/filled craters examined, each exhibited floors topographically lower than the surrounding terrain. Topographically, Mafic Mound more closely resembles volcanic domes and complexes elsewhere on the Moon. Due to its topography, compositional structure, and location near the center of SPA, Mafic Mound was interpreted to be a magmatic construct related to the formation and evolution of the basin.

2.3 The Compositional Structure of South Pole - Aitken Basin

The PLC technique excels at spatial analyses of spectral properties. Taking advantage of these strengths, PLC analyses of the region were expanded to investigate the geology of SPA. M^3 spectral analyses were combined with topography and imagery data to investigate the compositional structure of the basin. Based on surface composition, local stratigraphic relationships, and topography, several distinct zones across SPA were defined. The properties of these zones are described in the following subsections.

2.3.1 The SPA Compositional Anomaly and Central Depression

In Chapter 4, central SPA was found to exhibit a pronounced, roughly elliptical central depression over 500 km across. Most of the central depression exhibits relatively smooth topography and a paucity of impact craters. This smooth, crater-poor terrain continues in an irregular region of slightly higher topography just to the north. These relatively smooth surfaces exhibit many modified/filled craters and an unusual composition relative to the remainder of the basin interior. While most of the basin

exhibits Mg-rich pyroxenes, this smooth central terrain exhibits a surface composition dominated by pyroxenes richer in Ca,Fe (as inferred from longer-wavelength 1 μm and 2 μm spectral absorption bands). Based on this unusual composition, this region was designated the "central **SPA** Compositional **A**nomaly" (SPACA). Since characteristic SPACA materials were found to be homogeneously exposed in the walls and peaks of several large craters (~50-100 km), the SPACA deposit was interpreted to be several km thick in places. However, Mg-pyroxene-bearing materials were observed in the central peaks of several large craters across SPACA, suggesting an underlying Mg-pyroxene-bearing material and thus constraining the thickness of the Ca,Fe-pyroxene-bearing layer. The smooth terrain, paucity of impact craters, significant thickness, presence of filled/modified craters, and unusual composition across SPACA appear to be most consistent with extensive magmatic resurfacing postdating SPA formation.

2.3.2 The Mg-Pyroxene Annulus

Outside the resurfaced SPACA region, non-mare mafic materials within SPA were observed to be dominated by Mg-rich pyroxenes (Chapter 4). In an annulus immediately outside of SPACA, SPA materials continue to exhibit uniformly high pyroxene content, but are compositionally distinct from SPACA. These materials are fairly homogeneous in pyroxene abundance and composition, including material exposed in a range of crater sizes from small surficial craters to large impact basins. These observations were interpreted to indicate the presence of a thick, pervasive, relatively uniform layer of Mg-pyroxene-bearing material in this annulus.

2.3.3 The Heterogeneous Annulus

Outside the Mg-Pyroxene Annulus, feldspathic materials are heterogeneously interspersed with localized Mg-pyroxene-bearing materials similar to those in the Mg-Pyroxene Annulus (Chapter 4). This "Heterogeneous Annulus" is interpreted to represent proximal SPA ejecta mixed with the feldspathic substrate during massive ejecta deposition and faulting/slumping/inward translation during basin modification. Therefore, we interpret Mg-pyroxene-bearing materials in the Mg-Pyroxene Annulus and Heterogeneous Annulus to represent deep-seated materials exposed by the SPA-forming impact. On the other hand, the SPACA region appears to be extensively resurfaced, and therefore does not exhibit abundant, pristine basement materials exposed by the impact. This is an important point to consider for future sample return missions.

2.3.4 South Pole - Aitken Exterior

Non-mare materials outside of the Heterogeneous Annulus were found to exhibit an overwhelmingly feldspathic composition (Chapter 4). These materials mostly represent feldspathic crustal materials from outside the SPA transient cavity and proximal ejecta blanket. This region includes the main topographic rim of SPA as well as the surrounding highlands.

3 Interpretation and Implications of South Pole - Aitken's Compositional Structure

In the following sections, we synthesize the findings of Chapter 1-4. These findings are interpreted in the context of basin formation models, as well as models of lunar evolution and structure.

3.1 The Stratigraphy of South Pole - Aitken Basin

Drawing from the pyroxene abundance, pyroxene composition, geologic context, and topography across SPA (presented in Chapters 3 and 4), we propose a general stratigraphic cross section for the basin that is consistent with the integrated observations. This cross section is given in Fig. 1C. Our approach for developing the cross section is described below.

The SPA cross section is based on a topographic profile obtained from the LROC WAC DTM [Scholten *et al.*, 2012]. The location of this profile is shown in Fig. 1B. The topographic profile is shown with greater vertical exaggeration in Fig. 1A. This higher relief highlights several important features, including Mafic Mound, the central depression, and the distinctive smooth terrain in central SPA.

Surface compositional variations established in Chapters 3 and 4 from M^3 data are represented in the context of this topographic structure. The Ca,Fe-pyroxene-bearing SPA Compositional Anomaly is clearly associated with the central smooth terrain. Outside of this smooth terrain, the Mg-Pyroxene Annulus and Heterogeneous Annulus are associated with rougher, more heavily cratered terrain. The SPA Exterior is associated with the primary topographic rim of SPA and exhibits significantly higher elevations.

Insight into the sub-surface stratigraphy is derived from compositional assessments of materials exposed by large craters across SPA. A schematic representation of the compositional diversity in complex craters and basins across SPA is given in Fig. 5 of Chapter 4.

This schematic representation provides a regional overview of compositional trends. Additionally, local and regional stratigraphies can be inferred. Typically, lunar impact craters excavate material from depths equal to ~10% of their transient cavity diameters [e.g. *Melosh*, 1989]. This excavated material is expected to dominate the walls of an impact crater. Therefore, craters of different sizes can be used to probe different depths beneath the pre-impact surface.

Central peak craters are especially useful for deriving local stratigraphic relationships. Central peaks are thought to uplift and expose material from depths greater than the maximum depth of excavation [e.g. *Cintala and Grieve*, 1998]. Therefore, central peak craters can be used to directly infer local stratigraphies by comparing wall materials to peak materials. An example is given in Fig. 2. Bhabha (~70 km diameter) exhibits stark compositional differences between its central peak (Mg-pyroxene-bearing) and wall (Ca,Fe-pyroxene-bearing). Using the previously-discussed crater scaling laws, Bhabha wall materials are likely derived from ~5 km depth, while peak materials are derived from ~10 km depth. It follows that in this region, a deposit of Ca,Fe-pyroxene-bearing material at least 5 km thick overlies a Mg-pyroxene-bearing materials. The transition between these zones must lie at a depth between 5 and 10 km.

Using the schematic representation of crater compositions across SPA presented in Chapter 4, Fig. 2, regional stratigraphic trends are inferred (Fig. 1). While the precise stratigraphy may vary locally due to the complex geologic history of SPA, this general model is consistent with the overall observations and is relevant to the formation and evolution of the basin.

From local stratigraphic relationships, the SPACA region appears to exhibit two primary vertical zones. This is especially apparent at Bhabha, as discussed above. Local stratigraphic relationships at other craters (e.g. Finsen, Stoney, White, etc.) in the SPACA zone are also consistent with this inferred stratigraphy.

In contrast, the Mg-Pyroxene Annulus appears to consist of a vast, relatively uniform unit tens of km thick. Craters and basins of a wide range of sizes (1 km - 550 km) exhibit primarily Mg-pyroxene-bearing materials in walls, floors, central structures, and ejecta. Uniform exposures in large portions of Apollo (530 km) and Poincare (380 km) suggest that this Mg-pyroxene-bearing unit is at least 40-50 km thick, and there is no evidence for widespread, distinct compositional units in this region. Therefore, the materials in the Mg-Pyroxene Annulus must reflect a similarly thick and uniform source region. We interpret these materials to represent a deep, thick, monolithic Mg-pyroxene-bearing unit derived from beneath the feldspathic portion of the lunar crust. The deposit was probably emplaced via excavation during the SPA-forming impact, and therefore Mg-Pyroxene Annulus materials represent remnants from the transient cavity wall. Although these materials are highly brecciated and melted, their bulk composition would be representative of the source region.

This interpretation is supported by the properties of the Heterogeneous Annulus. Although the Heterogeneous Annulus exhibits significant diversity in pyroxene abundance, non-mare pyroxene-bearing materials throughout this zone are compositionally similar to those in the Mg-Pyroxene Annulus. As per the following discussion, the pyroxene-bearing materials in the Heterogeneous Annulus probably represent proximal ejecta from the SPA-forming impact.

Impact models suggest that the deepest-seated ejecta in an impact are typically emplaced close to the transient cavity rim [e.g. *Potter et al.*, 2012]. For SPA, most of the proximal ejecta is deposited within a region that then slumps and collapses inward during the collapse of the transient cavity (the "modification stage") [*Potter et al.*, 2012]. Therefore, the ejected material with the deepest origin largely remains within the observed topographic rim of SPA [*Potter et al.*, 2012]. The proximal ejecta initially lands exterior to the transient cavity on the feldspathic highlands. These substrate crustal materials would have undergone large-scale mixing with mafic SPA ejecta during two distinct phases of SPA formation: (1) massive, ballistic deposition of proximal ejecta, resulting in large-scale mixing with local materials [*Oberbeck*, 1975], and (2) entrainment during faulting, slumping, and inward translation during collapse of the transient cavity. These processes are consistent with the compositional properties observed across the Heterogeneous Annulus.

3.2 South Pole - Aitken as a Probe to the Lunar Interior

From these observations, we conclude that the Mg-pyroxene-bearing materials found pervasively across SPA represent deep-seated materials exposed by the SPA-forming impact. What is the petrologic origin of these materials?

In the following section, we consider several scenarios. Four scenarios representing well-documented lunar evolution models are summarized in Fig. 3. We briefly evaluate these scenarios using several constraints tied to observations and models:

A. Excavated materials are dominated by a Mg-rich pyroxene composition.

From M^3 spectra, these materials exhibit short-wavelength 1 μm and 2 μm bands, indicating Mg-rich pyroxenes. The shortest wavelengths observed for such

materials are ~915 μm for the 1 μm band and ~1870 μm for the 2 μm band, as seen in Fig. 7 of Chapter 4. Based on direct comparison with synthetic pyroxenes, this could indicate an average Mg# of ~75 or greater.

B. Excavated materials exhibit a small range in mafic mineral diversity.

Although some Ca,Fe-pyroxenes are observed across SPA [e.g. *Pieters et al.*, 2001; *Ohtake et al.*, 2014], these appear to be mostly confined to mare basalts and other resurfacing deposits (such as SPACA [Chapter 3]). Significant quantities of olivine are not observed in materials exposed by the SPA-forming impact, as reported by *Yamamoto et al.* [2012].

C. The Mg-pyroxene source region must be laterally extensive and tens of km

thick. The Mg-Pyroxene Annulus is hundreds of km across. Due to relatively homogeneous exposures of Mg-pyroxenes in very large craters and basins across the Mg-Pyroxene Annulus, it is inferred to be at least 40-50 km thick. This suggests a monolithic source region whose dimensions are at a minimum those of the Mg-Pyroxene Annulus.

D. The Mg-Pyroxene Annulus is relatively uniform in pyroxene abundance. The

abundance (and composition) of pyroxenes across the Mg-Pyroxene Annulus appears fairly uniform, suggesting a similarly uniform source region.

E. When considering source regions for Mg-pyroxene-bearing materials in SPA,

possible origin depths must be physically realistic according to impact and geophysical models. According to GRAIL crustal thickness models [*Wieczorek et al.*, 2010], the average lunar crust is ~40 km thick, while the thickest lunar crust is ~60 km thick. Many models of SPA formation suggest that the impact

excavated through the crust and into the mantle, due to maximum excavation depths of ~100-150 km [e.g. *Potter et al.*, 2012]. However, several models by *Schultz*, [1997], *Schultz and Crawford*, [2011], and *Potter et al.*, [2012] describe anomalous cases where SPA is associated with maximum excavation depths of only ~57 km, excavating only crustal materials. In any case, the proposed Mg-pyroxene source region must be physically realistic considering models of crustal thickness and SPA excavation depth.

- F. **Excavated materials may include a feldspathic component.** Materials across the Mg-Pyroxene Annulus are relatively bright, compared to mare basalts. This suggests that they are not ultramafic, and may include a substantial feldspathic component.

In Fig. 3, each scenario is represented on the same depth scale. Several context depths are indicated, including minimum and maximum SPA excavation depths derived from impact models [*Potter et al.*, 2012] and the average and largest lunar crustal thicknesses derived from GRAIL models [*Wieczorek et al.*, 2010]. The source region for Mg-Pyroxene Annulus material is shown in blue for each scenario. We are beginning to explore the advantages and disadvantages of each.

As mentioned above, it is feasible that SPA excavated primarily crustal materials, if excavation was anomalously shallow and the pre-impact crustal thickness was close to the maximum observed lunar value. Additionally, factors such as high impact angles could further reduce the maximum excavation depth [*Schultz*, 1997; *Schultz and Crawford*, 2011]. Because of this, it is important to investigate the possibility that the

Mg-pyroxene-bearing materials exposed by SPA are crustal in origin (in addition to mantle origin scenarios). In general, two possible sources for the mafic material in the lower crust have been proposed: (1) coexisting liquid trapped between floating anorthosite grains during magma ocean crystallization [e.g. *Warren, 1990; Wieczorek and Zuber, 2001*], or (2) subsequent magmatic activity such as dykes and plutons [*Reid et al., 1977; Ryder and Wood, 1977; Pieters and Wilhelms, 1985; Pieters and Tompkins, 1999; Shearer and Papike, 2005*]. Scenarios involving subcrustal excavation are also investigated.

Case 1: Shallow excavation, inherently mafic lower crust. Case 1 represents an inherently mafic lower crust due to trapped liquids during crustal formation. **Major Advantages:** An inherently mafic lower crust is consistent with the noritic mineralogy of the Mg-Pyroxene Annulus. Trapped magma ocean liquid may also be consistent with the slightly elevated Fe and incompatible element abundance observed across SPA. **Major Disadvantages:** Plagioclase formation (and thus crustal formation) does not begin in the lunar magma ocean until around 80% crystallization [e.g. *Elkins-Tanton et al., 2011*]. Therefore, crystallization of the lower crust must occur later, perhaps after 85-90% crystallization of the lunar magma ocean. Because of this, the coexisting liquid during lower crust formation would be fairly evolved. Since Mg tends to be incorporated in early-crystallizing minerals, late-stage liquids are relatively enriched in Fe. It follows that trapped lunar magma ocean liquid would produce very Fe-rich pyroxenes, which are not observed in large quantities in lunar non-mare soils [*Taylor et al., 1996; 2001; 2002; 2003; Noble et al., 2006*] and may not be consistent with the spectral properties of the Mg-pyroxene-bearing material in SPA. Additionally, *Tompkins and Pieters [1999]*

showed the lower crust to be fairly heterogeneous, which is not consistent with the ~40-50 km thick, homogeneous Mg-Pyroxene Annulus. **Implications:** While this scenario is generally consistent with the overall mineralogy of the Mg-Pyroxene Annulus, it requires anomalous SPA impact parameters to produce shallow excavation. If the Mg-Pyroxene Annulus source region is inherently mafic lower crust, this implies that the coexisting liquid at the time and place of lower crustal formation must have been of an appropriate composition to crystallize predominantly Mg-pyroxene. It also suggests that the farside crust was relatively thick at the time and place of the SPA-forming impact, since the impact did not penetrate the crust. Additionally the mafic-bearing lower crust must be fairly homogeneous and at least ~40 km thick, due to the observed thickness of the Mg-Pyroxene Annulus. If this is the case, the mafic lower crust would represent 2/3 or more of the total crustal thickness.

Case 2: Shallow excavation, Mg-suite crustal intrusions. This model also considers possible shallow excavation scenarios for SPA, but investigates a different source of mafic materials in the lower crust. In this scenario, these mafic materials originate as magmatic intrusions of "Mg-suite" materials. These Mg-suite materials are thought to have originated as unusual mantle melts that were emplaced soon after primary crustal formation [e.g. *Hess, 1994; Shearer and Papike, 1999; Elardo et al., 2011; Shearer et al., 2015*]. It is unclear if these Mg-suite materials represent a global phenomenon, or if they are localized within the Procellarum KREEP terrain. **Major Advantages:** Mg-suite materials are consistent with the Mg-rich pyroxene compositions observed across SPA. **Major Disadvantages:** An intrusive origin for these materials would likely result in a very heterogeneous lower crust, as Mg-suite plutons are thought

to sometimes differentiate into distinct mafic minerals via fractional crystallization [e.g. *Shearer et al.*, 2015], and the plutons are emplaced into a feldspathic crustal matrix.

Implications: Mg-suite crustal intrusions would result in a heterogeneous lower crust, in terms of both mafic abundance and composition. Therefore, this scenario is not consistent with the homogeneous nature of the Mg-Pyroxene Annulus. It is unlikely that such plutons could represent the primary source of Mg-pyroxenes across SPA.

Case 3: Intermediate excavation, Mg-suite layer at base of crust. This model considers an alternative emplacement scenario for Mg-suite magmas. In this scenario, ascending Mg-suite magmas unable to ascend into the crust would become trapped at the base of the crust, forming a fairly uniform layer [e.g. *Shearer et al.*, 2015 and references therein]. **Main Advantages:** Mg-suite materials are consistent with the Mg-rich pyroxene compositions observed across SPA. **Main Disadvantages:** It is unclear if such a process could result in a zone of uniform Mg-pyroxene-bearing material >40 km thick. The emplacement may be too thin, or may differentiate into different mafic components. Studies by *Prissel et al.*, [2016] suggest that Mg-suite magmas may be buoyant relative to the feldspathic crust, which would make the formation of such a thick layer at the base of the crust somewhat difficult. **Implications:** This model is consistent with the mineralogy of the observed Mg-pyroxene bearing materials, and relaxes the constraints on SPA's excavation depth. This scenario would require large-scale global production and distribution of Mg-suite magmas, possibly via a mechanism independent of KREEP distribution.

Case 4: Deep excavation, Mg-pyroxene-bearing upper mantle. Case 4 allows for the more conventional deep excavation models for SPA formation. In this case, SPA

does excavate entirely through the crust, exposing primarily upper mantle materials.

Main Advantages: The upper mantle is a vast, thick layer consistent with the homogeneous, >40 km thick source region suggested by the Mg-Pyroxene Annulus. This scenario is most consistent with the majority of SPA impact models [e.g. *Hammond et al.*, 2009; *Potter et al.*, 2012]. **Main Disadvantages:** It is unclear how a thick Mg-pyroxene-bearing layer in the upper mantle may have formed. If the mantle followed a general cumulate stratigraphy (apart from plagioclase flotation), upper mantle pyroxenes would likely be too Fe-rich to be consistent with materials exposed in SPA [e.g. *Elkins-Tanton et al.*, 2011]. Additionally, this cumulate stratigraphy would result in elevated KREEP abundances in the upper mantle. Excavation of abundant KREEP-bearing materials is not observed in SPA. Mantle overturn might account for some of these issues. Mg-rich pyroxenes are expected to crystallize early and be present in the lower mantle. Some of these lower mantle pyroxenes may be brought to the upper mantle via gravitational overturn [*Hess and Parmentier*, 1995]. But if overturn occurred, Mg-rich olivine would also ascend from the lower mantle be abundant in the upper mantle. Abundant olivine is not observed across SPA, suggesting that mantle overturn had not occurred at the time and place of the SPA-forming impact. **Implications:** Excavation of the upper mantle is consistent with the extensive, thick nature of the Mg-Pyroxene Annulus. However, upper mantle compositions as currently modeled are not consistent with the Mg-pyroxene-bearing materials exposed in SPA, either pre- or post- overturn. If SPA has exposed upper mantle materials, lunar evolution models must be revised to include some combination of (1) a more magnesian liquid late in lunar magma ocean crystallization, (2) overturn bringing Mg-pyroxenes to the upper mantle without a

significant olivine component, or (3) a very low KREEP abundance on the lunar farside upper mantle (due to an asymmetric distribution or gravitational overturn).

Synthesis: As considered here, none of these four cases are wholly consistent with the inferred stratigraphy of SPA. Furthermore, it would be an oversimplification to claim that any of these cases occurred in isolation. Instead, it is most likely that two or more of these scenarios conspired to produce the observed stratigraphy.

A multi-component Mg-pyroxene source is consistent with spectral observations of SPA materials. As seen in Fig. 7 of Chapter 4, absorption band centers reveal small variations in average pyroxene composition among Mg-Pyroxene Annulus materials observed in SPA. The shortest-wavelength (most Mg-rich) materials are associated with several craters in the southwest region of SPA and the Apollo basin. Based on comparisons with synthetic pyroxene band centers, the most Mg-rich pyroxenes could have Mg# of 75 or higher. However, other pyroxenes throughout the Mg-Pyroxene Annulus exhibit slightly longer-wavelength absorption bands, indicating somewhat more Ca and Fe. These pyroxenes are observed in exposures such as Bhabha's central peak, which may sample the SPA melt sheet [*Nakamura et al.*, 2009; *Moriarty et al.*, 2013].

It is important to consider the source of compositional variations amongst Mg-Pyroxene Annulus materials. This diversity could arise from (1) mixtures of the Mg-pyroxene source region material with different proportions of mare basalts, SPACA materials, and/or impact melts/breccias, (2) mixing of materials from multiple Mg-pyroxene source regions (such as inherently mafic lower crust and upper mantle materials), or (3) inherent diversity in the Mg-pyroxene source region. In any case, the exposed Mg-pyroxene-bearing materials across SPA most likely underwent extensive

brecciation, impact melting, and mixing of both lower crustal and upper mantle components.

3.3 Origin of the Central Depression

As noted in Chapter 3, impact models suggest that the SPA-forming impact produced large volumes of impact melt SPA [Hammond *et al.*, 2009; Potter *et al.*, 2012]. This impact melt may have formed a melt sheet at the center of SPA up to ~50 km thick [Vaughan and Head, 2014]. Impact melt sheets may shrink vertically by ~10%, due to non-isotropic cooling and crystallization [Vaughan *et al.*, 2013]. A central depression in Orientale, is thought to have been formed via this process [Vaughan *et al.*, 2013]. The ~560 km central depression in SPA may be an analogous structure. If so, this outlines the extent of the thickest, most coherent part of the SPA melt sheet.

The pronounced depression in central SPA is approximately 1 km lower than the surrounding terrain. Based on the ~10% vertical shrinking proposed by Vaughan *et al.* [2013], this suggests an original melt sheet thickness of ~10 km. This is significantly lower than the ~50 km melt sheet thickness proposed by Vaughan and Head [2014]. Either (1) the initial subsidence has been masked by later geologic processes (such as ejecta emplacement and/or volcanic flooding), (2) vertical shrinkage was significantly lower than 10% of melt sheet thickness, (3) the SPA melt sheet was significantly thinner than 50 km, or (4) the central depression in SPA was not formed via vertical shrinkage of a thick central melt sheet.

3.4 Origin of the South Pole - Aitken Compositional Anomaly

As established in Chapter 3, the South Pole Aitken Compositional Anomaly exhibits many telltale signs of resurfacing, such as a relatively smooth texture, an overall

paucity of impact craters and a disproportionate abundance of filled, breached, or otherwise modified craters. A paucity of craters greater than 20 km (as identified by LOLA data [Head *et al.*, 2010; Kadish *et al.*, 2011]) in diameter is clearly visible in Chapter 3, Fig. 3. Of the craters that are observed within SPACA, many exhibit significant fill, burial, or modification. Example modified crater morphologies are given in Chapter 2, Fig. 3. The SPACA terrain corresponds spatially to these resurfacing features, suggesting that central SPA was extensively resurfaced by Ca,Fe-pyroxene-bearing materials.

For comparison, it is important to also consider non-resurfacing scenarios. One alternative explanation for the origin of SPACA is a differentiated impact melt sheet [Ohtake *et al.*, 2014]. Hurwitz and Kring [2014] suggest that the SPA melt sheet could have differentiated to produce a several-km-thick surficial layer dominated by Ca-bearing pyroxenes, overlying layers with more Mg-rich pyroxenes. While this is consistent with the observed stratigraphy, it does not account for several other properties of SPACA, notably the deficit of impact craters summarized in Chapter 3, Fig. 3.

Vaughan and Head [2014] estimate that a ~50 km thick melt sheet formed in central SPA. Based on equations given by Vaughan *et al.*, [2013], a ~50 km thick SPA melt sheet would crystallize in ~5 myr. Even if all impacts occurring during the crystallization of the melt sheet failed to form craters, this ~5 myr window is too short to significantly affect the cratering history of the region, even if it occurred during a possible early epoch of enhanced impactor flux [Morbidelli *et al.*, 2012]. In fact, the crystallization time of the melt sheet may have been significantly shorter than 5 myr if the melt sheet was thinner than 50 km or entrained a large proportion of solid clasts.

Therefore, some additional process is required to significantly reduce the crater population of the SPACA region.

The impact melt scenario is also inconsistent with several other properties of SPACA. The population of flooded, buried, and otherwise modified craters throughout central SPA [Chapter 2, Chapter 3] provide clear evidence of a complex sequence of resurfacing events postdating the SPA impact, rather than a single event such as melt sheet crystallization. Additionally, the SPACA region extends hundreds of km north of the central depression. If the central depression does correspond to a thick central melt sheet that differentiated to form the observed stratigraphy, it is unlikely that thinner melt deposits outside the central melt pool would have undergone similar differentiation processes to form the same compositional sequence.

While impact melt differentiation cannot be ruled out, impact melt alone cannot fully account for the observed morphological properties of SPACA. Could magmatic resurfacing satisfactorily explain these observations? To address this question, we compare the observed properties of SPACA surface materials to known resurfaced areas on the lunar surface, i.e. mare basalts.

Localized mare and cryptomare deposits have been identified across SPA [*Pieters et al.*, 2001; *Yingst and Head*, 1999; *Petro et al.*, 2011; *Whitten et al.*, 2014]. However, SPACA Ca,Fe-pyroxene-bearing materials blanket a much larger, more continuous region than these localized deposits. The physical properties of SPACA may be more consistent with mega-scale volcanic flooding, similar to models proposed by *Whitten and Head* [2013]. These models suggest that the paucity of craters in central SPA is consistent with flooding resulting in a ~2 km layer thick throughout the center of the

basin. In fact, stratigraphic relationships observed using superposed impact craters (such as Bhabha, presented above) suggest that the Ca,Fe-pyroxene-bearing SPACA surface layer is up to ~5 km thick in places. This is significantly thicker than typical mare basalt flows [Hiesinger and Head, 2002]. However, accumulated mare basalts may reach up to ~10 km in thicknesses within nearside basins [Solomon and Head, 1980]. Therefore, a ~5 km thick surface deposit could be consistent with a volcanic origin.

Spectrally, SPACA surface materials exhibit shorter-wavelength 1 μm and 2 μm band centers than typical mare basalts, as indicated in Chapter 3, Fig 5+6. This corresponds to average pyroxene compositions slightly lower in Ca (and possibly Fe). Additionally, these SPACA materials are brighter than typical mare basalts, as seen in Chapter 3, Fig. 5. This brightness difference may indicate a higher plagioclase content or lower opaque content.

Mare basalts have been shown to exhibit a wide range in composition [e.g. *Heiken et al.*, 2001; *Warren*, 1996], and therefore it is possible that SPACA materials represent an endmember mare basalt composition, such as the rare very low titanium basalt samples identified in the Apollo collections [*Shearer et al.*, 2006 and references therein]. However, it is also possible, and perhaps likely, that SPACA materials represent a distinct magmatic product.

Geophysical models suggest that large impacts can trigger localized mantle convection and subsequent melting, especially for thin lithospheres and warm mantle temperatures [*Elkins-Tanton and Hagar*, 2005]. This melting can occur over tens of myr [*Elkins-Tanton and Hagar*, 2005], an order of magnitude (or more) longer than the cooling of the SPA melt sheet. Melts geophysically triggered by SPA would occur under

different conditions than typical mare basalts. The different pressures, temperatures, and degrees of melting and/or a different mantle source region could result in distinctive melt compositions.

4 Summary

In this dissertation, we have used Moon Mineralogy Mapper data to unravel the compositional structure and possible evolution of the South Pole - Aitken Basin. We defined four zones across SPA based on compositional and topographic properties. The innermost zone is the **South Pole - Aitken Compositional Anomaly**, an area with surface compositions dominated by Ca,Fe-bearing pyroxenes. This compositional anomaly also exhibits a paucity of impact craters, an abundance of modified/filled craters, and a relatively smooth surface. We've interpreted the SPACA terrain to have formed via extensive volcanic resurfacing. In places, this resurfacing deposit is up to ~5 km in thickness. Outside of SPACA lies the **Mg-Pyroxene Annulus**. This zone exhibits a vast, fairly uniform region of Mg-pyroxene-bearing materials greater than 40 km thick. Due to its massive extent and limited mineralogical diversity, the source region for these materials must have been a similarly large and uniform region. The most likely source region for these materials include some combination of inherently mafic lower crust, Mg-suite materials emplaced at the base of the crust, and Mg-pyroxene-bearing upper mantle materials. The presence of such a large, uniform zone of Mg-pyroxene-bearing materials is fairly challenging to resolve with existing models of lunar evolution, and serves as a constraint for future models. The **Heterogeneous Annulus** exhibits feldspathic materials with localized deposits of Mg-pyroxene-bearing materials. We interpret this zone to have

arisen via large scale mixing of proximal SPA ejecta with the feldspathic crust surrounding the transient cavity. This region would have collapsed during basin modification, further commingling the ejecta and crust into a zone within the final topographic rim of SPA. The **SPA Exterior** is composed mainly of feldspathic materials. At the center of SPA, a pronounced central depression may have resulted from cooling and crystallization of a thick central melt pool.

5 Outstanding Issues and Future Directions

Throughout this dissertation, our compositional analyses rely on relative relationships between absorption band centers and Fe,Mg,Ca content in pyroxenes. While these relative relationships are useful for identifying and characterizing compositional diversity in remote sensing data, the ability to make more quantitative compositional inferences is ultimately more desirable. Such quantitative assessments require a deep understanding of the properties of lunar materials, including statistics on the compositions and abundances of mineral phases. A large number of diverse samples with well-characterized compositions must be analyzed spectrally in order to better understand the link between composition and optical properties. Additionally, the optical effects of processes such as space weathering must be accounted for. The Lunar Rock and Mineral Characterization Consortium [*Isaacson et al.*, 2011] and Lunar Soil Characterization Consortium [*Noble et al.*, 2006] have made significant contributions to this effort, but many more samples with a wider range in compositions must be analyzed to be able to make more quantitative compositional assessments from remote sensing spectra. Additionally, further understanding of mixing processes, as well as the effects of opaques, glasses, and space weathering is highly important.

The ability to derive more detailed compositional information from remote sensing spectra would facilitate the identification of surface materials. This requires the next generation of orbital spectrometers. For instance, the unusual SPACA materials could be compared to the diverse mare basalts in the sample collection to determine if they represent a mare basalt endmember, or if they are a unique composition requiring unusual melting scenarios. Additionally, the Mg-rich pyroxenes elsewhere in SPA could be compared with Mg-suite samples to determine if they are consistent with these lithologies, or must represent a different source region such as the upper mantle.

With the high-resolution LOLA and LROC data available, it now may be possible to derive more precise ages from crater counting. From relative age relationships, many outstanding questions can be addressed. How long after SPA formation was the SPACA material emplaced? Was it emplaced in a single event, or is there evidence for various ages corresponding to multiple events? Was Mafic Mound emplaced around the same time as the SPACA deposit? If so, could it represent a source vent for SPACA magmas?

Truly groundbreaking lunar science is possible with continued analysis of existing and future remote sensing data and sample collections. The integration of multiple remote sensing datasets with sample analyses offers ample opportunity for innovative, well-justified science. Through diligent study of existing data, the next several years of lunar research will leave us exceptionally well-prepared for the next era of lunar science and exploration.

6 References

- Adams J. B. 1974. Visible and near-infrared diffuse reflectance spectra of pyroxenes as applied to remote sensing of solid objects in the solar system. *Journal of Geophysical Research* 79:32:4829-4836.
- Cintala, M. J., and R. A. F. Grieve (1998), Scaling impact melting and crater dimensions: Implications for the lunar cratering record, *Meteorit. Planet. Sci.*, 33, 889–912, doi:10.1111/j.1945-5100.1998.tb01695.x.
- Cloutis E. A. and Gaffey M. J. 1991. Pyroxene spectroscopy revisited: Spectral-compositional correlations and relationship to geothermometry. *Journal of Geophysical Research: Planets* 96:E5:22809-22826.
- Elardo, S.M., Draper, D.S. and Shearer, C.K., (2011), Lunar Magma Ocean crystallization revisited: Bulk composition, early cumulate mineralogy, and the source regions of the highlands Mg-suite. *Geochimica et Cosmochimica Acta*, 75(11), pp.3024-3045.
- Elkins-Tanton, L. T. and B. H. Hager (2005), Giant meteoroid impacts can cause volcanism, *Earth and Planet. Sci. Let.*, 239, 219-232.
- Elkins-Tanton, L. T., S. Burgess, and Q. Yin (2011), The lunar magma ocean: Reconciling the solidification process with lunar petrology and geochronology. *Earth and Planet. Sci. Let.*, 304, 326-336.
- Hammond, N. P., F. Nimmo, and D. Korykansky (2009), Hydrocode modeling of the South Pole Aitken Basin-forming impact, *Lunar and Planet. Sci. Conf, XL*, #1455
- Hazen R. M., Bell P. M., and Mao H. K. 1978. Effects of compositional variation on absorption spectra of lunar pyroxenes. *Proceedings of the Lunar and Planetary Science Conference IX*, pp. 2929-2934.

- Head, J.W., C.I. Fassett, S.J. Kadish, D.E. Smith, M.T. Zuber, G.A. Neumann, and E. Mazarico (2010), Global distribution of large lunar craters: Implications for resurfacing and impactor populations, *Science*, 329, 1504-1507, doi:10.1126/science.1195050.
- Heiken, G., Vaniman, D., & French, B. M. (1991). *Lunar sourcebook: A user's guide to the Moon*. CUP Archive.
- Hess, P.C., 1994. Petrogenesis of lunar troctolites. *Journal of Geophysical Research: Planets*, 99(E9), pp.19083-19093.
- Hess, P. C. and E. M. Parmentier (1995), A model for the thermal and chemical evolution of the Moon's interior: Implications for the onset of mare volcanism, *Earth Planet. Sci. Lett.*, 134, 501-514, doi:10.1016/0012-821X(95)00138-3.
- Hiesinger, H., Head, J. W., Wolf, U., Jaumann, R., & Neukum, G. (2002). Lunar mare basalt flow units: Thicknesses determined from crater size- frequency distributions. *Geophysical Research Letters*, 29(8).
- Hurwitz, D. M. and D. A. Kring (2014), Differentiation of the South Pole – Aitken basin impact melt sheet: Implications for lunar exploration, *J. Geophys. Res.*, 119:1110-1113.
- Isaacson P. J., Basu Sarbadhikari A., Pieters C. M., Klima R. L., Hiroi T., Liu Y., and Taylor L. A. 2011. The lunar rock and mineral characterization consortium: Deconstruction and integrated mineralogical, petrologic, and spectroscopic analyses of mare basalts. *Meteoritics and Planetary Science* 46:2:228-251.

- Kadish, S.J., C.I. Fassett, J.W. Head, D.E. Smith, M.T. Zuber, G.A. Neumann, and E. Mazarico (2011), A global catalog of large lunar crater (≥ 20 KM) from the Lunar Orbiter Laser Altimeter, *Lunar Plan. Sci. Conf., XLII*, abstract 1006.
- Klima R. L., Pieters C. M., and Dyar M. D. 2007. Spectroscopy of synthetic Mg-Fe pyroxenes I: Spin-allowed and spin-forbidden crystal field bands in the visible and near-infrared. *Meteoritics and Planetary Science* 42:2:235-253.
- Klima R. L., Dyar M. D., and Pieters C. M. 2011. Near-infrared spectra of clinopyroxenes: Effects of calcium content and crystal structure. *Meteoritics and Planetary Science* 46:3:379-395.
- Melosh, H. J. (1989), *Impact Cratering: A Geologic Process*, Oxford Univ. Press, New York, NY.
- Morbidelli, A., Marchi, S., Bottke, W.F. and Kring, D.A., 2012. A sawtooth-like timeline for the first billion years of lunar bombardment. *Earth and Planetary Science Letters*, 355, pp.144-151.
- Moriarty, D. P., Pieters, C. M., & Isaacson, P. J. (2013). Compositional heterogeneity of central peaks within the South Pole- Aitken Basin. *Journal of Geophysical Research: Planets*, 118(11), 2310-2322.
- Nakamura, R., T. Matsunaga, Y. Ogawa, S. Yamamoto, T. Hiroi, K. Saiki, N. Hirata, T. Arai, K. Kitazato, H. Takeda, T. Sugihara, S. Kodama, M. Ohtake, J. Haruyama, and Y. Yokota (2009), Ultramafic impact melt sheet beneath the South Pole – Aitken basin on the Moon, *Geophys. Res. Lett.*, 36, L22202.

- Noble S. K., Pieters C. M., Hiroi T., and Taylor L. A. 2006. Using the modified Gaussian model to extract quantitative data from lunar soils. *Journal of Geophysical Research* 111:E11009.
- Oberbeck, V. R. (1975). The role of ballistic erosion and sedimentation in lunar stratigraphy. *Reviews of Geophysics*, 13(2), 337-362.
- Ohtake, M., Uemoto, K., Yokota, Y., Morota, T., Yamamoto, S., Nakamura, R., Haruyama, J., Iwata, T., Matsunaga, T. and Ishihara, Y., 2014. Geologic structure generated by large- impact basin formation observed at the South Pole- Aitken basin on the Moon. *Geophysical Research Letters*, 41(8), pp.2738-2745.
- Petro, N. E., S. C. Mest, and Y. Teich (2011), Geomorphic terrains and evidence for ancient volcanism within northeastern South Pole - Aitken Basin, *Geol. Soc. Am.*, Special Paper 477, pp. 129-140.
- Pieters, C. M. and D. E. Wilhelms (1985), Origin of olivine at Copernicus, *Proceedings of the Fifteenth Lunar Planet. Sci. Conf.*, 2, *J. Geophys. Res.*, C415-C420.
- Pieters, C. M., J. W. Head, L. Gaddis, B. Jolliff, and M. Duke (2001), Rock types of South Pole - Aitken basin and extent of basaltic volcanism, *J. Geophys. Res.*, 106, 28,001–28,022, doi:10.1029/2000JE001414.
- Pieters C. M., Boardman J., Buratti B., Chatterjee A., Clark R., Glavich T., Green R., Head III J., Isaacson P., Malaret E., McCord T., Mustard J., Petro N., Runyon C., Staid M., Sunshine J., Taylor T., Tompkins S., Varanasi P, White M. 2009. The Moon Mineralogy Mapper (M³) on Chandrayaan-1. *Current Science* 96:4:500-505.

- Potter, R. W. K., G. S. Collins, W. S. Kiefer, P. J. McGovern, and D. A. Kring (2012), Constraining the size of the South Pole-Aitken basin impact, *Icarus*, 220, 730-743, doi:10.1016/j.icarus.2012.05.032
- Prissel, T. C., J. L. Whitten, S. W. Parman, J. W. Head (2016), On the Potential for Lunar Highlands Mg-suite Extrusive Volcanism & Implications Concerning Crustal Evolution, *Icarus*.
- Reid, A. M., A. R. Duncan, and S. H. Richardson (1977), In search of LKFM, *Proc. Lunar Sci. Conf.*, 8th, 2321-2338.
- Ryder, G. and J. A. Wood (1977), Serenitatis and Imbrium impact melts: Implications for large-scale layering in the lunar crust, *Proc. Lunar Planet. Sci. Conf.*, 8th, 655-668.
- Scholten, F, J. Oberst, K. D. Matz, T. Roatsch, M. Wahlisch, E. J. Speyerer, and M. S. Robinson (2012), GLD100: The near-global lunar 100 m raster DTM from LROC WAC stereo image data, *J. Geophys. Res.*, 117(E12).
- Schultz, P.H., 1997, March. Forming the south-pole Aitken basin-The extreme games. In *Lunar and Planetary Science Conference* (Vol. 28, p. 1259).
- Schultz, P. H. and D. A. Crawford (2011), Origin of nearside structural and geochemical anomalies on the Moon, *Geo. Soc. Am. Special Papers*, 477, 141-159, doi:10.1130/2011.2477(07).
- Shearer, C.K. and Papike, J.J., (1999). Magmatic evolution of the Moon. *American Mineralogist*, 84, pp.1469-1494.

- Shearer, C. K., Hess, P. C., Wieczorek, M. A., Pritchard, M. E., Parmentier, E. M., Borg, L. E., ... & Canup, R. M. (2006). Thermal and magmatic evolution of the Moon. *Reviews in Mineralogy and Geochemistry*, 60(1), 365-518.
- Shearer, C.K., Elardo, S.M., Petro, N.E., Borg, L.E. and McCubbin, F.M., (2015), Origin of the lunar highlands Mg-suite: An integrated petrology, geochemistry, chronology, and remote sensing perspective. *American Mineralogist*, 100(1), pp.294-325.
- Solomon, S. C., & Head, J. W. (1980). Lunar mascon basins: Lava filling, tectonics, and evolution of the lithosphere. *Reviews of Geophysics*, 18(1), 107-141.
- Sunshine J. M., Pieters C. M., and Pratt S. F. 1990. Deconvolution of mineral absorption bands – An improved approach, Chapter *Journal of Geophysical Research – Planets* 98:9075-9087.
- Taylor, L.A., A. Patchen, D.H. Taylor, J.G. Chambers, and D.S. McKay, 1996, X-ray digital imaging and petrography of lunar mare soils: Data input for remote sensing calibrations, *Icarus*, 124, 500-512.
- Taylor, L.A., Cahill, J.T., Patchen, A., Pieters, C., Morris, R.V., Keller, L.P., & McKay, D.S., 2001, Mineralogical and chemical characterization of lunar high-land regolith: lessons learned from mare soils. *Lunar & Planetary Sci. Conf.*, LPI CD-ROM # 2196.
- Taylor, L.A., A. Patchen, J. Cahill, C.M. Pieters, R.V. Morris, L.P. Keller, and D.S. McKay, (2002), Mineral and glass characterization of Apollo 14 soils. *Lunar & Planetary Sci. Conf. XXXIII*, LPI CD-ROM #1302. Taylor, L.A., Pieters, C.M., Patchen, A.,

- Taylor, D.H., Morris, R.V., Keller, L.P., and McKay, D.S., 2003, Mineralogical Characterization of Lunar Highland Soils, *Lunar & Planet. Sci. XXXIV*, LPI CD-ROM #1774
- Taylor, L. A., Pieters, C., Patchen, A., Taylor, D. H. S., Morris, R. V., Keller, L. P., & McKay, D. S. (2010). Mineralogical and chemical characterization of lunar highland soils: Insights into the space weathering of soils on airless bodies. *Journal of Geophysical Research: Planets*, 115(E2).
- Tompkins, S., and C. M. Pieters (1999), Mineralogy of the lunar crust: Results from Clementine, *Meteorit. Planet. Sci.*, 34, 25–41, doi:10.1111/j.1945-5100.1999.tb01729.x.
- Vaughan, W. M., J. W. Head, L. Wilson, and P. C. Hess (2013), Geology and petrology of enormous volumes of impact melt on the Moon: A case study of the Orientale basin impact melt sea, *Icarus*, 223:749-765.
- Vaughan, W. M. and J. W. Head III (2014), Impact melt differentiation in the South Pole – Aitken basin: Some observations and speculations, *Planet. Space Sci.*, 91, 101-106.
- Warren, P. H. (1990), Lunar anorthosites and the magma-ocean plagioclase-flotation hypothesis: Importance of FeO enrichment in the parent magma, *Am. Mineral.*, 75, 46-58.
- Warren, P. H., Claeys, P., & Cedillo-Pardo, E. (1996). Mega-impact melt petrology (Chicxulub, Sudbury, and the Moon): Effects of scale and other factors on potential for fractional crystallization and development of cumulates. *The Cretaceous-Tertiary event and other catastrophes in Earth history*, 105-124.

- Whitten, J. L. and J. W. Head (2013), Detecting volcanic resurfacing of heavily cratered terrain: Flooding simulations on the Moon using Lunar Orbiter Laser Altimeter (LOLA) data, *Planet. Space Sci.*, 85, 24-37, doi: 10.1016/j.pss.2013.05.013.
- Whitten, J. L. and J. W. Head III (2014), Lunar cryptomaria: Physical characteristics, distribution, and implications for ancient volcanism, *Icarus*, 247, 150-171.
- Wieczorek, M. A., and M. T. Zuber (2001), The composition and origin of the lunar crust: Constraints from central peaks and crustal thickness modeling, *Geophys. Res. Lett.*, 28, 4023 – 4026, doi:10.1029/2001GL012918.
- Wieczorek, M.A., Neumann, G.A., Nimmo, F., Kiefer, W.S., Taylor, G.J., Melosh, H.J., Phillips, R.J., Solomon, S.C., Andrews-Hanna, J.C., Asmar, S.W. and Konopliv, A.S., (2013), The crust of the Moon as seen by GRAIL. *Science*, 339(6120), pp.671-675.
- Yamamoto, S., Nakamura, R., Matsunaga, T., Ogawa, Y., Ishihara, Y., Morota, T., Hirata, N., Ohtake, M., Hiroi, T., Yokota, Y. and Haruyama, J., (2012), Olivine-rich exposures in the South Pole-Aitken basin. *Icarus*, 218(1), pp.331-344.
- Yingst, R. A. and J. W. Head III (1999), Geology of the mare deposits in South Pole – Aitken Basin as seen by Clementine UVVIS data, *J. Geophys. Res.*, 104(E8), 18957-18979.

Figures and Captions

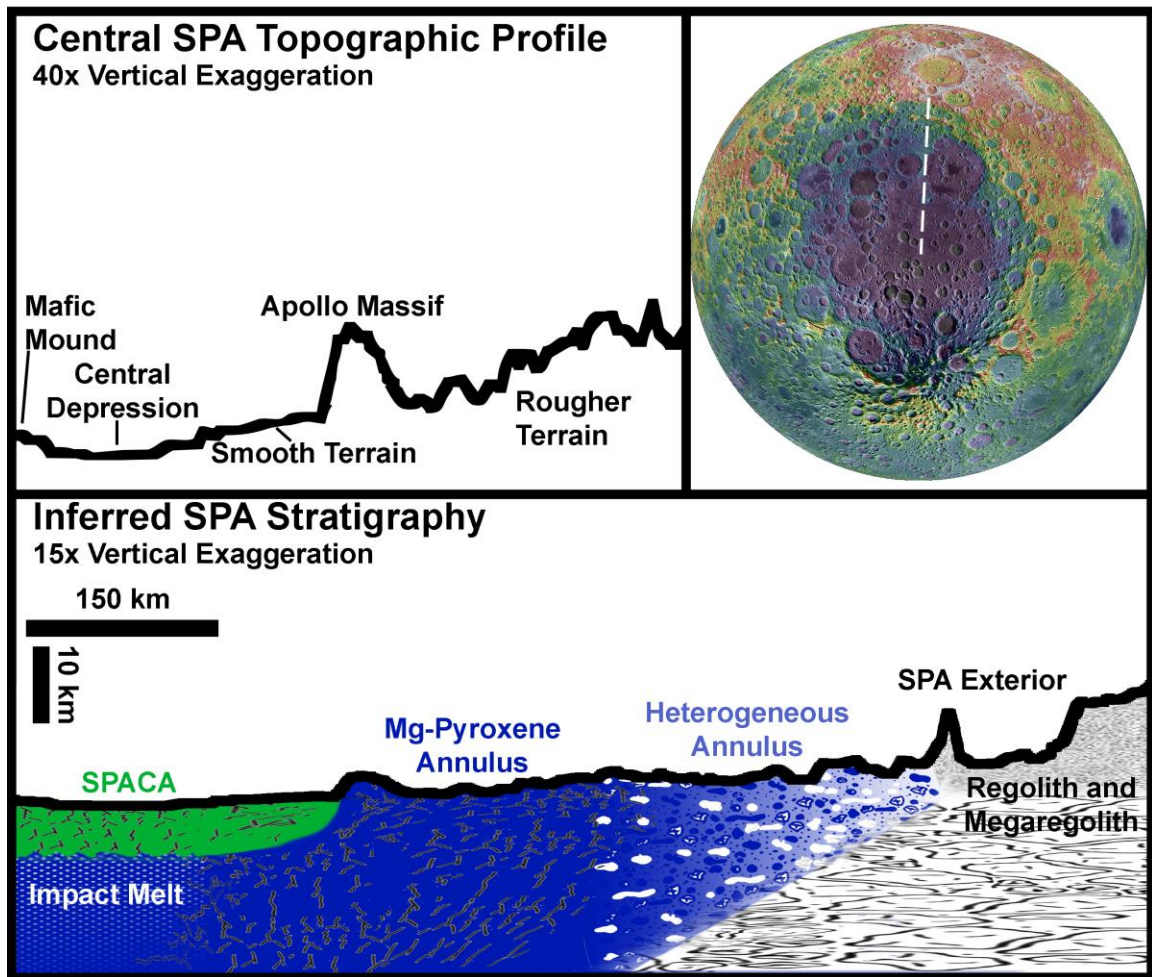


Fig. 1: (A/Top Left) A topographic profile of central SPA derived from Lunar Reconnaissance Orbiter Camera Wide Angle Camera Digital Terrain Model [Scholten *et al.*, 2012]. This profile represents a portion of the transect indicated in (B/Top Right). (C/Bottom) A generalized SPA stratigraphy, inferred from M³ observations and crater scaling relationships discussed in Chapters 3, 4, and 5. This cross section is based on the topographic profile indicated by the transect in (B/Top Right).

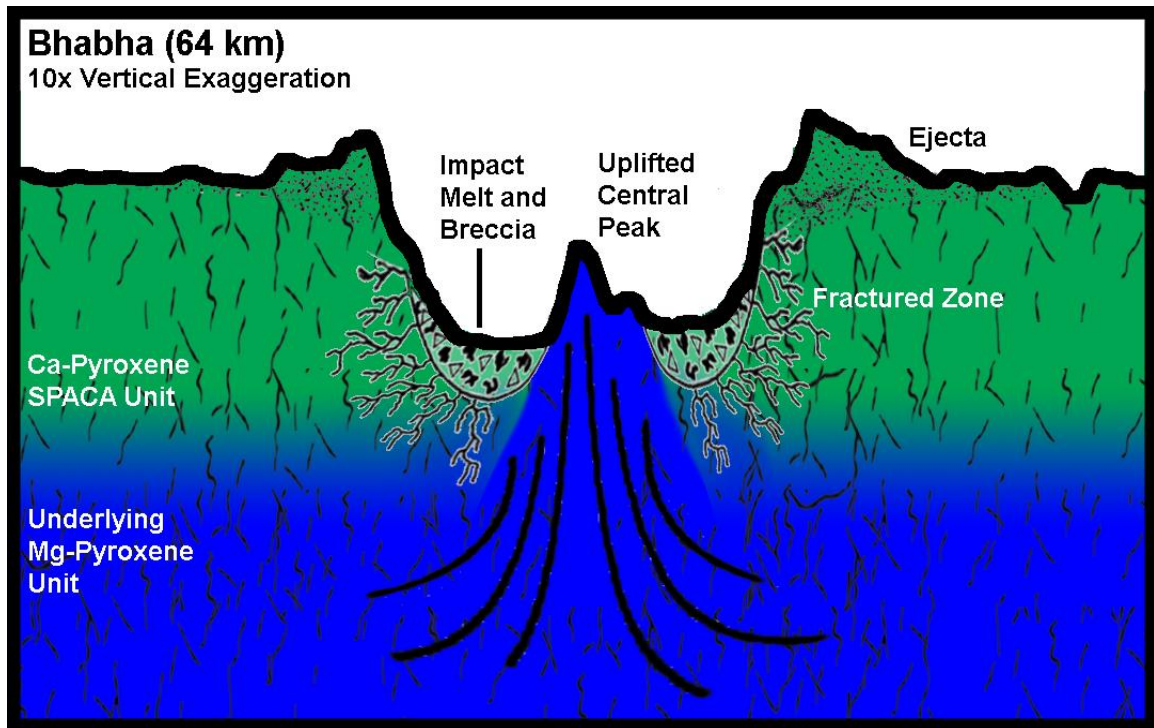


Fig. 2: A cross section demonstrating the inferred stratigraphy at Bhabha within the SPACA zone in central SPA. The SPACA surface material is homogeneously exposed in Bhabha's walls and ejecta, suggesting that the material is at least ~5 km thick. The Mg-pyroxene-bearing material in Bhabha's central peak indicates the presence of this material at ~10 km depth. This cross section was constructed using a topographic profile derived from the LROC WAC DTM [Scholten *et al.*, 2012], M^3 observations, and crater scaling relationships [Melosh, 1989; Cintala and Grieve, 1998].

Candidate Mg-Pyroxene Source Regions (Pre-SPA-Impact Stratigraphy)

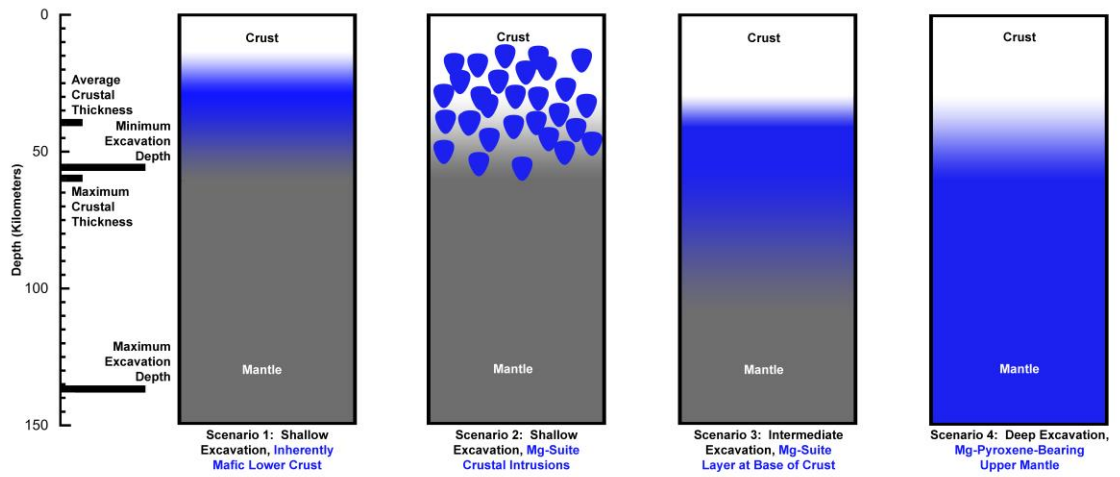


Fig. 3: A schematic representation of the four origin scenarios for Mg-pyroxene-bearing materials observed across SPA. Average crustal thicknesses are from GRAIL models [Wieczorek *et al.*, 2010]. Excavation depths are from numerical models of the SPA-forming impact [Potter *et al.*, 2012].

Appendix A: Description of the PLC technique and supplemental
figures for Chapter 1

Daniel P. Moriarty III [Daniel_Moriarty@Brown.edu]

Carle M. Pieters

Department of Earth, Environmental, and Planetary Sciences

Brown University

324 Brook Street

Providence, RI 02912

The PLC Method:

The following is a detailed description of two example applications of the Parabolas and Linear Continuum (PLC) technique. For this example, we use two RELAB spectra: one of synthetic pure orthopyroxene (En35, Fs65, RELAB #DL-CMP-025), one of synthetic pure clinopyroxene (En39, Fs34, Wo27, RELAB #DL_CMP-051). Both spectra are available on the RELAB website: <http://www.planetary.brown.edu/relab/>. The reflectance spectra, continuum fits, continuum-removed reflectance spectra, and parabola fits for these pyroxenes are given in Fig. S1.

The first step in PLC analysis is to fit and remove a continuum to the spectrum. PLC employs a two-part linear continuum fit to three tiepoints derived from the spectrum. The short-wavelength and long-wavelength tiepoints are fixed at wavelengths set by the user, whereas the middle tiepoint is automatically optimized for each spectrum. These tiepoints should represent tangent points to minimize values greater than 1 in the resulting continuum-removed spectrum. For single-spectrum fits, the "fixed" tiepoints can be individually adjusted by the user to obtain the best fit. For application to imaging spectrometer data such as data from Moon Mineralogy Mapper, these tiepoints must be fixed to allow fully automated processing. The best choices for these two tiepoints depend on the characteristics of the data, which involve a number of factors including composition, optical maturity, thermal state, and instrument properties. When selecting these tiepoints, it is important to account for several factors affecting reflectance properties at these wavelengths, including UV absorptions, thermal emission, and absorption bands from water and minerals including the pyroxene absorptions themselves.

For Moon Mineralogy Mapper spectra of pyroxene-bearing materials, good spectral fits can be achieved with short-wavelength tiepoints ranging from 650-750 nm and long-wavelength tiepoints ranging from 2500-2700 nm. Each tiepoint is derived from the average of three

consecutive wavelength channels (one on either side of the specified channel) to minimize the effects of noise on the continuum fit.

For the example pyroxene spectra, the short-wavelength tiepoint is set to 650 nm to target the spectral tangent point. The long wavelength tiepoint is set to 2595 nm - the longest possible wavelength channel allowing a tiepoint calculated from three consecutive channels, given that RELAB bi-directional reflectance spectra terminate at 2600 nm with a spectral resolution of 5 nm. For these pyroxene spectra, there is no long-wavelength tangent point within the measured spectral range, necessitating the use of the lonest available wavelength channels. A standard continuum fit using these tiepoints is given for the orthopyroxene spectrum in Fig. S1a.

In some RELAB pyroxene spectra (especially those with longer-wavelength absorption bands), the longest available band is not representative of the continuum, as it is within the 2 μm pyroxene absorption band (see the clinopyroxene spectrum in Fig. S1a). In this case, the estimated 2 μm continuum slope using the long-wavelength tiepoint can be unrealistically negative. When negative 2 μm slopes occur, an alternative flat continuum is used across the 2 μm region, extended from the middle tiepoint. This strategy avoids introducing improper distortions to the 2 μm band via removal of a clearly unrealistic continuum. An example of this flat 2 μm continuum is given for the clinopyroxene spectrum in Fig. S1a.

In spectra of pyroxene-bearing materials, the middle tiepoint varies from sample to sample. The PLC algorithm chooses the middle tiepoint from a predefined wavelength range using an automated fitting routine. For pyroxene-dominated spectra, this range should span the wavelength region between the 1 μm and 2 μm pyroxene bands, coinciding with an apparent peak in reflectance. To account for a range in pyroxene compositions, the middle tiepoint is selected from spectral channels between 1100 nm and 1800 nm. To select the middle tiepoint, the fitting routine calculates a continuum-removed spectrum using every possible middle tiepoint within the defined range. The routine identifies and selects the middle tiepoint that produces a continuum-removed spectrum with the fewest wavelength channels greater than one (within this middle

wavelength range). This essentially selects a middle tiepoint that serves as an "average tangent point" for both the 1 μm and 2 μm continuum. For the example orthopyroxene spectrum, the resulting middle tiepoint is located at 1450 nm. The middle tiepoint for the clinopyroxene spectrum is located at 1610 nm.

With these three tiepoints selected, a two-part linear continuum is fully defined for the spectrum. Two straight lines are fit, one from the short-wavelength tiepoint to the middle tiepoint; the other from the middle tiepoint to the long-wavelength tiepoint. Continuum values are calculated for each wavelength channel, extrapolating beyond the tiepoints if necessary. Each channel of reflectance data should have a corresponding continuum value.

After the estimated two-part linear continuum is calculated, a continuum-removed spectrum is produced by dividing the reflectance spectrum by the derived continuum. Continuum-removed spectra for the example pyroxenes are given in Fig. S1b.

To derive absorption band depths and centers, parabolas are fit to portions of the 1 μm and 2 μm absorption bands, targeting the band minimum. [NOTE: the general PLC approach does NOT attempt to separate superimposed absorptions.] To capture the wavelength variations of different pyroxene absorptions, a "sliding" parabola fitting approach is used. For each absorption band, the parabola fit is performed over a pre-defined wavelength range corresponding to the full range of possible absorptions. For the example pyroxene spectra, the 1 μm band fit is performed from 700 nm to 1200 nm, and the 2 μm band fit is performed from 1575 nm to 2600 nm. Parabola fitting is performed using a fixed number of contiguous channels (X), normally less than the total number of channels in the range investigated (in order to target the band minimum). The example orthopyroxene fit uses 65 channels (of a possible 100) for the 1 μm band and 100 channels (of a possible 205) for the 2 μm band. The clinopyroxene fit uses fewer channels (35) for both the 1 μm and 2 μm band fits. A parabola fit using the specified number of contiguous bands then "sweeps" through the specified range. First, the first X bands within the specified wavelength range are fit with a parabola. Next, a parabola is fit to X bands starting at the second

wavelength channel within the specified range. This continues until the final parabola fit is performed, using the final X bands within the specified wavelength range. Once all of these parabola fits have been performed (resulting in a number of parabola fits equal to one plus the number of wavelength channels in the specified range minus the number of contiguous channels used in the fit), the final parabola fit is selected by the parabola fit with the lowest residual. These fits can be visually checked when working with single-spectrum data. For automated application to remote sensing data, additional constraints can be emplaced to ensure that the fits are concave up and produce band centers at realistic values (such as ~900-1100 nm for the 1 μm band).

From the best-fit parabolas, the estimated band depths (EBD) and centers (EBC) are calculated. The band centers are calculated from the location of the minimum of the parabola. The band depths are calculated as 1-(Continuum Removed Reflectance) at the parabola minimum. The values derived from the example pyroxene spectra are given in Table S1.

In order to directly compare values for the estimated continuum slope across the 1 μm and 2 μm regions, normalized continuum slope (NCS) values are calculated for each region. The NCS is defined as the difference in measured reflectance across a 1 μm difference in wavelength, normalized to the reflectance at 700 nm. This common scaling of NCS values is essential to remove albedo effects on slope measurements. Comparison of NCS values can often be used to provide information on the composition and optical maturity of a material. For the example pyroxene spectra, the 1 μm NCS is calculated as the reflectance difference in the continuum between 800 nm and 700 nm, divided by the continuum value at 700 nm and multiplied by ten (to obtain the slope over a 1 μm range rather than the 100 nm range calculated). Similarly, the 2 μm NCS is calculated as 10x the reflectance difference in the continuum between 2400 nm and 2300 nm, also divided by the continuum value at 700 nm. The resulting NCS values for each example spectrum are given in Table S1.

Table S1: PLC Parameter Values for the Example Spectra

Spectrum	NCS1	NCS2	EBC1	EBC2	EBD1	EBD2
DL-CMP-025 (OPX)	0.483	0.127	933	2004	.737	.577
DL_CMP-051 (CPX)	0.123	000 (flat)	996	2292	.799	.546

Supplemental Figures

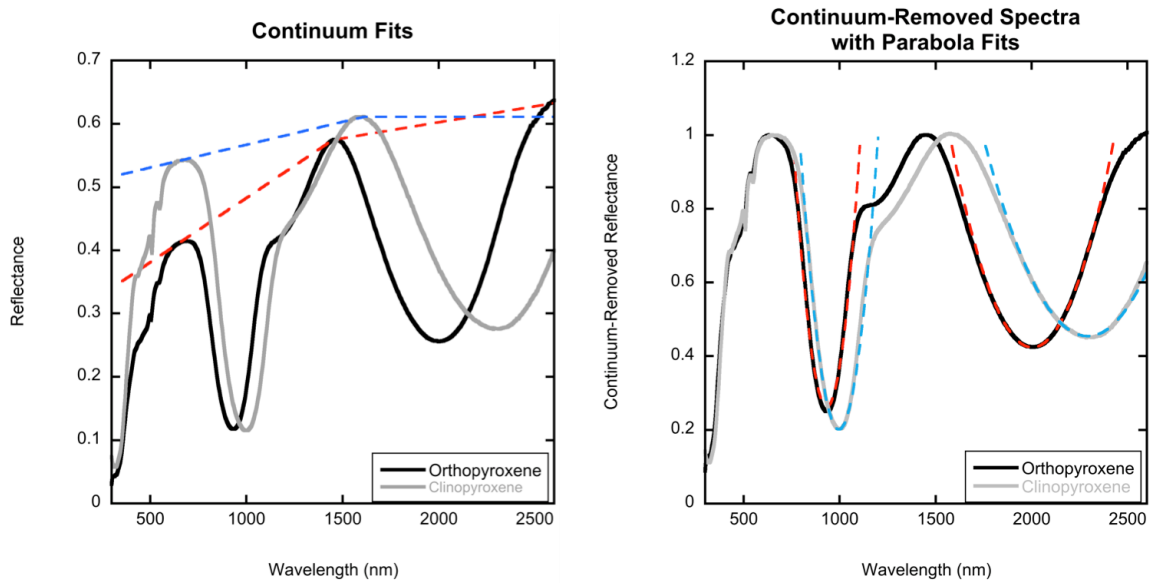


Fig. S1: Example continuum fit (left), continuum-removed spectrum, and parabola fits (right) for synthetic pure orthopyroxene En₃₅,Fs₆₅ (RELAB #DL_CMP-025) and synthetic pure clinopyroxene En₃₉, Fs₃₄, Wo₂₇ (RELAB #DL_CMP-051). A flat 2 μm continuum is used across the 2 μm region of the clinopyroxene spectrum rather than the negative continuum that would be derived from a long-wavelength tiepoint at 2595 nm.

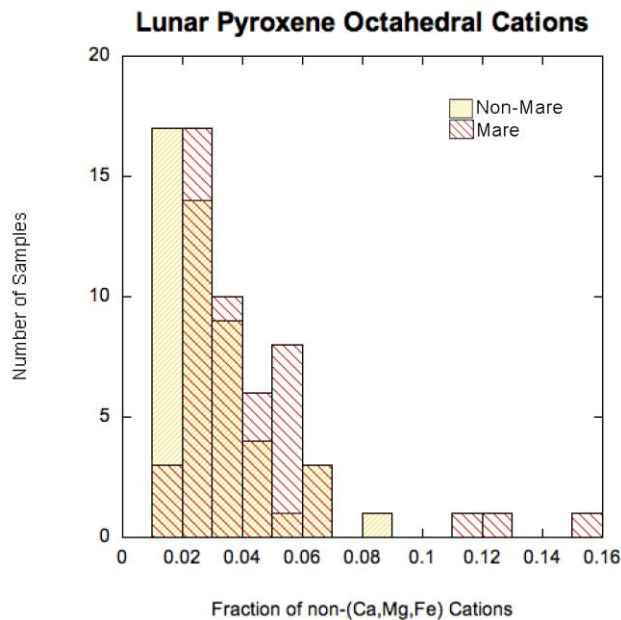


Fig. S2: This histogram summarizes the distribution of non-(Ca,Mg,Fe) cations for a collection of lunar pyroxenes derived from various mare and non-mare samples. While both mare and non-mare pyroxenes typically exhibit <6% non-(Ca,Mg,Fe) octahedral cations, mare pyroxenes are slightly more enriched in these non-quadrilateral elements. Compositional information was compiled in Papike et al. 1991 from the following sources: Agrell et al. 1970; Bence et al. 1970; Brown et al. 1970; Hollister and Hargraves 1970; Kushiro and Nakamura 1970; Smith et al. 1970; Boyd and Smith 1971; Dence et al. 1971; Gancarz et al. 1971; Hollister et al. 1971; Newton et al. 1971; Albee et al. 1972; Bence and Papike 1972; Hargraves and Hollister 1972; Weigand and Hollister 1973; Hodges and Kushiro, 1974; Papike et al. 1974; Dixon and Papike 1975; Dymek et al. 1975; McCallum and Mathez 1975; Sclar and Bauer 1975; Smyth 1975; Vaniman and Papike 1977; Laul et al. 1978; Vaniman and Papike 1980; and Shervais et al. 1985.

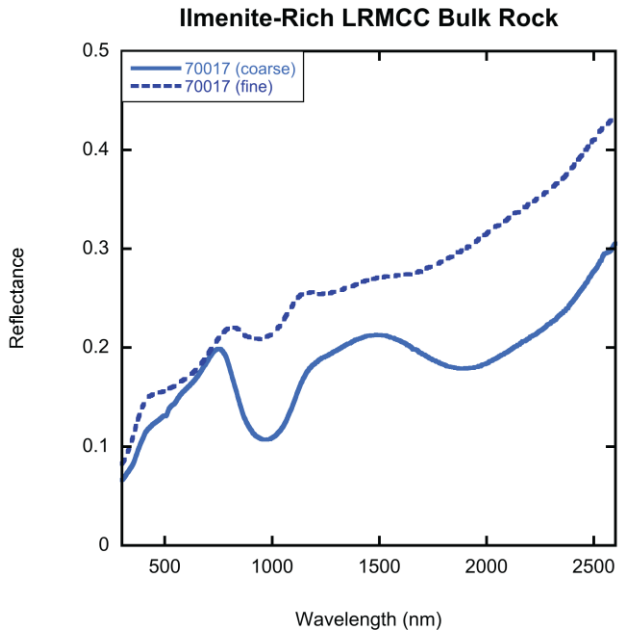


Fig. S3: These example LRMCC Apollo 17 Bulk Rock spectra exhibit the effects of high ilmenite content, namely a steep red-sloped continuum and distorted 1 μm and 2 μm pyroxene absorption bands.

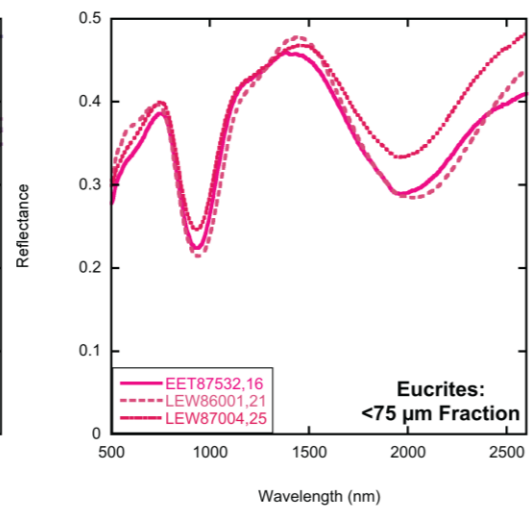
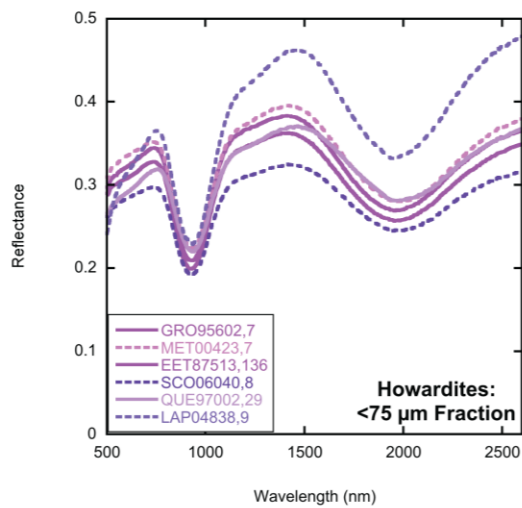
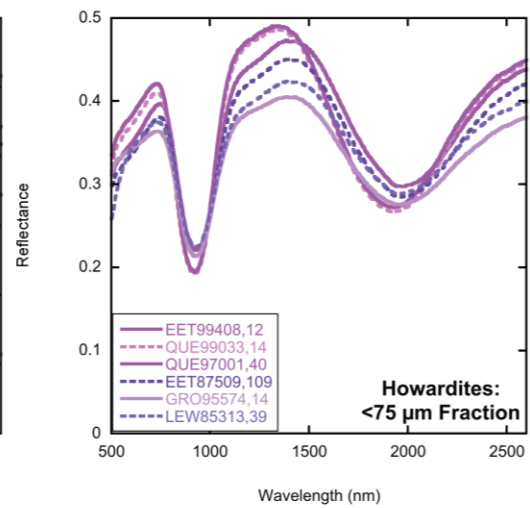
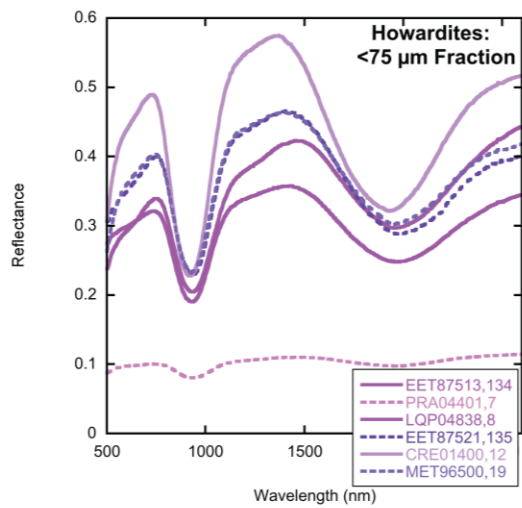
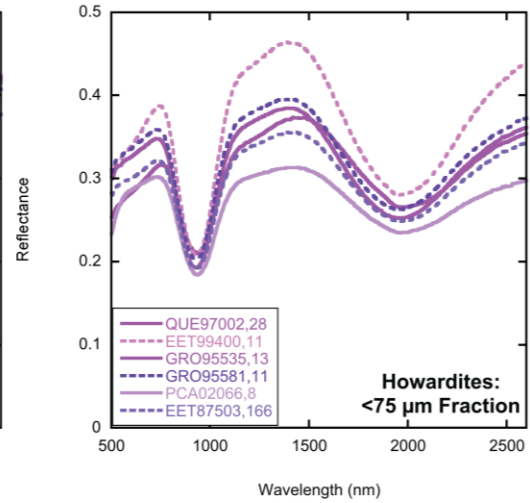
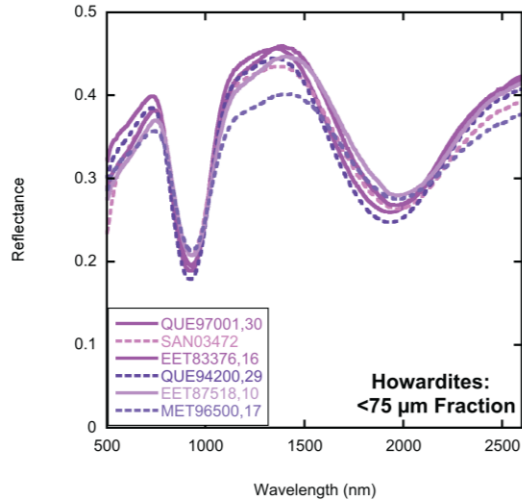


Fig. S4: Spectra for all HED samples from the collection with grain size $<75 \mu\text{m}$. (A-E) Howardites. (F) Polymict eucrites. Spectra for the <25 grain size fraction are available from RELAB at <http://www.planetary.brown.edu/relab/>.

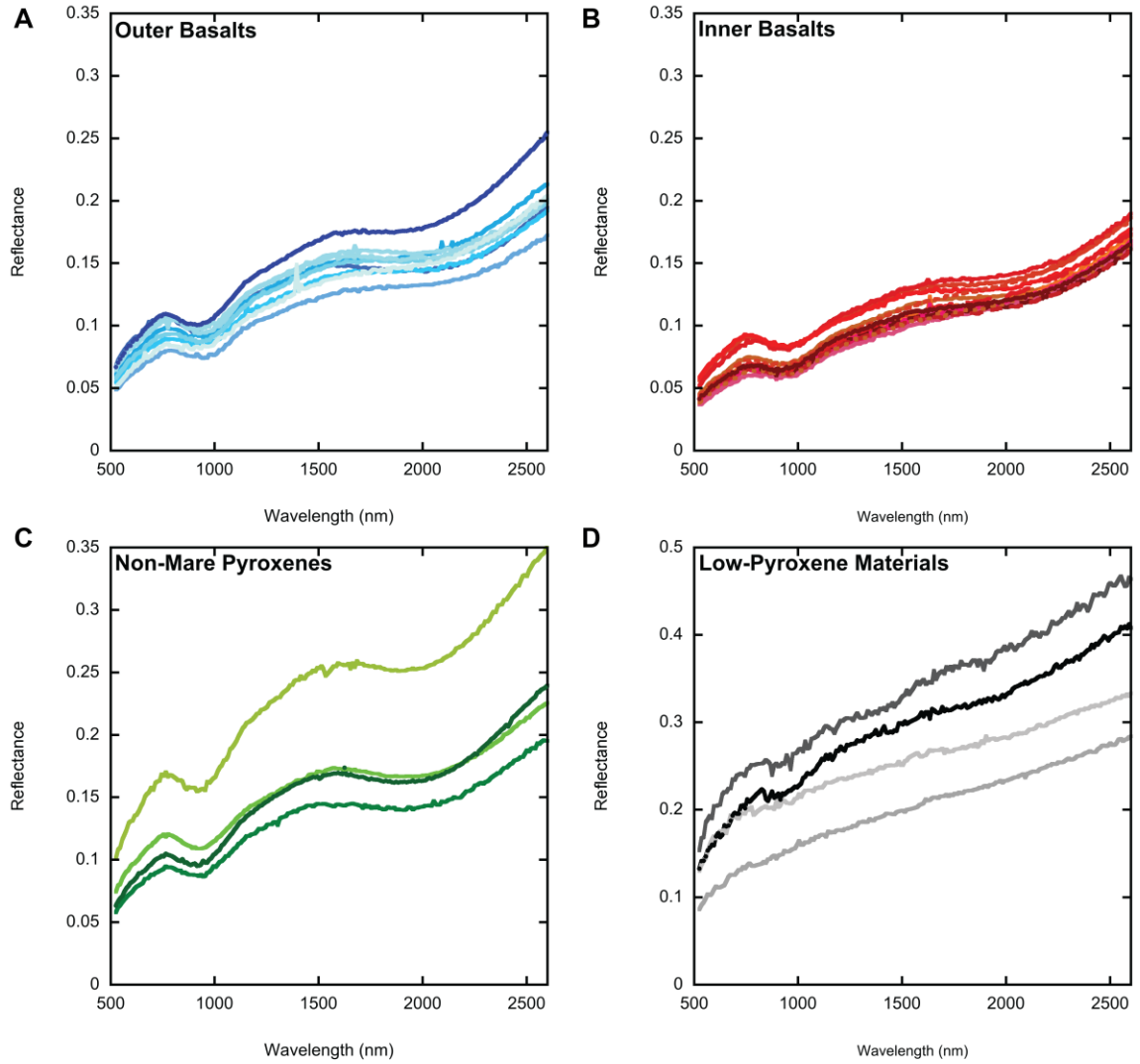


Fig. S5: Example M^3 target spectra for the four material types identified in the Humboldtianum Basin subregion: (A) inter-ring basalts, (B) central Mare Humboldtianum basalts, (C) non-mare materials with high pyroxene content, and (D) non-mare materials with low pyroxene content. The y-axis scale for (D) is different that for (A-C).

Appendix B: Location and description of all spectral and
topographic observations (Chapter 2)

Daniel P. Moriarty III [Daniel_Moriarty@Brown.edu]

Carle M. Pieters

Department of Earth, Environmental, and Planetary Sciences

Brown University

324 Brook Street

Providence, RI 02912

Supplemental Table 1: Location and Description of All Spectral and Topographic Observations

Feature Designation	Feature Type	Lat.	Lon.	Diameter	M3 Image-cube	Fig. No.	Spectrum Context	M³ X	M³ Y
Mafic Mound	Mound	58° S	162° W	~75 km	M3G200906 21T022743	3, 4, S1A	6 km crater on NW lobe	110	4774
						3, 4, S1A	6 km crater on NW lobe	121	4784
						2, 3, 4, S1A	Small crater on SE lobe	219	4928
						3, 4, S1A	10 km crater on SW lobe	48	4952
						3, 4, S1A	11 km crater on SW rim	94	4950
						3, 4, S1A	Small crater on S rim	156	4964
						3, 4, S1A	9 km crater on SE lobe	177	5023
						3, 4, S1A	8 km crater on SE lobe	224	5012
						3, 4, S1A	8 km crater on SE lobe	247	5023
						3, 4, S1A	6 km crater on SSE lobe	127	5093
Apollo Basin – South Mare	Mare	41.5° S	155° W		M3G200906 20T134543	2, 3A, S1B	Small crater	136	20567
						3A, S1B	Small crater	259	20118
						3A, S1B	Bright spot	16	20245
						3A, S1B	Small crater	110	20321
						3A,	Small crater	216	20343

						S1B			
						3A, S1B	Small crater	184	20393
Mare SW of Apollo	Mare	46° S	164° W		M3G200906 21T022743	3A, S1B	Small crater	86	2249
						3A, S1B	Bright spot	104	2332
						3A, S1B	Small crater	69	2404
						3A, S1B	Small crater	92	2490
						3A, S1B	Small crater	145	2500
						3A, S1B	~1 km crater	103	2561
						3A, S1B	Small crater cluster	162	2751
						3A, S1B	Small crater	147	2913
Mare NE of Bhabha	Mare	52° S	162° W		M3G200906 21T022743	3A, S1B	Small crater	259	3178
						3A, S1B	Small crater	168	3570
						3A, S1B	~1 km crater	176	3757
Cryptomare SW of Apollo	Cryptomare	47° S	155° W		M3G200906 20T134543	3A, S1C	4.5 km crater	223	20872
						2, 3A, S1C	Chain of ~2 km craters	265	20934
						3A, S1C	~1.5 km crater	256	21023
						3A, S1C	~1 km crater	285	21245

						3A, S1C	Small crater	174	21310
						3A, S1C	11 km crater	38	21322
						3A, S1C	3.7 km crater	110	21437
Bhabha	Central peak crater	55.5° S	165° W	70 km	M3G200906 21T065503	3A, S1D	Central peak	93*	27952 *
					M3G200906 21T022743	3A, S1K	Wall	132	4327
						3A, S1K	Wall	103	4330
						3A, S1K	Wall	47	4480
Dryden	Central peak crater	33° S	156° W	54.5 km	M3G200906 20T134543	3A, S1D	Central peak	161*	18507 *
						3A, S1D		161	18507
Finsen	Central peak crater	42.5° S	178° W	73 km	M3G200906 22T041041	3A, S1D	Central peak	80*	2878*
Van de Graaf	Central peak crater	27° S	172° E	240.5 km	M3G200906 23T012541	3A, S1D	Central peak	91*	24282 *
White	Central peak crater	45° S	159° W	42 km	M3G200906 20T181042	3A, S1D	Central peak	78*	26237 *
Stoney	Central peak crater	55.5° S	156. 5 W	47.5 km	M3G200906 20T134543	3A, S1D	Central peak	76	23029
						3A, S1D		77	23038
hf1	Hummocky floor crater	50.6° S	157. 8° W	17 km	M3G200906 20T134543	3D, 3G, 4B, S1F,	Rim	13	22141

						S2A			
						3D, S1E, S2A	Floor	5	22094
hf2	Hummocky floor crater	51.3° S	157° W	16 km	M3G200906 20T134543	3D, S1F, S2A	Rim	81	22262
						3D, S1E, S2A	Floor	60	22228
						3D, S1E, S2A	~1 km floor crater	69	22213
hf3	Hummocky floor crater	42.3° S	163° W	13 km	M3G200906 21T022743	3D, S1F, S2A	Rim	151	1684
						3D, S1F, S2A	Rim	133	1693
						3D, S1E, S2A	Floor	119	1664
hf4	Hummocky floor crater	44.6° S	164° W	10 km	M3G200906 21T022743	3D, S1F, S2A	Rim	43	2165
						3D, S1E, S2A	Floor	34	2132
						3D, S1E, S2A	Floor	40	2141
						3D, S1E,	Floor	53	2145

						S2A			
hf5	Hummocky floor crater	48.4° S	163.7° W	14 km	M3G200906 21T022743	3D, S1F, S2A	Rim	81	2952
						3D, S1F, S2A	Rim	78	2861
						3D, S1E, S2A	Floor	69	2907
						3D, S1E, S2A	Floor	78	2936
hf6	Hummocky floor crater	54.2° S	164.1° W	8.5 km	M3G200906 21T022743	3D, S1F	Rim	32	4151
						3D, S1E	Floor	37	4125
						3D, S1E	~0.5 km floor crater	44	4106
hf7	Hummocky floor crater	55.8° S	160.4° W	8.8 km	M3G200906 21T022743	3D, S1F, S2A	Rim	282	4502
						3D, S1E, S2A	Floor	284	4486
						3D, S1E, S2A	Floor	275	4482
White W	Flat floor crater	42.4° S	163.6° W	24 km	M3G200906 21T022743	3B, 3E, 4B, S1H,	Rim	117	1735

						S2B			
						3B, S1G, S2B	Floor	74	1724
						3B, S1G, S2B	Floor	96	1681
ff1	Flat floor crater	47.3° S	161. 1° W	5.2 km	M3G200906 21T022743	3B, S1H, S2B	Rim	272	2717
						3B, S1G, S2B	Floor	273	2703
ff2	Flat floor crater	47.2° S	161. 3° W	6.25 km	M3G200906 21T022743	3B, S1H, S2B	Rim	249	2739
						3B, S1G, S2B	Floor	248	2722
ff3	Flat floor crater	47.8° S	161. 8° W	4.9 km	M3G200906 21T022743	3B, S1H, S2B	Rim	204	2811
						3B, S1G, S2B	Floor	216	2800
ff4	Flat floor crater	47.8° S	162. 2° W	4.7 km	M3G200906 21T022743	3B, S1H, S2B	Rim	185	2826
						3B, S1G, S2B	Floor	188	2809
ff5	Flat floor crater	50.6° S	161. 9° W	12 km	M3G200906 21T022743	3B, S1H,	Rim	210	3417

						S2B			
						3B, S1G, S2B	Floor	184	3402
						3B, S1G, S2B	Floor	209	3396
ff6	Flat floor crater	51.7° S	163. 7° W	26.6 km	M3G200906 21T022743	3B, S1H, S2B	Rim	23	3563
						3B, S1G, S2B	Floor	54	3648
						3B, S1G, S2B	~1 km floor crater	58	3606
						3B, S1G, S2B	~1 km floor crater	43	3595
ff7	Flat floor crater	52° S	162° W	9.2 km	M3G200906 21T022743	3B, S1H, S2B	Rim	172	3673
						3B, S1G, S2B	~0.5 km rim crater	163	3691
						3B, S1G, S2B	Floor	172	3673
						3B, S1G, S2B	Floor	147	3666
ff8	Flat floor crater	53.3° S	161. 8° W	10.9 km	M3G200906 21T022743	3B, S1H,	Rim	189	3977

						S2B			
						3B, S1G, S2B	Floor	188	3937
						3B, S1G, S2B	Floor	191	3943
ff9	Flat floor crater	54.4° S	160. 2° W	15.6 km	M3G200906 21T022743	3B, S1H, S2B	Rim	294	4244
						3B, S1H, S2B	Rim	272	4227
						3B, S1G, S2B	Floor	294	4227
						3B, S1G, S2B	~0.5 km floor crater	298	4197
bc1	Buried crater	45.9° S	164. 4° W	7 km	M3G200906 21T022743	3C, S1J	Rim	11	2429
						3C, S1I	Floor	4	2410
bc2	Buried crater	46° S	164° W	4.7 km	M3G200906 21T022743	3C, S1J, S2C	Rim	40	2437
						3C, S1I, S2C	Floor	47	2424
						3C, S1I, S2C	0.5 km floor crater	51	2432
bc3	Buried crater	46.3° S	164.	17 km	M3G200906	3C,	Rim	7	2441

			4° W		21T022743	3F, 4B, S1J, S2C			
						3C, S1J, S2C	Rim	42	2453
						3C, S1J, S2C	Rim	23	2524
						3C, S1J, S2C	2 km rim crater	44	2502
						3C, S1I, S2C	Floor	16	2513
						3C, S1I, S2C	0.5 km floor crater	15	2488
bc4	Buried crater	45.9° S	163. 6° W	3.8 km	M3G200906 21T022743	3C, S1J	Rim	82	2429
						3C, S1I	Floor	76	2419
bc5	Buried crater	45.8° S	162. 4° W	8.75 km	M3G200906 21T022743	3C, S1J, S2C	Rim	178	2460
						3C, S1I, S2C	1 km rim crater	175	2472
						3C, S1I, S2C	Floor	162	2445
bc6	Buried crater	46.7° S	162.	6 km	M3G200906	3C,	Rim	167	2579

			5° W		21T022743	S1J, S2C			
						3C, S1I, S2C	Floor	164	2566
bc7	Buried crater	47.5° S	162° W	7 km	M3G200906 21T022743	3C, S1J, S2C	0.5 km rim crater	207	2722
						3C, S1I, S2C	0.75 km floor crater	200	2752
bc8	Buried crater	50.1° S	161. 3° W	5.5 km	M3G200906 21T022743	3C, S1J, S2C	Rim	241	3304
						3C, S1I, S2C	Floor	242	3278
bc9	Buried crater	50.7° S	161. 4° W	5.75 km	M3G200906 21T022743	3C, S1J, S2C	Rim	235	3430
						3C, S1I, S2C	Floor	240	3409

Table S1. This table provides background information for each spectral and topographic measurement presented in the paper and supporting information. A description of each column is as follows:

1. A designation for each feature characterized in these analyses. Official nomenclature is used where available. Most of the modified craters documented here do not have official names and are assigned the following designations: hf# for hummocky-floor craters, ff# for flat-floor craters, and bc# for buried craters.
2. An informal classification of the type of feature designated by (1).
3. Central latitude of the feature.
4. Central longitude of the feature.
5. Diameter of the feature (where applicable).
6. The name of the Moon Mineralogy Mapper image-cube covering the designated feature used to obtain spectra.
7. A list of figures including the specified M³ spectrum (for composition-related figures) or overall feature (for topography-related figures).
8. A brief description of the specific context within the broader feature for each spectrum obtained.
9. X-coordinate of the Moon Mineralogy Mapper image-cube corresponding to the central pixel from which the individual spectrum was derived. Spectra were obtained from 3x3 pixel averages.

10. Y-coordinate of the Moon Mineralogy Mapper image-cube corresponding to the central pixel from which the individual spectrum was derived. Spectra were obtained from 3x3 pixel averages.

* Starred M³ coordinates for several central peak spectra indicate spectral averages for larger areas (up to hundreds of pixels).

Appendix C: Supplemental Figures for Chapter 2

Daniel P. Moriarty III [Daniel_Moriarty@Brown.edu]

Carle M. Pieters

Department of Earth, Environmental, and Planetary Sciences

Brown University

324 Brook Street

Providence, RI 02912

Introduction

Here, we provide the complete set of spectral, topographic, and gravitational data used in these analyses. Fig. S1 is a LOLA topographic map of the Mafic Mound area overlaid on WAC imagery, essentially a larger version of Fig. 1c overlaid on Fig. 1b. Fig. S2 shows each Moon Mineralogy Mapper spectrum analyzed to produce the band center plots in Fig. 3 in the main text. Fig. S3 gives topographic profiles for additional Mafic Mound transverses as well as several modified craters mentioned in the text. Fig. S4 is a map of the GRAIL Bouguer gravitational anomaly for the SPA region.

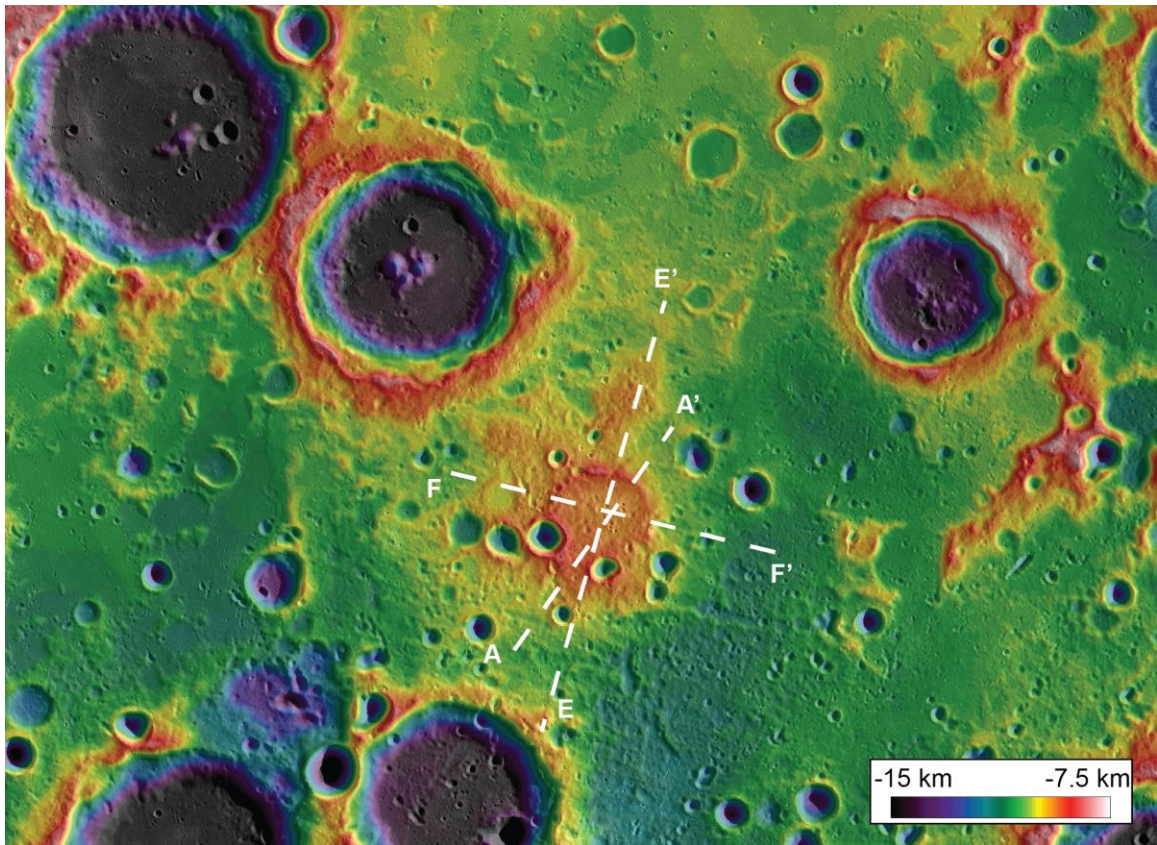


Figure S1. Lunar Orbiter Laser Altimeter (LOLA) topography (16 pixels per degree) [Smith et al., 2010] overlaid on a Lunar Reconnaissance Orbiter Wide Angle Camera (WAC) mosaic (100 m per pixel) [Robinson et al., 2010] for the Mafic Mound region. Transverses A,E-F show the locations for the topographic profiles given in Figs. 4 and S3.

Fig. S2:

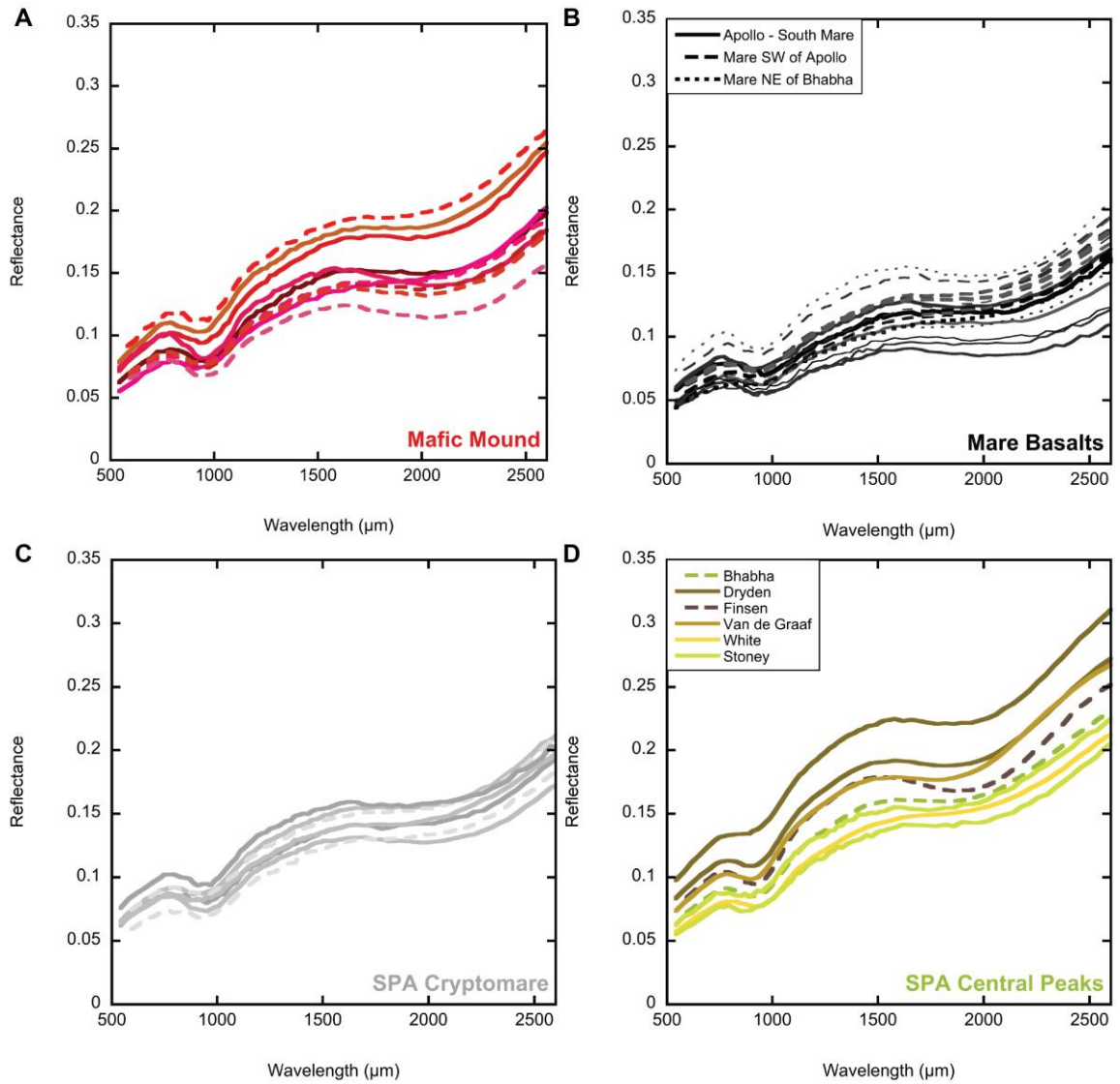


Fig. S2 (con't):

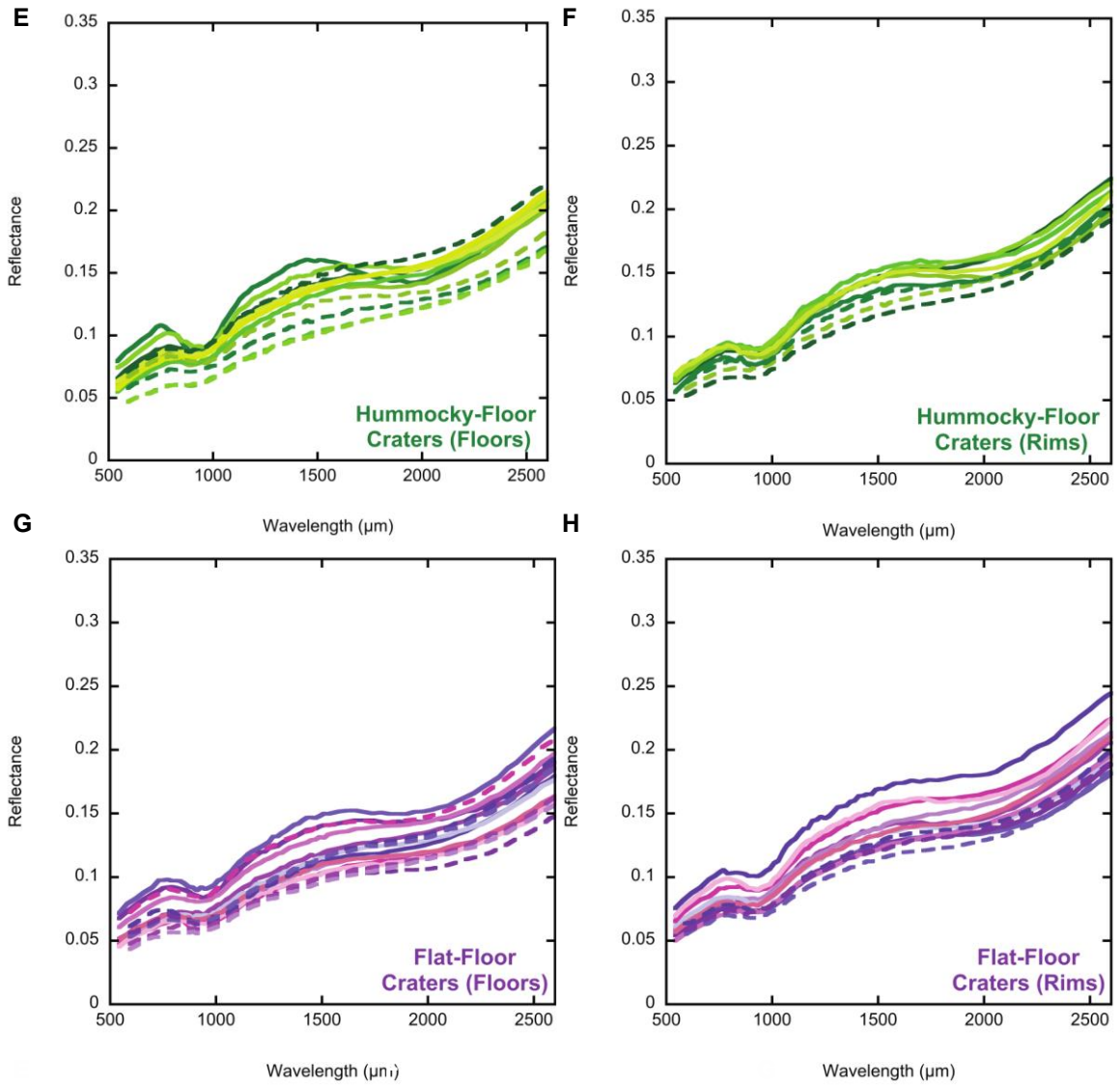


Fig. S2 (con't):

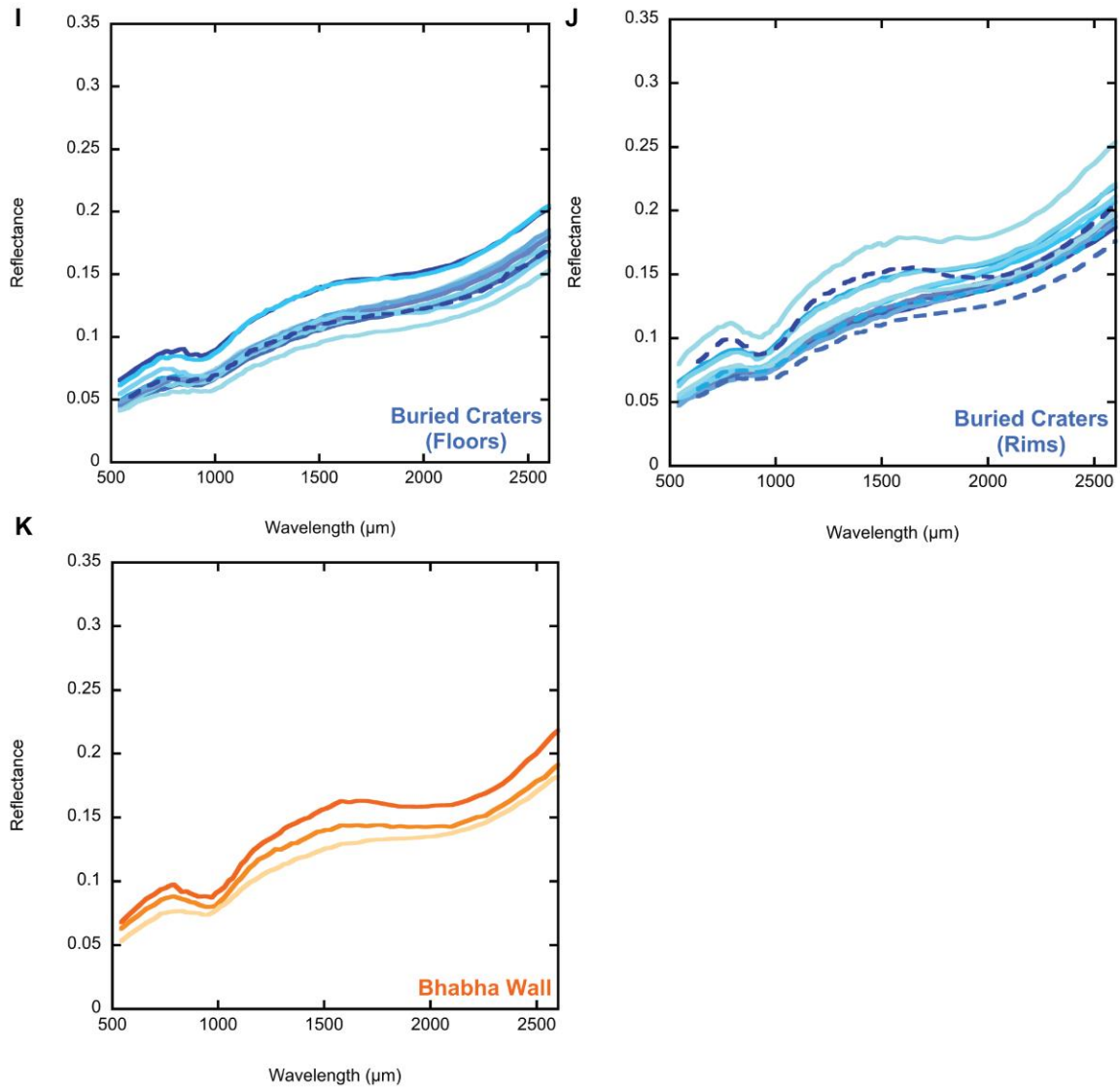


Figure S2. The complete set of Moon Mineralogy Mapper spectral observations used in these analyses, including spectra from (A) Mafic Mound, (B) example SPA mare basalts, (C) example SPA cryptomare basalts, (D) central peaks of several complex craters within SPA , (E) example hummocky-floor crater floors from within SPA, (F) rims of these hummocky-floor craters, (G) example flat-floor crater floors from within SPA, (H) rims of these flat-floor craters, (I) example buried crater floors from within SPA, (J) rims of these buried craters, and (K) Bhabha's wall. Spectra were collected as 3x3 pixel averages from steep slopes and fresh craters to minimize the contributions of developed soils. The 1 μm and 2 μm band centers for each spectrum were

measured using PLC analysis [Moriarty and Pieters, 2015] and are presented in Fig. 3. The precise locations and other information about these observations are presented in Table S1.

Fig. S3:

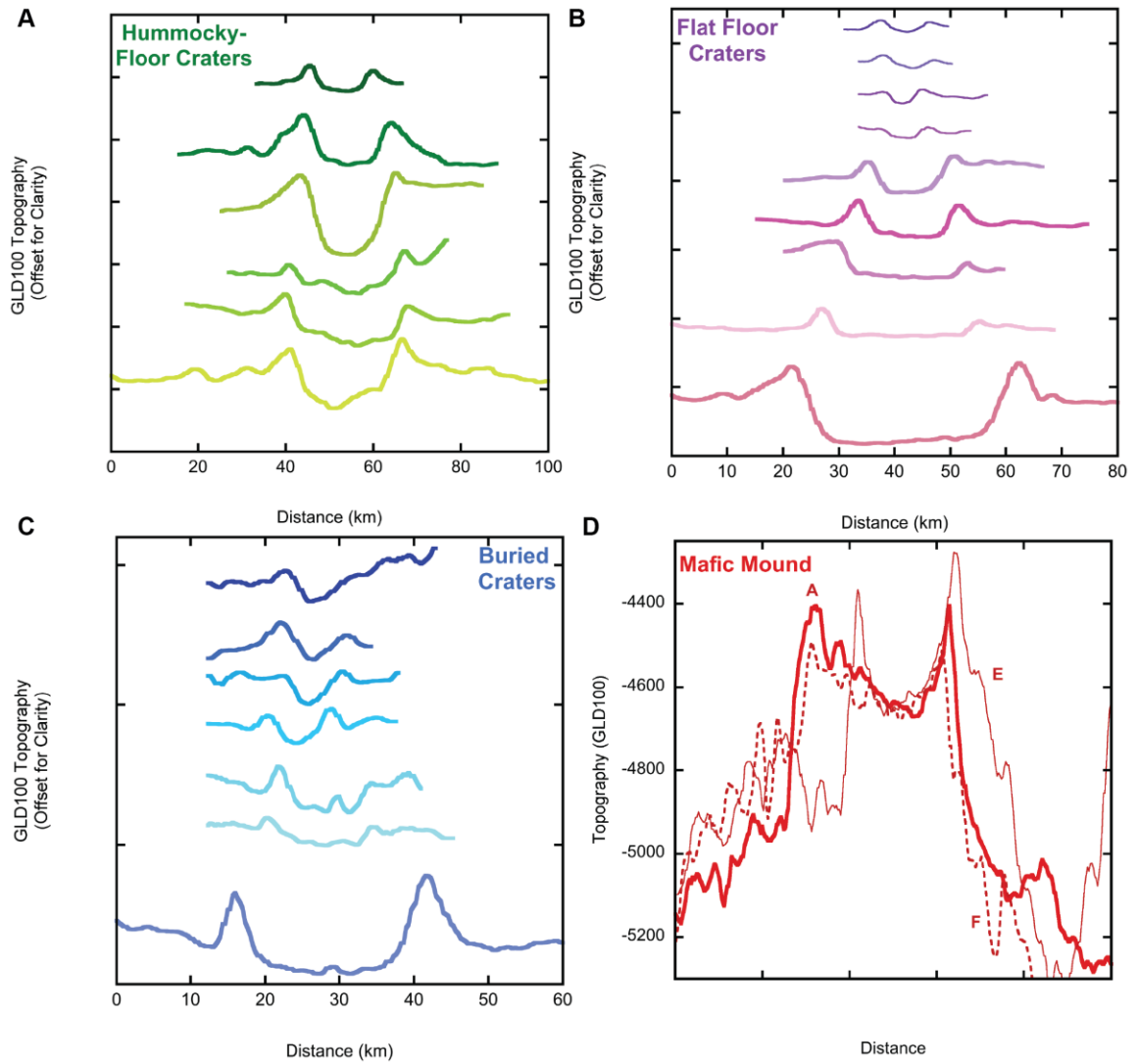


Figure S3. Topographic profiles for several example modified craters (A-C) and additional Mafic Mound transverse (D). The transverse for Mafic Mound are given in Fig. S1. Topographic data was obtained using the WAC GLD100 digital terrain model [Scholten et al. 2012]. For A-C, each tick mark on the Y-axis represents 1 km. The locations of each crater are given in Table S1.

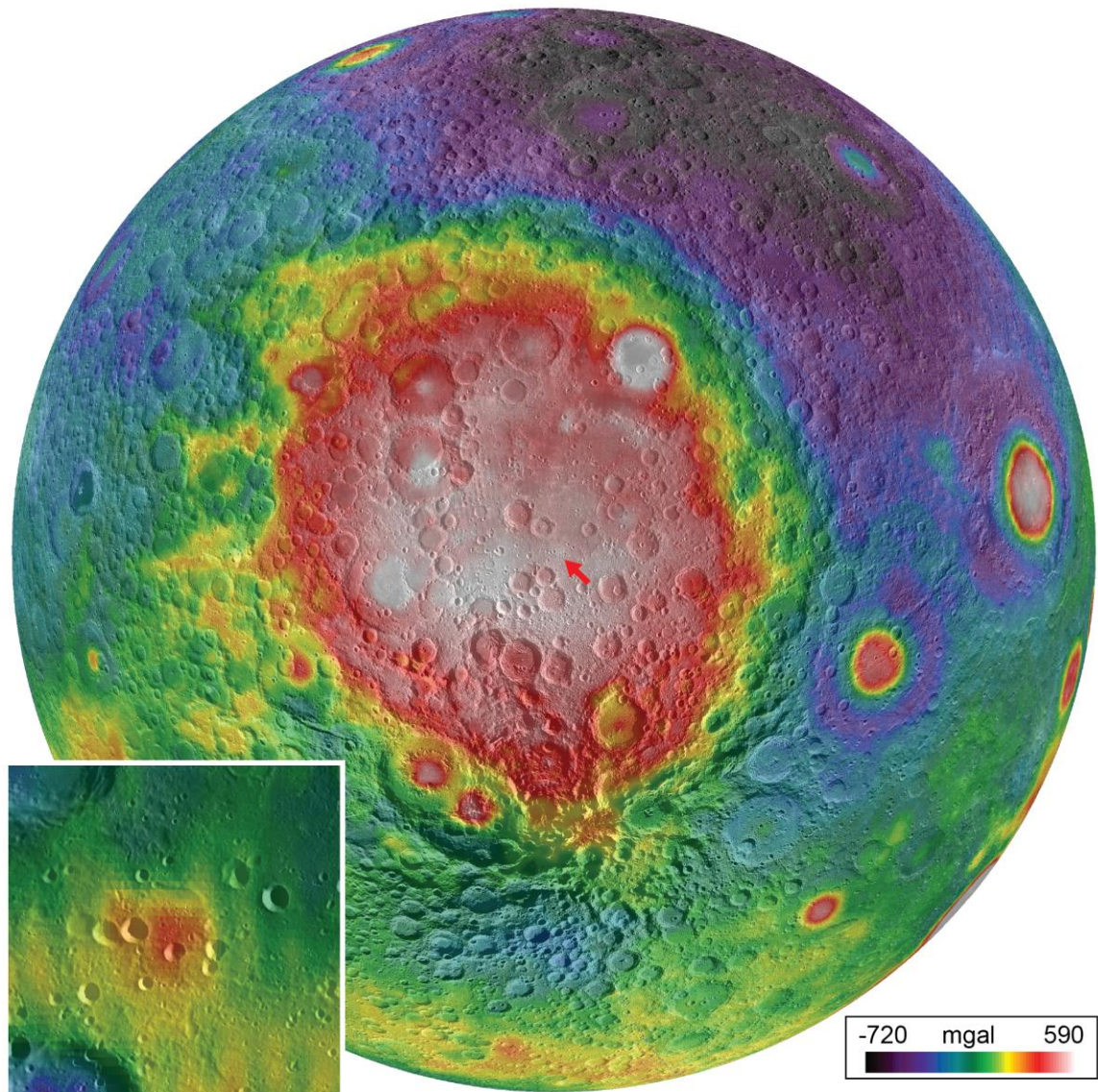


Figure S4. Bouguer gravity anomaly derived by GRAIL [Zuber et al. 2013] centered on Mafic Mound. The gravity field uses a spherical harmonic model to degree and order 600. Spatial resolution is 8 pixels per degree. The GRAIL data are overlaid on a 100 m per pixel WAC mosaic [Robinson et al. 2010]. The location of Mafic Mound is indicated by the red arrow. Inset: local Bouguer anomaly of the Mafic Mound region. The Mafic Mound structure is clearly associated with a localized positive Bouguer anomaly. For the inset, the color stretch (280 mgal to 490 mgal) has been adjusted to highlight local variations. These GRAIL Bouguer anomaly data are publicly available through the Planetary Data System.

Appendix D: Supplemental Spectra for Chapters 3,4,5

Daniel P. Moriarty III [Daniel_Moriarty@Brown.edu]

Carle M. Pieters

Department of Earth, Environmental, and Planetary Sciences

Brown University

324 Brook Street

Providence, RI 02912

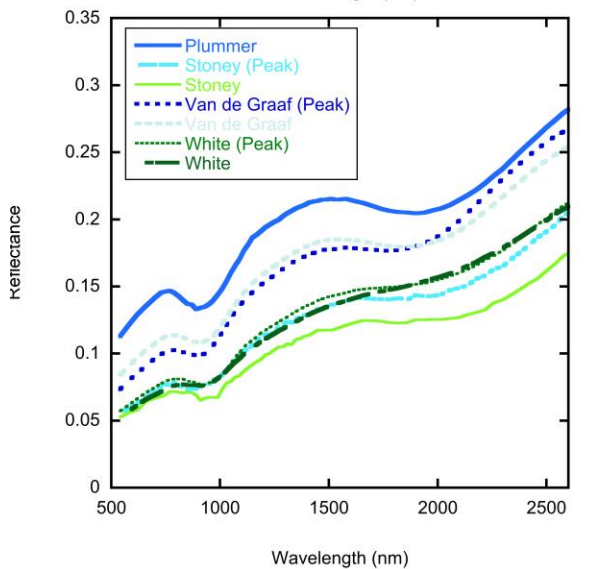
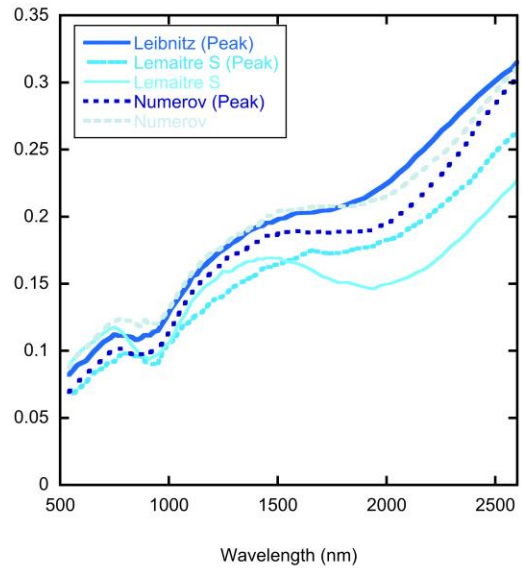
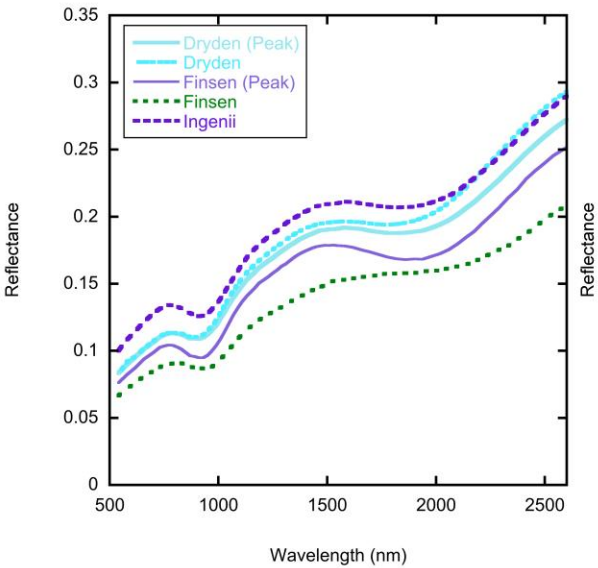
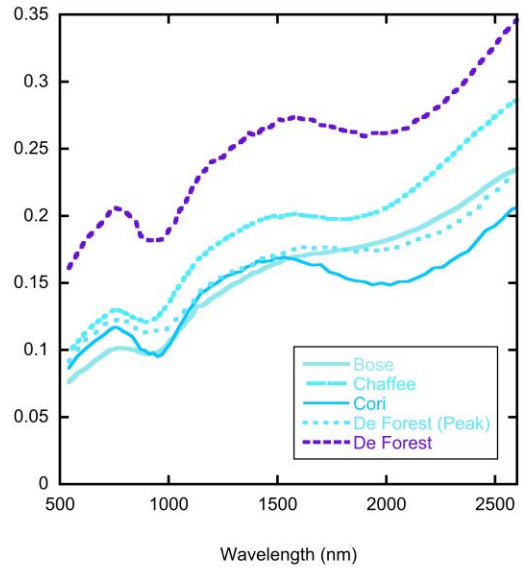
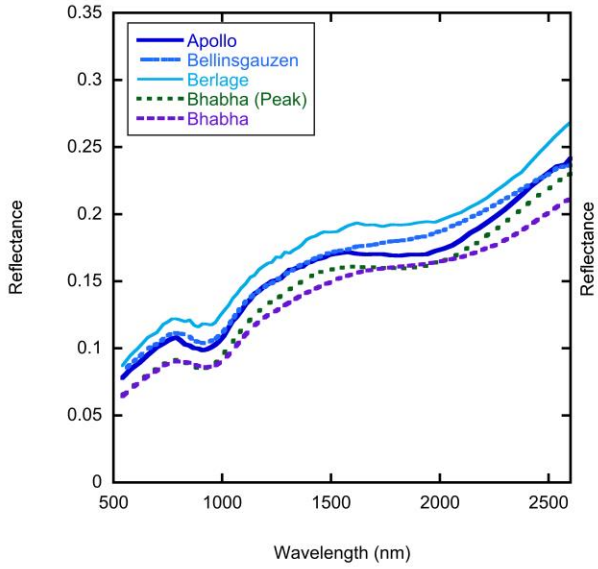


Fig. 1: Moon Mineralogy Mapper spectra for several complex craters listed in Chapter 4, Table 1. All spectra were derived from 3x3 pixel averages from OP2C1 data. All spectra are derived from crater walls unless otherwise specified. Mg-pyroxene-bearing materials are plotted in blue/purple. SPACA surface materials are plotted in greens. For more information on each crater, see Chapter 4, Table 1.